

Electronic Thesis and Dissertation Repository

2-20-2020 11:00 AM

Experimental Investigation on the Impact of Wall Heating on Mixed Convection Turbulent Boundary Layer Flow Structure

Kadeem Dennis, *The University of Western Ontario*

Supervisor: Siddiqui, Kamran, *The University of Western Ontario*

A thesis submitted in partial fulfillment of the requirements for the Doctor of Philosophy degree in Mechanical and Materials Engineering

© Kadeem Dennis 2020

Follow this and additional works at: <https://ir.lib.uwo.ca/etd>

Recommended Citation

Dennis, Kadeem, "Experimental Investigation on the Impact of Wall Heating on Mixed Convection Turbulent Boundary Layer Flow Structure" (2020). *Electronic Thesis and Dissertation Repository*. 6860. <https://ir.lib.uwo.ca/etd/6860>

This Dissertation/Thesis is brought to you for free and open access by Scholarship@Western. It has been accepted for inclusion in Electronic Thesis and Dissertation Repository by an authorized administrator of Scholarship@Western. For more information, please contact wlsadmin@uwo.ca.

Abstract

The hydrodynamic and thermal boundary layers are known to be key regulators of the interfacial transport of mass, momentum and heat, which are crucial in a wide range of engineering and environmental applications. The boundary layers encountered in these applications are often turbulent in nature and characterized by the presence of three-dimensional motion and non-linear dissipative phenomena. The presence of heat transfer between the bulk fluid and the solid wall increases flow complexity due to the interaction of the buoyant force with flow inertia and non-linear coupling between thermo-fluid variables. As a key contributor to multiple engineering systems and environmental phenomena, advancement of the current knowledge on turbulent boundary layer dynamical behaviors is crucial.

In the present study, turbulent boundary layer flow over a heated horizontal smooth wall was investigated utilizing an experimental approach. The current state-of-the-art techniques for 3D flow characterization are often limited in their broad applicability. The present knowledge is improved upon with the development of a novel technique based on volumetric illumination with a multi-color pattern. In the absence of heat transfer, the turbulent boundary layer is known to contain a wide range of dynamical phenomena whose behaviors still lack a comprehensive understanding. The present study investigated the unheated turbulent boundary layer utilizing a unique implementation of the Particle Image Velocimetry (PIV) technique to characterize the three-dimensional (3D) nature of the flow and reported new findings on near-wall turbulent flow behavior. In the presence of heat transfer, once the buoyant force magnitude is sufficiently large, thermals detach and rise from the heated wall. The characteristics of thermals in a heated turbulent boundary layer was investigated in 3D utilizing PIV. A novel image processing algorithm was developed to detect thermals. The modification to the turbulent boundary layer velocity field by wall heating was studied utilizing PIV data. Results indicate that boundary layer behavior is influenced by the buoy-

ant force via modification to the turbulent velocity field and associated velocity statistics. This study provides multiple new contributions on flow characterization techniques and the behaviors of the turbulent boundary layer in the presence and absence of heat transfer.

Keywords: turbulent boundary layer, particle image velocimetry, flow visualization, image processing, statistics, turbulent flow, flow measurement, heat transfer

Summary for Lay Audience

Fluid mechanics is one of the broadest areas of physics with a wide variety of practical applications. Often topics of interest in fluid mechanics feature the interaction of fluid and solid object where mass and energy are exchanged. As fluid passes over a solid, a thin region of fluid adjacent to the solid forms known as the boundary layer. The most well-known boundary layer is the atmospheric boundary layer (ABL) produced by air in the Earth's atmosphere passing over the Earth's surface. Every form of life on Earth is influenced by the behavior of the atmospheric boundary layer. The energy exchange between the ABL and Earth's surface governs the wind loading experienced by structures such as buildings and bridges. Thermal energy, i.e. heat, and mass exchange (e.g. evaporation) strongly influence the strength of tropical storms and winter blizzards. The distribution of emissions, greenhouse gases, and particulate matter are all governed by ABL behaviors. In light of the far-reaching impact and near ubiquity of boundary layer flows, many physical processes that determine boundary layer behavior are unknown or not well-understood.

In the present study, boundary layer behavior in the presence of heating from the solid surface was investigated. As boundary layer flow often features highly three- motion, a new technique was developed to describe this fluid flow. Next, experiments were performed in the boundary layer to investigate and characterize some boundary layer phenomena that were not well-understood in the past. The findings of this study show that heat transfer from the solid drives unique fluid phenomena that modify overall boundary layer behavior in a non-linear manner. The conclusions of this study can be used by scientists and engineers to improve engineering systems and produce more advanced predictive models of the atmospheric boundary layer.

Co-Authorship Statement

This integrated article doctoral thesis is organized into six chapters where four chapters are co-authored papers by Kadeem Dennis and Kamran Siddiqui. In each of the four co-authored papers, Kadeem Dennis was responsible for the design and execution of experiments, data collection and analysis, and manuscript writing. This comprised 90% of work for each chapter. Kamran Siddiqui provided raw resources, technical support, directional guidance, and manuscript editing which in total comprised 10% of the work for each co-authored paper. All of the co-authored papers in this thesis are planned to be submitted to peer-reviewed journals in 2020.

- Chapter 2 documents the development a novel flow characterization technique. It is intended to be submitted to *Experiments in Fluids*.
- Chapter 3 details a three-dimensional investigation into unheated turbulent boundary layer dynamics and is intended to be submitted to *Physics of Fluids*.
- Chapter 4 is on the detection and characterization of thermals in the heated turbulent boundary layer. This chapter is intended to be submitted to *Experimental Thermal and Fluid Science*.
- Chapter 5 documents the modification of turbulent boundary layer statistics in the presence of wall heating. This chapter is intended to be submitted to *Physics of Fluids*.

Dedication

This thesis is dedicated to my family, friends, coworkers, colleagues, and students who have all in some way influenced me. Without them I would not have made it this far. I am deeply grateful to all of you for your support and presence even in a seemingly trivial form. Thank you. "What an unbelievable four years it has been."

Acknowledgments

I would like to acknowledge and thank the Natural Sciences & Engineering Research Council of Canada (NSERC), the Ontario Ministry of Training, Colleges & Universities, the American Society of Mechanical Engineering (ASME), and the University of Western Ontario for their support.

Contents

Abstract	ii
Summary for Lay Audience	iv
Co-Authorship Statement	v
Dedication	vi
Acknowledgements	vii
List of Tables	xii
List of Figures	xiii
List of Appendices	xxi
Nomenclature	xxii
1 Introduction	1
1.1 The Boundary Layer	4
1.1.1 Historical Background	4
1.1.2 Laminar Boundary Layer Theory	6
1.1.3 Turbulent Boundary Layer Theory	14
Turbulent Boundary Layer Structure	21

1.2	Contemporary Boundary Layer Research	29
1.2.1	Unheated Turbulent Boundary Layer	33
1.2.2	Heated Turbulent Boundary Layer	38
1.3	Experimental Measurement Techniques	50
1.4	Research Objectives	58
1.4.1	Knowledge Gaps	59
	Experimental Measurement Techniques	59
	Mixed Convection Turbulent Boundary Layer	60
1.4.2	Thesis Layout	61
	Bibliography	62

2	A Color Permutation Algorithm for Three-Dimensional Flow Characterization	74
2.1	Introduction	74
2.2	The Color Permutation Method	78
2.3	Three-Dimensional Streak Placement Algorithm	80
2.3.1	Calibration	81
2.3.2	Pre-processing of Particle Streak Images	84
2.3.3	Depth Position Estimation	88
2.3.4	Three-Dimensional Reconstruction	89
2.3.5	Final Spatial Conversion	91
2.4	Synthetic Image Results	91
2.5	Effect of Streak Segment Length	96
2.6	Discussion and Conclusions	100
	Bibliography	101

3	An Investigation of the Near-Wall Multi-modal Turbulent Velocity Behaviour in the Boundary Layer	105
3.1	Introduction	105
3.2	Experimental Setup and Methods	109
3.3	Results	112
3.3.1	Mean Statistics	112
3.3.2	Statistical Description of Turbulent Flow Behavior	118
3.3.3	Instantaneous Turbulent Velocity Field Analysis	125
3.3.4	On the Mechanism of Multi-Modal $\phi(u')$ Formation	131
3.4	Conclusions	144
	Bibliography	144
4	Visualization and Characterization of Thermals in a Heated Turbulent Bound- ary Layer	151
4.1	Introduction	151
4.2	Experimental Setup	154
4.3	Visualization of Thermal-like Phenomena	157
4.4	Thermal Detection Technique	162
4.4.1	Verification	166
4.5	Characterization of Thermal Behaviors	176
4.5.1	Thermal Motion	184
4.6	Conclusion	189
	Bibliography	190
5	The Influence of Unstable Thermal Stratification on Near-Wall Turbulent Boundary Layer Characteristics	194
5.1	Introduction	194

5.2	Experimental Setup	198
5.3	Results	201
5.3.1	Mean Turbulent Statistics	207
	Vertical Stream-wise Plane	207
	Cross Stream Plane	211
5.3.2	Modification to Wall-Normal Turbulent Velocity Component	212
5.4	Conclusion	222
	Bibliography	223
6	Conclusions	227
A	PIV Uncertainty	235
	Bibliography	237
B	Introduction to Digital Image Processing	239
	Bibliography	246
	Curriculum Vitae	248

List of Tables

3.1	Friction velocity (u_*) estimates from each technique.	114
3.2	Normalized wall coordinates (y^+) of horizontal planes.	124
3.3	Approximate percentiles of POD energy content required to manifest multi-modality in $\phi(u')$ distribution.	136
4.1	Summary of experimental conditions.	156
4.2	Performance of segmentation algorithms considered in the vertical stream-wise plane.	170
4.3	Performance of segmentation algorithms considered in the horizontal plane 3.5 mm above the wall.	172
4.4	Performance of segmentation algorithms considered in the cross stream plane.	174
4.5	Estimated production layer thickness from vertical stream-wise plane thermal detection probability profiles.	180
5.1	Summary of experimental conditions.	199
5.2	Mean standard deviation and kurtosis of v' for a selection of cases.	219
5.3	Secondary peak magnitude of $v'v'^+$ at each Richardson number case.	221

List of Figures

1.1	Streak photograph taken by Prandtl of flow past a horizontal flat plate. The flow is seeded with reflective particles. Adapted from Schlichting [10].	7
1.2	Photograph of channel flow taken by Reynolds during the colored filament experiment. (a) Shows the path of the filaments laminar flow while (b) shows the evolution of filaments in turbulent flow. The primary flow direction is indicated by the white arrow. Adapted from Schlichting [10].	8
1.3	Sketch of boundary layer flow over a horizontal flat plate.	11
1.4	Plot of the skin friction coefficient vs Reynolds number showing the laminar Blasius solution with experimental data of laminar and turbulent flows by Liepmann and Dhawan. Adapted from Schlichting [10].	14
1.5	Mean stream-wise velocity profile in inner-layer scaling. Circles are from experimental data by Klebanoff, dashed curve shows the Direct Numerical Simulation (DNS) results by Spalart, dotted curve shows the DNS by Kim et. al., and the solid line is derived from boundary layer theory. Each constituent sub-layer is indicated. Adapted from Pope [14].	23
1.6	Profiles of the Reynolds stress components and turbulent kinetic energy in inner layer scaling for (a) the whole boundary layer and (b) zoomed on a section of the near-wall region. Adapted from Pope [14].	24
1.7	Contribution of each transport process to the total turbulent kinetic energy in the near-wall region. Adapted from Schlichting [10].	25

1.8	Velocity spectra of the turbulent boundary layer measured at three y-coordinates. Adapted from Schlichting [10].	27
1.9	Sequence of images showing formation of a hairpin vortex from vortex tubes. Adapted from Davidson [11].	31
1.10	Sketch of heated horizontal wall with quiescent fluid above.	39
1.11	Visualization of thermals rising from a heated horizontal flat plate. Adapted from Sparrow [49].	41
1.12	Velocity defect (a) and temperature defect (b) profiles across the boundary layer adapted from Arya [59] for stable and unstable turbulent boundary layers.	46
1.13	Profiles of four turbulent properties adapted from Hattori et. al [63]. (a) Reynolds shear stress, (b) wall normal turbulent heat flux, (c) stream wise turbulent heat flux, (d) wall normal turbulent intensity.	48
1.14	Detected coherent structures in the turbulent boundary layer, (a) without the buoyant force (b) with the buoyant force. Adapted from Li et. al. [64].	50
1.15	Sample PIV image pair (a) and (b) and one respective interrogation window (c) and search window (d).	54
1.16	Rigid translation of the interrogation window (red) inside the corresponding search window (blue) for an arbitrary translation $\Delta i, \Delta j$	54
1.17	Image of particle trajectories where color corresponds to the depth position found using the RVV technique. Adapted from Prenel [88].	57
2.1	(a) Five discrete colors and (b) one possible permutation of them.	80
2.2	Illustration of two discrete core regions and corresponding transition region.	81

2.3	Schematics of the two planes used for the calibration of (a) cross view and (b) measurement view. The light source in both views is oriented normal to the page.	83
2.4	Two intersecting streaks segmented as a single object in white.	85
2.5	(a) Streaks separated into ligaments after using the fiber separating method. (b) Detected overlapping region (white), the associated vertices (red), and detected intersection point (blue).	86
2.6	Images of the discretization process. (a) Shows the selected streak start point (green square), second streak and third segment points (red diamonds) and the distance between streak segment points. (b) Illustrates the resulting streak segments after watershed segmentation where each streak segment point is denoted with a red circle.	88
2.7	Synthetic images tested with the color permutation algorithm. (a) Contains the single streak image and (b) contains the intersecting streak image. . . .	92
2.8	Discretized streaks in the camera viewing plane. The single streak is shown in (a). The intersecting streaks in (b) have already been reconnected.	93
2.9	Three-dimensional view of the exact and discretized streak trajectories for (a) the single streak image and (b) the intersecting streak image. In both tests the streak segment length (b) was 20 pixels.	95
2.10	Original streak shape in white compared with discretized streak in red for three streak segment lengths. (a) $b = 178$. (b) $b = 78$. (c) $b = 18$	98
2.11	Median hue reconstruction of discretized streaks for two streak segment lengths (a) $b = 78$ and (b) $b = 18$	99
3.1	Schematic of wind tunnel test section. The measurement planes are also illustrated.	110

3.2	Mean stream-wise velocity profiles at different Reynolds numbers. Reference DNS data of Wu and Moin [36] and the Law of the Wall formulation ($u^+ = \frac{1}{\kappa} \ln y^+ + 5$ and $u^+ = y^+$) where $\kappa = 0.41$	115
3.3	Mean profiles of (a) planar turbulent kinetic energy, (b) stream-wise Reynolds stress, (c) wall-normal Reynolds stress (d) Reynolds shear stress for all tested Re_θ . DNS data from Wu and Moin provided as reference [36].	117
3.4	PDF of u'^+ over the entire horizontal plane and in the line of intersection between horizontal plane and vertical stream-wise plane at $Re_\theta = 700$ and $y = 3.5$ mm.	120
3.5	PDFs of u'^+ in the horizontal plane (right column) and corresponding intersecting region in the vertical stream-wise plane (left column) at various heights from the bottom wall, (a) 1.5 mm, (b) 3.5 mm, (c) 7.5 mm, (d) 12.5 mm.	122
3.6	Instantaneous turbulent velocity fields from the horizontal plane experiments at $Re_\theta = 280$ located at (a) 1.5 mm and (b) 3.5 mm above the wall. Mean boundary layer flow is in the positive x-direction.	127
3.7	(a) Instantaneous turbulent vorticity field with superimposed turbulent velocity vectors. (b) Detected vortices (white) for this vorticity field after vorticity threshold is applied. Horizontal plane experiment at $y = 3.5$ mm and $Re_\theta = 280$. Mean boundary layer flow is in the positive x-direction.	129
3.8	PDFs of u'^+ for detected vortices, non-vortices, and the overall distribution based on applied vorticity threshold technique. The vortices and non-vortices PDFs are normalized with the overall PDF.	130
3.9	Stream-wise POD eigenspectra for all tested Reynolds numbers at 1.5 mm and 3.5 mm above the bottom wall.	132

3.10	Stream-wise cumulative POD eigenspectra for all tested Reynolds numbers at 1.5 mm and 3.5 mm above the horizontal wall.	133
3.11	PDFs of u' at $Re_\theta = 700$ based on POD reconstructions using different percentiles of the total POD energy; E_{75} (blue), E_{85} (red), E_{95} (black), and E_{100} (green).	135
3.12	PDFs of u'^+ at $Re_\theta = 1000$ based on POD reconstructions of bottom 85% (0% to 85%) and top 15% (85% to 100%) of the cumulative POD energy.	137
3.13	PDFs of natural logarithm normalized dissipation based on reconstructions of the POD of the estimated dissipation rate. The distributions are separated based on the cumulative energy thresholds from the u' POD.	139
3.14	POD reconstruction of turbulent velocity vector fields from horizontal plane experiments at $Re_\theta = 1000$ located 3.5 mm above the wall. Panel (a) contains the reconstruction from E_{0-20} , (b) E_{20-40} , (c) E_{40-60} , (d) E_{80-100} . Mean boundary layer flow is in the positive x -direction.	143
4.1	Diagram of the experimental setup.	156
4.2	A set of images depicting the formation of thermals in all three measured planes at three Richardson numbers: 0.05 (top row); 0.3 (middle row); and 2.0 (bottom row). The field of view in the vertical stream-wise plane is 6 cm by 4.5 cm; horizontal plane: 23 cm by 17 cm; cross-stream plane: 8 cm by 5 cm.	160
4.3	An image illustrating the thermal and the surrounding flow. Inset depicts the difference in texture, quantified by local entropy, between high seed density background flow and low seed density thermal regions.	163
4.4	Illustration of the texture-based segmentation technique steps. Raw image is from $Ri_L = 2.0$ horizontal plane experiment, 3.5 mm above the wall.	165

4.5	Sample images showing original images (top row) and segmented images from the thermal detection technique (bottom row). Detected thermals are shown in black in the segmented images. Vertical stream-wise plane images are from experiment performed at $Ri_L = 0.3$, horizontal plane images from $Ri_L = 1.0$, and cross-stream images from $Ri_L = 2.0$	167
4.6	Sequence of images showing the quantities used for thermal detection verification.	170
4.7	Comparison of the original image and manual segmentation to the tested thermal detection techniques. These images are from the vertical plane experiment at $Ri_L = 2.0$	171
4.8	Comparison of the original image and manual segmentation to the multi-threshold and texture-based thermal detection techniques. These images are from the horizontal plane experiment at $Ri_L = 0.3$	173
4.9	Comparison of the original image and manual segmentation to the multi-threshold and texture-based thermal detection techniques. These images are from the cross plane experiment at $Ri_L = 0.3$	175
4.10	Mean thermal area coverage ($\overline{C_T}$) versus Richardson number for all measurement planes.	177
4.11	Plots of P_T versus y for all Ri_L from experiments performed in the vertical stream-wise plane. Inset contains the same profiles in a magnified view of the near-wall region.	178
4.12	Wall-normal distribution of P_T in the cross stream plane for all Ri_L considered.	181
4.13	Plots of P_T versus z for all Ri_L from experiments performed in the (a) $y = 3.5$ mm and (b) $y = 7.5$ mm horizontal plane.	183

4.14	Top row: Region of interest for velocity estimation in the original images of (left) roll-up signature in the vertical stream-wise plane and (right) rising thermal signature in the cross-stream plane. Bottom row: Detected thermal boundaries for each frame in the corresponding image pairs.	186
4.15	Estimated thermal velocity magnitude (V_T) versus the spatially-averaged surrounding velocity magnitude (V_S) at $Ri_L = 2.0$ for (a) roll-up signatures in the vertical stream-wise plane and (b) rising thermals in the cross-stream plane.	188
5.1	Diagram of the experimental setup.	199
5.2	204
5.2	A set of PIV images (left column) and corresponding instantaneous turbulent velocity vector field superimposed on a colormap of instantaneous planar turbulent kinetic energy (right column). The top panel corresponds to $Ri_L = 0.3$ and the bottom panel corresponds to $Ri_L = 0.03$. The top row in each panel is taken from the vertical stream-wise plane where mean flow is from left to right. The bottom row in each panel is from the cross-stream plane where mean flow is out of the page. All PIV images have been cropped and brightness/contrast enhanced.	205
5.3	Fraction of velocity vectors available for computation at different distances above the wall for (a) vertical stream-wise plane and (b) cross-stream plane.	206
5.4	Arrangement of the mean stream-wise velocity profiles in a 2×2 grid based on Re_θ	208
5.5	Mean stream-wise velocity profiles only for the heated wall cases expressed in inner layer coordinates.	208

5.6	Vertical profiles of $\overline{u'u'^+}$ (left column) and $\overline{v'v'^+}$ (right column) in wall coordinates for heated and unheated cases obtained in the vertical stream-wise plane. The plots are grouped according to Re_θ	210
5.7	Vertical profiles of $\overline{u'v'^+}$ for heated and unheated cases, in the vertical stream-wise plane, expressed in wall coordinates. Plots are grouped according to Re_θ	211
5.8	Vertical profiles of $\overline{w'w'^+}$ (left column) and $\overline{v'v'^+}$ (right column) in wall coordinates for heated and unheated cases obtained in the cross stream plane. The plots are grouped according to Re_θ	213
5.9	PDFs of v' for heated and unheated cases obtained in the vertical stream-wise plane. The plots are grouped according to Re_θ	215
5.10	Time history of v'^+ signal at a point 4 cm above the wall. (a) is from the $Ri_L = 0.3$ case ($Re_\theta = 700, T_W = 90$ °C) and (b.) is from the $Ri_L = 0.01$ case ($Re_\theta = 1700, T_W = 45$ °C) in the vertical stream-wise plane.	216
5.11	Time history of v'^+ signal at a point 4 cm above the wall. (a) is from the unheated $Re_\theta = 700$ case and (b.) is from the unheated $Re_\theta = 1700$ case in the vertical stream-wise plane.	218
5.12	PDFs of $v'v'^+$ for heated and unheated cases obtained in the vertical stream-wise plane. The plots are grouped according to Re_θ	221
5.13	Plot of the secondary peak in $\phi(v'v'^+)$ versus Ri_L	222
B.1	The <i>Coins</i> image (a) and its corresponding histogram (b).	241
B.2	The <i>Coins</i> image segmented via (a) gray level threshold at 100 and (b) segmented using Otsu's method where the calculated threshold was 126.	245

List of Appendices

Appendix A: PIV Uncertainty 235
Appendix B: Introduction to Digital Image Processing 239

Nomenclature

Abbreviations

Gr	Grashof number
PIV	Particle Image Velocimetry
Stereo-PIV	Stereoscopic Particle Image Velocimetry
Tomo-PIV	Tomographic Particle Image Velocimetry
Pr	Prandtl number
Re	Reynolds number
Ra	Rayleigh number
Ri	Richardson number
RVV	Rainbow Volumic Velocimetry
TKE	Turbulent Kinetic Energy

Mathematical Symbols

β	volumetric coefficient of thermal expansion	K^{-1}
C_p	isobaric specific heat capacity	$Jkg^{-1}K^{-1}$
C_v	isochoric specific heat capacity	$Jkg^{-1}K^{-1}$

$\frac{d}{d*}$	total derivative with respect to *	dimensionless
$\frac{\partial}{\partial*}$	partial derivative with respect to *	dimensionless
δ	boundary layer thickness	m
E	total system energy	J
e	internal energy	J
g	gravitational acceleration	ms^{-2}
h	enthalpy	J
k	thermal conductivity	$Wm^{-1}K^{-1}$
κ	von Karmann constant	dimensionless
∇	gradient operator	dimensionless
P	pressure	Pa
x	x-position variable	m
y	y-position variable	m
z	z-position variable	m
q''	heat flow per unit area (heat flux)	$\frac{W}{m^2}$
\bar{R}	specific ideal gas constant	$Jkg^{-1}K^{-1}$
ρ	density	kgm^{-3}
T	temperature	K
t	time	s
τ	shear stress	Pa
θ	momentum thickness	m
K	turbulent kinetic energy	m^2s^{-2}
u	x-directed velocity	ms^{-1}
v	y-directed velocity	ms^{-1}
w	z-directed velocity	ms^{-1}

\vec{v}	velocity vector	ms^{-1}
V	volume	m^3
μ	dynamic viscosity	$kgm^{-1}s^{-1}$
ν	kinematic viscosity	ms^{-2}
$\bar{\Omega}$	vorticity	s^{-1}

Superscripts

$\bar{*}$	time-average of *
+	inner layer scaling of quantity
'	fluctuation of property about the time average

Chapter 1

Introduction

In the field of fluid mechanics, one of the most frequently studied topics is the interaction between fluid and solid. Often the motivation for studying this topic is to better understand the exchange of mass and energy between fluid and solid. The energy exchange can take the form of both mechanical energy, e.g. a hydroelectric turbine, and thermal energy, e.g. a heat exchanger. The exchange of mass and energy between fluid and solid has a major impact on multiple areas of engineering and environmental science.

As fluid passes over and around a solid body, the body experiences a drag force in the direction parallel to the relative motion between the fluid and solid body. The drag force is a manifestation of the mechanical energy exchange between solid and fluid. The drag force is produced by two phenomena. First, the fluid must move to accommodate the solid's shape. This behavior manifests in the fluid as a non-uniform pressure distribution around the solid generating "form drag". The fluid must also stick to the solid surface due to viscous effects, thus producing "friction drag". Drag plays a major role in the operation of numerous practical engineering applications, such as in transportation systems where it is necessary to overcome drag via engine fuel consumption to either accelerate or main-

tain constant velocity of the vehicle. Buildings and structures are subjected to complex wind loads. The drag force generated by wind loading can lead to structural instability and failure which has been observed in the past [1, 2]. As many engineering structures feature complex geometries such as bridges and power transmission towers, predicting drag becomes challenging. A significant challenge in estimating drag on structures originates from predictions of wind behavior in the atmosphere. It is thus desirable to improve the current knowledge of atmospheric wind behavior to facilitate the development of improved predictive wind models and drag reduction systems. These are two applications where drag reduction is desirable. In contrast, there are applications where increased drag is beneficial such as in aviation where flaps and spoilers are used to slow down aircraft before landing. Generally, it is desirable to manipulate drag as needed for a specific application. To achieve this goal there must be a comprehensive understanding of how drag is generated.

At a solid-fluid interface, there is often an exchange of thermal energy. This is frequently utilized in heat exchangers where a working fluid undergoes a thermal energy transfer to or from the adjacent solid boundary. In some applications, it is desirable to heat or cool the solid surface. One application is in photovoltaic (PV) panels where it is desirable to cool PV cells whose temperature increases when absorbing solar radiation. Increasing PV cell temperature is undesirable as it decreases electrical conversion efficiency [3]. In engineering systems that involve convective heat transfer, an improved understanding of the near-interfacial fluid behavior is crucial to improve the thermal performance of these systems.

In addition to the exchange of both mechanical and thermal energy across a solid-fluid interface, mass and species transport is also encountered in a range of applications. The interaction of the Earth's surface and surrounding atmosphere is a major application of the mass/species transport processes. As air passes over a body of water, mass exchange

occurs via evaporation and species transport into the water body. Both water vapor in the atmosphere, i.e. humidity, and the bulk water temperature in the body of water are known to influence global and local weather patterns [4, 5]. Over land, a similar mass exchange occurs where particulate matter and gaseous species are transported by fluid motion in the atmosphere. In all atmosphere-surface interactions, heat exchange may directly impact local mass transfer via buoyancy-induced secondary flow. This behavior has been observed over land in the modification of Radon gas transport into the atmosphere [6]. A better understanding fluid behavior in these solid-fluid interactions is important for improved characterization and parameterization of various atmospheric phenomena, leading to more advanced weather and species transport predictive models.

In applications dealing with solid-fluid interactions, often the bulk fluid passes over a solid surface forming a region of fluid adjacent to the surface known as the boundary layer. The boundary layer is often very thin relative to the solid object dimensions and exhibits a more viscous behavior than the bulk fluid flow. The boundary layer is one of the major regulators of interfacial energy and mass exchange. The importance of the boundary layer to these exchanges has led to the development of multiple correlations for the engineering parameters that describe friction drag, convective heat transfer, and mass/species transfer [7–9]. Several of these correlations are empirical in nature as the governing boundary layer phenomena are not well understood. It is of interest to the engineering and scientific community to advance the current knowledge on boundary layer dynamics to facilitate design and performance improvements in multiple engineering systems and enhance predictive models in the atmospheric and environmental sciences.

1.1 The Boundary Layer

1.1.1 Historical Background

During the 19th century, fluid mechanics researchers were divided regarding how to proceed after the Navier-Stokes equations were established. The equations were well known, but their complexity made them very difficult to utilize in describing viscous fluid flows. As a result, fluids research began to split into two groups, one working on ideal fluids, i.e. fluids with zero viscosity – inviscid fluids, and the other on viscous fluids [10]. Ideal fluid theory could not explain concepts such as pipe losses, pressure loss as a fluid passes through a pipe, and drag while viscous fluid work was highly empirical making it unsuitable for generalized studies [10]. There was no unifying technique to describe real fluids through the Navier-Stokes equations.

At the turn of the century in 1904, Ludwig Prandtl published a work that for the first time linked ideal and viscous fluid theory. He experimentally showed that as a fluid moved past a solid body, a small region of fluid near the solid surface exhibited viscous behavior, while the bulk fluid away from this region behaved in an inviscid manner. This is caused by the physical phenomena where fluid directly in contact with a solid locally adheres to the solid surface, later named the “no-slip” condition. This results in the adherent fluid moving with the same velocity as the solid and a small viscous region where the fluid velocity gradually changes between the solid’s velocity and the bulk fluid velocity. Originally named the “frictional layer”, this small region is now known as the hydrodynamic boundary layer [10]. In the wake of Prandtl’s findings followed substantial developments in the budding field of aerodynamics that could now better characterize flow over an airfoil [10].

Just before the start of the 20th century, Osborne Reynolds reported that bulk fluid flows can transition from the orderly laminar flow regime to the disordered turbulent flow regime [10].

As with the main body of a fluid flow, a boundary layer can also become turbulent. While early boundary layer theory centered around laminar boundary layers, the contributions of Reynolds and later Prandtl helped to extend the theory to describe turbulent boundary layers [10]. Even today, a century after turbulent boundary layers were first characterized, there are still many aspects of these boundary layers that remain unknown.

Turbulence is present in a majority of practical fluid dynamics problems, from the planetary scale flow in the atmosphere to the millimeter scale flow of medicine through a needle. Turbulence has been observed for hundreds of years. Some of the earliest sketches of the phenomena were created by Leonardo da Vinci [11]. When Reynolds studied turbulence he initially described it as “sinuous motion” suggesting that the flow path is highly curvilinear [12]. Taylor devised a simple experiment in 1923 where flow between concentric cylinders was analyzed [11]. The outer cylinder was fixed while the inner cylinder was rotating. At low rotation speeds the resulting flow field was observed to be one dimensional and followed the rotation of the inner cylinder. At high speeds, the flow formed what is now known as turbulent Taylor vortices which generate a three dimensional flow field [11]. In this flow field, seemingly random motion of fluid particles was observed [11]. Indeed, turbulence is generally a phenomena that produces three dimensional stochastic and chaotic motion of fluid particles.

Building upon the works of Prandtl, Taylor and von Kármán further described turbulence a phenomenon generated by friction forces in the boundary layer in 1937 [12]. The friction forces in the boundary layer are produced by the fluid’s viscosity. If one vigorously mixes fluid initially at rest then leaves it alone, turbulence will dissipate energy via viscous or friction forces until the fluid returns to rest. As such turbulence is known to be a dissipative phenomena [11]. Turbulence also has a highly complex nature. This can be observed by performing repeated velocity measurements of a turbulent flow. Any minute variations in

experimental conditions will lead to a substantial change in measured fluid velocity at a given instant [11].

In turbulent boundary layers, complex turbulent motion greatly influences energy and mass transfer [7, 10, 13]. The boundary layer acts as an energy transfer system, carrying mechanical energy, thermal energy, and mass/species between bulk fluid and solid. In the classic experiment of flow over a stationary flat plate, the boundary layer is responsible for transporting the flat plate's momentum (zero in this case) to the fluid. Turbulence plays a pivotal role in this process by strongly modifying fluid motion within the boundary layer, making turbulence a major component of momentum transfer.

1.1.2 Laminar Boundary Layer Theory

Consider the flow of an ideal gas, such as air, toward and over a fixed perfectly smooth horizontal flat plate. The flat plate is very thin, infinitely wide, and infinitely long. The boundary layer that forms over the flat plate connects the undisturbed fluid moving at some velocity to the fluid at rest on the plate's surface due to the "no-slip" condition. Prandtl's streak photography in Figure 1.1 demonstrates the velocity change caused by the boundary layer. Longer white streaks correspond to regions of high velocity while the short streaks defining low velocity near the plate qualitatively show the effects of the boundary layer.

By examining the boundary layer at various points from the leading edge of the plate, one finds that the boundary layer grows as the fluid travels down the plate. At a location near the leading edge of the plate, streamlines in the boundary layer are parallel to each other, much like a typical laminar flow. This behavior defines the laminar boundary layer. The concept of boundary layer thickness or size, particularly in laminar boundary layers, is an arbitrary measure often taken to be the distance from the surface to where the velocity is 99% of the undisturbed fluid velocity [10]. The boundary layer thickness is one of the key

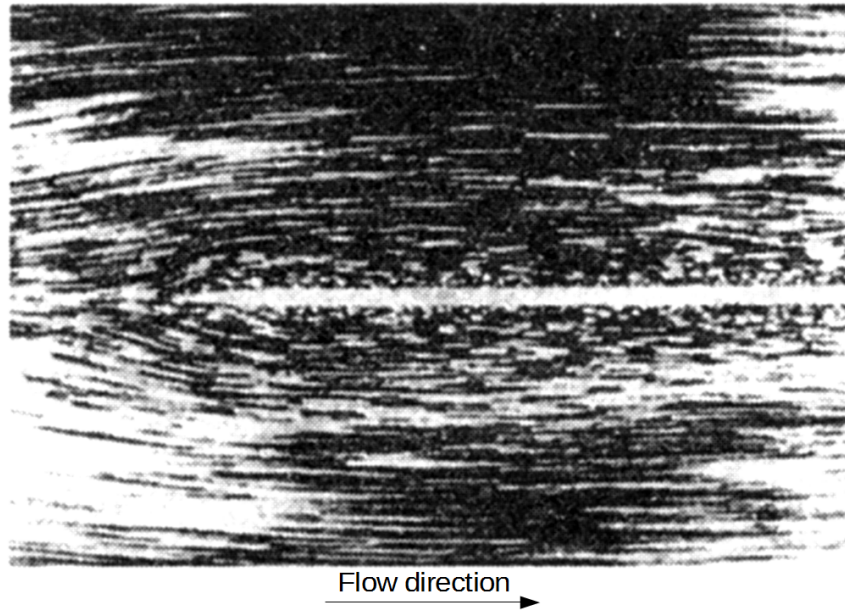


Figure 1.1: Streak photograph taken by Prandtl of flow past a horizontal flat plate. The flow is seeded with reflective particles. Adapted from Schlichting [10].

characteristics that appears frequently in mathematical descriptions.

The well known work of Reynolds in 1883 was one of the first detailed descriptions of turbulent flow in a channel [10]. His experiment involved seeding water with colored filaments for visualization. The experiment showed that at low fluid velocities, the injected filaments would follow the parallel streamlines of the laminar flow as shown in Figure 1.2a. When the flow speed was increased the previously straight path of the filaments became complex and three dimensional. The streak path in Figure 1.2b has been mixed in all directions by turbulence while the dye continues to be carried through the channel.

Reynolds suggested that there is a non-dimensional group that defines the transition between laminar and turbulent flow [11]. Now known as the *Reynolds* number, it represents the ratio of inertial and viscous forces in a fluid given by equation 1.1. Velocity, u , density, ρ , and a characteristic length scale, L , in the numerator represent fluid inertia while

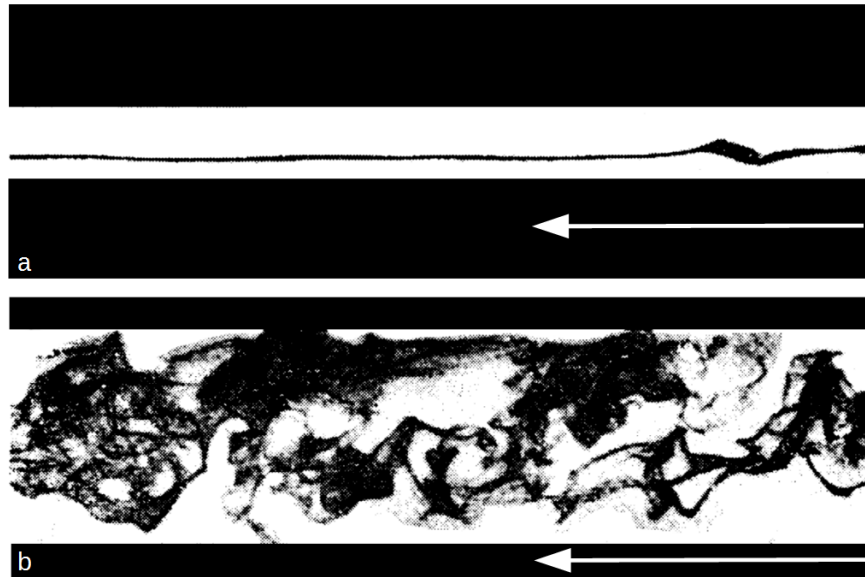


Figure 1.2: Photograph of channel flow taken by Reynolds during the colored filament experiment. (a) Shows the path of the filaments in laminar flow while (b) shows the evolution of filaments in turbulent flow. The primary flow direction is indicated by the white arrow. Adapted from Schlichting [10].

dynamic viscosity, μ , in the denominator represents the viscous force.

$$Re = \frac{\rho u L}{\mu} \quad (1.1)$$

The transition of a laminar flow to turbulence is a process that centers around flow stability. A flow is said to be stable if any disturbances induced in the flow are dampened, primarily by viscosity. The ability of a flow to remain stable has been shown to be a function of the Reynolds number [10]. As the Reynolds number increases, the inertial force grows larger relative to the viscous force in a laminar flow. At some sufficiently high Reynolds number, the molecular diffusion of momentum driven by the viscous force, is insufficient

to dissipate flow instabilities whose magnitude increases with the inertial force. This leads to local flow instability magnitudes growing and the bulk flow begins the transition to turbulence. Increasing the Reynolds number further continues to amplify the magnitude of flow instabilities leading to a fully established turbulent flow domain. The transition from laminar to fully turbulent flow occurs over a range of Reynolds numbers. For simplified calculations however, often a critical Reynolds number is utilized as an indicator of laminar to turbulent transition. In typical smooth pipe and channel flows this critical value is about 2000, while in highly controlled experiments it has been shown that a pipe flow can be laminar up to $Re \approx 40,000$ [10].

The Reynolds number can also be calculated for boundary layer flows. In the case of flow over a flat plate, the characteristic length scale is given by the distance from the leading edge of the plate. At locations near the leading edge, this length scale will be small. One can conclude that for flow over a smooth horizontal flat plate, the boundary layer will always be laminar near the leading edge. Moving further downstream on the plate will also ensure that at some point the boundary layer becomes turbulent. The work of Dryden found that there is a range of critical Reynolds numbers for a flat plate boundary layer to transition to turbulence, generally between 10^5 and 10^6 [10]. Often a single number of $5 \cdot 10^5$ is used as a guideline.

The mathematics to describe boundary layers of any kind begins with the governing equations of fluid mechanics. This derivation will be for flows whose velocity is much less than the speed of sound and for flows that do not change in time – “steady flows”. This allows fluid to be treated as incompressible, or having constant density, reducing the conservation of mass to a statement of zero velocity divergence as shown in equation 1.2.

$$\vec{\nabla} \cdot \vec{v} = 0 \quad (1.2)$$

$$u \frac{\partial u}{\partial x} + v \frac{\partial u}{\partial y} + w \frac{\partial u}{\partial z} = -\frac{1}{\rho} \frac{\partial P}{\partial x} + \nu \left(\frac{\partial^2 u}{\partial x^2} + \frac{\partial^2 u}{\partial y^2} + \frac{\partial^2 u}{\partial z^2} \right) \quad (1.3)$$

$$u \frac{\partial v}{\partial x} + v \frac{\partial v}{\partial y} + w \frac{\partial v}{\partial z} = -\frac{1}{\rho} \frac{\partial P}{\partial y} + \nu \left(\frac{\partial^2 v}{\partial x^2} + \frac{\partial^2 v}{\partial y^2} + \frac{\partial^2 v}{\partial z^2} \right) \quad (1.4)$$

$$u \frac{\partial w}{\partial x} + v \frac{\partial w}{\partial y} + w \frac{\partial w}{\partial z} = -\frac{1}{\rho} \frac{\partial P}{\partial z} + \nu \left(\frac{\partial^2 w}{\partial x^2} + \frac{\partial^2 w}{\partial y^2} + \frac{\partial^2 w}{\partial z^2} \right) \quad (1.5)$$

Next is the conservation of momentum. The body forces are assumed to be zero and gravitational forces are negligible for small laboratory boundary layers. This produces the Navier-Stokes equations in expanded form shown in 1.3 to 1.5 for a Newtonian fluid.

To consider boundary layer flow along an infinitely long and wide obstacle, the governing equations will be limited to a two-dimensional analysis where the x -axis is parallel to the axis of the object and the y -axis is normal to the object as illustrated in Figure 1.3. Due to symmetry only the boundary layer above the obstacle is considered. The figure further depicts, the variation of mean stream-wise velocity with distance from the wall, $\overline{U}(y)$, along with a sketch of the developing boundary layer shape. Writing these out gives the system of equations in 1.6 to 1.8. The third velocity component, w , is set to zero and all gradients in the z direction are set to zero in this 2D analysis.

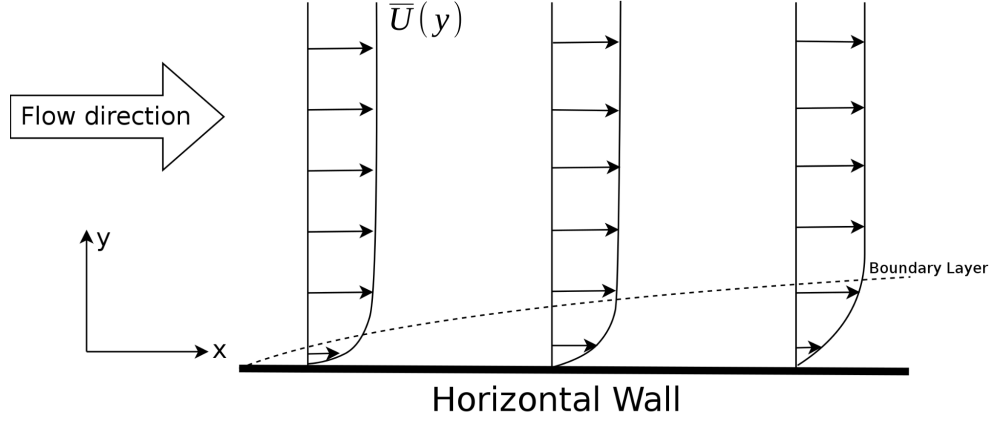


Figure 1.3: Sketch of boundary layer flow over a horizontal flat plate.

$$\frac{\partial u}{\partial x} + \frac{\partial v}{\partial y} = 0 \quad (1.6)$$

$$u \frac{\partial u}{\partial x} + v \frac{\partial u}{\partial y} = -\frac{1}{\rho} \frac{\partial P}{\partial x} + \nu \left(\frac{\partial^2 u}{\partial x^2} + \frac{\partial^2 u}{\partial y^2} \right) \quad (1.7)$$

$$u \frac{\partial v}{\partial x} + v \frac{\partial v}{\partial y} = -\frac{1}{\rho} \frac{\partial P}{\partial y} + \nu \left(\frac{\partial^2 v}{\partial x^2} + \frac{\partial^2 v}{\partial y^2} \right) \quad (1.8)$$

This system of equations will now be non-dimensionalized using the length, time, and mass scales of the flow, defined in 1.9 and 1.10. Spatial variables are scaled by the characteristic dimension of the obstacle, L , velocities are scaled by the free stream velocity, U , the kinematic viscosity, ν , is normalized by both velocity and characteristic dimension to give the Reynolds number, finally the pressure is normalized by density and velocity.

$$\hat{x} = \frac{x}{L} \quad \hat{u} = \frac{u}{U} \quad \frac{1}{Re} = \frac{\nu}{UL} \quad \hat{P} = \frac{P}{\rho U^2} \quad (1.9)$$

$$\bar{v} = \hat{v} \sqrt{Re} \quad \bar{y} = \hat{y} \sqrt{Re} \quad (1.10)$$

Inserting these into Eqns. 1.6 through 1.8, simplifying then performing an order of magnitude analysis to eliminate the small magnitude variables produces the steady Prandtl boundary-layer equations in Eqns. 1.11 to 1.13.

$$\frac{\partial \hat{u}}{\partial \hat{x}} + \frac{\partial \bar{v}}{\partial \bar{y}} = 0 \quad (1.11)$$

$$\hat{u} \frac{\partial \hat{u}}{\partial \hat{x}} + \bar{v} \frac{\partial \hat{u}}{\partial \bar{y}} = -\frac{\partial \hat{P}}{\partial \hat{x}} + \frac{\partial^2 \hat{u}}{\partial \bar{y}^2} \quad (1.12)$$

$$0 = -\frac{\partial \hat{P}}{\partial \bar{y}} \quad (1.13)$$

The original system of three coupled non-linear partial differential equations in Eqns. 1.6 to 1.8 has been greatly simplified by this analysis. The greatest change occurred in the y-momentum equation where all terms except pressure have vanished. This means pressure does not change across the boundary layer, enabling the pressure of the free stream to be imposed at all points in the boundary layer. This eliminates pressure as an unknown in the boundary layer and the stream-wise pressure gradient is given by the free stream flow behavior. This leaves only the two velocities to be solved. These equations have been solved numerically and leads to a solution that is independent of the Reynolds number [10].

The simplifications used to derive the Prandtl boundary layer equations have been used to provide an exact solution to the dimensional boundary layer equations. For laminar flow over a horizontal flat plate, the Blasius solution is an exact solution that describes all parts

of the boundary layer. Calculated in 1908, it is the first analytical solution of the boundary layer equations.

Two key features of all boundary layers is the wall shear stress and the boundary layer thickness. The boundary layer thickness from the Blasius solution is given by Eqn. 1.14 and the wall shear stress is given by Eqn. 1.15.

$$\delta \approx 5 \sqrt{\frac{\nu x}{U}} \quad (1.14)$$

$$\tau_w = 0.332 \mu U \sqrt{\frac{U}{\nu x}} \quad (1.15)$$

These relations indicate that for a given fluid and free stream velocity, the boundary layer thickness and wall shear stress are only functions of the stream-wise spatial coordinate (x). This highlights one unique boundary layer behavior known as self-similarity. This is observed where the shape of a given boundary layer's velocity profile does not change but simply scales according to the stream-wise spatial coordinate. Experimental data taken over a range of Reynolds numbers has exhibited this behavior where all gathered velocity profiles showed excellent agreement with the profile predicted by the Blasius solution [10].

The Blasius solution provides a complete description of laminar boundary layer flow over a horizontal flat plate. The experimental works that set out to validate the Blasius solution show very good agreement with theory with Reynolds numbers up to 10^5 provided the flow is laminar in nature. If one attempts to use Eqn. 1.14 and 1.15 for a turbulent flow at the same Reynolds number, a significant increase in wall shear stress and boundary layer thickness will be observed. The difference in normalized wall shear stress, or skin friction coefficient, C_f , is shown in Figure 1.4. The change in C_f is so large that it cannot possibly be explained using the framework of the boundary layer equations.

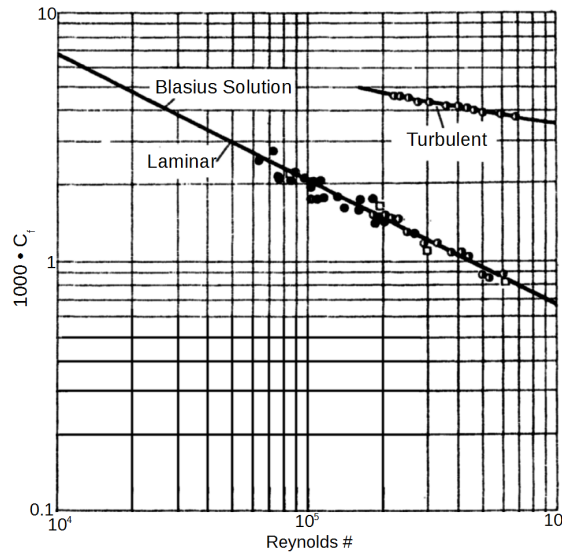


Figure 1.4: Plot of the skin friction coefficient vs Reynolds number showing the laminar Blasius solution with experimental data of laminar and turbulent flows by Liepmann and Dhawan. Adapted from Schlichting [10].

1.1.3 Turbulent Boundary Layer Theory

A new approach is required to mathematically describe a turbulent boundary layer. The goal of this approach is to explain the substantial difference in boundary layer and generally all fluid characteristics, such as the skin friction coefficient when compared to laminar flow. As the governing equations are known to accurately describe all fluid there must exist some mathematical formulation to make the governing equations more suited to describing turbulent flow. Reynolds decomposition is one well-known technique to characterize turbulent flows. In this approach each fluid variable is split into its time-averaged component and the amount of deviation about the time average, known as the fluctuating component. This is shown in Eqn. 1.16 for the u velocity component where the time-averaged velocity is \bar{u} and the fluctuating velocity is u' .

$$u = \bar{u} + u' \quad (1.16)$$

By definition the time average of the fluctuating component is zero. This approach has the advantage that laminar flow behavior is recovered when the fluctuating component is set to zero. Physically, this approach describes a turbulent flow as a laminar flow (the time average) with chaotic turbulent motion (the fluctuations) superimposed.

This decomposition is now applied to the continuity equation, Eqn. 1.6, and the Navier-Stokes equations for an incompressible Newtonian fluid where only two-dimensional motion is considered, Eqn. 1.7 and 1.8. Starting with the continuity equation, replacing velocity with the decomposed terms produces Eqn. 1.17 which expands to Eqn. 1.18. Taking the time-average of this whole equation eliminates the fluctuating terms. The only terms that remain are the steady terms leaving the continuity equation unchanged by Reynolds decomposition as shown in Eqn. 1.19.

$$\frac{\partial(\bar{u} + u')}{\partial x} + \frac{\partial(\bar{v} + v')}{\partial y} = 0 \quad (1.17)$$

$$\frac{\partial\bar{u}}{\partial x} + \frac{\partial\bar{v}}{\partial y} + \frac{\partial u'}{\partial x} + \frac{\partial v'}{\partial y} = 0 \quad (1.18)$$

$$\frac{\partial\bar{u}}{\partial x} + \frac{\partial\bar{v}}{\partial y} = 0 \quad (1.19)$$

Performing the same substitution into the Navier-Stokes equations produces the following:

$$\begin{aligned}
(\bar{u} + u') \frac{\partial(\bar{u} + u')}{\partial x} + (\bar{v} + v') \frac{\partial(\bar{u} + u')}{\partial y} &= -\frac{1}{\rho} \frac{\partial(\bar{P} + P')}{\partial x} + \nu \left(\frac{\partial^2(\bar{u} + u')}{\partial x^2} + \frac{\partial^2(\bar{u} + u')}{\partial y^2} \right) \\
(\bar{u} + u') \frac{\partial(\bar{v} + v')}{\partial x} + (\bar{v} + v') \frac{\partial(\bar{v} + v')}{\partial y} &= -\frac{1}{\rho} \frac{\partial(\bar{P} + P')}{\partial y} + \nu \left(\frac{\partial^2(\bar{v} + v')}{\partial x^2} + \frac{\partial^2(\bar{v} + v')}{\partial y^2} \right)
\end{aligned}$$

Expanding and time-averaging these whole equations eliminates any terms containing an isolated fluctuating term (u' , v' , or P'). However the product of fluctuating terms such as $u'u'$ are non-zero when time-averaged and must remain. This results in the simplified 2D Reynolds Averaged Navier-Stokes (RANS) equations 1.20 and 1.21.

$$\bar{u} \frac{\partial \bar{u}}{\partial x} + \bar{v} \frac{\partial \bar{u}}{\partial y} = -\frac{1}{\rho} \frac{\partial \bar{P}}{\partial x} + \nu \left(\frac{\partial^2 \bar{u}}{\partial x^2} + \frac{\partial^2 \bar{u}}{\partial y^2} \right) - \left(\frac{\partial \overline{u'u'}}{\partial x} + \frac{\partial \overline{u'v'}}{\partial y} \right) \quad (1.20)$$

$$\bar{u} \frac{\partial \bar{v}}{\partial x} + \bar{v} \frac{\partial \bar{v}}{\partial y} = -\frac{1}{\rho} \frac{\partial \bar{P}}{\partial y} + \nu \left(\frac{\partial^2 \bar{v}}{\partial x^2} + \frac{\partial^2 \bar{v}}{\partial y^2} \right) - \left(\frac{\partial \overline{u'v'}}{\partial x} + \frac{\partial \overline{v'v'}}{\partial y} \right) \quad (1.21)$$

The majority of the RANS equations are identical to their traditional Navier-Stokes counterparts. There is however a new term present on the far right of the RANS equations. This term contains only the product of fluctuating velocities and arises due to the non-linearity of the advection term (spatial derivatives on the left hand side). This new term when multiplied by density has the same units as pressure and viscous stress, and it has been dubbed the “turbulent stress” or the “Reynolds stress”. The Reynolds stress can be expressed in general as a three-dimensional symmetric tensor shown in Eqn. 1.22.

$$-\rho \begin{bmatrix} \overline{u'u'} & \overline{u'v'} & \overline{u'w'} \\ \overline{u'v'} & \overline{v'v'} & \overline{v'w'} \\ \overline{u'w'} & \overline{v'w'} & \overline{w'w'} \end{bmatrix} \quad (1.22)$$

The Reynolds stress highlights a method for turbulent velocity fluctuations to influence the mean flow. Mathematically this formulation causes the turbulent velocity fluctuations to manifest as a stress term and can therefore be described as increasing the total stress experienced by the mean fluid flow. However, the Reynolds stress is not a real stress and only a product of this mathematical description. Therefore, it is referred to as an *apparent* stress due to turbulent motion within a fluid. In turbulent flows the Reynolds stress magnitude can easily surpass the viscous stress magnitude making it impossible to neglect the contribution of this apparent stress. Within the turbulent boundary layer, the Reynolds stress is only small relative to the viscous stress in the region extremely close to wall.

The Reynolds stress' behavior and it's influence on the mean fluid motion is a major part of classical and on-going turbulence research. With a clearly quantified pathway for turbulent fluctuations to influence the mean flow defined, it is of interest to characterize the nature of the fluctuations. The relative magnitude of the turbulent velocity fluctuations is given by the turbulent intensity defined in Eqn. 1.23 for the u velocity component measured N times. This quantity is the standard deviation of the velocity normalized by the mean velocity. The turbulent intensity is expected to be large in magnitude in flows where the turbulent fluctuations are significant relative to the mean velocity.

$$T_I = \frac{1}{\bar{u}} \sqrt{\frac{\sum_{i=1}^N (u_i - \bar{u})^2}{N-1}} \quad (1.23)$$

In addition to the relative magnitude of the turbulent motion, it is also possible to describe the kinetic energy associated with turbulent fluctuations. This is known as the turbulent kinetic energy (TKE), K , defined in Eqn. 1.24. The TKE has been used extensively for describing and modeling the behavior of turbulence in both experimental and computational research.

$$K = \frac{1}{2} \overline{(u'^2 + v'^2 + w'^2)} \quad (1.24)$$

A transport equation for the TKE has been developed to describe the mathematical and physical transport processes governing this quantity. For an incompressible two-dimensional steady flow with constant material properties the K -equation is defined in Eqn. 1.25 [10]. Overall, this equation states “the rate of change of turbulent kinetic energy equals the sum of TKE diffused by viscosity, TKE production, turbulent transport of kinetic energy, and energy dissipation”.

$$\begin{aligned}
\rho \left(\bar{u} \frac{\partial K}{\partial x} + \bar{v} \frac{\partial K}{\partial y} \right) &= \mu \left(\frac{\partial^2 (K + \overline{u'^2})}{\partial x^2} + \frac{\partial^2 (K + \overline{v'^2})}{\partial y^2} + 2 \frac{\partial^2 (\overline{u'v'})}{\partial x \partial y} \right) \\
&\quad - \rho \left(\overline{u'^2} \frac{\partial \bar{u}}{\partial x} + \overline{u'v'} \frac{\partial \bar{v}}{\partial x} + \overline{u'v'} \frac{\partial \bar{u}}{\partial y} + \overline{v'^2} \frac{\partial \bar{v}}{\partial y} \right) - \frac{\partial (\overline{u'(P' + \rho K)})}{\partial x} - \frac{\partial (\overline{v'(P' + \rho K)})}{\partial y} \\
&\quad - \mu \left[2 \overline{\left(\frac{\partial u'}{\partial x} \right)^2} + 2 \overline{\left(\frac{\partial v'}{\partial y} \right)^2} + \overline{\left(\frac{\partial u'}{\partial y} + \frac{\partial v'}{\partial x} \right)^2} \right] \quad (1.25)
\end{aligned}$$

The first term defines the rate of change of TKE due to advection, specifically TKE carried by the mean flow. The second term which is multiplied by the dynamic viscosity is the viscous diffusion term and describes turbulent energy transported by inter-molecular dynamics. The turbulence production term is next whose elements are the product of a Reynolds stress component and a mean velocity gradient. This indicates that turbulent kinetic energy is generated by interaction of turbulent fluctuations and the mean flow. Next is the turbulent transport term which indicates the sum of fluctuating pressure and TKE are both utilized. Each element in this addition represents a different physical phenomena. The turbulent velocity-pressure product represents energy lost due to work performed by the fluctuating pressure. Similarly, the product of K and a fluctuating velocity represents turbulent kinetic energy transported by the velocity fluctuations, known as the triple-correlation. The last term in the K -equation describes the dissipation of turbulent kinetic energy to internal energy in the form of molecular motion quantified by the viscosity.

Multiple important processes can be identified from the turbulent kinetic energy equation. The turbulent production term indicates that turbulence can extract energy from the mean flow to supply the dissipative and diffusive processes. In some flow configurations, such as a turbulent wall jet, it is possible for turbulent motion to supply the mean flow with energy [10]. However in general, energy extracted from the mean flow and transformed

into turbulent motion does not return to the mean flow. Turbulence can only be transported until it eventually dissipates. This is consistent with the previously discussed observation where fluid at rest is vigorously mixed then left alone. Turbulence extracts energy imparted to the fluid by the mixer and dissipates energy until the fluid returns to rest. This behavior highlights the significance of both the turbulent production and dissipation terms, as the other processes outlined act to transport pre-existing turbulent motion.

For the conservation of energy, Reynolds decomposition can also be applied noting that the fluctuating temperature (T') is defined with the same methodology as the turbulent velocity and pressure fields. The Reynolds averaged conservation of energy is presented in Eqns. 1.26 for incompressible steady 2D flow with constant thermophysical properties [10].

$$\begin{aligned} \rho C_p \left(\bar{u} \frac{\partial \bar{T}}{\partial x} + \bar{v} \frac{\partial \bar{T}}{\partial y} \right) &= k \left(\frac{\partial^2 \bar{T}}{\partial x^2} + \frac{\partial^2 \bar{T}}{\partial y^2} \right) - \rho C_p \left(\frac{\partial \overline{u'T'}}{\partial x} + \frac{\partial \overline{v'T'}}{\partial y} \right) \\ &+ \mu \left[2 \left(\frac{\partial \bar{u}}{\partial x} \right)^2 + 2 \left(\frac{\partial \bar{v}}{\partial y} \right)^2 + \left(\frac{\partial \bar{u}}{\partial y} + \frac{\partial \bar{v}}{\partial x} \right) \right] + \mu \left[2 \overline{\left(\frac{\partial u'}{\partial x} \right)^2} + 2 \overline{\left(\frac{\partial v'}{\partial y} \right)^2} + \overline{\left(\frac{\partial u'}{\partial y} + \frac{\partial v'}{\partial x} \right)^2} \right] \quad (1.26) \end{aligned}$$

This equation reads, “the rate of change of the mean temperature field is equal to the sum of heat conduction, turbulent heat transport, direct energy dissipation, and turbulent energy dissipation”. Going through each of the terms in this equation reveals interesting processes present in turbulent flows. First, the advection term on the left of the equal sign denotes thermal energy transported by the mean flow. The second term describes heat conducted through the fluid given by Fourier’s law. The next term contains the product of fluctuating velocity and temperature fields. Physically it represents temperature fluctuations associated with turbulent velocity fluctuations. Known as the turbulent heat transfer it acts to modify heat conduction as an *apparent* conduction, similar to the Reynolds stress as an apparent

stress. The fourth term describes energy dissipated directly from the mean flow to internal energy via viscous dissipation. The final term is the turbulent energy dissipation which appeared in the K -equation.

From the Reynolds averaged conservation of energy, the Reynolds decomposition technique has presented two unique features of thermal energy transport. First is the turbulent heat flux term, which manifests as a pathway for turbulent motion to influence heat transfer in the mean flow. The second feature is the presence of multiple methods to dissipate energy. The first is directly from the mean flow and the second is from the turbulent motion, which itself feeds on the mean flow.

The Reynolds averaging technique has identified key parameters and behaviors of interest. All governing equations in Reynolds averaged form did not lose any mean flow terms, ensuring the mean flow behaviors cannot be ignored. In the RANS and conservation of energy equations, the newly generated Reynolds stress and turbulent heat flux terms both appear to modify the fundamental fluid stress and heat conduction. The turbulent kinetic energy transport equation expanded on the Reynolds stress by quantifying a mechanism for kinetic energy transfer from mean flow to turbulent motion. Finally, both kinetic and thermal energy are eventually dissipated by viscosity to internal energy. For characterizing the turbulent boundary layer, it is of interest to describe the characteristics of these mean flow and turbulent quantities.

Turbulent Boundary Layer Structure

Consider the flow of an incompressible Newtonian fluid over an infinite horizontal flat plate as illustrated in Figure 1.3. There is no heat transfer between the plate and fluid. A laminar boundary layer forms at the leading edge of the plate whose characteristics closely follow the Blasius solution. At some position downstream the boundary layer will transition to

turbulence. At a point further downstream the effects of transition have vanished and the boundary layer is fully turbulent. To characterize the turbulent boundary layer, first, the mean velocity profile is illustrated in Figure 1.5.

In this figure, the stream-wise velocity is normalized to produce $\overline{u^+}$ with a quantity known as the “friction velocity” and the distance above the wall is normalized to give y^+ using the friction velocity and kinematic viscosity as shown in Eqn. 1.27. The friction velocity is derived from the wall shear stress. Using the friction velocity and kinematic viscosity for normalization produces inner-layer scaling as these quantities best describe the length and time scales of the near-wall region in the turbulent boundary layer.

$$u^+ = \frac{u}{u_t} \quad y^+ = \frac{yu_t}{\nu} \quad \text{where} \quad u_t = \sqrt{\frac{\tau_w}{\rho}} \quad (1.27)$$

The turbulent boundary layer is comprised of several sub-layers. Starting from the wall at $y^+ = 0$ and $u^+ = 0$ and moving away from the wall, the viscous sublayer is encountered first. In this layer, boundary layer flow is strongly governed by viscous forces while there is little to no turbulent motion present. The relationship between u^+ and y^+ in this layer is given by Eqn. 1.28. The edge of the viscous sublayer is located at $y^+ = 5$. Above this point the effects of turbulence become significant relative to viscous effects.

$$u^+ = y^+ \quad \text{Viscous Sublayer} \quad (1.28)$$

$$u^+ = f(y^+) \quad \text{Buffer Layer. Exact equation found by Gersten \& Herwig [10]} \quad (1.29)$$

$$u^+ = \frac{1}{\kappa} \ln(y^+) + C \quad \text{Logarithmic Layer} \quad (1.30)$$

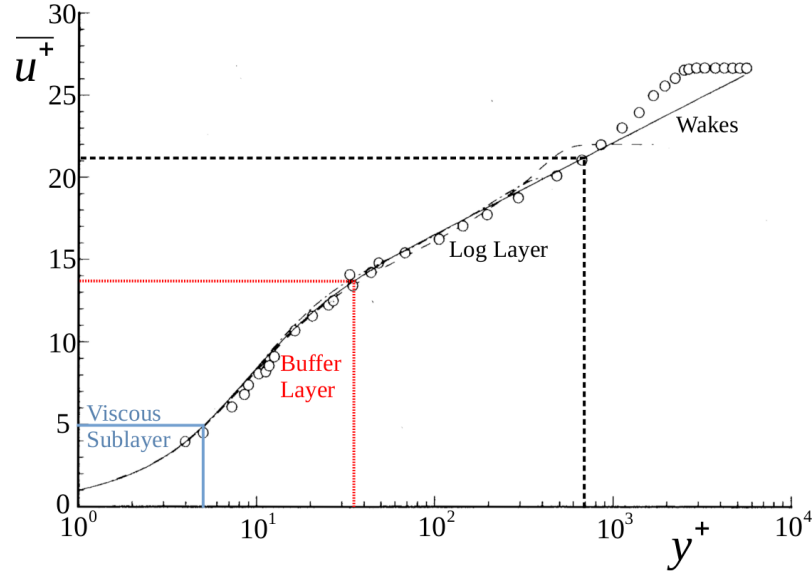


Figure 1.5: Mean stream-wise velocity profile in inner-layer scaling. Circles are from experimental data by Klebanoff, dashed curve shows the Direct Numerical Simulation (DNS) results by Spalart, dotted curve shows the DNS by Kim et. al., and the solid line is derived from boundary layer theory. Each constituent sub-layer is indicated. Adapted from Pope [14].

After the viscous sublayer is the buffer layer. This layer contains the inflection point of the velocity profile at $y^+ \approx 15$. The exact relationship between u^+ and y^+ in this layer is far more complex than the sublayer and has been calculated from fundamental theory [10, 14]. The buffer layer covers the region between $5 \leq y^+ \leq 40 - 70$ where the upper limit of this layer covers a range of y^+ values [10, 11, 14]. Next is the logarithmic layer where there is a log-linear relationship between u^+ and y^+ as shown in Eqn. 1.30 where $\kappa = 0.41$ and $C = 5$. In this layer turbulent effects are significant but comparatively weaker than the buffer layer. The upper limit of the logarithmic layer is often not as clearly defined as the buffer layer and viscous sublayer limits. Generally, the log-layer equation is valid provided $\frac{y}{\delta} < \sim 0.2$ corresponding to $y^+ \approx 500 - 1000$ [11, 14]. Finally, the wake region lies above the log-layer and here the effects of boundary layer turbulence are weak.

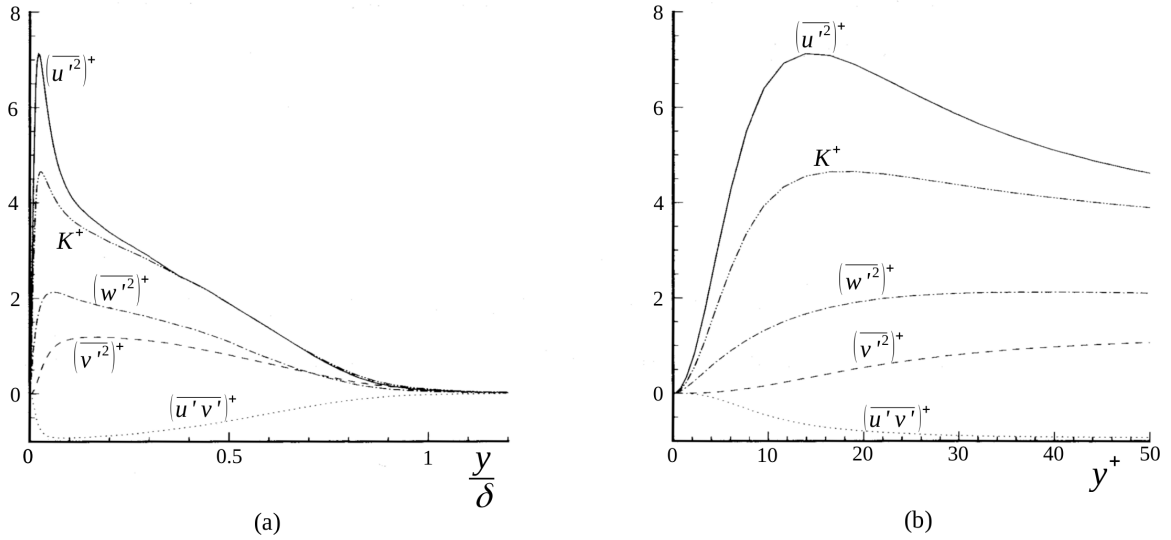


Figure 1.6: Profiles of the Reynolds stress components and turbulent kinetic energy in inner layer scaling for (a) the whole boundary layer and (b) zoomed on a section of the near-wall region. Adapted from Pope [14].

The behaviors of the Reynolds stress components and turbulent kinetic energy are now investigated. These quantities are time-averaged and normalized in inner-layer scaling then plotted against distance from the wall. First these profiles are observed over the whole boundary layer as illustrated in Figure 1.6a. All profiles start from zero at the wall, reach a peak at $\frac{y}{\delta} \sim 0.1$ before gradually returning to zero at the upper edge of the boundary layer. The stream-wise Reynolds stress, $\overline{u'^2}^+$, shows the greatest magnitude at about 7 followed by the span-wise stress and wall-normal stress, $\overline{w'^2}^+$ and $\overline{v'^2}^+$. The shear stress, $\overline{u'v'}^+$, is always negative with a peak magnitude of about unity. Due to the high magnitude of the stream-wise stress, this term is dominant in the TKE calculation resulting in a TKE profile that resembles the $\overline{u'^2}^+$ profile. The peak TKE is approximately four before decreasing towards zero at the free-stream.

Zooming in on these profiles to a near-wall section of the boundary layer generates Figure 1.6b. Comparing this graph to the previously defined limits of each sub-layer indicates

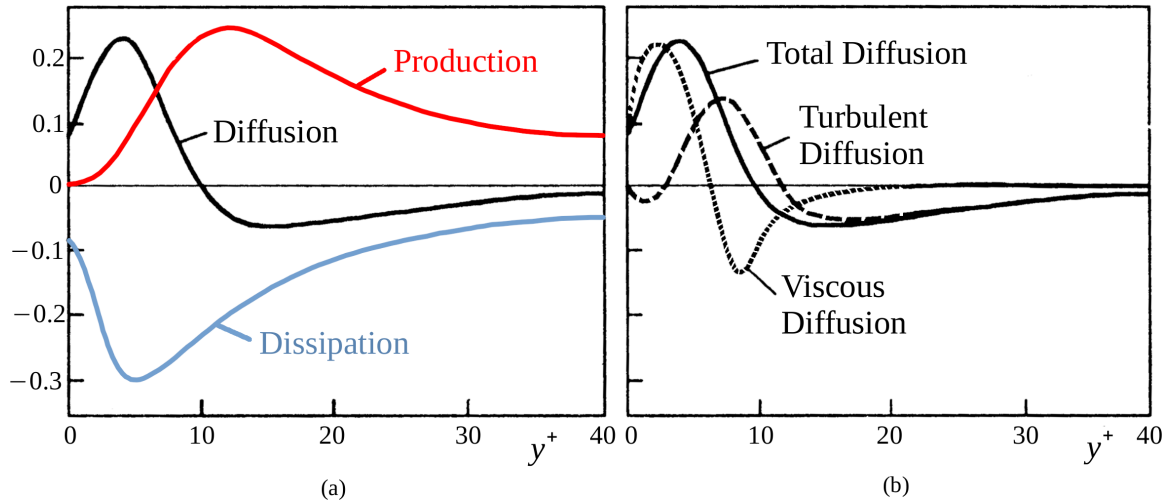


Figure 1.7: Contribution of each transport process to the total turbulent kinetic energy in the near-wall region. Adapted from Schlichting [10].

that in the viscous sublayer, the Reynolds stresses and TKE all rapidly approach zero as expected due to strong viscous effects. The peak stream-wise Reynolds stress and TKE are found in the buffer layer, specifically at $y^+ \approx 15$ coinciding with the velocity profile's inflection point. Continuing towards the log layer shows all stresses and TKE start to decrease with increasing y^+ . The peak value in the TKE profile is of interest as it defines the buffer layer as the most energetic region in the boundary layer. It is likely then that buffer layer behaviors are of great importance to the overall transportation of momentum, heat, and mass/species. The physical processes defined by the K -equation are of interest to determine which TKE transport process(es) is(are) responsible for producing the peak TKE. The relative contribution of each process to the overall TKE budget is presented in Figure 1.7.

In the left panel of the figure there are three profiles corresponding to production, diffusion (combined viscous and turbulent), and dissipation in the near-wall region. In the viscous sublayer it is expected to find terms strongly related to fluid viscosity, the terms containing

dynamic viscosity in the K -equation, to be dominant and indeed this is true. The dissipation and diffusion terms are dominant in magnitude for $y^+ \leq \approx 7$. On the right panel, the breakdown of total diffusion is presented and as expected viscous diffusion reaches its peak within the viscous sublayer. Moving into the buffer layer shows a decrease in dissipation and diffusion while the production reaches its peak at $y^+ \approx 12$ in good agreement with the observed peak TKE. At this position above the wall, the total diffusion is negative as both constituent diffusion terms are negative. Moving further away from the wall into the log layer indicates that diffusion tends toward zero faster than both production and dissipation. Once y^+ is sufficiently large, turbulent kinetic energy production is balanced by energy dissipation.

From these graphs it is clear that turbulent kinetic energy production and dissipation are two highly important quantities. It has already been established that turbulent production draws energy from the mean flow, however production is not significant when very close to the wall. The energy supplied by the mean flow, i.e. the energy produced by inertia within the fluid, is used for one of two purposes. In the very near-wall region, $y^+ < 11$, energy from the mean flow is primarily dissipated directly by viscous forces. This process was observed in the conservation of energy, equation 1.26, as the direct dissipation term. Further away from the wall however, viscous effects are weak therefore all energy flows into producing turbulent motion and eventually that turbulent motion dissipates energy. As the viscosity dominant region is very small relative to the boundary layer thickness, it is of interest to describe the mechanisms governing how turbulent motion receives and eventually dissipates energy from the mean flow.

The methods of characterizing turbulence presented thus far have been statistical in nature as the focus has been on the mean velocity and deviations from the mean. Another approach to characterizing turbulence is to calculate the frequency content of a turbulent velocity

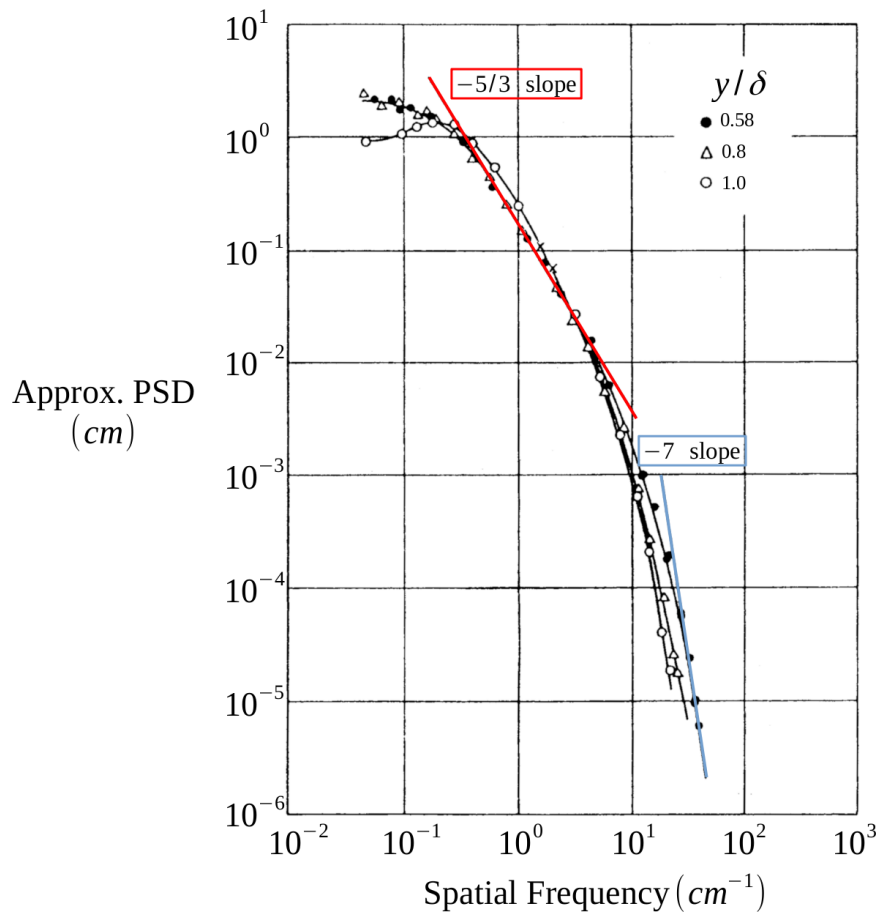


Figure 1.8: Velocity spectra of the turbulent boundary layer measured at three y -coordinates. Adapted from Schlichting [10].

signal using the Fourier Transform. This approach facilitates the identification of low and high frequency variations in fluid velocity. When the Fourier Transform of the turbulent velocity is calculated, the distribution known as the velocity spectra is found. An example of one such spectra in the turbulent boundary layer is presented in Figure 1.8.

The abscissa in this graph presents the wave number, a measure of spatial frequency, while the ordinate presents the approximate power spectral density (PSD). This graph would appear the same if temporal data was used where the abscissa would present frequency. The magnitude of energy (PSD) associated with each wave number is illustrated in this graph.

From the detailed analysis of Kolmogorov and others in the mid 1900's three key regions of the velocity spectra can be identified as being critical to the behavior of turbulence [14]. First, the very low wave numbers represent the largest spatial scales, i.e. the integral scale, or largest eddies in the turbulent flow. As the figure shows, these eddies contain the largest magnitude in the power spectra and are named the “energy-containing eddies”. These eddies are primarily responsible for extracting kinetic energy from the mean flow, i.e. turbulence production. Due to their large size integral scale eddies are relatively unaffected by viscous forces. Smaller eddies extract energy from the energy-containing eddies. These eddies occupy the middle part of the spectra with a slope of $\approx -\frac{5}{3}$ known as the “inertial subrange”, which constitutes the second region. Continuing onward, even smaller eddies extract energy from the eddies in the inertial subrange. These eddies are known as dissipative eddies that produce the ≈ -7 slope of the dissipation range in the spectral at high wave numbers. Dissipative eddies are extremely small and described using the Kolmogorov length scale. At this length scale viscous forces are dominant causing kinetic energy to dissipate through molecular or viscous dissipation. This behavior is reflected in the Reynolds number which is known to be unity at this length scale, representing an equal magnitude of flow inertia and viscous force.

Overall in turbulent flows energy enters the turbulent motions from the mean flow and takes the form of large integral scale eddies. These eddies pass energy to a sequence of smaller and smaller eddies until viscous dissipation can directly convert turbulent kinetic energy into internal energy, i.e. molecular motion. This process is known as the energy cascade. In 1922 before the work of Kolmogorov, Richardson provided a summary of the cascade hypothesis:

Big whorls have little whorls,
Which feed on their velocity;
And little whorls have lesser whorls,
And so on to viscosity.

-Richardson

Classical turbulent boundary layer research established numerous key insights and mathematical descriptors. The processes of boundary layer formation, transition to turbulence, interaction of turbulence with the mean flow, and turbulent characteristics were all derived from theory or documented through experimental observations. However, not all classical research is entirely accurate. The energy cascade process is generally understood as a well-organized sequence of eddies passing energy between each other. However there are turbulent flow phenomena where this process does not occur and instead energy flows from the small-scales towards the large scales or the smallest eddies directly extract energy from much larger eddies [11]. This is one of many motivations for recent contemporary research on the fundamental nature of turbulence eddies. A more thorough understanding of turbulent boundary layer flow is needed.

1.2 Contemporary Boundary Layer Research

Classical work on the turbulent boundary layer established a fundamental understanding on the interaction of turbulent motion and the mean flow. Recently however, the behavior of turbulence in the boundary layer has been the focus of highly active and on-going research. A hallmark of turbulence is the rotating, swirling or recirculating motion inside the fluid. An eddy in a broad sense refers to any region of recirculating fluid. Eddies are known

to occur over a range of length scales from as large as the flow itself to many orders of magnitude smaller. Vorticity (Ω) is the curl of the velocity field given by Eqn. 1.31. An eddy with non-zero vorticity is defined as a vortex.

$$\vec{\Omega} = \frac{1}{2} \vec{\nabla} \times \vec{v} \quad (1.31)$$

A fluid flow with zero vorticity is said to be irrotational, however there are exceptional cases where a fluid can appear to rotate while having zero vorticity [9]. As the velocity in a fluid is continuous within the entire fluid domain, vorticity is therefore defined over the same domain. This facilitates 2D and generally 3D continuous regions of non-zero vorticity referred to as vortex lines in 2D or vortex tubes in 3D [11]. In any turbulent flow there exist numerous vortex tubes with a wide range of dimensions. When vortex tubes organize into a single group, it is said that a coherent structure has formed. Generally a region of fluid is referred to as a coherent structure if its' vortex lines can organize themselves, hold together for a long time, and repeatedly appear in the flow [11]. The presence, characteristics, and significance of coherent structures in all turbulent flows is a highly active research area.

In the turbulent boundary layer one typical coherent structure reported is the hairpin vortex. It is formed when many vortex lines along the solid surface the boundary layer passes over gather into a vortex tube. The tube can be deformed by any turbulent fluctuations in the surroundings. It is possible then for the tube to deform into a curved shape as shown in Figure 1.9 [11]. The flow field around the curved tube is very similar to a torus which can advect itself forward. This leads to the tube rising upward from the surface and attempting to stand vertically, with it's highest point in the buffer layer or lower log layer as shown in side view in Figure 1.9.

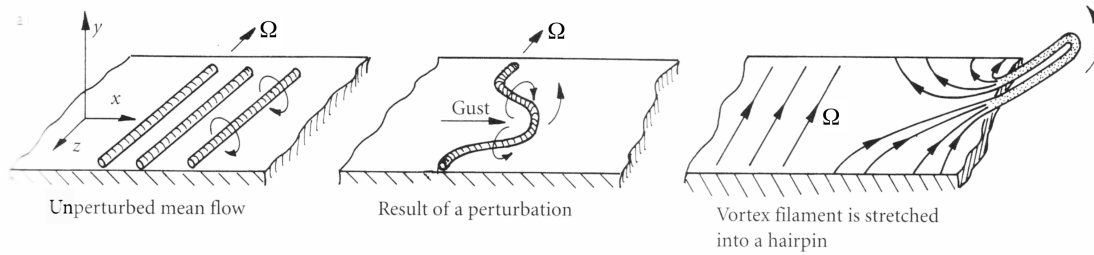


Figure 1.9: Sequence of images showing formation of a hairpin vortex from vortex tubes. Adapted from Davidson [11].

As the tube rises, the top experiences a higher surrounding velocity than the bottom [11]. This causes the tube to stretch into a hairpin like shape and reach equilibrium at roughly a 45 degree angle above the surface [11]. For the hairpin vortex to remain stable at this angle the effects of shear due to the surrounding flow and vortex lift must balance [11]. Due to the rotation direction of the hairpin vortex shown in the middle panel of Figure 1.9, the hairpin tends to expel fluid in front of itself which opposes the mean flow. It is therefore expected that there will be a stagnation point somewhere nearby the front of the hairpin vortex [15, 16]. This stagnation point will be on the left of the hairpin depicted in the right-most panel of Figure 1.9. On all sides of the stagnation point a shear layer is expected to form. These structures are three-dimensional and quite small in diameter, presenting challenges to directly observe and identify hairpins. Experimental studies overcome this challenge by utilizing the characteristic features such as the stagnation point as an identifying signature [15].

This characteristic signature is only applicable to hairpin vortices with sufficient strength relative to the surroundings to produce a stagnation point. This method cannot be broadly applied to detect all coherent structures in a given turbulent flow. Several methods have been developed to identify coherent structures. One of the simplest techniques is to use a vorticity threshold. In this approach, all locally connected points in space whose vorticity

exceeds a given threshold are said to be a coherent structure. This method performs poorly in turbulent boundary layers and is sensitive to the selection of threshold [17].

Alternative methods have been developed that are based on the velocity gradient tensor defined in Eqn. 1.32 using Cartesian coordinates. This tensor can be decomposed into a symmetric part, known as the strain rate (\vec{S}), and a skew-symmetric part, vorticity. Two widely adopted techniques based on the velocity gradient tensor are the Q-criterion and λ_2 -criterion [17–19].

$$\nabla\vec{v} = \begin{bmatrix} \frac{\partial u}{\partial x} & \frac{\partial u}{\partial y} & \frac{\partial u}{\partial z} \\ \frac{\partial v}{\partial x} & \frac{\partial v}{\partial y} & \frac{\partial v}{\partial z} \\ \frac{\partial w}{\partial x} & \frac{\partial w}{\partial y} & \frac{\partial w}{\partial z} \end{bmatrix} = \vec{S} + \vec{\Omega} \quad (1.32)$$

The Q-criterion defines a vortex as a region where Q, the second invariant of the velocity gradient tensor, is positive [18]. This invariant defined in Eqn. 1.33 is based on the trace (*tr*) of the velocity gradient tensor which can be expressed in terms of the vorticity and strain rate. From this definition, a vortex is said to exist where the vorticity magnitude exceeds the strain rate magnitude.

$$Q = \frac{1}{2}[(tr(\nabla\vec{v}))^2 - tr((\nabla\vec{v})^2)] = \frac{1}{2}(\vec{\Omega}^2 - \vec{S}^2) \quad (1.33)$$

The λ_2 -criterion similarly uses the strain rate and vorticity. For this approach, the eigenval-

ues of $\Omega^2 - S^2$ are calculated and sorted in ascending order. A vortex is defined as regions where the second eigenvalue is negative [19]. The Q-criterion and λ_2 -criterion have been demonstrated to correctly identify identical structures in planar flows [17]. In addition, both techniques have been successfully employed as tools more robust than a vorticity threshold to detect coherent structure in the turbulent boundary layer [18, 20].

Proper Orthogonal Decomposition (POD) is a mathematical method for coherent structure identification and decomposition. First used in turbulent flows by Lumley [21] in 1967 this technique has been enhanced and applied to many other turbulence problems such as shear layers, boundary layers, and mixed convection flow [22, 23]. The principle of POD is to decompose a measured quantity into a linear combination of several eigenfunctions, known as POD modes. The goal of this approach is to formulate the most accurate decomposition by minimizing the difference between the measured quantity and the decomposition [21]. POD modes facilitate tracking of coherent structures through their kinetic energy. Previous research has demonstrated that in certain flows only a few POD modes are required to capture over half of the total kinetic energy [24]. By observing the spatial and temporal evolution of POD modes and their energy, it is possible to identify coherent structures and their characteristics in a turbulent flow [24]. There has been discussion on the significance of POD modes as either mathematical artifacts or manifestations of fluid physics. Greig et. al. [25] have summarized the work that demonstrated POD modes are descriptors of physical flow structures.

1.2.1 Unheated Turbulent Boundary Layer

The first model for describing hairpin vortex formation and dynamics came in 1952 based on an analysis of the Navier-Stokes equations [15, 26]. Other early works were able to identify structures in the boundary layer, observe complex phenomena, and determine the

turbulent boundary layer characteristics [26, 27]. These studies confirmed the presence of three-dimensional coherent structures in the boundary layer, but there was no suitable mathematical description of these phenomena [28].

Kline et. al. [27] used hydrogen bubbles to visualize streak structures in the viscous sub-layer. Their pictures illustrated the 3D nature of turbulent boundary layers [26, 27]. Classical boundary layer theory states that the buffer layer has the largest value of turbulent production. The hot-wire anemometry velocity data found in this study confirmed this theory but did not provide a physical explanation [27].

A phenomenon known as “ejection” or “bursting” was identified by Runstadler et. al. [29] as a process of turbulent production where the viscous sub-layer periodically shoots fluid upward into the buffer and log layer [26]. The bursting phenomenon has been studied using a technique, known as conditional sampling that classifies events into the four quadrants of the Cartesian coordinate plane for two velocity components, u' and v' [26, 30, 31]. The two negative Reynolds stress producing events are defined by quadrants II and IV. In quadrant II, u' is negative while v' is positive. This indicates fluid at low speed is pulled upward in a bursting or ejection event [31]. On the other hand, quadrant IV shows u' positive and v' negative describing fluid with high speed rushing towards the wall in what is named a sweeping event. Two positive Reynolds stress producing events were also observed. Quadrant III, given by negative u' and v' , defines slow fluid being pulled toward the wall. Finally, quadrant I given by positive u' and v' , occurs when high speed fluid is pulled away from the wall [31].

Burst events were also found from time series data by performing the variable integral time average (VITA) technique [32]. One study observed that in the buffer layer, a burst or quadrant II event causes the Reynolds stress to reach nine times its local time-averaged value clearly demonstrating the amount of turbulence that can be produced in this region

[32, 33].

The concept of four unique events has been applied to hairpin vortices to define the characteristic stagnation point and shear layer in front of them [16]. The motion associated with these four classes of event have been found to affect coherent structures. Kim et al. [34, 35] detected hairpin like structures in the boundary layer through Large Eddy Simulation (LES) and DNS and reported their stretching in the presence of an ejection or burst event [33]. They also found that structures in the shape of Ω can detach and create a ring vortex. Lastly, their DNS was able to capture the near-wall streaky structures observed in experiments [33, 35].

Further investigation of vortex dynamics involving the conditional sampling events were documented by Jeong et al. [20]. They used DNS database data to find stream-wise streak structures in the buffer layer that were generally aligned with the mean flow. In contrast to earlier studies, they did not find very long stream wise vortices nor did they find a substantial number of hairpin vortices [20]. The stream-wise vortices they found occurred in pairs and had a tendency to be slightly misaligned with the mean flow as well as lifted slightly upward instead of being completely parallel to the bottom wall [20]. These vortex pairs have been reported to produce velocity fluctuations that contribute significantly toward the Reynolds stress [20, 33].

Head and Bandyopadhyay [36] through flow visualization observed several hairpin-like structures in the boundary layer, which they termed as the “forest of hairpins” and were conceptually proposed as the fundamental building blocks in the turbulent boundary layer [33]. Similarly, a DNS study of a turbulent boundary layer confirmed that the “forest of hairpins” exists for both transitional and fully turbulent flows [33, 37]. The findings of these two studies continue to generate substantial controversy about the organization of hairpins and questions on their importance in boundary layer processes [33, 38].

The number of hairpin vortices in the turbulent boundary layer has been examined by Schlatter et. al. [38] who reconfirmed the “forest of hairpins” via DNS at $Re_\theta = 300$ and 600 where θ is the momentum thickness. They argue that hairpin vortices are a remnant of turbulent transition and in a fully developed turbulent boundary layer at higher Reynolds numbers, they vanish. They report that, at $Re_\theta = 1200$, the hairpins account for only 6% of all structures while at $Re_\theta = 4300$ they found only 2% of structures were hairpins [38]. The results of this study showed that while hairpins exist in abundance, their presence depends on the flow conditions. Furthermore, in a fully developed turbulent boundary layer, hairpin vortices are too rare to be considered a fundamental or representative structure of turbulence.

Hairpin vortex formation was the focus of a study by Liu et. al. [39] who performed DNS at $Re_\theta = 1000$ and used the λ_2 -criterion in conjunction with vortex filaments to identify coherent structures. In contrast to the earlier reported studies, their findings show that hairpin vortices are not produced by the deformation of the near wall structures known as Λ vortices. Instead, hairpins are generated by shear layer instability over these Λ vortices [39]. They proposed a model for turbulence generation where shear layer instability is responsible for generating vortices of all length scales. Naming shear layers as the “mother of turbulence”, they further assert that the smallest length scale is not the Kolmogorov scale but the scale of smallest shear layer [39].

Experimentally, Adrian and co-workers [15] used Particle Image Velocimetry (PIV) to study the boundary layer flow at $Re_\theta = 930$, 2370 and 6845. They identified regions of interest in the flow using the vorticity and defined the characteristic 2D projection of a hairpin structure on a vector field. The projection has three key features that were predicted to be hairpin vortex identifiers. The first is the vector field through the hairpin head whose vectors are similar to the tangent lines on a circle. The second is the stagnation point and

third is the shear layer that forms when fluid pushed from the center of the hairpin meets the stream-wise mean flow.

From the vector fields obtained, the authors concluded that hairpin vortices tend to travel in organized groups at the same relative speed. They further observed an abundance of these structures in the boundary layer, in agreement with past experimental observations [36]. The authors proposed a mechanism that as hairpin groups travel they drive the momentum transferring burst events [15]. While turbulence in the boundary layer is fundamentally a three-dimensional phenomenon, this study was the first to experimentally identify and quantify the presence and effects of hairpin vortices.

Conventional PIV is able to generate a two dimensional flow field with high accuracy but it cannot determine all three velocity components simultaneously. The Stereoscopic PIV (Stereo-PIV) technique computes all three components of velocity by using projection frames from two cameras. This was used by Dennis and Nickels [40] to detect and measure coherent structures in a turbulent boundary layer [33]. Experiments were performed at $Re_\theta = 4700$, and vortices were identified using a swirling strength condition that gives nearly identical results to the λ_2 -criterion [41]. This study was able to identify and visualize hairpin vortices that grew with distance from the wall. Detected vortices stood about 40 degrees up from the bottom wall in agreement with hairpin vortex theory. The results of this study allowed the authors to conclude that these hairpin vortices are a good basis for statistically characterizing the structures in the turbulent boundary layer [33].

Recently, an advanced technique based on PIV known as Tomographic PIV (Tomo-PIV) has been applied to the turbulent boundary layer at $Re_\theta = 1900$ by Elsinga [42]. By identifying coherent structures with the Q-criterion, they detected hairpin vortices and found their dynamics in good agreement with previous PIV studies.

The turbulent boundary layer contains numerous unique and dynamic phenomena such as

coherent structures, near-wall streaks and bursting and sweeping events. The near-wall region, specifically the buffer layer and adjacent portions of the viscous sublayer and logarithmic layer is of great interest as the phenomena in this region are known to influence the formation of coherent structures. Recent work has investigated the presence and significance of large scale stream-wise streak structures found in the log layer [43, 44]. Closer to the wall a process has been identified by both Waleffe and Kim [45, 46] and Jimenez [47] where near wall streaks can self-sustain in a cyclical process. The process involves stream-wise vortices that form the near-wall streaks which become unstable and reforms stream-wise vortices. The impact of the large-scale log layer streak structures on the near-wall cycle has been investigated by Hutchins [48] who reported that the large scale motions can regulate the near-wall cycle.

1.2.2 Heated Turbulent Boundary Layer

Heat transfer between solid and fluid is a unique phenomena capable of inducing bulk fluid motion via buoyancy. To better understand how this occurs and its applicability to boundary layer flows, consider a smooth horizontal flat plate as illustrated in Figure 1.10 where an ideal gas is present above the plate. In this configuration there is initially no bulk fluid motion and the fluid is at temperature T_∞ . The horizontal plate is heated and held at a constant temperature T_w that is greater than the bulk fluid temperature.

Thermal energy exchange between fluid and solid begins extremely close to the heated wall where inter-molecular energy transfer happens. Due to the no-slip condition there are fluid molecules directly in contact with the wall. These molecules receive thermal energy from the heated wall via conduction. In general, there exists a relatively thin conductive layer where heat transfer is driven primarily by conduction.

As the fluid temperature rises, it's temperature-dependent thermophysical properties change

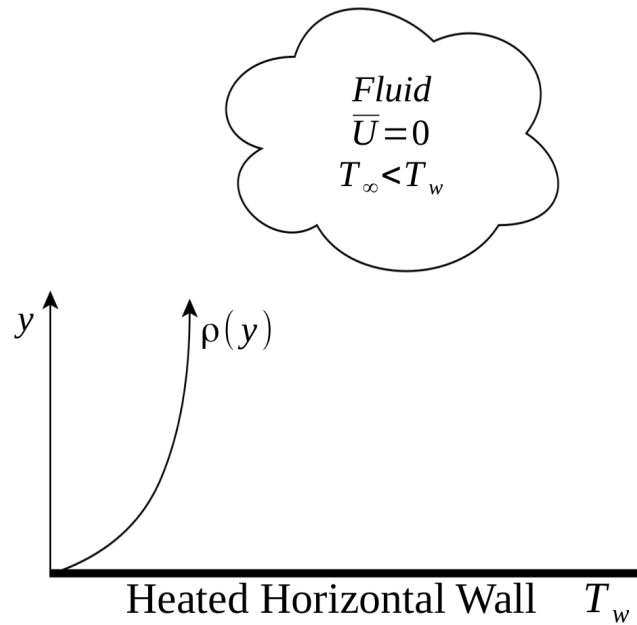


Figure 1.10: Sketch of heated horizontal wall with quiescent fluid above.

according to the equation of state. For ideal gases, the most often used equation of state is the ideal gas law in Eqn. 1.34. In this thermofluid problem the fluid pressure at the wall is exerted by the bulk fluid and remains constant. In the ideal gas law, \bar{R} is the specific gas constant. Any increase in temperature must be offset by a decrease in density to maintain constant pressure. This generates a wall-normal density variation, $\rho(y)$, within the fluid as shown in the figure.

$$P = \rho \bar{R} T \quad (1.34)$$

This conclusion is applicable to a broad range of fluids that exhibit the same behavior. Raising the temperature of a fluid generally leads to a decrease in density. The lower density fluid in the near wall region is influenced by the buoyant force which acts to lift fluid upward. The viscous force opposes the buoyant force and attempts to prevent fluid

motion. The competition between these two forces is quantified by the non-dimensional group known as the *Grashof* number (Gr) in Eqn. 1.35 [8].

$$Gr_L = \frac{gL^3\beta_\infty\Delta T}{\nu^2} \quad (1.35)$$

The numerator of Gr describes the influence of buoyancy as it contains gravitational acceleration, the horizontal plate length (L), the temperature difference between wall and bulk fluid (ΔT), and the coefficient of volumetric thermal expansion (β_∞) calculated at the bulk fluid temperature. This coefficient defined in Eqn. 1.36 is derived from the equation of state and represents the propensity of a fluid to change density when heated. The viscous force is represented in the denominator by the kinematic viscosity.

$$\beta_\infty = - \left[\frac{1}{\rho} \frac{\partial \rho}{\partial T} \right]_\infty \quad (1.36)$$

For small values of Gr , the buoyant force cannot overcome viscous resistance and no fluid motion occurs. Increasing the relative strength of the buoyant force leads to the formation of buoyancy driven fluid motion, known as natural convection. The behavior of fluids in many natural convection problems is one of the fundamental topics of convective heat transfer [8].

In the problem of fluid over a heated horizontal plate problem, natural convection produces a unique fluid behavior visualized in Figure 1.11. In this image parcels of fluid known as thermals are observed rising over a horizontal heated flat plate. Each thermal is a relatively high temperature, low density, mass of fluid whose associated buoyant force has overcome

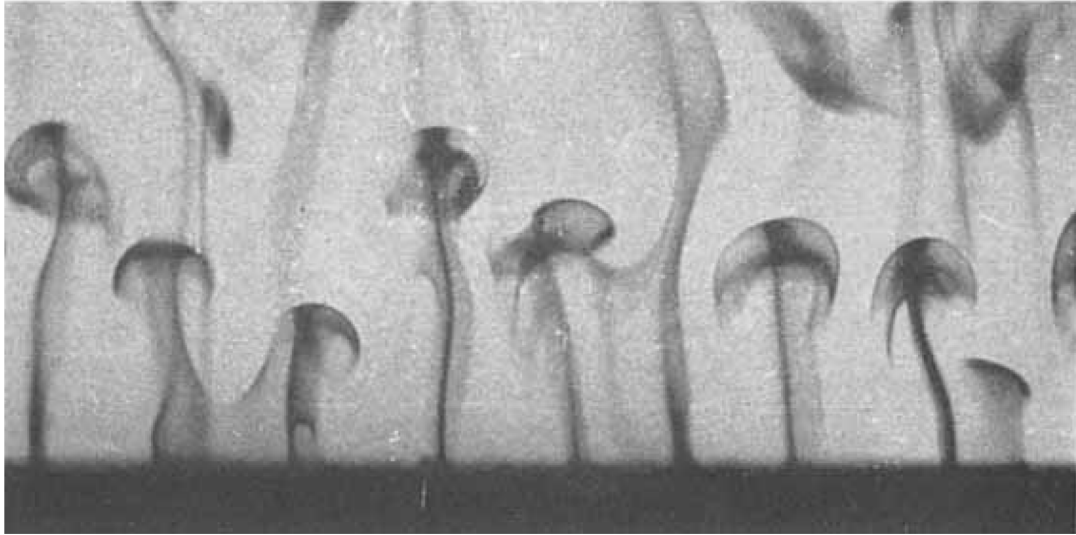


Figure 1.11: Visualization of thermals rising from a heated horizontal flat plate. Adapted from Sparrow [49].

the local viscous force. This allows each thermal to intermittently break away from the wall and freely rise.

In this configuration, heat transfer from the horizontal wall generates a region of relatively high temperature, low density fluid in the immediate vicinity of the wall. Further away from the wall, fluid has a lower temperature with higher density. This places higher density fluid above lower density fluid. As the gravitational force is larger on the high density fluid compared to the low density fluid, this state is unstable and known as a thermally unstable stratification. In contrast, a thermally stable stratification occurs when high density fluid is below low density fluid. This state can be produced by cooling the horizontal plate to below the bulk fluid temperature. In this case, fluid falls due to a stronger relative influence of gravity.

The presence of heat transfer can generate bulk fluid motion in a previously quiescent fluid due to temperature dependent changes in density that produce the buoyant force when

heated or a stronger relative gravitational force when cooled. Often in practical applications, quiescent conditions are not present and some bulk fluid motion not driven by the buoyant force exists. This leads to a boundary layer flow of bulk temperature T_∞ over a solid surface with temperature $T_w \neq T_\infty$. This temperature difference leads to the formation of another boundary layer known as the thermal boundary layer, where the temperature gradients are significant. Depending on wall and bulk fluid temperatures it is possible to achieve either a stable or unstable thermal stratification in the presence of a mean boundary layer flow.

The behavior of both stable and unstably stratified turbulent boundary layers has been the topic of many prior research studies. For a stable stratified turbulent boundary layer, it was first hypothesized by Richardson that turbulence has to compete with gravity [50, 51]. This led to the formulation of a dimensionless parameter now known as the Richardson number, Ri , that describes the relative influence of buoyancy and flow inertia [50]. High Richardson numbers, $Ri \gg 1$ in Eqn. 1.37, are associated with primarily buoyancy driven flows such as natural convection with a very weak mean flow. Very low Richardson numbers, $Ri \ll 1$, correspond to inertia dominant flows such as those found in forced convection. Finally the mixed convection state occurs when $Ri \approx 1$. Physically this means the buoyant force and inertial force are of comparable magnitude. Generally, under stably stratified conditions turbulence cannot sustain itself against gravity which leads to a significant decrease in turbulent intensity [50]. In contrast, unstable stratification in the presence of a turbulent boundary layer leads to the buoyant force interacting with inertia-driven turbulence.

Over the 60 years of research that has followed the first definition of the Richardson number, its formulation has varied among the research community. The Richardson number can be defined locally in space and time leading to the “flux” Richardson number which describes the relative contributions of turbulent shear production and buoyancy-driven pro-

duction [50]. The “gradient” Richardson number is another local non-dimensional group that describes the relative strength of mass transport due to buoyancy, represented by the density gradient, and momentum transport, represented by the mean velocity gradient [50]. The Richardson number is more frequently defined as a global parameter to describe a given flow. Some considerations of a global Ri adopt the convention where $Ri > 0$ refers to stable stratification, $Ri < 0$ implies unstable stratification, and $Ri = 0$ is the unheated case. Another frequently reported definition expresses the Richardson number as the ratio of Grashof and Reynolds numbers as indicated in Eqn. 1.37. In this equation, L is the characteristic length scale, U , the mean freestream velocity, g , gravitational acceleration, ΔT , the temperature difference between bulk fluid and solid, and β the coefficient of thermal expansion [52]. This definition imposes the condition that $Ri \geq 0$ as only the magnitude of the temperature difference is considered. Stable or unstable stratification in these cases is imposed by the experimental setup or computational domain. The literature review in this chapter will present Ri as defined by the respective original authors and clearly identify whether thermal stratification was stable or unstable.

$$Ri_L = \frac{Gr_L}{Re_L^2} = \frac{gL\beta\Delta T}{U^2} \quad (1.37)$$

Early studies of boundary layer flow with heat transfer sought to characterize the bulk behavior of the flow. Nicholl [50] experimentally studied unstable boundary layers in air. With a temperature difference of 80 °C and $Re_{\delta^*} = 600$ they were able to detect convective motion associated with natural convection competing with turbulence in the unstable boundary layer. They proposed a flow structure of convective cells being superimposed on the boundary layer flow [50]. This hypothesis was proven by Maughan et. al. [53] who

visualized the secondary flow in a water tunnel. They argued that the secondary buoyancy-driven flow causes hydrodynamic instability in the primary mean flow which begins turbulent transition if the mean flow was laminar [53].

The effects of heat transfer on turbulent transition has been further studied experimentally. Gilpin et. al. [54] demonstrated that thermal instability can cause boundary layer transition at much lower Reynolds numbers than expected. The phenomena of buoyancy-affected turbulent transition has also been seen at low Reynolds numbers. Gajusingh et. al. [55] experimentally studied flow above a heated wall using PIV. Their results supported previous research where buoyancy induces turbulence in an originally laminar flow [55].

The transportation processes that carry heat through the turbulent boundary layer have been studied both numerically and experimentally. In order to analyze the transport phenomena associated with coherent structures, Chen et. al. [56] used temperature as a passive scalar to be carried through the flow. They performed experiments with a 12°C temperature difference at $Re_\delta = 29,000$ and an estimated $Ri_\delta = 0.0017$ using Eqn. 1.37 (i.e with very weak buoyancy effects). In this study, temperature acted as a tracer facilitating coherent structure tracking. The authors reported that regions of turbulence were associated with warm fluid [56]. Burst events detected in the boundary layer were also found to happen simultaneously with temperature changes, suggesting that the heat is transferred by this process [56].

Numerically the same approach has been used by Araya and Castillo [57] who performed a DNS study of the turbulent boundary layer at $Re_\theta = 2300$. They used temperature as a passive scalar and performed visualization of streaky structures at $y^+ = 15$. Their results show that the velocity and temperature fluctuations are well correlated demonstrating that turbulence helps to transport temperature, in agreement with prior experimental findings [57].

In addition to streaky structures, the “forest of hairpins” found by Wu and Moin [37] was studied by the same authors in a passive scalar DNS study [58]. Using $Re_\theta = 80$ to 1950, they allowed a turbulent boundary layer to develop and measured the transport of temperature. They found that regions of dense hairpin vortices correlate well with regions of high temperature demonstrating that hairpin vortices are essential to turbulent transport [58].

It has been established that coherent structures play a key role in heat transport through the turbulent boundary layer. The passive scalar and small temperature difference studies neglected the effects of the buoyant force. The effect of buoyancy on turbulent fluid variables has been studied numerically and experimentally with emerging findings on coherent structures that are modified by buoyancy.

Arya [59] performed wind tunnel experiments with stable and unstable boundary layers at $Re_\delta = 1 \cdot 10^5$ to $3.5 \cdot 10^5$. For the stable experiments, $Ri_\delta = 0.01$ to 0.099 while for unstable stratification tests $Ri_\delta = -0.05$ to -0.326 . The Richardson number defined in this study is shown in Eqn. 1.38 where ΔT is the temperature difference across the boundary layer, δ is the boundary layer thickness, $\overline{U_\infty}$ is the mean free-stream velocity, T_0 is the average boundary layer temperature, and g is gravitational acceleration. Velocity and temperature data were obtained via hot-wire probes. Detailed turbulent statistics were only computed for the stable stratification experiments.

$$Ri = \frac{g\delta \Delta T}{T_0 \overline{U_\infty}^2} \quad (1.38)$$

The velocity defect profile across the boundary layer is shown in Figure 1.12a and the temperature defect curve is shown in Figure 1.12b [59]. These plots indicate that the most thermally stabilized boundary layer has the greatest momentum and thermal defects. This

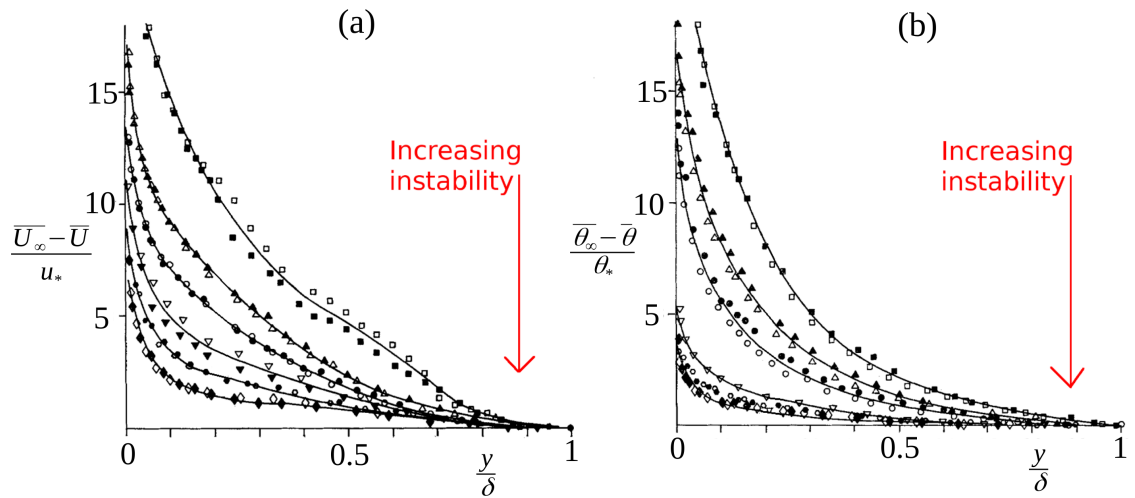


Figure 1.12: Velocity defect (a) and temperature defect (b) profiles across the boundary layer adapted from Arya [59] for stable and unstable turbulent boundary layers.

marks a substantial reduction in boundary layer mixing, suggesting turbulence is reduced. The profiles at the bottom of both plots are much flatter across the boundary layer showing lower defects. This is indicative of increased near wall mixing driven by more near wall turbulence. As the velocity and temperature are larger near the wall, the heat transfer rate and skin friction coefficient were both reported to increase [59].

The turbulent intensity was also calculated for the vertical velocity component in the thermally stable turbulent boundary layer. Results showed that increasing stability reduced the wall normal turbulent intensity [59]. The same trend was seen in the stream wise and span wise turbulent intensities showing that turbulence is reduced in all directions. These results were used as a basis to describe a previously defined mechanism through which buoyancy dampens turbulence in stable boundary layers. The buoyant force acts like a sink and only influences the vertical velocity [59]. This causes both of the remaining fluctuating velocities to decrease along with the velocity gradient, lowering the turbulence production rate. Similar results were found in the cold plate analog where fluid passes below a cooler horizontal plate and sinks [60].

Elatar and Siddiqui [23, 61] performed experiments in a heated square channel where $Re_D \approx 350$ to 750 and $\frac{Gr}{Re^2} = 9$ to 206 , where (D) is the hydraulic diameter of the channel. From PIV data, they used POD to identify coherent structures, specifically near wall convective cells produced by the buoyant force. The POD results show alternating regions of warm fluid moving upward and cool fluid moving downward [23]. From the PIV vector field obtained near the heated wall, long streaky structures were identified. These structures were associated with thermals rising from the surface [61].

Elatar and Siddiqui [62] sought to characterize the structures identified in mixed convection at low Reynolds numbers. Their experimental setup used $Re_D = 350$ to 750 and $\frac{Gr}{Re^2} = 9$ to 206 . The Q-criterion was used to detect coherent structures from PIV vector fields in planes normal and parallel to the heated wall. They found that far away from the wall, there were few coherent structures but the ones identified had high kinetic energy. In contrast, coherent structures near the wall were more numerous but generally carried less energy [62].

The number of coherent structures in an unstable boundary layer has been further assessed by Hattori et. al. [63] who performed one of the first DNS studies of thermally stable and unstable turbulent boundary layers including the effects of buoyancy. Their simulations used $Re_\theta = 1000$ in air with $Ri_\theta = 0.01$ defined according to Eqn. 1.37 where θ is the momentum thickness of the boundary layer for both stable and unstable cases. In the stable boundary layer, their results indicate that the near wall streaky structures tend to vanish. In contrast, the unstable boundary layer shows an increased number of near wall structures compared to the neutral boundary layer.

In addition to observing changes in the near wall structures, boundary layer stability also affected the turbulent profiles. The Reynolds stress, turbulent heat flux and turbulent intensity were all calculated and plotted in inner layer scaling as shown in Figure 1.13. The Reynolds shear stress in the stable boundary layer was found to substantially decrease

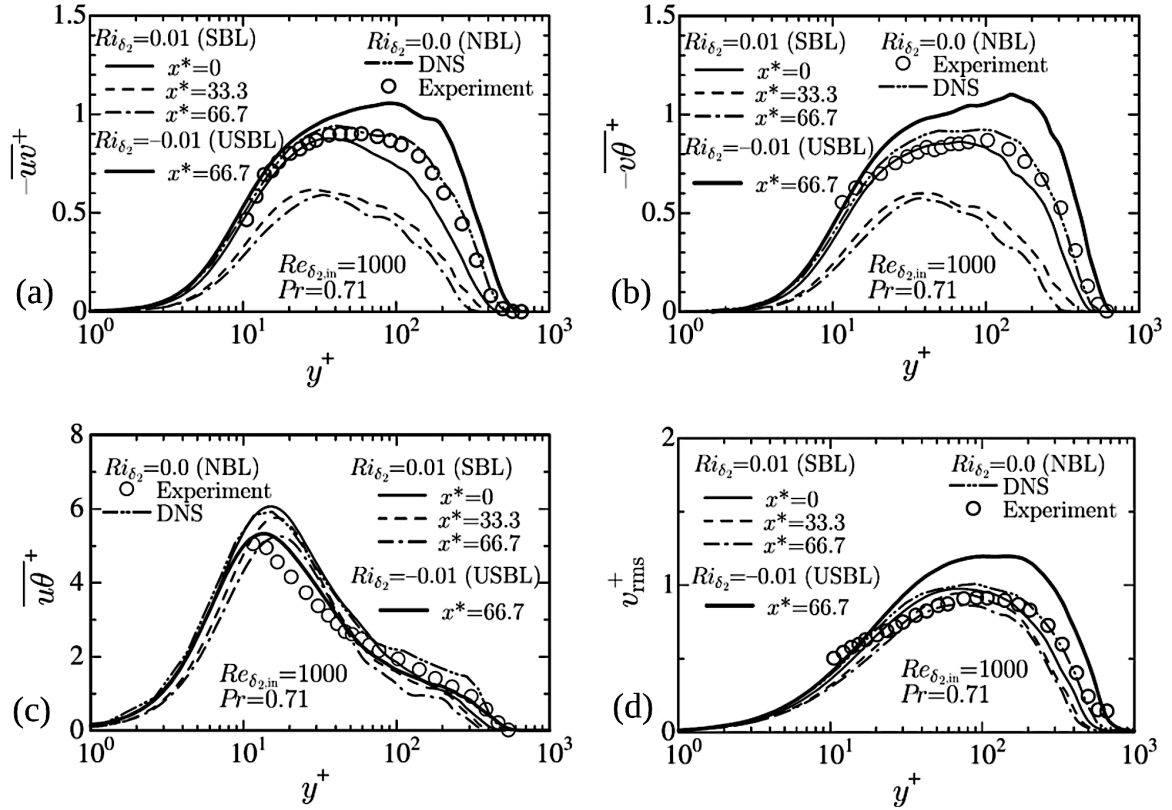


Figure 1.13: Profiles of four turbulent properties adapted from Hattori et. al [63]. (a) Reynolds shear stress, (b) wall normal turbulent heat flux, (c) stream wise turbulent heat flux, (d) wall normal turbulent intensity.

compared to the neutral boundary layer as shown in Figure 1.13a. In the unstable boundary layer however, the Reynolds shear stress increased and the peak stress was found further away from the wall compared to the neutral and stable boundary layers [63].

The stream wise and wall-normal turbulent heat fluxes were plotted in Figure 1.13b and Figure 1.13c. The stream wise turbulent heat flux showed a small increase in peak value for the stable boundary layer. Making the boundary layer unstable however did not substantially change the heat flux compared to the neutral boundary layer [63]. The wall-normal result however is completely different. The stable boundary layer shows a very clear decrease in heat flux. On the other hand, the unstable boundary layer has a clear increase

in heat flux [63]. As with the Reynolds shear stress, the peak value of turbulent heat flux in the unstable boundary layer occurs furthest away from the wall. In Figure 1.13d, the wall-normal turbulent root-mean-square (RMS) velocity is graphed. The calculated RMS velocity was not reported to change substantially in the stable boundary layer. In contrast, the unstable boundary layer shows a significant increase in RMS velocity and has its peak at a greater distance from the wall compared to the stable and neutral boundary layers [63].

These results are in agreement with past experiments that showed an increase in wall-normal turbulent intensity [59]. Furthermore, a mechanism of producing these changes in turbulent properties is discussed. Buoyancy in the unstable boundary layer increases the wall-normal velocity fluctuations which enhances shear stress and wall-normal heat flux [63]. A very similar mechanism has been described for the stable boundary layer where buoyancy extracts energy from the wall-normal velocity component [59].

The effect of buoyancy on coherent structures was the focus of a DNS study by Li et. al. [64]. They used a momentum thickness based $Re_\theta = 1100$ in air with $Gr_\theta = 13,000$, corresponding to $Ri_\theta = 0.01$ as per Eqn. 1.37 for the unstable boundary layer. Their results showed similar trends in near wall turbulent properties as Hattori et. al.'s [63] simulation. The iso-surfaces detected using the λ_2 -criterion show coherent structures that appear to be stretched vertically, up to 1.6 times the unheated boundary layer thickness as shown in Figure 1.14. Furthermore, they found that the buoyant force tends to align coherent structures with the wall-normal vector [64]. In contrast, it was found that near wall streaks were displaced closer to the wall. Hairpin vortex theory states that the head of the hairpin sits at approximately 45 degrees to the bottom wall. Their results found that in the presence of heat, hairpin vortex inclination rose to around 60 degrees and the size of detected vortices decreased [64].

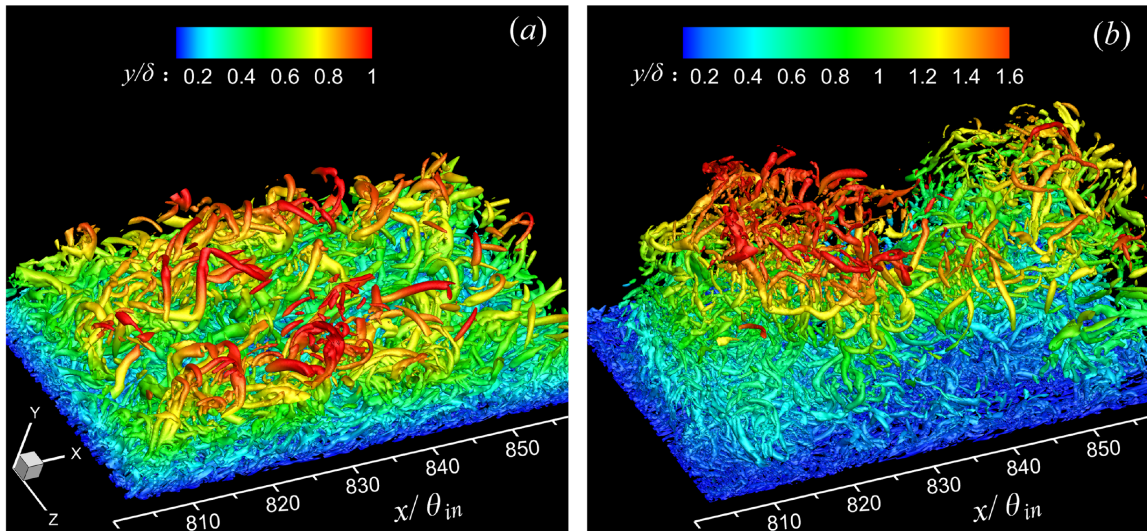


Figure 1.14: Detected coherent structures in the turbulent boundary layer, (a) without the buoyant force (b) with the buoyant force. Adapted from Li et. al. [64].

1.3 Experimental Measurement Techniques

Turbulent fluid flows are three-dimensional by nature and the behavior of these flows is key to understanding the fundamental processes in many natural phenomena and engineering systems. Solving the governing equations for turbulent flows is mathematically and computationally challenging. As a result, research has been heavily reliant on experimental tools and techniques to obtain deeper insight into the underlying dynamics and provide an improved flow characterization. In order to obtain a complete description of a turbulent flow, all three velocity components need to be captured simultaneously. This presents a major on-going challenge in experimental research on turbulent flow. While many techniques have been developed in the past to measure turbulent velocities and visualize flow trajectories, each technique has its own benefits and limitations.

Hot-wire anemometry is a velocimetry technique where a thin heated wire is placed in a

flow. As the fluid passes over the wire it cools via convection. The amount of heat required to maintain a constant wire temperature is related to the local fluid velocity. The wire diameter is typically kept very small, on the order of a few microns, to reduce thermal inertia and response time, which allows measurements with very high time resolution, excellent spatial resolution, and sampling rates on the order of MHz [65, 66]. With multiple hot wires arranged in specific configurations, two or all three components of velocity can be measured simultaneously.

Being a point-measurement technique, hot-wire anemometry has a limitation of measuring velocity at one precisely defined location in space. Multiple hot wires or single hot wire traversing could be used for mapping a flow field but this is often limited by available resources. Another challenge is the intrusive nature of the instrument, which limits measurements and may face mounting issues. Hot-wire anemometry is successful when data collection is only needed at a single well-defined point in space with high temporal resolution to resolve a very wide range of turbulent time scales.

Optical techniques utilize light and often seed particles to measure the velocity field remotely, reducing intrusion upon the flow field. These techniques can be performed in a wide range of geometries provided optical access is available. Laser Doppler Velocimetry (LDV) is an alternative to hot-wire anemometry which uses the Doppler frequency shift of light scattered by seed particles to measure one or more components of velocity in a non-intrusive manner. This technique has been successfully applied to turbulent flows measuring up to three velocity components [67, 68]. Like hot-wire anemometry however, LDV is a point measurement technique.

In other optical techniques, cameras are used to capture images that are processed into detailed two and three-dimensional flow fields. These techniques are also non-intrusive and provide velocity data in both time and space. The spatial resolution (i.e. spatial sampling

rate magnitude) of the velocity data is typically much higher than the temporal resolution (i.e. temporal sampling rate magnitude), although with the advancement of illumination and camera technologies, substantial improvements in both time and space resolution is realizable. In addition, advancements in computing technology have also enabled fast processing of large image data sets, making optical methods a common choice for turbulent flow measurement and characterization.

Planar Particle Image Velocimetry is one optical measurement technique that utilizes a laser light sheet and camera to measure two components of velocity in a plane. PIV first evolved from speckle metrology or scattered light speckle metrology (SLS) before arriving at its current form in 1991 [69–72]. Unlike single point techniques, PIV offers a complete two-dimensional velocity field of a fluid and today remains among the best available techniques of obtaining detailed velocity data.

The core elements of a modern digital PIV system include a digital camera, PC, laser, synchronization unit, laser optics, and a suitable seed particle. The light beam exiting the laser is focused using a spherical lens and formed into a thin laser light sheet with the cylindrical lens. The camera is placed facing the light sheet with the camera lens focused on the sheet. During experiments, as seed particles pass through the laser light sheet they reflect light which is captured by the camera. The laser timing is controlled using a synchronization unit to ensure each laser pulse occurs during the exposure time of each frame captured by the camera. Images are recorded onto a PC for analysis. By varying the time between consecutive laser light pulses (Δt) and the camera's frame rate, a wide range of fluid motion time-scales can be captured.

PIV analysis is performed on consecutive pairs of images and comprised of multiple steps to reduce error and improve velocity estimation accuracy. The primary component of PIV image analysis is the cross-correlation. The first image in a given pair is split into many “in-

terrogation windows” while the second image is split into many larger “search windows”. Each interrogation window corresponds to a unique search window. A sample image pair with one interrogation window and search window is shown in Figure 1.15.

In the figure, frame one is captured first and frame two is captured a short time, Δt , after frame one. The interrogation window is taken from frame one and the search window is taken from frame two. The different sizes of the interrogation window and search window enables the interrogation window to rigid translate within its corresponding search window as shown in Figure 1.16. The 2D cross-correlation between interrogation window and search window is calculated for all possible rigid translations $(\Delta i, \Delta j)$ of the interrogation window within the search window.

The interrogation window translation that produces the largest cross-correlation magnitude $(\Delta i_{Max}, \Delta j_{Max})$ is taken as the interrogation window displacement. This defines the distance that the interrogation window, specifically the seed particles pictured in the interrogation window, translated during the time between each laser pulse i.e. each captured image in the pair. The local planar velocity is estimated by dividing the calculated displacement by the time between laser pulses shown in Eqn. 1.39. This process is applied to all interrogation windows and search windows in an image pair to produce a two-dimensional velocity field.

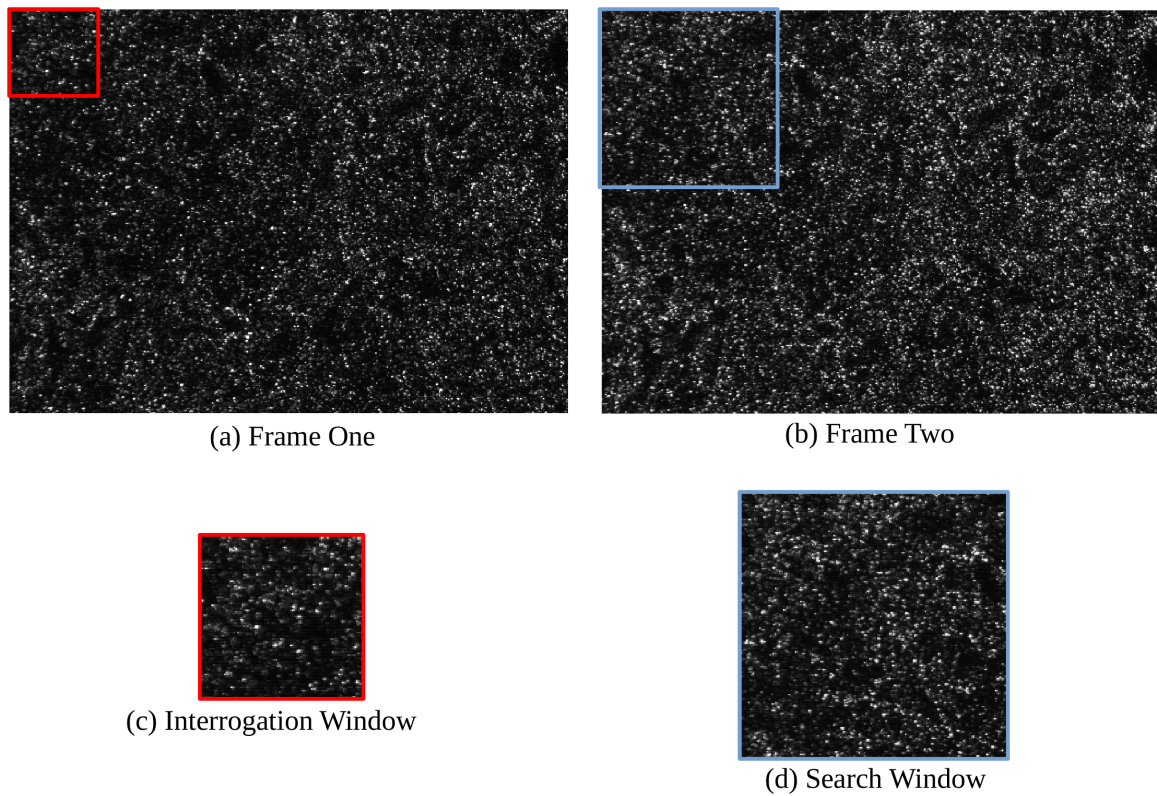


Figure 1.15: Sample PIV image pair (a) and (b) and one respective interrogation window (c) and search window (d).

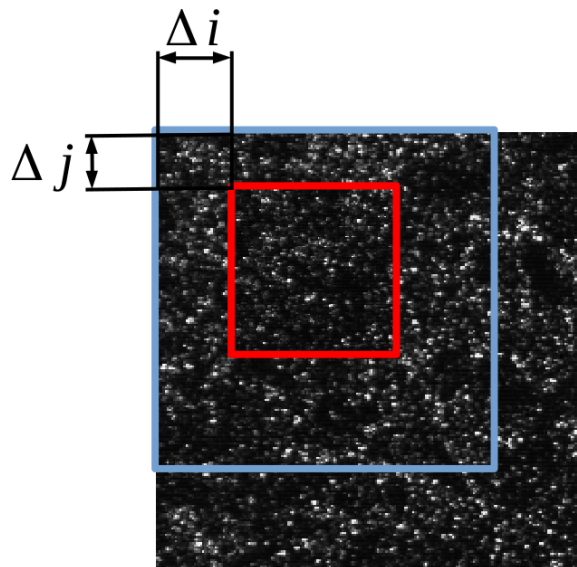


Figure 1.16: Rigid translation of the interrogation window (red) inside the corresponding search window (blue) for an arbitrary translation $\Delta i, \Delta j$.

$$(u, v) = \left(\frac{\Delta i_{Max}}{\Delta t}, \frac{\Delta j_{Max}}{\Delta t} \right) \quad (1.39)$$

One limitation of planar PIV is the ability to measure only two components of velocity. While the laser sheet can be moved to provide velocity fields over several planes, the out of plane velocity can never be measured simultaneously with the other two components.

A solution to this issue has been developed in the form of the Stereoscopic PIV technique that constructs a 3D velocity field by having two off-axis cameras recording particles' movement within a laser sheet [73]. From the two images captured, all three velocity components are calculated. This technique has been successfully applied to turbulent flows [40]. While the Stereoscopic PIV technique computes a 3D velocity field, the calculations are based on mathematical projections of a planar light sheet (i.e. images of a plane are used to determine motion within a volume). This has led to studies that have found the out-of-plane velocity component is of questionable accuracy, which limits the computations of, out-of-plane gradients [74, 75].

Tomographic PIV is recent advancement that employs four or more cameras at different viewing angles to observe seed particles passing through a laser-illuminated volume. Images from all cameras are used to reconstruct a 3D velocity field through one of many complex calculation schemes [76–78]. The core of Tomo-PIV is to use several cameras to detect the same particle from multiple angles which enables calculation of its exact coordinates. This technique improves upon Stereoscopic PIV by calculating all three velocity components and their gradients. Elsinga et. al. [42, 79] successfully applied Tomo-PIV to a turbulent boundary layer and supersonic boundary layer to characterize three-dimensional coherent structures.

While capable of computing all three velocity components, Tomographic PIV is known to produce errors in velocity measurement [80, 81]. This is due to the influence of ghost particles, defined as false particles detected when identifying the same particle from multiple perspectives. Ghost particles introduce velocity errors that have the tendency to smear particle velocities over the measurement volume [80, 81]. As a result, velocity gradients are under predicted. This effect is amplified in high shear flows such as near the wall in a turbulent boundary layer [80–82]. Both Stereoscopic and Tomographic PIV utilize multiple cameras that are expensive and require precise alignment. Alignment is of great importance as the accuracy of the computed vector field depends on camera angle [74, 75]. Furthermore, the algorithms for velocity computation and image processing are relatively complex.

To capture a three-dimensional flow field without using several cameras, multiple new approaches have been developed each utilizing color to represent out-of-plane motion. In this approach, the white light emitted from a source is transformed into discrete color layers or the continuous visible light spectrum, either by the use of grating or more complicated optics [83, 84]. The generated multi-color illuminated volume is oriented such that the color change of a particle is used to quantify the out-of-viewing-plane velocity component. A liquid-crystal display (LCD) projector has been used to create up to six discrete color layers for PIV measurements which generated a three-dimensional flow field [85, 86]. LCD projectors have also been used to generate an adjustable polychromatic spectrum for 3D particle tracking velocimetry measurements that is easily adjustable [87]. LCD projectors are easy to use and enable simple color distribution adjustment, making them suitable for multi-color measurement techniques.

Recently, Rainbow Volumic Velocimetry (RVV) has emerged as a promising technique to visualize and measure three-dimensional flow fields. The technique works by converting

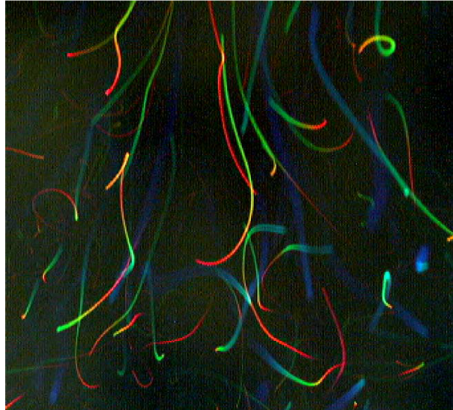


Figure 1.17: Image of particle trajectories where color corresponds to the depth position found using the RVV technique. Adapted from Prenel [88].

white light into the polychromatic spectrum using blazed reflecting grating, producing a multi-color illuminated volume [88, 89]. Particles in the seeded flow are then imaged as they reflect light while passing through the volume. By tracking particle position, two planar velocity components are computed while the third component is estimated by the color change of reflected light. Colored streaks captured by Prenel et. al. [88] shown in Figure 1.17 demonstrate three dimensional particle paths found with the RVV technique. As the technique utilizes color variations in the plane perpendicular to the camera field of view, the out-of-plane velocity component's accuracy is strongly dependent upon and known to decrease with increases in the each color's beam [88]. To reduce the significance of this effect the overall light beam width needs to be kept small, reducing the effective measurement volume size. Recent works have improved upon RVV by utilizing specialized camera optics to ensure the entire measurement volume is in focus on the camera and have extended the volume depth through the use of multiple blazed gratings [90, 91]. These advancements have greatly improved the broad applicability of RVV, however the volume depths remain limited to approximately 50 mm without the use of more resource intensive blazed grating configurations.

There are multiple emerging techniques that utilize novel illumination methods to produce data suitable for three-dimensional flow visualization and measurement. Dennis and Siddiqui have developed a multi-color grid technique for 3D flow characterization [92]. The color grid pattern facilitated color changes to correspond to motion in two directions however their early results indicate the technique is of limited use due to interference between the colors of adjacent grids and no practical analysis algorithm was presented. Park et. al. improved the multi-color PIV technique by varying the color distribution in time to improve out-of-plane spatial resolution and uncertainty in six color layer measurements [93]. This technique however reduces temporal resolution to achieve this goal making it applicably limited to flows with relatively weak out-of-plane motion.

1.4 Research Objectives

This literature review has established some fundamental boundary layer flow behaviors. The boundary layers encountered in a majority of practical systems are turbulent and feature some heat transfer. As a result these flows are characterized by stochastic three-dimensional motion, turbulent structures, and complex dissipative processes. In addition, heat transfer further increases complexity due to the presence of the buoyant force and non-linear coupling of the thermofluid variables. The system of governing equations for turbulent boundary layer flow, a system of non-linear coupled differential-algebraic equations, has no exact solution. A mathematical decomposition of these equations however, provides several key insights into some turbulent flow behaviors, such as, the presence of apparent fluid stress and heat conduction due to turbulent motion. Due to the innate complexity of the governing equations and fundamental flow behaviors, experiments are the primary avenue for advancing the current knowledge on turbulent boundary layer flow behavior.

1.4.1 Knowledge Gaps

Experimental Measurement Techniques

Presently most flow measurement techniques determine only one or two simultaneous velocity components. Planar PIV has taken a leading role as a widely adopted experimental measurement technique due to its relative simplicity in implementation and a well-established successful history of characterizing turbulent flows. As only two velocity components are measured however, this limits the estimation and characterization of key quantities such as the turbulent kinetic energy, which is a critical step towards an improved understanding on the nature of turbulent flows. Stereoscopic PIV and Tomographic PIV are resource intensive and have technical challenges in accurately measuring all three velocity components. RVV is a promising alternative that could produce a 3D velocity field from a single camera by utilizing color to define out-of-plane motion but is limited to small volumes.

In recent years, there has been growing interest in the development of a 3D flow measurement system that uses color to describe out-of-plane motion. These emerging methods often provide both qualitative flow visualization and quantitative simultaneous estimates of all three velocity components. However, many of these techniques are very early in their respective developments and no single technique has demonstrated broad applicability and acceptance. These emerging techniques require further development in data analysis and implementation refinement before they are realized as widely acceptable for three-dimensional flow characterization.

The objective for this part of the study is the following:

- Develop a volumetric illumination technique and associated data analysis algorithm for three-dimensional flow characterization.

Mixed Convection Turbulent Boundary Layer

Heat in the horizontal flat plate turbulent boundary layer is often treated as simply a passive scalar that is carried by the fluid. This is a good description only if the buoyant force is negligible compared to inertial forces in the boundary layer. When these forces are comparable, as in the case of mixed convection, the buoyant force produced by heat transfer has a significant effects on the boundary layer such as influencing turbulent transition and enhancing or dampening turbulence.

The current body of literature has documented that the buoyant force has a profound influence on turbulent boundary layer dynamics. However, the process of how buoyancy produces changes in boundary layer turbulence is not well understood. There is a lack of work on characterizing thermals' behavior as a secondary flow structure and the associated influence on key turbulent quantities. Prior work on the dynamics of this flow often focus on describing mixed convection turbulent boundary layer behaviors at only one Richardson number.

The objectives for this part of the study are as follows:

- Determine the behavior of thermals in the mixed convection turbulent boundary layer over a range of Richardson numbers.
- Identify and characterize the mechanism(s) responsible for the modification of turbulent boundary layer structure over a range of Richardson numbers.
- Investigate and characterize the mechanism(s) that govern the modification to turbulent statistics by wall heating within the mixed convection turbulent boundary layer.

The range of Richardson numbers tested must provide sufficient information to describe the transition from buoyancy dominant to inertia dominant mixed convection turbulent boundary layer flow. Therefore multiple flow conditions are tested in a range that includes buoy-

ancy dominant, $Ri > 1$, inertia dominant, $Ri < 1$, and equal influences, $Ri \approx 1$, of inertia and the buoyant force on flow dynamics.

1.4.2 Thesis Layout

The content of this thesis is organized as follows:

- Chapter 1 discusses the significance boundary layer flow and the fundamentals of boundary layer theory. A review of the classical and modern literature is presented on turbulent boundary layers in the presence and absence of wall heating. A review of state-of-the-art experimental fluid velocity measurement techniques is also presented. The highly three-dimensional motion and complex dynamical nature of mixed convection turbulent boundary layer flow requires a thorough investigation in multiple topics.
- Chapter 2 details the development of a novel method for three-dimensional flow characterization and details the developed data analysis algorithm. Presently, experimental techniques are the primary method for performing measurement and characterization of turbulent flows. The newly developed flow measurement technique contributes and advances the body of literature on three-dimensional flow characterization. The developed technique is applicable to three-dimensional flows including turbulent boundary layer flow.
- Chapter 3 reports on a three-dimensional investigation of near-wall unheated turbulent boundary layer dynamics. In order to study the mixed convection turbulent boundary layer, it is necessary to first produce a unheated turbulent boundary layer flow. The experiments documented in this chapter are on the unheated turbulent boundary layer which form a basis to compare findings from mixed convection turbulent boundary layer experiments. This chapter presents new insights on the near-wall

behaviors of the turbulent boundary layer.

- Chapter 4 presents a technique to detect thermals in flow visualization images and characterizes the three-dimensional structure and characteristics of thermals in the mixed convection turbulent boundary layer.
- Chapter 5 characterizes the modification of turbulence in the boundary layer by wall heating. The thermal detection method described in the previous chapter is utilized in this chapter to facilitate the characterization of the dynamic processes that govern the modification of turbulent statistics by wall heating in the mixed convection turbulent boundary layer.
- Chapter 6 summarizes this study, draws conclusions from presented findings, and provides recommendations for future work.

Bibliography

- [1] D. Voss, “Collapse of the Tacoma Narrows Bridge,” *APS News: This Month in Physics History*, vol. 25, no. 10, 2016. [Online]. Available: APS, <https://www.aps.org/publications/apsnews/201611/physicshistory.cfm>. [Accessed August 8, 2019].
- [2] J.K. Finch, “Wind Failures of Suspension Bridges, or, Evolution and Decay of the Stiffening Truss,” *Engineering News Record*, pp. 74–79, March 13, 1941.
- [3] V.B. Omubo-Pepple, C. Israel-Cookey, and G.I. Alaminokuma, “Effects of Temperature, Solar Flux and Relative Humidity on the Efficient Conversion of Solar Energy to Electricity,” *European Journal of Scientific Research*, vol. 35, no. 2, pp. 173–180, 2009.
- [4] S. Brand, “The Effects on a Tropical Cyclone of Cooler Surface Waters due to Upwelling and Mixing Produced by a Prior Tropical Cyclone,” *Journal of Applied Meteorology*, vol. 10, pp. 865–874, 1971.
- [5] W.M. Gray, “The Formation of Tropical Cyclones,” *Meteorology and Atmospheric Physics*, vol. 67, pp. 37–69, 1998.
- [6] S. Pal, M. Lopez, M. Schmidt, M. Ramonet, F. Gilbert, I. Xueref-Remy, and P. Cialis, “Investigation of the atmospheric boundary layer depth variability and its impact on

- the ^{222}Rn concentration at a rural site in France,” *Journal of Geophysical Research*, vol. 120, pp. 623–643, 2015.
- [7] W.M. Kays, M.E. Crawford, and B. Weigand, *Convective Heat and Mass Transfer*. Boston, MA: McGraw-Hill Higher Education, 4th ed., 2005.
- [8] F.P. Incropera, F.P. Dewitt, T.L. Bergman, and A.S. Lavine, *Fundamentals of Heat and Mass Transfer*. New York, NY: John Wiley & Sons, 6 ed., 2007.
- [9] P.J. Pritchard, *Fox and McDonald’s Introduction to Fluid Mechanics*. Hoboken, NJ: John Wiley & Sons Inc., 8th ed., 2011.
- [10] H. Schlichting and K. Gersten, *Boundary Layer Theory*. Springer, 8th ed., 1999.
- [11] P. Davidson, *Turbulence: An Introduction for Scientists and Engineers*. Oxford, UK: Oxford University Press, 2nd ed., 2015.
- [12] J.O. Hinze, *Turbulence: An Introduction to Its Mechanism and Theory*. New York: NY, McGraw-Hill Book Company Inc., 1959.
- [13] A. Bejan, *Convection Heat Transfer*. Hoboken, NJ: John Wiley & Sons Inc., 3rd ed., 2004.
- [14] S.B. Pope, *Turbulent Flows*. Cambridge, UK: Cambridge University Press, 2000.
- [15] R.J. Adrian, C.D. Meinhart, and C.D. Tomkins, “Vortex organization in the outer region of the turbulent boundary layer,” *Journal of Fluid Mechanics*, vol. 422, pp. 1–54, 2000.
- [16] J.M. Wallace, R.S. Brodkey, and H. Eckelmann, “Pattern-recognized structures in bounded turbulent shear flows,” *Journal of Fluid Mechanics*, vol. 83, no. 4, pp. 679–693, 1977.

- [17] V. Holmen, “Methods for vortex identification,” Master’s thesis, Lund University, 2012.
- [18] J.C.R. Hunt, A.A. Wray, and P. Moin, *Eddies, Streams, and Convergence Zones in Turbulent Flows*. Center for Turbulence Research. Proceedings of the Summer Program, 1988.
- [19] J. Jeong, and F. Hussain, “On the identification of a vortex,” *Journal of Fluid Mechanics*, vol. 285, pp. 69–94, 1995.
- [20] J. Jeong, F. Hussain, W. Schoppa, and J. Kim, “Coherent structures near the wall in a turbulent channel flow,” *Journal of Fluid Mechanics*, vol. 332, pp. 185–214, 1997.
- [21] P. Holmes, J.L. Lumley, G. Berkooz, and C.W. Rowley, *Turbulence, Coherent Structures, Dynamical Systems and Symmetry*. Cambridge, UK: Cambridge University Press, 2nd ed., 2012.
- [22] N. Aubry, P. Holmes, J.L. Lumley, and E. Stone, “The dynamics of coherent structures in the wall region of a turbulent boundary layer,” *Journal of Fluid Mechanics*, vol. 192, pp. 115–173, 1988.
- [23] A. Elatar, and K. Siddiqui, “The effect of mixed convection on the structure of channel flow at low Reynolds numbers,” *International Journal of Heat and Fluid Flow*, vol. 46, pp. 29–42, 2014.
- [24] L. Diddipatla, *Wake Dynamics and Passive Flow Control of a Blunt Trailing Edge Profiled Body*. PhD thesis, University of Western Ontario, 2010.
- [25] D. Greig, K. Siddiqui, P. Karava, and A. Elatar, “Investigation of fundamental flow mechanisms over a corrugated waveform using proper orthogonal decomposition and

- spectral analyses,” *International Journal of Thermal Sciences*, vol. 96, pp. 160–172, 2015.
- [26] S.K. Robinson, “Coherent motions in the turbulent boundary layer,” *Annual Review of Fluid Mechanics*, vol. 23, pp. 601–639, 1991.
- [27] S.J. Kline, W.C. Reynolds, F.A. Schraub, and P.W. Runstadler, “The structure of turbulent boundary layers,” *Journal of Fluid Mechanics*, vol. 30, no. 4, pp. 741–773, 1967.
- [28] P.S. Klebanoff, “Some Preliminary Results of Visual Studies of the Flow model of the Wall Layers of the Turbulent Boundary Layer,” *Journal of Applied Mechanics: Discussion. Transactions of the ASME*, 1960.
- [29] P.W. Runstadler, S.J. Kline, and W.C. Reynolds, *An experimental investigation of the flow structure of the turbulent boundary layer*. No. MD8. Stanford University California, 1963.
- [30] S.S. Lu, and W.W. Willmarth, “Measurements of the structure of the Reynolds stress in a turbulent boundary layer,” *Journal of Fluid Mechanics*, vol. 60, no. 3, pp. 481–511, 1973.
- [31] J.M. Wallace, H. Eckelmann, and R.S. Brodkey, “The wall region in turbulent shear flow,” *Journal of Fluid Mechanics*, vol. 54, no. 1, pp. 39–48, 1972.
- [32] R.F. Blackwelder, and R.E. Kaplan, “On the wall structure of the turbulent boundary layer,” *Journal of Fluid Mechanics*, vol. 76, no. 1, pp. 89–112, 1976.
- [33] J.M. Wallace, “Highlights from 50 years of turbulent boundary layer research,” *Journal of Turbulence*, vol. 13, no. 53, pp. 1–70, 2013.

- [34] J. Kim, and P. Moin, “The structure of the vorticity field in turbulent channel flow. Part 2. Study of ensemble-averaged fields,” *Journal of Fluid Mechanics*, vol. 162, pp. 339–363, 1986.
- [35] J. Kim, P. Moin, and R. Moser, “Turbulence statistics in fully developed channel flow at low Reynolds number,” *Journal of Fluid Mechanics*, vol. 177, pp. 133–166, 1987.
- [36] M.R. Head, and P. Bandyopadhyay, “New aspects of turbulent boundary-layer structure,” *Journal of Fluid Mechanics*, vol. 107, pp. 297–338, 1981.
- [37] X. Wu, and P. Moin, “Direct numerical simulation of turbulence in a nominally zero-pressure-gradient flat-plate boundary layer,” *Journal of Fluid Mechanics*, vol. 630, pp. 5–41, 2009.
- [38] P. Schlatter, Q. Li, R. Orlu, F. Husain, and D. Henningson, D., “On the near-wall vortical structures at moderate Reynolds numbers,” *European Journal of Mechanics B/Fluids*, vol. 48, pp. 74–93, 2014.
- [39] C. Liu, Y. Yan, and P. Lu, “Physics of turbulence generation and sustenance in a boundary layer,” *Computers & Fluids*, vol. 102, pp. 353–384, 2014.
- [40] D.J.C. Dennis and T.B. Nickels, “Experimental measurement of large-scale three-dimensional structures in a turbulent boundary layer. Part 1. Vortex packets,” *Journal of Fluid Mechanics*, vol. 673, pp. 180–217, 2011.
- [41] J. Zhou, R.J. Adrian, S. Balachandar, and T.M. Kendall, “Mechanisms for generating coherent packets of hairpin vortices in channel flow,” *Journal of Fluid Mechanics*, vol. 387, pp. 353–396, 1999.
- [42] G. Elsinga, *Tomographic particle image velocimetry and its application to turbulent boundary layers*. PhD thesis, Delft University of Technology, 2008.

- [43] N. Hutchins, and I. Marusic, “Evidence of Very Long Meandering Features in the Logarithmic Region of Turbulent Boundary Layers,” *Journal of Fluid Mechanics*, vol. 579, pp. 1–28, 2007.
- [44] N. Hutchins, and I. Marusic, “Large-scale Influences in Near-wall Turbulence,” *Philosophical Transactions of the Royal Society A*, vol. 365, pp. 647–664, 2007.
- [45] F. Waleffe and J. Kim, *How Streamwise Rolls and Streaks Self-sustain in a Shear Flow*. in Self-sustaining Mechanisms of Wall-bounded Turbulence. Southampton, UK and Boston, USA: Computational Mechanics Publications, 1997.
- [46] F. Waleffe and J. Kim, *How Streamwise Rolls and Streaks Self-sustain in a Shear Flow: Part 2*. American Institute of Aeronautics and Astronautics. Albuquerque, USA, 1998.
- [47] J. Jimenez and A. Pinelli, “The Autonomous Cycle of Near-wall Turbulence,” *Journal of Fluid Mechanics*, vol. 389, pp. 335–359, 1999.
- [48] R. Mathis, N. Hutchins, and I. Marusic, “Large-scale Amplitude Modulation of the Small-scale Structures in Turbulent Boundary Layers,” *Journal of Fluid Mechanics*, vol. 628, pp. 311–337, 2009.
- [49] E.M. Sparrow, R.B. Husar, and R.J. Goldstein, “Observations and other characteristics of thermals,” *Journal of Fluid Mechanics*, vol. 41, no. 4, pp. 793–800, 1970.
- [50] C.I.H. Nicholl, “Some dynamical effects on a turbulent boundary layer,” *Journal of Fluid Mechanics*, vol. 40, no. 2, pp. 361–384, 1970.
- [51] L.F. Richardson, *The Supply of Energy from and to Atmospheric Eddies*. Royal Society Publishing, 1920.

- [52] J. Turner, *Buoyancy Effects in Fluids*. Cambridge, UK: Cambridge University Press, 1973.
- [53] J.R. Maughan, and F.P. Incropera, “Secondary flow in horizontal channels heated from below,” *Experiments in Fluids*, vol. 5, pp. 334–343, 1987.
- [54] R.R. Gilpin, H. Imura, and K.C. Cheng, “Experiments on the Onset of Longitudinal Vortices in Horizontal Blasius Flow Heated from Below,” *Journal of Heat Transfer*, vol. 100, pp. 71–77, 1978.
- [55] S.T. Gajusingh, and M.H.K. Siddiqui, “The influence of wall heating on the flow structure in the near-wall region,” *International Journal of Heat and Fluid Flow*, vol. 29, pp. 903–915, 2008.
- [56] C. Chen and R. Blackwelder, “Large-scale motion in a turbulent boundary layer: a study using temperature contamination,” *Journal of Fluid Mechanics*, vol. 89, no. 1, pp. 1–31, 1978.
- [57] G. Araya and L. Castillo, “DNS of turbulent thermal boundary layers up to $Re = 2300$,” *International Journal of Heat and Mass Transfer*, vol. 55, pp. 4003–4019, 2012.
- [58] X. Wu, and P. Moin, “Transitional and turbulent boundary layer with heat transfer,” *Physics of Fluids*, vol. 22, p. 8, 2010.
- [59] S.P.S. Arya, “Buoyancy effects in a horizontal flat-plate boundary layer,” *Journal of Fluid Mechanics*, vol. 68, no. 2, 1975.
- [60] S. Komori, H. Ueda, F. Ogino, and T. Mizushima, “Turbulence structure in unstable-stratified open-channel flow,” *Physics of Fluids*, vol. 25, no. 9, pp. 1539–1546, 1982.

- [61] A. Elatar, and K. Siddiqui, “The influence of bottom wall heating on the mean and turbulent flow behavior in the near wall region during mixed convection,” *International Journal of Thermal Sciences*, vol. 77, pp. 233–243, 2014.
- [62] A. Elatar, and K. Siddiqui, “The characteristics of coherent structures in low Reynolds number mixed convection flows,” *Fluid Dynamics Research*, vol. 47, p. 33, 2015.
- [63] H. Hattori, T. Houra, and Y. Nagano, “Direct numerical simulation of stable and unstable turbulent thermal boundary layers,” *International Journal of Heat and Fluid Flow*, vol. 28, pp. 1262–1271, 2007.
- [64] D. Li, K. Luo, and J. Fan, “Buoyancy effects in an unstably stratified turbulent boundary layer flow,” *Physics of Fluids*, vol. 29, p. 17, 2017.
- [65] G. Comte-Bellou, “Hot-Wire Anemometry,” *Annual Review of Fluid Mechanics*, vol. 8, pp. 209–231, 1976.
- [66] A.K. Prasad, “Particle image velocimetry,” *Current Science*, vol. 79, no. 1, pp. 51–60, 2000.
- [67] W.K. George, and J.L. Lumley, “The laser-Doppler velocimeter and its application to the measurement of turbulence,” *Journal of Fluid Mechanics*, vol. 60, no. 2, pp. 321–362, 1973.
- [68] S.M. Olcmen and R.L. Simpson, “A five-velocity-component laser-Doppler velocimeter for measurements of a three dimensional turbulent boundary layer,” *Meas. Sci. Technol.*, vol. 6, pp. 702–716, 1995.
- [69] R.J. Adrian, “Particle-imaging techniques for experimental fluid mechanics,” *Annual Review of Fluid Mechanics*, vol. 23, pp. 261–304, 1991.

- [70] R.J. Adrian, R.J. and J. Westerweel, *Particle Image Velocimetry*. Cambridge, UK: Cambridge University Press, 2011.
- [71] T.D. Dudderar and P.G. Simpkins, “The development of scattered light speckle metrology,” *Optical Engineering*, vol. 21, no. 3, pp. 396–399, 1982.
- [72] R.S. Sirohi, *Speckle Metrology*. Marcel Dekker Inc, 1993.
- [73] M.P. Arroyo, and C.A. Greated, “Stereoscopic particle image velocimetry,” *Meas. Sci. Technol.*, vol. 2, pp. 1181–186, 1991.
- [74] R. Fei, and W. Merzkirch, “Investigations of the measurement accuracy of stereo particle image velocimetry,” *Experiments in Fluids*, vol. 37, pp. 559–565, 2004.
- [75] K. Peterson, *Single camera, three-dimensional particle tracking velocimetry*. PhD thesis, University of Michigan, 2012.
- [76] G.E. Elsinga, A. Schroder, and C.E. Willert eds., *Particle Image Velocimetry: New Developments and Recent Applications. Tomographic 3D-PIV and Applications*. Springer, 2008.
- [77] G.E. Elsinga, F. Scarano, B. Wieneke, and B.W. van Oudheusden, “Tomographic particle image velocimetry,” *Experiments in Fluids*, vol. 41, pp. 933–947, 2006.
- [78] G.E. Elsinga, B.W. van Oudheusden, and F. Scarano, *Experimental assessment of Tomographic PIV accuracy*. 13th International Symposium on Applications of Laser Techniques to Fluid Mechanics. Lisbon, Portugal, 2006.
- [79] G.E. Elsinga, R.J. Adrian, B.W. van Oudheusden, and F. Scarano, “Three-dimensional vortex organization in a high-Reynolds-number supersonic turbulent boundary layer,” *Journal of Fluid Mechanics*, vol. 644, pp. 35–60, 2010.

- [80] C. Atkinson, S. Coudert, J. Foucaut, M. Stanislas, and J. Soria, “The accuracy of tomographic particle image velocimetry for measurements of a turbulent boundary layer,” *Experiments in Fluids*, vol. 50, pp. 1031–1056, 2011.
- [81] G.E. Elsinga, J. Westerweel, F. Scarano, and M. Novara, “On the velocity of ghost particles and the bias errors in Tomographic PIV,” *Experiments in Fluids*, vol. 50, pp. 825–838, 2011.
- [82] D. Michaelis and B. Wieneke, *Comparison between Tomographic PIV and Stereo PIV*. 14th International Symposium on Applications of Laser Techniques to Fluid Mechanics. Lisbon, Portugal, 2008.
- [83] T.J. McGregor, D.J. Spence, and D.W. Coutts, “Laser-based volumetric color-coded three-dimensional particle velocimetry,” *Optics and Lasers in Engineering*, vol. 45, pp. 882–889, 2007.
- [84] B. Ruck, “Color-coded tomography in fluid mechanics,” *Optics & Laser Technology*, vol. 43, pp. 375–380, 2011.
- [85] Y. Murai, N. Yonezawa, Y. Oishi, Y. Yasaka, and T. Yumoto, *Color particle image velocimetry improved by decomposition of RGB distribution integrated in depth direction*. ASME-JSME-KSME Joint Fluids Engineering Conference (AJKFluids 2015). Seoul, Korea, 2015.
- [86] Y. Murai, T. Yumoto, Y. Oishi, and Y. Tasaka, Y, *Color tomographic PIV improved by removal of color contamination*. 10th International Symposium on Particle Image Velocimetry. Delft, The Netherlands, 2013.
- [87] T. Watamura, Y. Tasaka, and Y. Murai, “LCD-projector-based 3D color PTV,” *Experimental Thermal and Fluid Science*, vol. 47, pp. 68–80, 2013.

- [88] J.P. Prenel and Y. Bailly, “Recent evolutions of imagery in fluid mechanics: From standard tomographic visualization to 3D volumic velocimetry,” *Optics and Lasers in Engineering*, vol. 44, pp. 321–334, 2006.
- [89] D. Zibret, Y. Bailly, C. Cudel, and J.P. Prenel, *Direct 3D flow investigations by means of Rainbow Volumic Velocimetry*. Proceedings of PSFVIP-4. Chamonix, France, 2003.
- [90] J. Xiong, R. Idoughi, A. Aguirre-Pablo, A. Aljedaani, X. Dun, Q. Fu, S.T. Thoroddsen, and W. Heidrich, *Rainbow Particle Imaging Velocimetry for Dense 3D Fluid Velocity Imaging*. ACM Transactions on Graphics (Proceedings of SIGGRAPH), 2017.
- [91] J. Xiong, Q. Fu, R. Idoughi, and W. Heidrich, *Reconfigurable Rainbow PIV for 3D Flow Measurement*. International Conference on Computational Photography (ICCP2018), 2018.
- [92] K. Dennis and K. Siddiqui, *A Multi-Color Grid Technique for Volumetric Velocity Measurements*. In Proceedings of 2017 ASME Fluids Engineering Division Summer Conference (FEDSM2017), 2017.
- [93] H.J. Park, Y. Sugano, Y. Tasaka, and Y. Murai, *Three-Dimensional Measurement of Smoke Density Distribution with Switching of Volumetric Color Illumination Patterns*. ASME-JSME-KSME Joint Fluids Engineering Conference (AJKFluids 2019). San Francisco, California, USA, 2019.

Chapter 2

A Color Permutation Algorithm for Three-Dimensional Flow Characterization

2.1 Introduction

The study of fluid flow behavior is one of the fundamental topics in engineering covering a wide range of applications. Numerous approaches have been adapted to investigate and characterize the dynamical aspects of a given flow. Numerical approaches are used to simulate fluid behavior through the governing fluid flow equations while experimentation provides direct measurements and observation of real fluid flows. The experimental approach utilizes several tools to obtain both qualitative and quantitative description of fluid phenomena.

A majority of fluid flow in practical engineering applications are three-dimensional and turbulent in nature, thus characterized by highly complex motion governed by dissipative

processes. One of the biggest challenges in experimentally characterizing turbulent flows is to simultaneously detect and quantify three-dimensional motion in both time and space. In the past, several techniques to perform 3D flow characterization have been developed. These techniques quantify 3D motion via the complete velocity field. Due to recent advances in image processing and computing, optical techniques utilizing digital cameras have grown in popularity. These methods rely upon the observation of tracer particles moving with the fluid flow and use complex mathematical schemes to calculate fluid velocity [1–4]. While these techniques have made major advancements, challenges remain in fully-capturing three-dimensional flow velocity. Hence experimentalists often rely upon visualization and relatively simple characterization techniques to gain insight into 3D flow phenomena.

Rainbow Volumic Velocimetry (RVV) has been developed recently to visualize and measure three-dimensional flow fields. The technique utilizes the full polychromatic light spectrum by reflecting visible white light from blazed grating [5, 6]. This produces a multi-color illuminated volume for seed particles to travel through and reflect light to a single camera. The camera is positioned such that color changes in the volume occur normal to the camera's viewing plane. As a seed particle moves through the volume, its planar movement is captured through the corresponding streak positioning in the viewing plane of the camera whereas, its depth position is tracked through the changes in the color of the light reflected by the particle. The 3D velocity field is estimated from color streak images using image analysis.

The velocity component normal to the camera-viewing plane (i.e. the out-of-plane or depth-wise component) in the RVV technique is known to be heavily influenced by the width of the volume, hence each constituent color, in addition to the associated perspective effects [5]. To reduce these effects, the width of the measurement volume needs to be kept

small, on the order of 10 mm [5]. To minimize the width of each color band, RVV utilizes the maximum number of colors available, i.e. the continuous polychromatic spectrum. When images are captured with a digital camera, the polychromatic spectrum is discretized into the colors available in digital image processing. The distribution of colors in the polychromatic spectrum produced by grating cannot be easily controlled. One alternative to this approach is to use many adjacent monochromatic bars for illumination. However, these discrete color volumes have visible gaps that limit spatial resolution in the out-of-plane direction [5, 7]. Recently LCD projectors have been used for multi-color volumetric illumination without gaps to characterize 3D flow fields [7–9].

As LCD projectors facilitate simple manipulation of the color distribution in the measurement volume, one technique to help reduce uncertainty in measuring the third velocity component is to change the color distribution in the measurement volume. By generating multiple polychromatic spectra distributions, the width of each color band can be further reduced for a given volume width. A similar technique involves changing the order of the color bands in time, according to the refresh rate of the LCD projector. Both of these techniques have been successfully implemented [7, 10]. However, repeating the polychromatic spectrum introduces ambiguity in seed particle position and changing the order of the color bands in time limits temporal resolution. From the visualization aspect, these advancements make captured color images less intuitive as the observed color is not a simple function of motion in the out-of-viewing plane direction.

A multi-color grid technique has been developed by the present authors for 3D flow characterization [11]. The technique used a multi-color grid generated by an LCD projector where beam color variations occurred in multiple planes relative to the camera field of view. This enables color changes that correspond to motion in two directions. The results demonstrated the possibility to capture 3D motion with this approach [11]. The results also

show that by increasing the number and combination of colors in the grid, the spatial resolution of the technique can be improved. However, the technique was found to be weak in cases where detected tracer particle's color deviates from the colors in the grid pattern due to color interference between adjacent regions.

As the literature review shows, RVV is able to provide intuitive flow visualization and enable three-dimensional velocity measurement through color encoding, however it is restricted to small volumetric depths to minimize error. More recent color-encoding techniques show promise for high quality 3D flow characterization as they all provide detailed visualization images that contain sufficient information to extract 3D velocity data however these methods require further development prior to being fully realized as velocimetry techniques. At present these new techniques have limited spatial resolution, especially when capturing out-of-plane motion. In addition, these methods face challenges in the associated image analysis methods that are very early in their respective development.

In the present study, a three-dimensional flow characterization method is reported, which is based on a novel approach of color-layer permutation to increase spatial resolution. An image analysis algorithm is developed to implement this method. The paper first presents and discusses the operating principle of the novel color permutation approach, then the analysis algorithm is thoroughly described. Synthetic tests are performed to demonstrate the viability of the method.

This chapter discusses multiple topics in image processing in detail. See Appendix B for introductory material to image processing.

2.2 The Color Permutation Method

The previously proposed multi-color grid technique by the present authors utilizes a grid pattern to define several color-coded volumes [11]. Each color appears only once in every row and column, which allows for color changes to describe motion in two directions. A strength of this approach is that the multi-color grid can be made with a large number of colors. The theoretical limit on this is the number of colors available in image processing tools. However, the pixel shift is still required to resolve potential ambiguities based on the color information alone. Modern digital cameras are capable of capturing images over 3000×3000 pixels, about 10 Megapixels, in size. Hence, there is no major need to use color encoding to improve spatial resolution in camera's viewing plane. In the out-of-plane direction, the maximum number of colors is the continuous polychromatic spectrum, as used in RVV. A digital approach to RVV is to use all colors available in image processing in discrete color layers. This defines an upper limit on the number of discrete color layers used.

The method of color permutations, as proposed in this paper by the authors, removes this limit by permuting the colors used in the volume to extend the volume depth and keep the width of each color small, reducing error in resolving the out-of-plane component of motion. The order of colors in a permutation is selected such that all colors in the volume have unique neighboring colors i.e. two particular colors are adjacent to each other only once. The number of possible permutations satisfying this condition for a given set of colors is a combinatorics problem similar to the "dinner table" problem [12]. The color permutations impose a condition on the measurement volume where once a particle changes color, its position in the out-of-plane direction becomes known. This resolves ambiguities in particle position introduced when colors are repeated in the volume. Simultaneously, the in-plane position of a particle is tracked using the pixel shift captured by the camera image, allowing

tracking of the particle's three-dimensional movement.

An example of the color permutation method using five colors is shown in Figure 2.1a. One possible permutation of these five colors enables the creation of eleven discrete color layers as shown in Figure 2.1b. This defines eleven discrete positions in the out-of-plane direction. This approach discretizes the continuous variable describing the out-of-plane position into eleven discrete positions. Hence smooth continuous out-of-plane motion is represented by a digital "stair-case" approximating the true motion. As the number of discrete out-of-plane positions increases, the associated discretization error tends to diminish.

Ideal illumination will produce a color discontinuity between adjacent color layers. However, when illumination is provided by a real source such as an LCD projector, a smooth gradient exists between colors in adjacent color layers. This leads to the color interference behavior previously seen by the authors [11]. In the present approach, this color gradient that lies on the boundary between neighboring color layers, the so-called transition region, has been utilized as a measurement position (see Figure 2.2). The region away from the color interference (i.e. transition region), where the color distribution is near-uniform, can be termed the core region. That is, the core region lies within a color layer and is neighbored by a transition region (see Figure 2.2). The transition region can thus be defined as the position halfway between neighboring color layers.

By definition, the transition region is where the color distribution is non-uniform and the exact color distribution is unknown. As color is directly related to the depth position, it is desirable to keep the transition region small to reduce uncertainty. This can be quantified with the transition region size, T , relative to the core region size, C , for a given color layer (see Figure 2.2). If $T > C$, then the particular color layer is expected to encounter significant uncertainty in resolving depth position as the transition region and its associated unknown color distribution is larger than the core region. To minimize such uncertainty, it is

important to ensure that $T \ll C$. This will ensure that the majority of the color distribution for the given color layer is known.

The division of the color layers into core and transition regions, result in a substantial increase in the number of so-called depth positions in particle’s streak (i.e. the spatial resolution in the out-of-plane direction). If n is the number of discrete color layers, then by considering both core and transition regions, $2n - 1$ discrete depth positions can be defined. For example, the five-color eleven-layer permutation shown in Figure 2.1b, results in 21 depth positions. Thus, increasing the number of colors in a given volume increases the number of permutations (i.e. the color layers), enabling a larger number of depth positions.

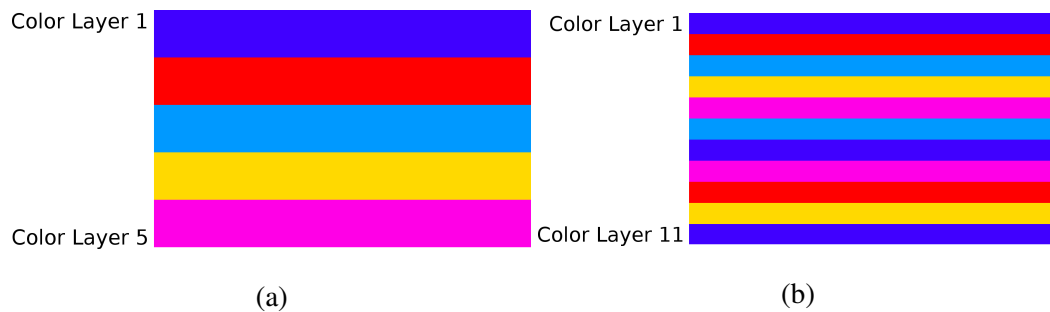


Figure 2.1: (a) Five discrete colors and (b) one possible permutation of them.

2.3 Three-Dimensional Streak Placement Algorithm

The analysis algorithm to convert multi-color streak images of seed particles into three-dimensional trajectories has five main steps. The first step is to calibrate the illuminated measurement volume using a sequence of images taken from two orthogonal directions. These images are used to define a coordinate system for the volume and the distribution of colors within the volume. Next, each captured image of particle streaks within the given measurement volume is preprocessed with noise-removal, streak identification, and streak discretization techniques. In a given streak, each color that appeared is then used

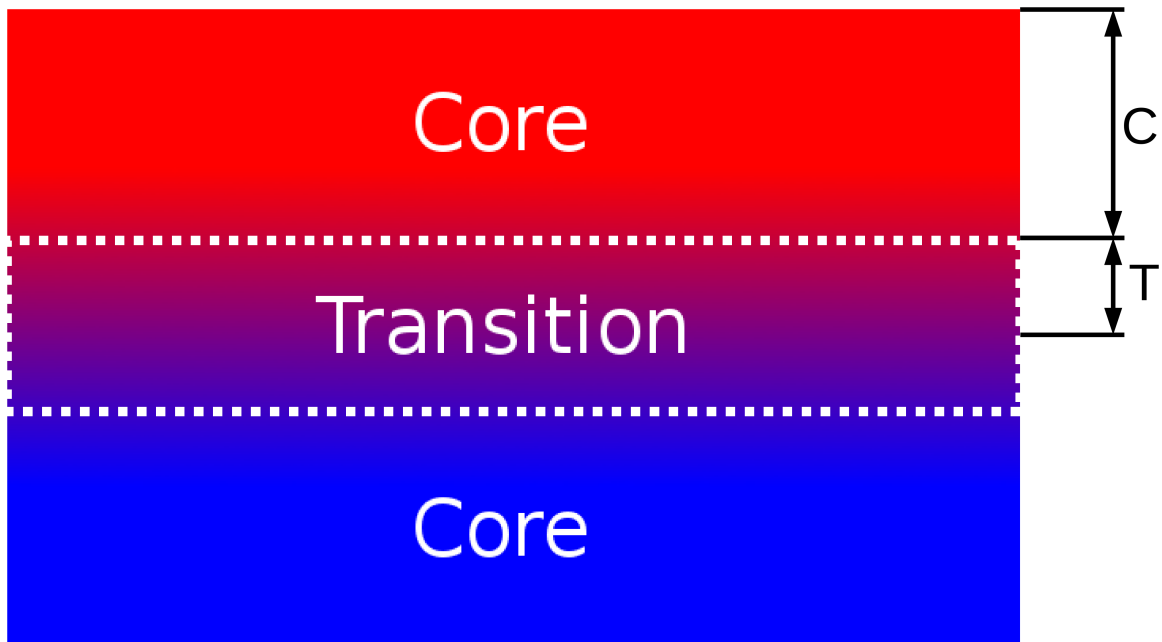


Figure 2.2: Illustration of two discrete core regions and corresponding transition region.

to estimate the corresponding out-of-plane position. Three-dimensional reconstruction is performed next based on the estimated out-of-plane positions. Finally, the reconstructed streak trajectory is placed in physical space. This algorithm has been fully implemented using MATLAB. The details of each step are presented and described in the following subsections.

2.3.1 Calibration

The illuminated volume has known dimensions in physical 3D space hence, each single-colored layer in the illuminated volume has known dimensions and position. The goal of calibration is to define the illuminated volume as seen by the camera (i.e. the digital space), and the transformation from digital space to physical space. For calibration, two orthogonal views of the illuminated volume, free of tracer particles, are considered which are called the measurement-view and the cross-view, as shown in Figure 2.3.

The measurement-view represents the camera-viewing plane in the actual experiments (y - z plane in the present case). The cross-view is perpendicular or out-of-plane with respect to the measurement-view (x - y plane in the present case), where the x -axis corresponds to the direction of color change. Calibration images in the cross-view capture the distribution of colors, i.e. spatial coordinates and color values of each core and transition region, in the measurement volume. It is important to note that the colors obtained during calibration represent the width-averaged values (i.e. averaged along the z -axis). Images in both viewing planes of a fixed reference point are required to relate the spatial coordinates in both planes.

For any sufficiently large finite depth, the perspective effects in the camera-viewing plane become important, which can influence the true spatial position of a particle. For this purpose, the images of a marked ruler at two depth locations (along x -axis at the boundaries of the measurement volume) can be utilized. With the known depth, the perspective effect can be quantified, and corrections are implemented in the final spatial conversion process.

To quantify the color observed in cross-view calibration images, the images are converted to the Hue-Saturation-Value (HSV) color model. This model is used as an alternative to the well-known Red-Green-Blue (RGB) model and has seen widespread adoption in the image processing community [13]. The HSV model describes color using three independent components; hue, saturation and value. The “hue” component expresses pure color such as “red”, “green”, or “violet” in the range $[0, 1]$ or $[0, 360]$. The “saturation” component describes the intensity of color often quantified in the range $[0, 1]$ or $[0, 255]$. Low values of saturation indicate low intensity of the color and vice-versa. The “value” component describes the brightness of the color and is also quantified over the range $[0, 1]$ or $[0, 255]$. See Smith [13] for more details about the HSV model.

The cross-view calibration images captured by the camera are visually similar to the per-

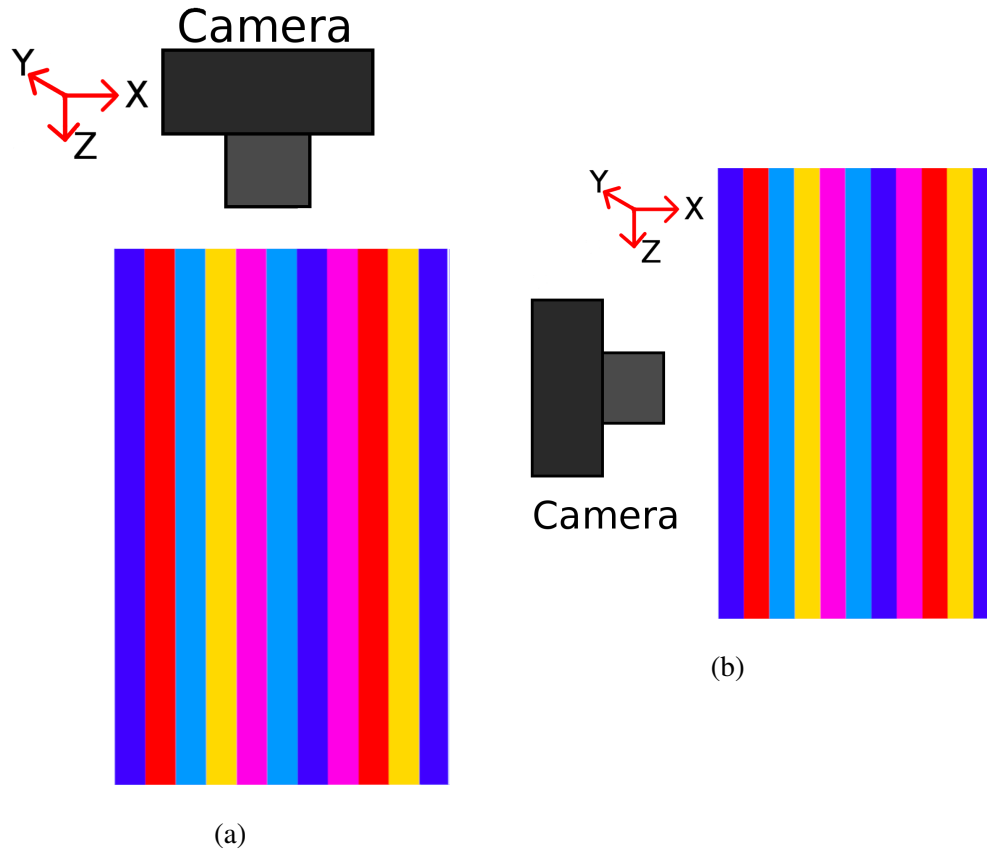


Figure 2.3: Schematics of the two planes used for the calibration of (a) cross view and (b) measurement view. The light source in both views is oriented normal to the page.

muted color layers example shown in Figure 2.1b. Hence, the histogram of the hue data in these calibration images shows a multi-modal distribution where each peak is associated with one of the colors (hues) present. Each of these peaks is then fitted to a normal distribution. The resulting mean and standard deviation are then used to formally define the core and transition regions (see Figure 2.2). A hue threshold is defined as three times the standard deviation of the hue distribution. Thus, an interval based on the mean hue and the hue threshold defines the boundaries of the core region. The region bounded between two core regions is then defined as the transition region.

The x -coordinate of each core and transition region is defined at the center of each respec-

tive region. The measurement-view and cross-view images of the fixed reference point are used to relate the y-coordinates seen in each view using the control-point or landmark registration technique, which is used to align two images based on specific common features [14, 15].

The transformation from digital space to physical space is performed using the known spatial coordinates of core and transition regions in addition to images of the ruler in both the cross view and measurement view. From this information, digital dimensions are converted into physical length dimensions and include perspective effects via linear regression.

2.3.2 Pre-processing of Particle Streak Images

Once the measurement volume is calibrated, color streak images corresponding to three-dimensional seed particle motion in the real experiments are acquired. The background subtraction is performed in the first step of the preprocessing algorithm to isolate colored streaks on a dark background. In the next step, images are converted from RGB (as captured by the camera) to the HSV color model. Each image is then segmented based on a user-defined threshold on the value channel to identify and separate bright regions from the background, resulting in a binary image.

Segmentation of the HSV converted image must also be performed using a user-defined threshold on the saturation channel. This is needed due to a singularity in the HSV model, where a zero value of saturation leads to erroneous results. Hence, saturation must be non-zero. Segmentation using a non-zero saturation channel threshold produces another binary image. These two binary images from segmentation on the value channel and saturation channel respectively, are then combined using element-wise multiplication. This produces a third binary image which corresponds to the streaks present in the given image. Noise in the binary mask images is then filtered with a 3×3 local median filter. Next, the

morphological operations of dilation, area thresholding and erosion are performed on the mask images removing noise and improving streaks' morphology.

The threshold segmentation technique used here only selects the region above the threshold. Hence, streaks that pass in-front of or behind each other are identified as a single continuous region and appear in the image as intersecting each other. An example of this behavior is illustrated in Figure 2.4 where the intersection of two streaks appears as a single white region. It is very likely that intersecting streaks have different color signatures which the camera observes as a mixture of colors from each streak. This prevents the detection and tracking of individual streaks within the overlapping (apparent intersection) region and hence, the correct 3D placement.

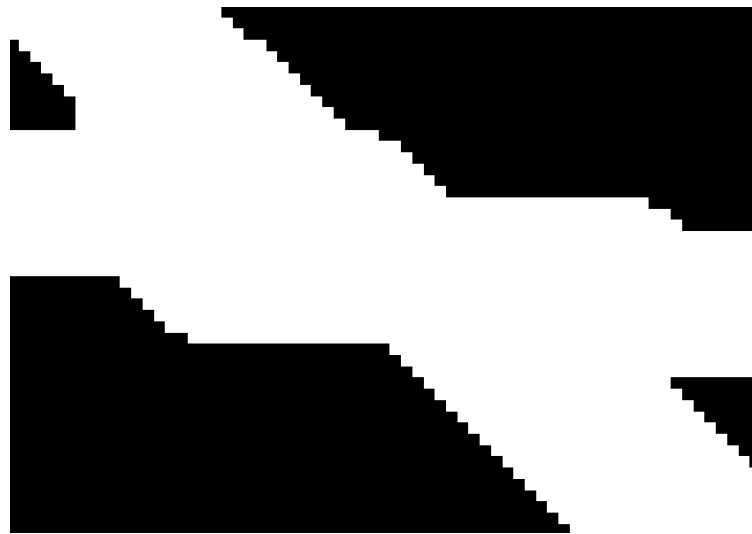


Figure 2.4: Two intersecting streaks segmented as a single object in white.

To correct this behavior, the apparently intersecting streaks must be separated. This is performed by first separating streaks into their respective ligaments using an approach described by Soille [16] for separating overlapping fibers. This technique uses skeletonization by influence zones (SKIZ) to separate fibers based on their respective image skeletons. Figure 2.5a shows the separated streak ligaments correspond to the two intersecting streaks in

Figure 2.5b. Once the ligaments are separated, the overlapping region is then determined as the convex polygon whose vertices are the points on the intersecting streak edges where the streaks were separated into ligaments. This region is removed from the overlapping streaks.

In the next step, an ellipse is fitted to the detected overlapping area such that the second moment of area is preserved. The properties of the ellipse and its orientation with respect to the horizontal are recorded and used for the 3D reconstruction at a later stage. In the next step, any remnant noise in the images is removed by a filtering operation applied to all detected objects in a given image. This filtering operation is based on the eccentricity, solidity, and equivalent diameter of each object. The output at the end of this step is a binary image containing detected streaks, in full length (non-overlapping) or sectional form (overlapping).



(a)

(b)

Figure 2.5: (a) Streaks separated into ligaments after using the fiber separating method. (b) Detected overlapping region (white), the associated vertices (red), and detected intersection point (blue).

The discretization of the detected streaks (full length or sectional) is performed next. This process converts each of the streaks (full or sectional) into a series of discrete segments. The segment length, b , is a user-defined parameter, which determines the spatial resolution of the reconstructed path of a given particle in 3D space.

The discretization process begins by determining one end point of the given streak along the streak center-line, named the starting point. Next a series of points along the streak center-line are selected such that the distance between consecutive points is b , as illustrated in Figure 2.6. These points, including the starting point, are referred as streak segment points. A binary image is then generated where each of the streak segment points is white and the rest of the image is black. This image is used for watershed segmentation where the calculated ridgelines are used to break the streak into many segments as illustrated in the bottom panel of Figure 2.6.

For each streak segment, the median hue of the streak is then calculated and the information is stored along with the coordinates of the corresponding segment point. This information is later used for three-dimensional placement. The sensitivity of the segment length on resulting discretization is detailed in section 2.5.

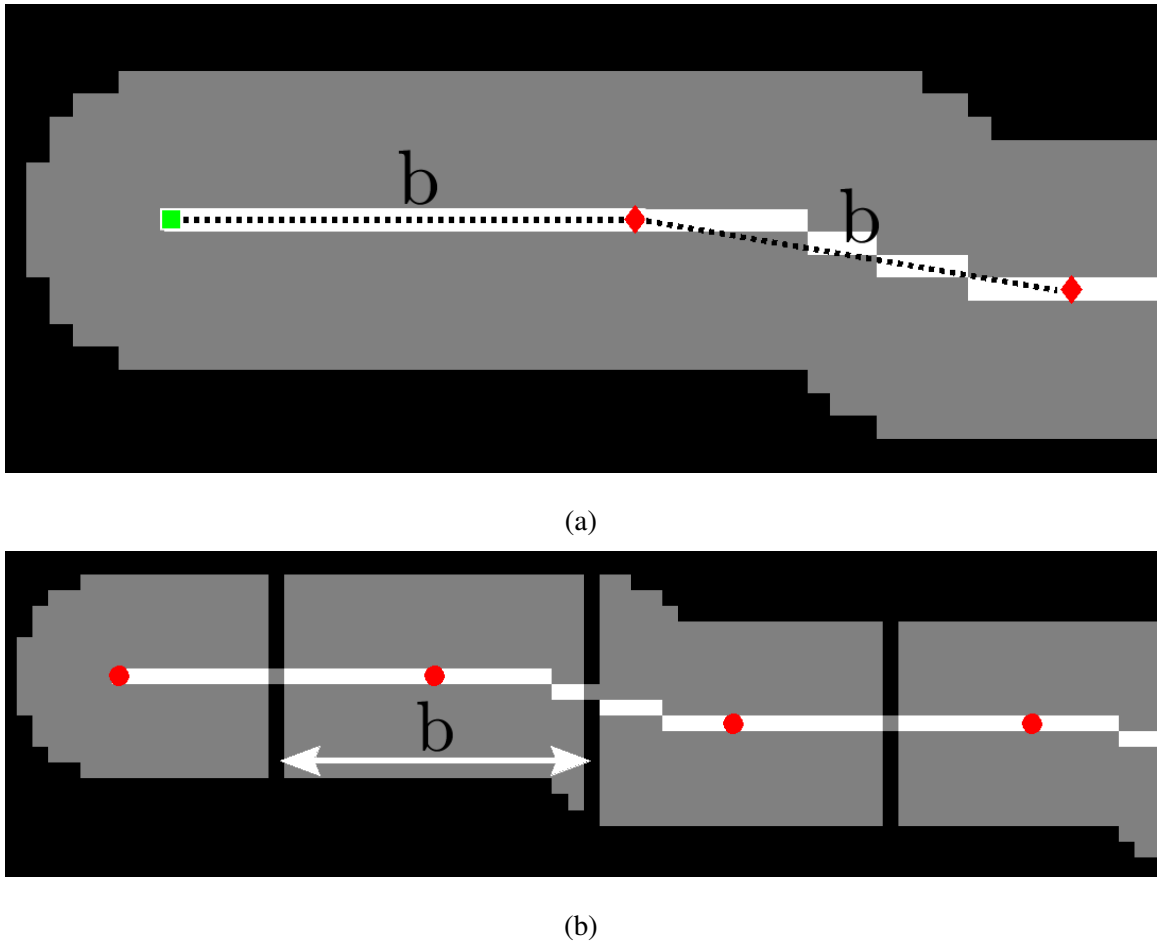


Figure 2.6: Images of the discretization process. (a) Shows the selected streak start point (green square), second streak and third segment points (red diamonds) and the distance between streak segment points. (b) Illustrates the resulting streak segments after watershed segmentation where each streak segment point is denoted with a red circle.

2.3.3 Depth Position Estimation

The median hue values of the discretized segments of a given streak are then used to estimate the depth position of each corresponding segment. The depth position of each streak segment is estimated by comparing the median hue of the given segment with the hue range of the core region within each color layer. If the median hue falls within the hue range, then

the given segment is affiliated with the corresponding color layer's core region. If the median hue does not fall within the hue ranges for any of the color layers, then the segment is considered to be within the transitional region i.e. the overlapping region between two adjacent color layers. This information along with the streak segment points and median hues are used for the three-dimensional reconstruction of the streak.

2.3.4 Three-Dimensional Reconstruction

A given image is expected to contain multiple particle streaks. From the camera's viewing perspective, some of these streaks appear to intersect each other at one or more points. In an earlier section, the process of detecting the intersection points of such streaks is described, in which the intersection region is removed resulting in broken streak ligaments. The first step of the reconstruction process is to reconnect the corresponding broken ligaments of a given streak based on local geometric similarity around the intersection point. In the neighborhood of the intersection point, two disconnected ligaments of a given streak are not expected to undergo major directional changes with respect to the camera's viewing plane. Thus, the slope of the streak ligaments in the camera's viewing plane before and after intersection should be approximately constant. This principle is adapted here to reconnect the broken ligaments of a given streak around the intersection point. For this purpose, the algorithm first detects the broken ends of each ligament in the vicinity of the intersection area and computes the corresponding slopes. Two ligaments with the closest slopes are assumed to be belonging to the same streak and hence connected linearly through the intersection point.

The procedure is then repeated to connect all broken streaks in the image. Note that due to color mixing in the overlap region, the coordinates of the intersection point are not defined based on the hue value. In case of an odd number of broken ligaments in a given

intersection region, the ligaments with closest slopes are paired and the remaining ligament is considered as the end of the corresponding streak.

After all streaks are reconnected, it is necessary to detect whether there is a color change within the streak or it is monochromatic over its entire length, and consequently reject monochromatic streaks. This is because, a fully monochromatic streak cannot be placed depth-wise (i.e. same color layer will appear multiple times due to color permutation). Hence, the change in color of the streak implies the movement of the particle in the depth (out-of-plane) direction. The hue variation over the streak length is determined based on the median hue of a given segment and its neighbors.

The depth positions of the streak segments in transitional regions are determined. This is achieved by comparing the estimated depth positions before and after transition. As continuity of streaks in camera's viewing plane has already been verified via successful segmentation, streak continuity in the depth direction must also be ensured. This is achieved by imposing a condition that a given streak must undergo a hue change from at least one discrete color layer to another adjacent discrete color layer.

As the color permutation method uses the same color multiple times in a given volume, the hue value in a given streak segment that corresponds to a particular core region is not sufficient to place that segment at the correct depth location. As the seed particle moves from one core region to another core region, it passes through the transition region. Since there is a unique color combination for two adjacent core regions and the corresponding transition region, this information is used to place streak segments at the correct depth locations. Discrete depth positions are assigned by incrementally labeling core regions with odd numbers and transition regions with even numbers (each between two odd numbers).

2.3.5 Final Spatial Conversion

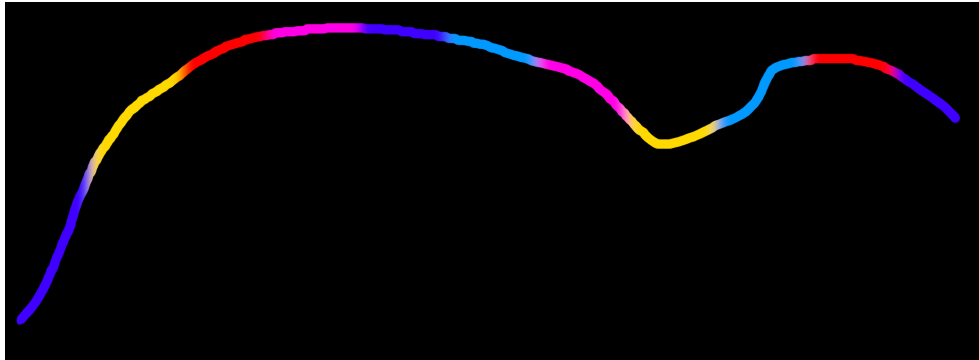
The three-dimensional reconstruction of each streak as described in the previous section provides coordinates of each segment in a given streak (i.e. their coordinates in the measurement view plane), and the depth information in the form of the core or transition number in which that segment is located. The last procedure of the algorithm is to convert this data into the real length units describing the positions of each streak's 3D movement within the measurement domain in physical space.

This process converts the layer number of each streak segment to a depth position in physical units based on the calibration information obtained through the cross-view calibration image. As discussed earlier, the streak signatures in the depth (x) direction are influenced by perspective effects as observed from the measurement view. Hence, at a given x location, the perspective correction needs to be applied to find the true spatial position. The linear regression discussed in the calibration section is used to correct for perspective effects and provides the conversion scale for streak segments' positions in the measurement plane from pixels to physical units.

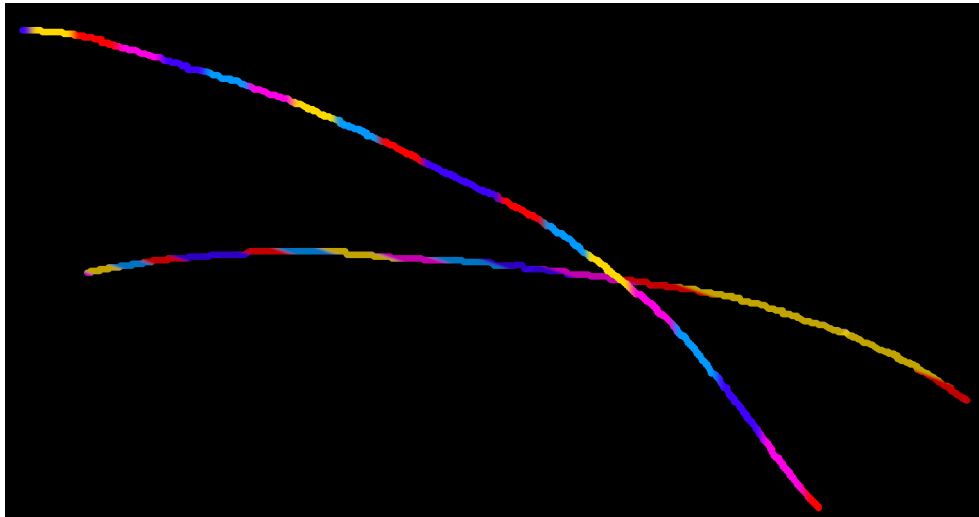
2.4 Synthetic Image Results

To demonstrate the functionality and accuracy of the algorithm's implementation, it is tested with synthetic images. These images have streaks with predefined 3D positions so that the path predicted by the algorithm can be compared to the true particle trajectory. As previously mentioned, the continuous out-of-plane coordinate, x , is discretized into 21 unique positions as an implementation of this new color-layers permutation method. The x -coordinate of the true streak trajectory in this synthetic testing has been discretized facilitating simple comparison of the results produced by the algorithm to the true trajectory.

For all tests the streak segment length (b) was set to 20 pixels. The color distribution used in these tests is the five-color, eleven-layer volume shown earlier in Figure 2.1b. To produce smooth transitions between adjacent color layers, smoothing with a 2D Gaussian kernel was performed where $\sigma = 10$. Two synthetic images were generated, one with a single streak and the other with two streaks intersecting each other as shown in Figure 2.7. As the figure shows, the streaks change colors rapidly corresponding to highly three-dimensional motion.



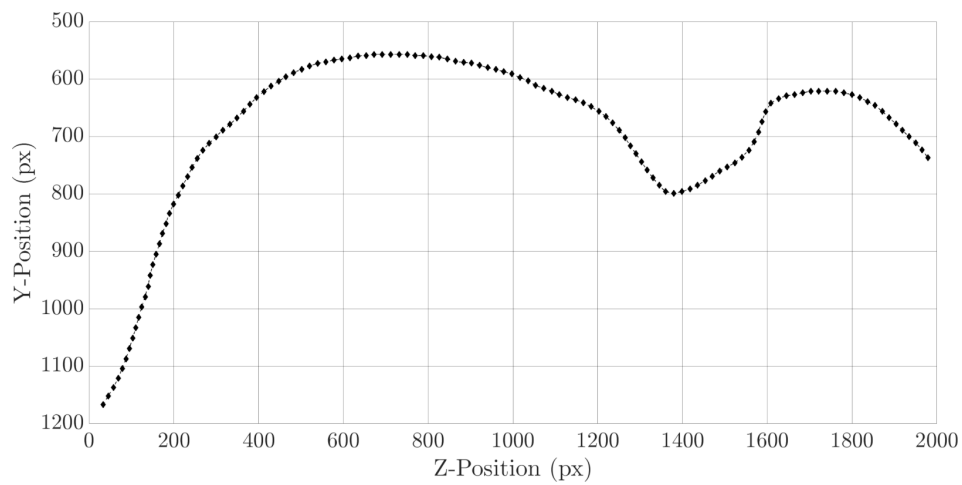
(a)



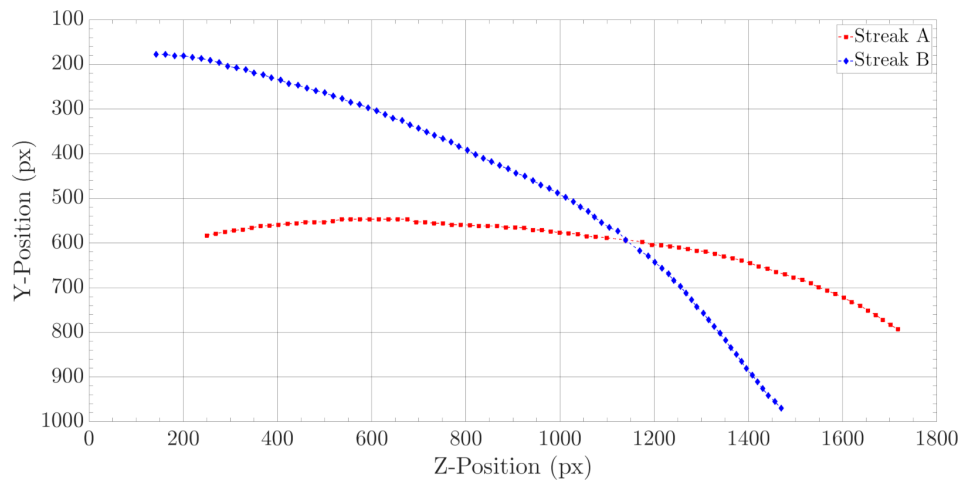
(b)

Figure 2.7: Synthetic images tested with the color permutation algorithm. (a) Contains the single streak image and (b) contains the intersecting streak image.

The early steps of the algorithm detects and discretizes the streak(s) present in a given image. Figure 2.8 shows the single streak and intersecting streaks in their discretized form. Three-dimensional reconstruction is performed next to place all streak segments into their respective 3D positions. This produces the 3D trajectories of each streak. The 3D trajectories of the given streaks detected by the algorithm are compared with the true trajectories of the corresponding synthetic streaks. The results are depicted in Figure 2.9.



(a)

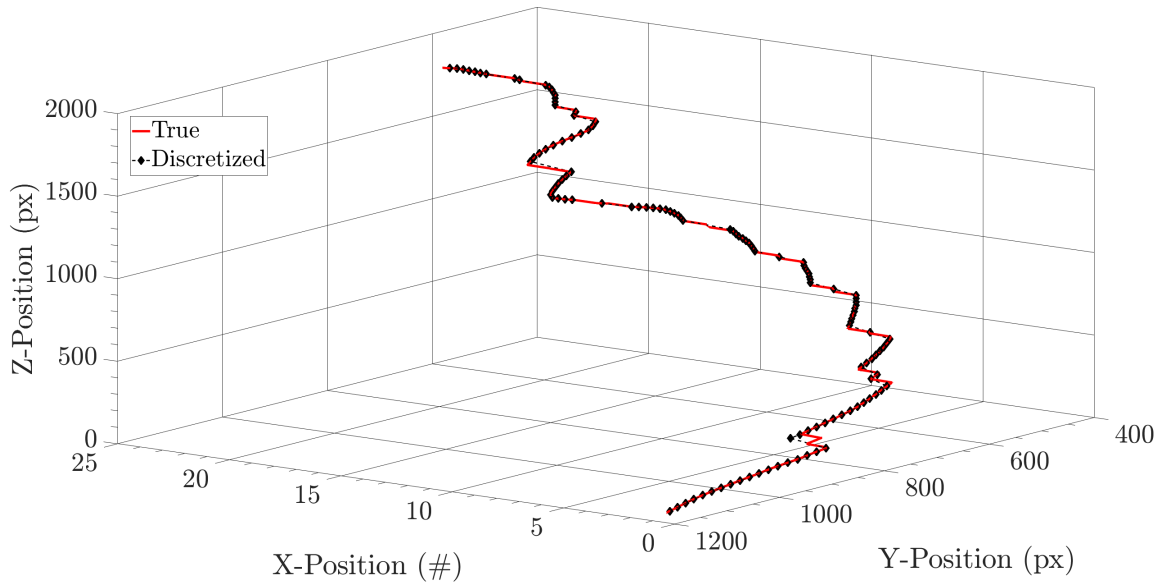


(b)

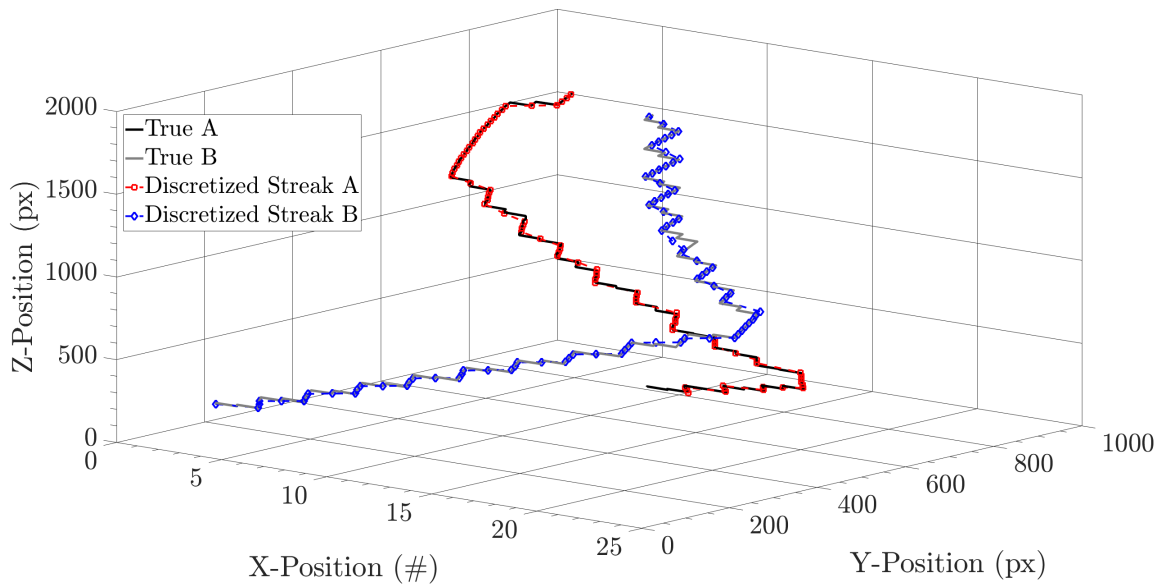
Figure 2.8: Discretized streaks in the camera viewing plane. The single streak is shown in (a). The intersecting streaks in (b) have already been reconnected.

The results show a very good agreement between the 3D trajectory of each streak estimated by the algorithm and its corresponding true path. Very few local differences are observed between the estimated and true paths. For example, in Figure 2.9a, differences are observed at $y \approx 800, x = 2$ and $y \approx 500, x = 6$, both of which are associated with transition regions between two color layers. In Figure 2.9b, some differences are observed for streak B around the intersection point at $x = 14, y \approx 600$, which is likely due to the removal of the intersecting region and approximations used to reconnect the streaks.

These observed differences were further investigated by comparing each segment's 3D position to the true 3D position. For the single streak, 5 of 126 segments were not placed in the correct depth position. For each of these segments, the true trajectory depth position was in a transition region while the algorithm placed the corresponding segment in the adjoining core region. For the two intersecting streaks, streak A had 7 of 78 segments with an incorrect depth position than the true trajectory while 6 of 82 segments in streak B were incorrect. In streak A, the seven incorrect segments were all placed in core depth positions while the true path was in the adjacent transition region. In streak B, two of the six incorrectly placed segments were located in core depth positions where the true trajectory was in the adjacent transition. Consequently, four of six incorrect segments in streak B were placed in transition while the true trajectory was in the adjacent core region. The distance between calculated intersection point and the true intersection point was 15% (3 pixels) of the streak segment length.



(a)



(b)

Figure 2.9: Three-dimensional view of the exact and discretized streak trajectories for (a) the single streak image and (b) the intersecting streak image. In both tests the streak segment length (b) was 20 pixels.

2.5 Effect of Streak Segment Length

The results presented thus far have demonstrated that the presented algorithm accurately detects and tracks the trajectories of particle streaks that change colors due to 3D movement. As several parameters are involved in the algorithm, the sensitivity of the key parameters is investigated in this section.

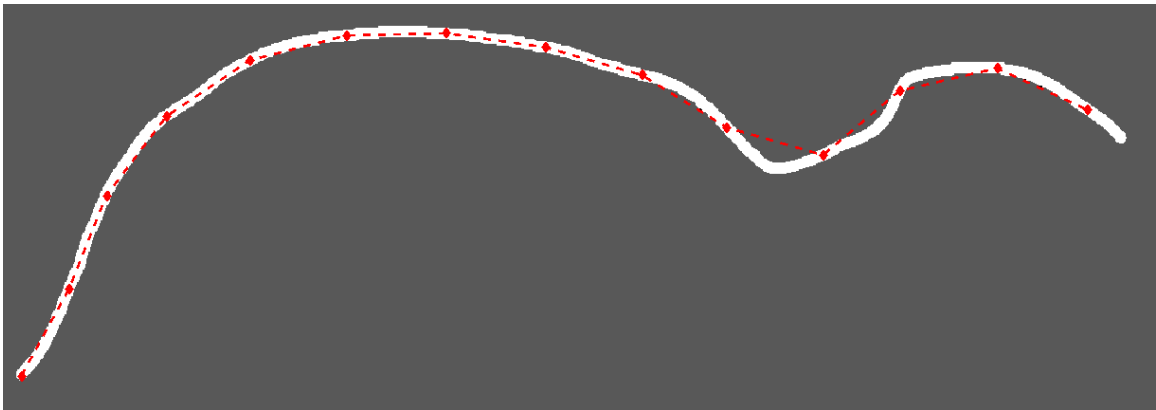
The streak segment length parameter (b) controls the resolution of the streak discretization, which controls the spatial resolution of the streak trajectory. As the technique must resolve both streak shape and the hue evolution along the streak, it is of interest to investigate how b influences the accuracy of the trajectory estimation. Figure 2.10 shows the estimated trajectories for three different values of b . The figure shows as expected, that the length of the streak segments influences the accuracy of the trajectory detection. Longer streak segment lengths i.e. lower discretization resolution (Figure 2.10a) may not be able to accurately track sharp changes in the streak trajectory. Smaller streak segment lengths, i.e. higher discretization resolution, allows accurate detection of these fine features in the streak trajectory (Figure 2.10c).

To quantify the effect of streak segment length on shape resolving, the length of the discretized streak is approximated as the sum of the Euclidean distance between neighboring streak segment points for all streak segments. The correct streak length is taken as the length of the center-line through the streak. It was found that decreasing the streak segment length reduces the error. At $b = 178$, the error was found to be 7%, which reduces to about 5% at $b = 78$ and less than 1% for $b = 18$.

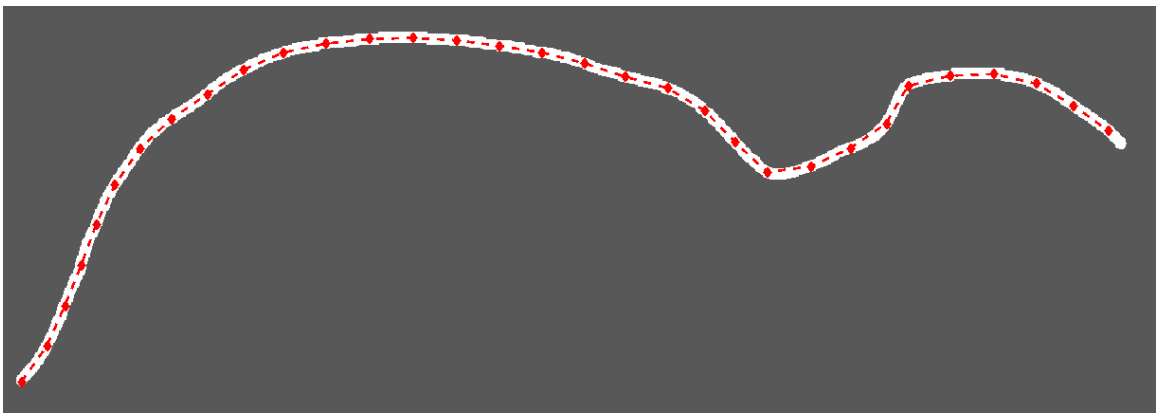
The length of streak segments influences the associated hue value since the algorithm considers the median hue value as the representative hue for the given streak segment. Figure 2.11 shows the median hue values of streak segments for $b = 78$ and $b = 18$. Results clearly

demonstrate that the streak segment length has an impact on the segment hue values, which in turn influence the placement of the segment in the color layer and hence, the accuracy of the trajectory detection.

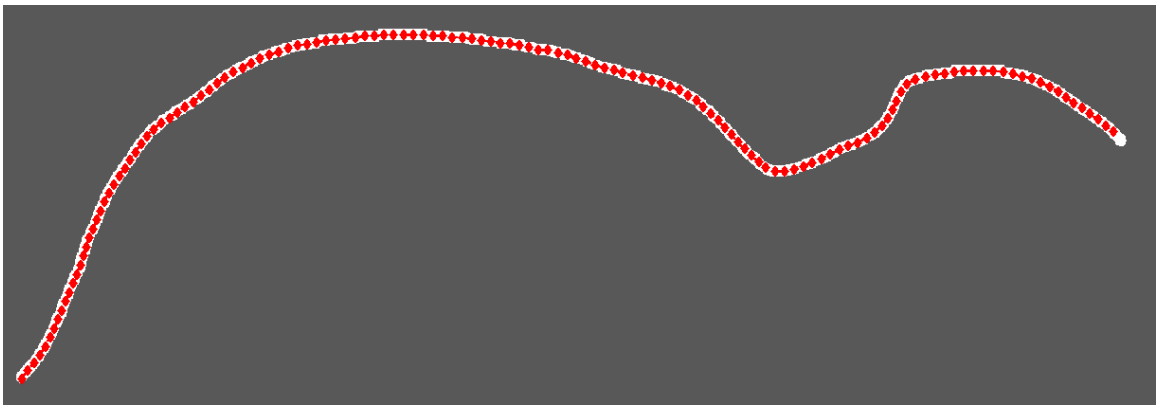
The influence of the streak segment length on the hue resolution was quantified by subtracting the median hue of each segment from the corresponding hue distribution in that segment. This was repeated for all segments and then the average was taken. This average indicates the mean error associated with the use of median hue to represent the hue distribution in streak segments. It was found that the mean hue difference along the streak decreases with decreasing streak segment length. At $b = 78$ the mean hue difference is about 20 hues which decreased to 10 hues when the streak segment length is 18. The above analysis indicate that smaller streak segments lead to better resolution of the hue distribution and properly captures the fine features of the streak, leading to the higher accuracy of the streak trajectory detection.



(a)

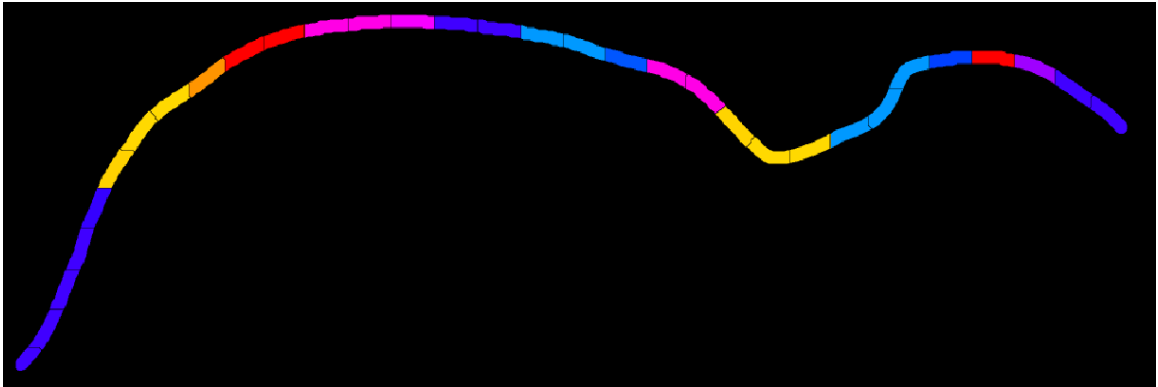


(b)

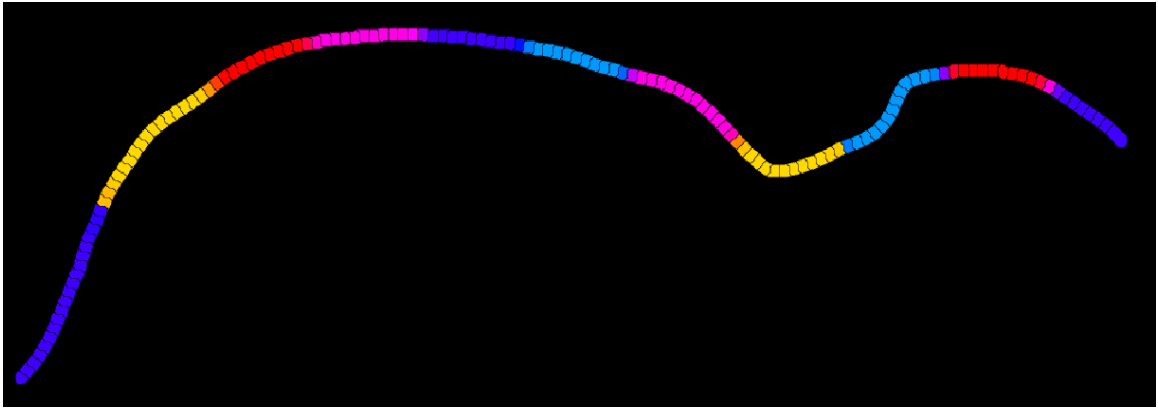


(c)

Figure 2.10: Original streak shape in white compared with discretized streak in red for three streak segment lengths. (a) $b = 178$. (b) $b = 78$. (c) $b = 18$.



(a)



(b)

Figure 2.11: Median hue reconstruction of discretized streaks for two streak segment lengths (a) $b = 78$ and (b) $b = 18$.

2.6 Discussion and Conclusions

An algorithm was developed and presented that utilizes a unique method of color permutations to track particle streaks in 3D space. As each layer has unique neighbors, a change in color of the particle streak accurately identifies the corresponding position along the depth (out-of-plane) coordinate.

One advantage of this algorithm is that it is designed to be implemented with one color camera and one light source, reducing the material resources required for experimental implementation. While the results presented here are from a MATLAB software implementation, this analysis algorithm can be written in other programming languages. The color permutation method is designed to be scalable as the number of possible out-of-camera-plane measurement positions varies strongly with the number of colors. Hence, an experimenter can add or remove colors and permutations as needed to satisfy the requirements of a given experiment (i.e. the depth spatial resolution). Hence, the proposed color permutation method has an excellent potential for high resolution three-dimensional measurement.

The algorithm has been validated against synthetic images, which demonstrated its accuracy in detecting streaks and predicting their trajectories in 3D space. However, it needs to be tested using real experimentally acquired images of well-documented flow fields for further verification and identification of any practical limits. It is expected that practical limits will arise due to the finite depth of field of a camera lens, background noise, and camera sensitivity. In addition, the process of selecting tracer particles must consider color changes in reflected light due to scattering.

Theoretically, a very large number depth positions are possible with color permutations as the number of depth position increases with the square of the number of colors present in

the color permutation volume. However, it is anticipated that any practical implementation will not realize the potentially large number of color permutations (i.e. depth positions) due to the effects of color interference between adjacent color layers. The quality of light source used in a given implementation is anticipated to be the greatest contributor to such a limit.

The behavior of streaks in an experimental implementation of this method is important to the success of this algorithm. Given the algorithm's nature as a streak characterization technique, a relatively low seed particle density is desirable. This is important due to the process of reconnecting broken streak ligaments that heavily depends on the shapes of the streaks that appear overlapping in the camera view, and hence could affect the accuracy of connecting the correct ligaments.

The technique in its current form determines particles' displacement in a 3D space. However, it cannot estimate the local velocities due to the lack of time stamping within a given image. Future work should be focused on advancements to this algorithm to enable local velocity estimations by implementing time signatures during the image exposure.

Bibliography

- [1] R.J. Adrian, “Particle-imaging techniques for experimental fluid mechanics,” *Annual Review of Fluid Mechanics*, vol. 23, pp. 261–304, 1991.
- [2] M.P. Arroyo, and C.A. Greated, “Stereoscopic particle image velocimetry,” *Meas. Sci. Technol.*, vol. 2, pp. 1181–186, 1991.
- [3] G.E. Elsinga, F. Scarano, B. Wieneke, and B.W. van Oudheusden, “Tomographic particle image velocimetry,” *Experiments in Fluids*, vol. 41, pp. 933–947, 2006.
- [4] G.E. Elsinga, B.W. van Oudheusden, and F. Scarano, *Experimental assessment of Tomographic PIV accuracy*. 13th International Symposium on Applications of Laser Techniques to Fluid Mechanics. Lisbon, Portugal, 2006.
- [5] J.P. Prenel and Y. Bailly, “Recent evolutions of imagery in fluid mechanics: From standard tomographic visualization to 3D volumic velocimetry,” *Optics and Lasers in Engineering*, vol. 44, pp. 321–334, 2006.
- [6] D. Zibret, Y. Bailly, C. Cudel, and J.P. Prenel, *Direct 3D flow investigations by means of Rainbow Volumic Velocimetry*. Proceedings of PSFVIP-4. Chamonix, France, 2003.
- [7] T. Watamura, Y. Tasaka, and Y. Murai, “LCD-projector-based 3D color PTV,” *Experimental Thermal and Fluid Science*, vol. 47, pp. 68–80, 2013.

- [8] Y. Murai, T. Yumoto, Y. Oishi, and Y. Tasaka, Y, *Color tomographic PIV improved by removal of color contamination*. 10th International Symposium on Particle Image Velocimetry. Delft, The Netherlands, 2013.
- [9] Y. Murai, N. Yonezawa, Y. Oishi, Y. Yasaka, and T. Yumoto, *Color particle image velocimetry improved by decomposition of RGB distribution integrated in depth direction*. ASME-JSME-KSME Joint Fluids Engineering Conference (AJKFluids 2015). Seoul, Korea, 2015.
- [10] H.J. Park, Y. Sugano, Y. Tasaka, and Y. Murai, *Three-Dimensional Measurement of Smoke Density Distribution with Switching of Volumetric Color Illumination Patterns*. ASME-JSME-KSME Joint Fluids Engineering Conference (AJKFluids 2019). San Francisco, California, USA, 2019.
- [11] K. Dennis and K. Siddiqui, *A Multi-Color Grid Technique for Volumetric Velocity Measurements*. In Proceedings of 2017 ASME Fluids Engineering Division Summer Conference (FEDSM2017), 2017.
- [12] B. Aspvall and F. Liang, *The Dinner Table Problem*. Stanford Department of Computer Science. Report no. STAN-(X-80-829), 1980.
- [13] A.R. Smith, "Color Gamut Transform Pairs," *Computer Graphics*, vol. 12, no. 3, pp. 12–19, 1978.
- [14] L. Costa and R. Cesar, *Shape Classification and Analysis: Theory and Practice*. Boca Ration, FL: CRC Press., 2nd ed., 2009.
- [15] A. Goshtasby, *2-D and 3-D Image Registration*. Hoboken, NJ: John Wiley & Sons Inc., 2005.

- [16] P. Soille, *Morphological Image Analysis Principles and Applications*. Berlin: Springer-Verlag, 1999.

Chapter 3

An Investigation of the Near-Wall Multi-modal Turbulent Velocity Behaviour in the Boundary Layer

3.1 Introduction

When fluid flows over a solid surface, a very thin layer of fluid adjacent to the surface forms known as the hydrodynamic boundary layer. While the boundary layer is often very thin relative to the object dimensions, the boundary layer strongly influences the transport of momentum and scalars (i.e. heat, mass, and species) which are often the parameters of interest. In many engineering and natural applications, the boundary layer encountered is turbulent in nature, hence highly three-dimensional motion coupled with dissipative processes greatly increase flow complexity. Advancements in the current understanding of boundary layer transport processes has a major impact on multiple scientific and engineering fields including drag reduction in various systems, heat exchanger design, and the atmospheric

sciences [1]. While the impact of boundary layer transport processes is significant to numerous fields, the underlying governing mechanisms in the turbulent boundary layer are not well-understood. To advance the current knowledge on these transport processes, a deeper insight into the dynamics of the turbulent boundary layer is vital.

The turbulent boundary layer is composed of several layers that govern overall flow dynamics. The inner region consisting of the viscous sublayer, buffer layer, and logarithmic layer plays a crucial role in the overall dynamics of the turbulent boundary layer. Within the inner layer, dynamical turbulent phenomena that influence interfacial momentum and scalar exchange have been the focus of several experimental and numerical studies [2–7]. The buffer layer is known to be the region where turbulent production is strongest, therefore the turbulent phenomena found in this layer are central for the understanding of interfacial transport processes. Within the buffer layer, near-wall streaks have been previously reported as stream-wise oriented regions of high and low magnitude u' , however, the physical process governing their behavior was not well-reported [5]. This led to several experimental investigations focused on characterizing the key turbulent statistics including turbulent production and Reynolds stresses in this region. The often discussed “bursting” and “sweeping” phenomena and their associated turbulent statistics have been the topic of numerous studies as significant contributors towards the Reynolds stress [8–11]. The physical cause for the “bursting” motion was suggested to be near-wall streak structures based on a quadrant analysis [12]. Recent computational research confirmed this conclusion via investigation of the dynamics of near-wall streak structures in the buffer layer [4]. The observed streaks were found to occur in pairs that were slightly misaligned with the mean boundary layer flow and the streaks extended over a long stream-wise domain.

The probability density function (PDF) is one of the most well-known tools for basic statistical analysis. The PDFs of the turbulent velocity components provide useful graphical

information on the velocity magnitudes, biases, and departures from the mean that are quantified via low and high order statistical moments. In a typical homogeneous turbulent flow, the turbulent velocity PDFs manifest as a normal or Gaussian distribution due to the collective influence of a myriad of turbulent structures, a consequence of the Biot-Savart law and central limit theorem [13]. However, the turbulent velocity PDF is not required to be strictly Gaussian in nature. Indeed, non-Gaussian turbulent velocity and turbulent velocity gradient statistics have been reported in turbulent flows and their nature is an on-going field of research [14–16]. Presently it is known that the intermittent nature of turbulence produces non-Gaussian PDFs [14, 17–19].

The turbulent velocity PDFs and associated statistics have also been reported in the literature [16, 20–23]. Frenkiel and Klebanoff [16] measured the stream-wise turbulent velocities in the logarithmic layer and the outer region using the hot-wire probe. They specifically discussed the results in the buffer layer ($y^+ \approx 10$) due to its unexpected result. The authors anticipated non-Gaussian behavior in the PDF of the stream-wise turbulent velocity due to strong intermittency, driven by the local turbulent phenomena. However, the resulting PDF did not show evidence of such intermittency [16]. Andreopoulos et. al. [23] in a later study reported the stream-wise turbulent velocity PDFs at multiple locations in the inner region. From the PDFs, the higher order statistical moments, skewness (3rd order moment) and kurtosis (4th order moment), were computed and reported to follow non-Gaussian behavior in the viscous sublayer and the buffer layer. However, these quantities tended to become Gaussian as the measurement location moved from the buffer layer into the logarithmic layer [23]. They attributed the non-Gaussian behavior in the viscous and buffer layers to velocity intermittency associated with turbulent phenomena such as “bursting” and “sweeping” [23]. Similar trends of Gaussian versus non-Gaussian nature of skewness and kurtosis as a function of the location above the wall in the boundary layer have been

reported in other studies [20, 21].

In the log layer, the turbulent velocity PDF has been reported to exhibit an approximately Gaussian behavior. Quantifying the deviations from Gaussian behavior has been the topic of some research studies [16, 24–26]. These studies have described an approximation of the turbulent velocity PDF using the Gram-Charlier expansion [16, 26]. There have been observations of PDFs with very similar skewness and kurtosis values at multiple y^+ coordinates primarily in the log layer [20, 21, 23]. This suggests a possible self-similarity in the underlying turbulent velocity PDFs. The significance and details of this apparent self-similarity have been the topic of further investigation where the phenomenon was confirmed to occur in the log layer [24].

Research on the near-wall region of the turbulent boundary layer has established the presence of highly three-dimensional dynamical phenomena. The buffer layer is well-known for its role in the generation and propagation of turbulent structures, such as near wall streaks, that greatly influence momentum and scalar transport. These strong turbulent phenomena have been previously reported to generate intermittency in the local stream-wise velocity signal, which leads to non-Gaussian velocity behavior. However, the present understanding of the turbulent stream-wise velocity PDF is provided primarily by its characterization in the wall-normal direction, with specific focus on the logarithmic layer. This approach assumes spatial uniformity of the stream-wise velocity in the stream-wise and span-wise directions. In a carefully conducted experiment, this behavior is expected for the mean flow, however, the instantaneous turbulent velocity is not expected to be spatially uniform due to the spatio-temporal intermittency associated with turbulent structures and events originating/occurring in the near-wall region. Previous reports on the turbulent stream-wise velocity PDFs have neglected the significance of the spatially varying local turbulent phenomena in the buffer layer, hence a comprehensive understanding of three-

dimensional boundary layer dynamics in this region is presently lacking. Thus, there is a need for a better characterization of the 3D spatial distribution of the turbulent velocity PDF within the turbulent boundary layer to obtain a deeper insight into the underlying processes and better understanding of turbulent boundary layer dynamics.

The objective of this study is to experimentally characterize the three-dimensional nature of the turbulent velocity PDFs within the buffer layer of the turbulent boundary layer. The multi-plane Particle Image Velocimetry (PIV) technique is utilized in the present study to measure two-dimensional velocity vector fields with high spatial resolution over multiple planes with respect to the mean flow direction [27–31]. From the computed velocity fields, numerous turbulent velocity PDFs and turbulent vector fields are generated. Observations of the PDF behaviors are used to drive more advanced analysis, including Proper Orthogonal Decomposition, to describe the governing physical processes manifested in the observed PDFs.

3.2 Experimental Setup and Methods

A closed loop, low-disturbance wind tunnel was used to conduct experiments. Air was driven by a variable-speed axial-flow fan able to produce speeds up to 60 m/s in the test section with a background turbulence rating of 0.5–0.9% over the wind speed range of 3–60 m/s. The background turbulence was previously characterized using Laser Doppler Velocimetry (LDV). The low background turbulence rating was achieved through several flow conditioning screens upstream of the test section. The wind tunnel has an active cooling system to maintain a test section air temperature of 20 °C.

A schematic of the wind tunnel test section is shown in Figure 3.1. The test section is 46 cm × 46 cm in cross-section and 114 cm long. The top and side walls of the test section

were made of clear acrylic for optical access. The bottom wall of the test section was made from aluminium coated in smooth matte black vinyl to reduce light reflection. A $6.3 \text{ mm} \times 6.3 \text{ mm} \times 43 \text{ cm}$ steel rod was placed at the entrance of the test section to act as a boundary layer trip. Experiments were conducted at five free stream velocities of $U = 1.0, 2.5, 4.5, 6.0$ and 7.5 m/s . The corresponding Reynolds numbers based on the momentum thickness are $Re_\theta \approx 280, 700, 1000, 1400$ and 1700 .

The multi-plane PIV technique was used to measure two-dimensional velocity fields within the boundary layer formed over the bottom wall. PIV measurements were conducted in multiple planes as depicted in Figure 3.1. All measurements and results are referenced using the coordinate system defined in the figure. The vertical stream-wise plane of measurements was centered in the wind tunnel at $z \approx 23 \text{ cm}$, measuring the u and v velocity components in the x - y plane. To characterize the complex dynamics of flow in the near-wall region, measurements in the horizontal plane were conducted at four heights from the wall corresponding to $y = 1.5, 3.5, 7.5,$ and 12.5 mm , each of which captured the u

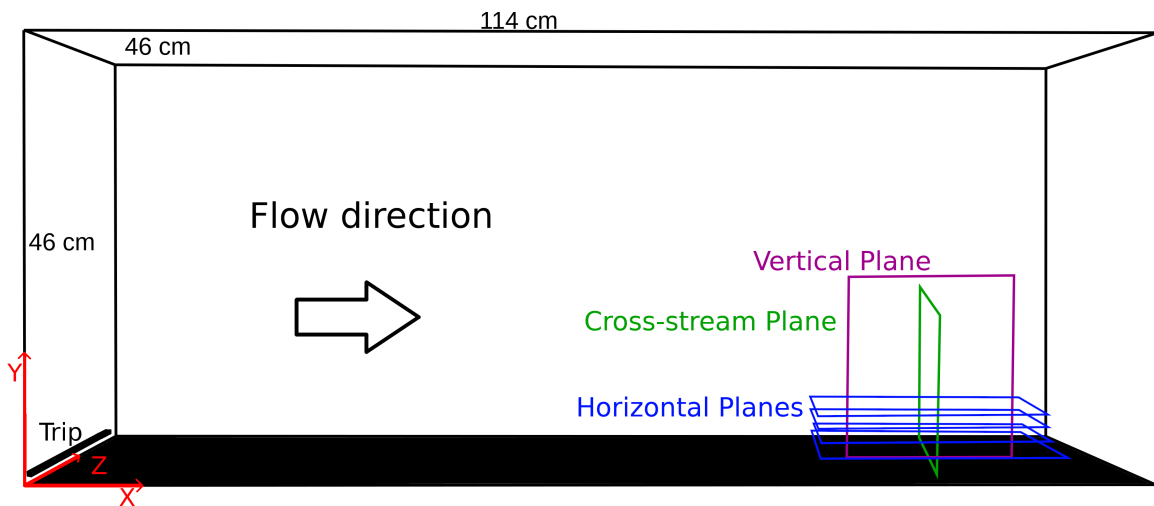


Figure 3.1: Schematic of wind tunnel test section. The measurement planes are also illustrated.

and w velocity components in the x - z plane. Lastly, the vertical cross-stream plane (y - z plane) measurements were conducted at $x \approx 81$ cm which measured the v and w velocity components. Measurements in all planes were taken about 128 boundary layer trip heights downstream to ensure there was no remnant signature of the trip bar in the measured flow fields.

The PIV system used in experiments was comprised of a dual-cavity 120 mJ Nd:YAG laser (120XT 532 nm, SoloPIV) producing laser illumination at 15 Hz per cavity. A 12-Megapixel CMOS camera (Flare, IO Industries) recording with a resolution of 4096×3072 pixels was used to acquire images via an image acquisition system (DVR Express CORE, IO Industries). Two camera lenses, 50 mm f/1.4 and 70-300 mm f/4 (Sigma Corp.) were used in experiments. A set of optics was used to transform the laser light beam into a 1 mm thick light sheet. A four-channel pulse delay generator (555-4C, Berkeley Nucleonics) synchronized with the camera was used to control the timing of the laser pulses. The air in the wind tunnel was seeded with theatrical fog (Directors Choice, UltraTec) from a fog machine. Fog was injected upstream of the test section and flow conditioning screens. The fog was circulated throughout the wind tunnel for several minutes before PIV image recording commenced to ensure uniform distribution of seed particle.

For all experiments, a minimum of 10,000 images were captured at 30 Hz, corresponding to at least 5,000 instantaneous vector fields generated at 15 Hz. Recorded PIV images were exported to a desktop computer for processing. The processing of image pairs was performed using an in-house code written in MATLAB to obtain instantaneous velocity fields. The code uses the Fast Fourier Transform (FFT) cross-correlation with 50% overlap and utilizes square interrogation windows between 32×32 pixels and 64×64 pixels and corresponding search windows between 64×64 pixels and 128×128 pixels respectively. This produced a nominal spatial resolution between 0.4 mm/vector (vertical stream-wise plane)

and 1.3 mm/vector (horizontal plane). A local median filter was used to identify and correct outliers in the velocity vector fields. The number of detected and corrected spurious vectors in each experiment was less than 1%. An Adaptive Gaussian Window (AGW) scheme was implemented to interpolate the velocity vectors onto a regular grid. The uncertainty associated with PIV velocity computation was estimated based on the errors associated with particle size, AGW interpolation, velocity gradients, peak locking, image dynamic range, and out-of-plane motion. The uncertainty estimation in the velocity was based on the approaches developed by Cowen and Monismith, and Prasad et. al. [32, 33]. Experiments conducted at $Re_\theta = 1700$ were used to estimate uncertainty in this study as this experimental condition produced the largest magnitude of velocity gradients. The maximum velocity measurement uncertainty was estimated to be ± 6.3 cm/s corresponding to 0.8% of the free-stream velocity.

3.3 Results

3.3.1 Mean Statistics

To confirm the consistency of the turbulent boundary layer formed in the present study using the given experimental setup and generated test conditions, key time-averaged quantities such as the low-order turbulent statistics and mean stream-wise velocity profile were compared with results reported in the literature. This comparison was performed using the velocity data in the vertical stream-wise plane, which is the most frequently reported orientation in the literature.

Figure 3.2 presents the mean stream-wise velocity profile in wall coordinates at various Reynolds numbers that were considered in the vertical stream-wise plane. The friction velocity in the experimental data was estimated using two distinct methods. The first method,

provided by Clauser [34], determines the friction velocity from the mean stream-wise velocity profile. By fitting the measured velocity profile to the log law of the wall, Eqn. 1.30, the friction velocity is computed. The other estimate was from the turbulent velocity components in the constant stress layer where the friction velocity is calculated according to Eqn. 3.1 [35]. Due to the planar nature of the PIV technique used in this study, it was not possible to simultaneously measure all three velocity components. To estimate the friction velocity using this equation, the span-wise turbulent velocity component (w') was assumed to have the same magnitude as the wall-normal component (v'), producing Eqn. 3.2 after simplification.

$$u_* = (\overline{u'v'^2} + \overline{u'w'^2})^{\frac{1}{4}} \quad (3.1)$$

$$u_* = (2\overline{u'v'^2})^{\frac{1}{4}} \quad (3.2)$$

The friction velocity estimated from each method is presented in Table 3.1. As the results show, at all tested Re_θ , there was a minor difference in the computed friction velocity magnitudes estimated from the two methods. The estimate provided by Eqn. 3.2 was equal to or slightly ($\approx 5\%$) greater than the estimate from the log layer slope. This comparison confirms the accuracy of the estimated friction velocity. The values of friction velocity from the log layer slope method are used in subsequent analyses.

The mean stream-wise velocity profiles in Figure 3.2 indicate that the logarithmic layer is fully resolved and the expected log-linear trend is also exhibited. At the two highest Reynolds numbers, only a few points are present in the buffer layer. As the Reynolds number decreased, more points are captured in the buffer layer and as expected these velocity profiles deflect downward from the log-law. The canonical Law of the Wall formulation for

Re_θ	Log Layer Slope (cms^{-1})	Constant Stress (cms^{-1})
280	5.3	5.4
700	13	13
1000	21	22
1400	28	30
1700	35	37

Table 3.1: Friction velocity (u_*) estimates from each technique.

the logarithmic layer and viscous sublayer (extended until it intersected the log-law) and Direct Numerical Simulation (DNS) data by Wu and Moin [36] are also plotted in the figure as reference. The results show that the current mean velocity profiles agreed reasonably well with the reference profiles. The shape factor, estimated from the stream-wise velocity profile, was found to cover the range between 1.25 (at $Re_\theta = 1700$) and 1.55 (at $Re_\theta = 280$) which is consistent with the shape factor reported in many previous low Reynolds number turbulent boundary layer research studies (reviewed in [20]).

The key turbulent statistics are presented in Figure 3.3 as average profiles of the planar turbulent kinetic energy (TKE) ($\overline{k_{xy}^+}$), stream-wise Reynolds stress ($\overline{u'^2}^+$), wall-normal Reynolds stress ($\overline{v'^2}^+$), and Reynolds shear stress ($\overline{u'v'}^+$). The experimental TKE profiles (Figure 3.3a) all reached a peak $\overline{k_{xy}^+}$ of about 3.5 in the buffer layer before decreasing. $Re_\theta = 280$ shows a slightly smaller peak $\overline{k_{xy}^+}$ magnitude. As y^+ increases, each $\overline{k_{xy}^+}$ curve tends toward zero as expected. The DNS results in general were slightly higher in magnitudes, however $Re_\theta = 1000$ shows good agreement with the corresponding profile from the current experiments. The results also show similar Reynolds number dependency in both experimental and DNS results for $y^+ > 200$. However, for $y^+ < 200$, the Reynolds number dependency was found to be weaker in DNS results.

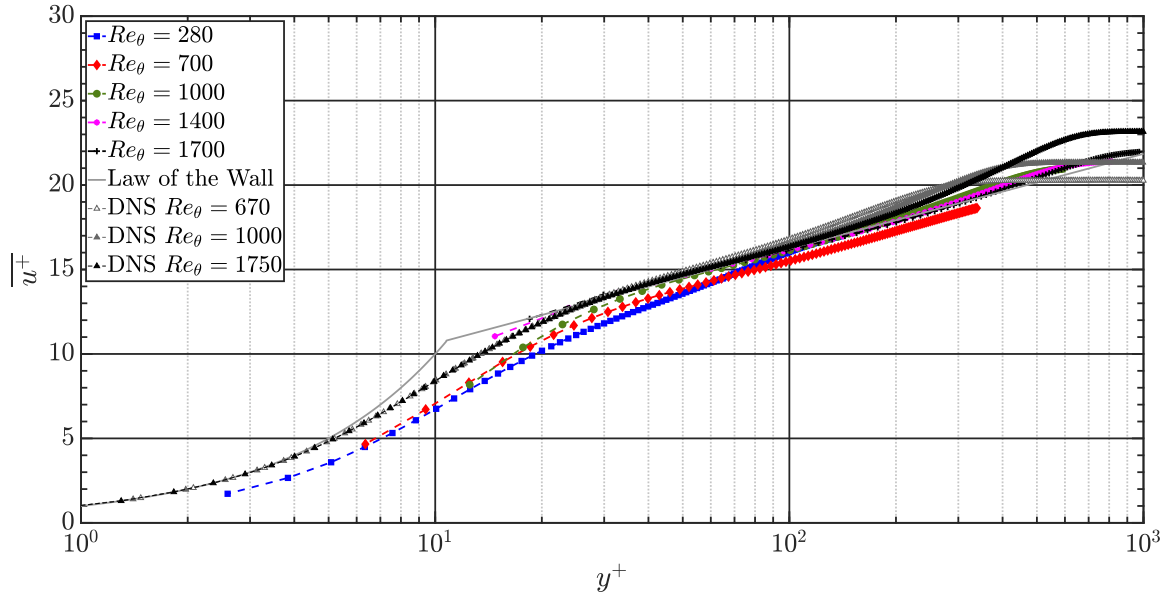
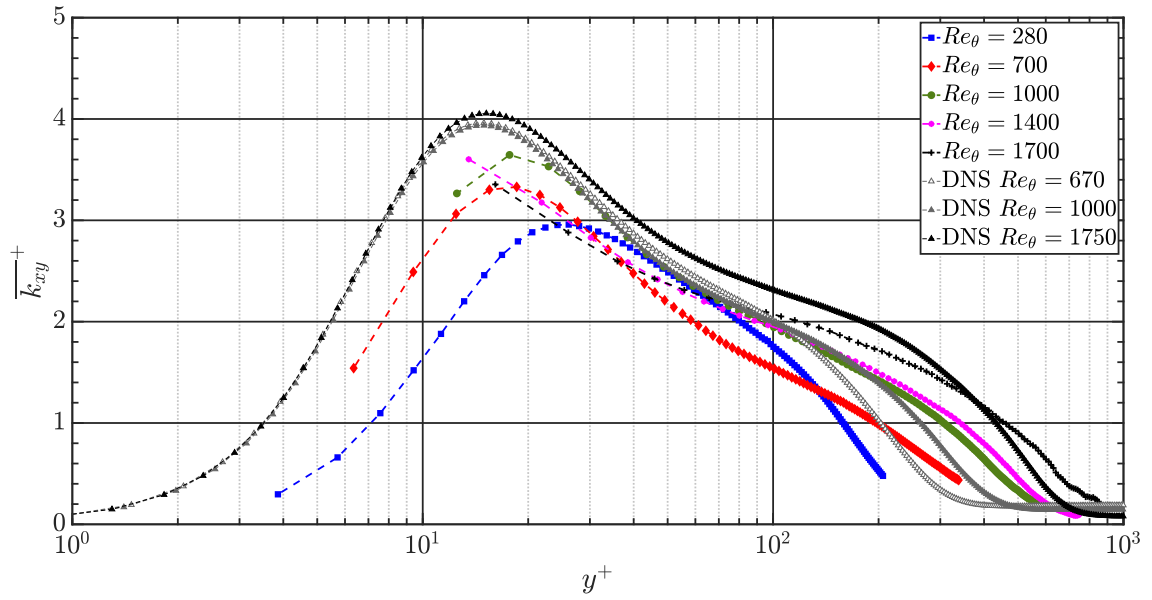
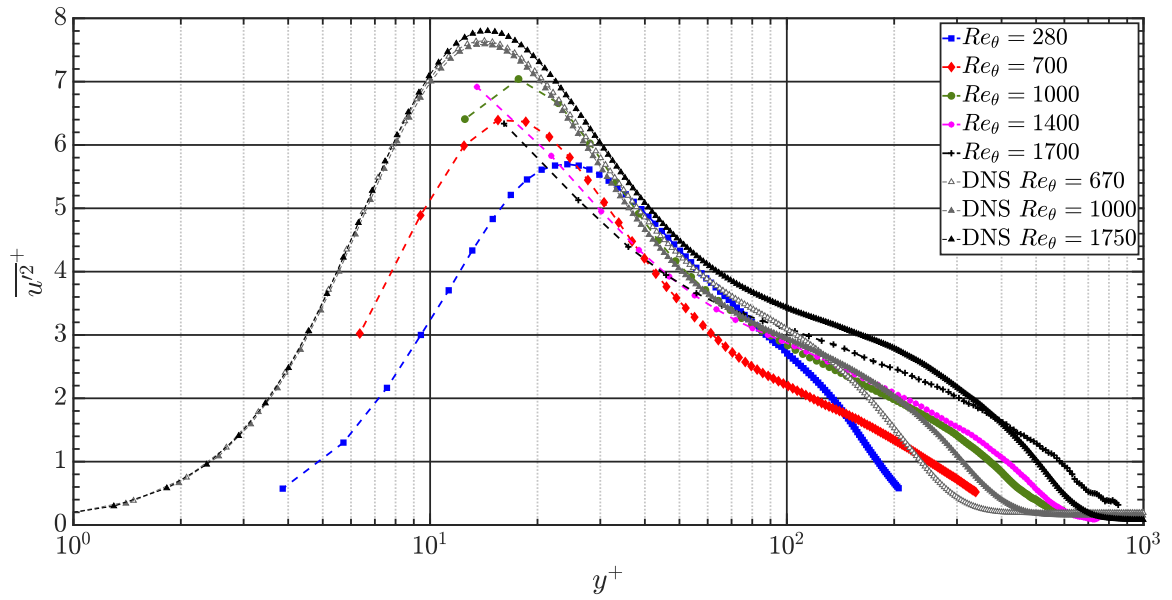


Figure 3.2: Mean stream-wise velocity profiles at different Reynolds numbers. Reference DNS data of Wu and Moin [36] and the Law of the Wall formulation ($u^+ = \frac{1}{\kappa} \ln y^+ + 5$ and $u^+ = y^+$) where $\kappa = 0.41$.

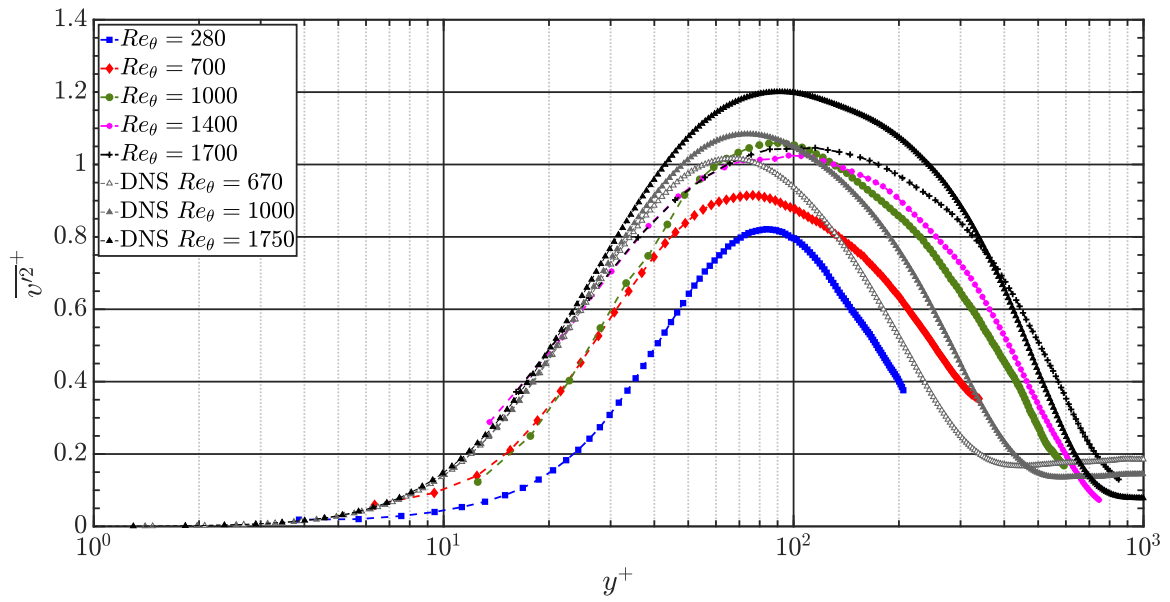
In low Re_θ turbulent boundary layer flows, a similar Re_θ -based variation of the Reynolds stress and turbulent velocity profiles is a common observation in the literature [20]. The mean stream-wise Reynolds stress profile (Figure 3.3b) shows relatively good agreement between the DNS and current experimental profiles in the buffer and log layers, and more closer agreement again at $Re_\theta = 1000$. The peak locations were also consistent between the DNS and current experimental results, but the magnitudes of DNS profiles were relatively higher. Figure 3.3c presents the wall-normal Reynolds stress profiles with similar trends and similar peak locations of both DNS and current experimental profiles. The overall magnitudes of wall-normal Reynolds stress profiles of both experimental and DNS were found to be in a comparable range in the buffer and log layers. The profiles also show similar Reynolds number dependency. The Reynolds shear stress profiles (Figure 3.3d) also show relatively good agreement between the DNS and current experimental profiles



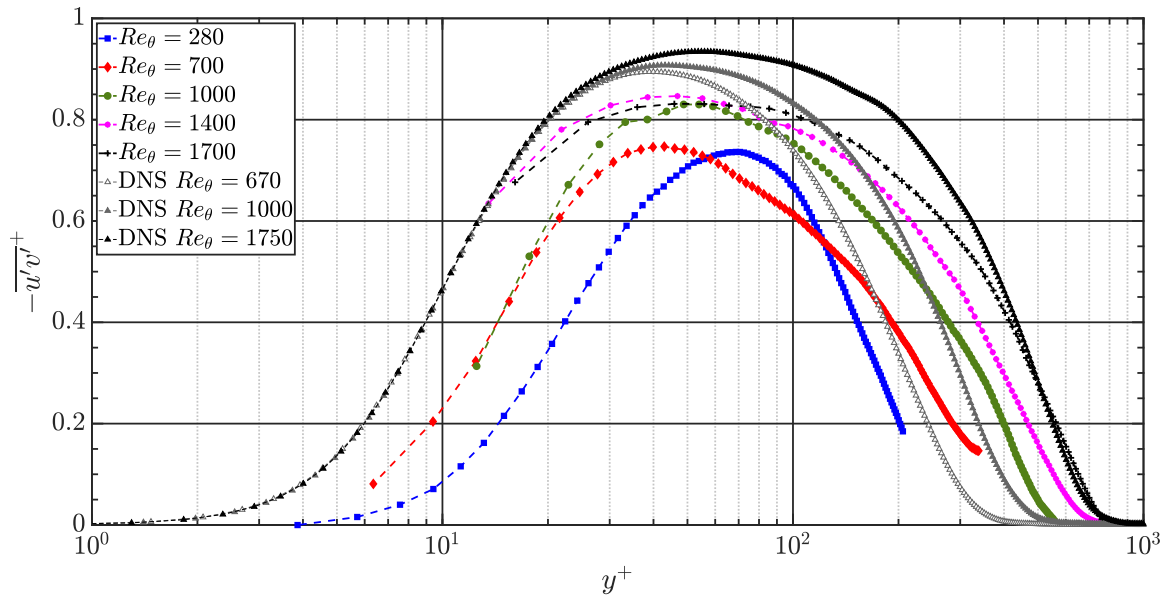
(a)



(b)



(c)



(d)

Figure 3.3: Mean profiles of (a) planar turbulent kinetic energy, (b) stream-wise Reynolds stress, (c) wall-normal Reynolds stress (d) Reynolds shear stress for all tested Re_θ . DNS data from Wu and Moin provided as reference [36].

with magnitudes in a comparable range in the buffer and log layers.

The above presented results indicate that the measured mean and turbulent flow behavior in the present study is in good agreement with established theory and previous findings. The results at $Re_\theta = 280$ exhibited the most different behavior compared to other higher Reynolds number cases. This is likely due to the weak turbulence magnitude in the flow at this Reynolds number. It has been discussed in the literature that the minimum Reynolds number required to sustain boundary layer turbulence is on the order of $Re_\theta = 300$ [20]. As the experimental results at $Re_\theta = 280$ clearly presented the identifiable buffer and logarithmic layers, these results can be accepted while acknowledging weaker turbulence as compared to that at higher Re_θ . The overall good agreement between the results from the present study and reported DNS data confirms that the measured flow fields in the turbulent boundary layer are well-suited for more advanced flow analyses.

3.3.2 Statistical Description of Turbulent Flow Behavior

Due to the nature of the velocity measurement technique employed in this study, in a given experimental run, only two velocity components were measured simultaneously. The orientation of measurement planes in this study, horizontal, vertical cross-stream, and vertical stream-wise, are mutually orthogonal. Therefore, any selection of two planes, such as one horizontal plane and one vertical stream-wise plane, must intersect in a line. Along this line, one measured velocity component is common to both intersecting planes. If this common velocity component measured along the intersection line of perpendicular measurement planes is statistically similar to the velocity component over each entire measurement plane, then it can be inferred that the statistical nature of this velocity component has weak spatial dependency, in each plane, in directions perpendicular to the common axis. For example, the vertical stream-wise plane (x - y plane) and vertical cross-stream plane (y - z

plane) intersect in a line where the vertical (v) velocity component at the same location was recorded in both sets of measurements. Weak spatial dependency of v in x is inferred if v measured over the entire x - y plane is statistically similar to v measured in the intersection line between the x - y plane and y - z plane.

Figure 3.4 illustrates the PDF (ϕ) of u'^+ (i.e. stream-wise turbulent velocity, u' , normalized by the friction velocity) at $y = 3.5$ mm and $Re_\theta = 700$ obtained from the common intersecting line in the stream-wise vertical plane (common x -axis) and the entire horizontal plane (x - z plane). The excellent agreement between the entire u' field and the intersection line indicates that the PDF of u' is not strongly dependent in z -direction. This behavior was observed over all horizontal planes considered in this study and at all tested Reynolds numbers. Through a similar analysis of the v' and w' velocity distributions in their respective planes and intersecting lines, it was observed that v' and w' have no strong dependencies in x and z -directions, respectively. As expected from boundary layer theory, the turbulent velocities demonstrate the strongest variation in the wall-normal direction. This result affirms that all three turbulent velocity components do not possess strong spatial variations in the x and z -directions.

As reported previously, the stream-wise fluctuating velocity (u') is the greatest contributor to the turbulent kinetic energy, Reynolds stresses, and turbulent production in the near-wall region of the turbulent boundary layer [37]. To characterize the behavior of this important velocity component in 3D, the horizontal plane measurements describing $u'(x, z)$ at four heights above the wall and the vertical stream-wise plane describing $u'(x, y)$ were utilized. The distribution of $\phi(u')$ at a given height above the wall illustrates the cumulative effects of multiple turbulent phenomena. Figure 3.5 depicts the $\phi(u')$ distribution in the horizontal plane at various heights from the bottom wall (right pane) and in the corresponding intersecting regions of the vertical stream-wise plane (left pane), at all Reynolds numbers used

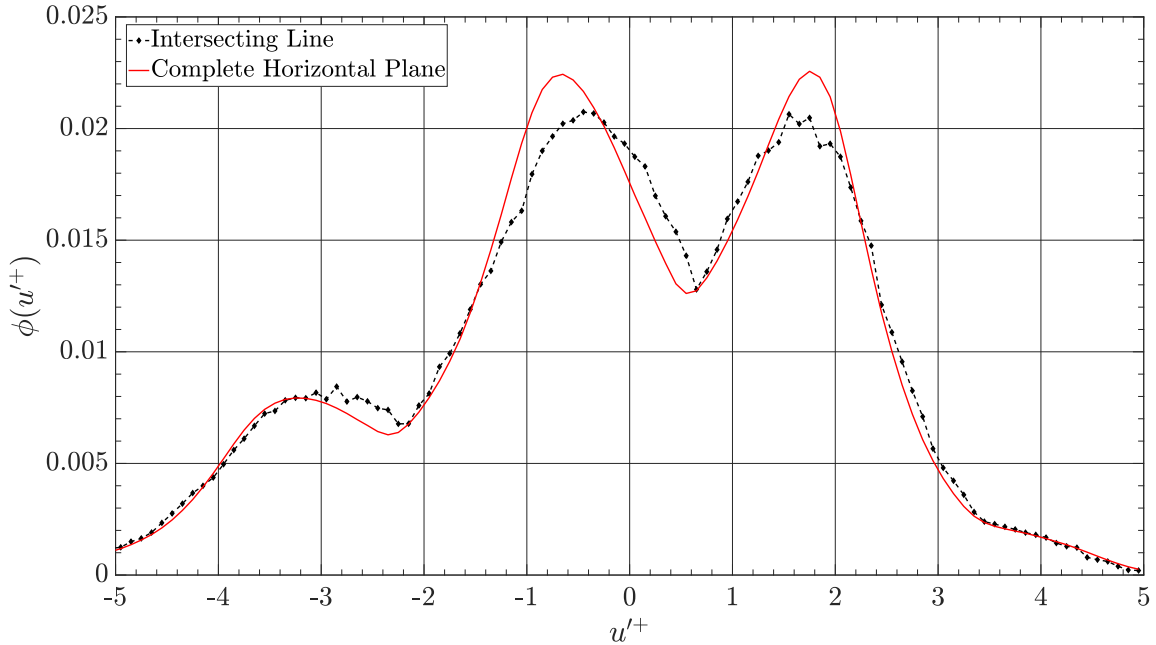
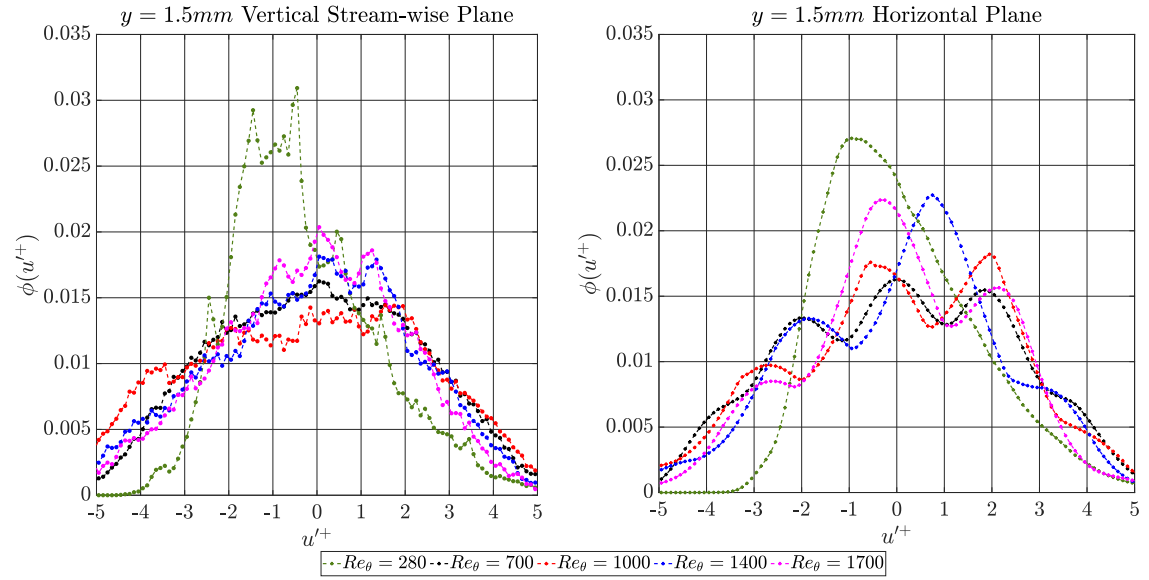


Figure 3.4: PDF of u'^+ over the entire horizontal plane and in the line of intersection between horizontal plane and vertical stream-wise plane at $Re_\theta = 700$ and $y = 3.5$ mm.

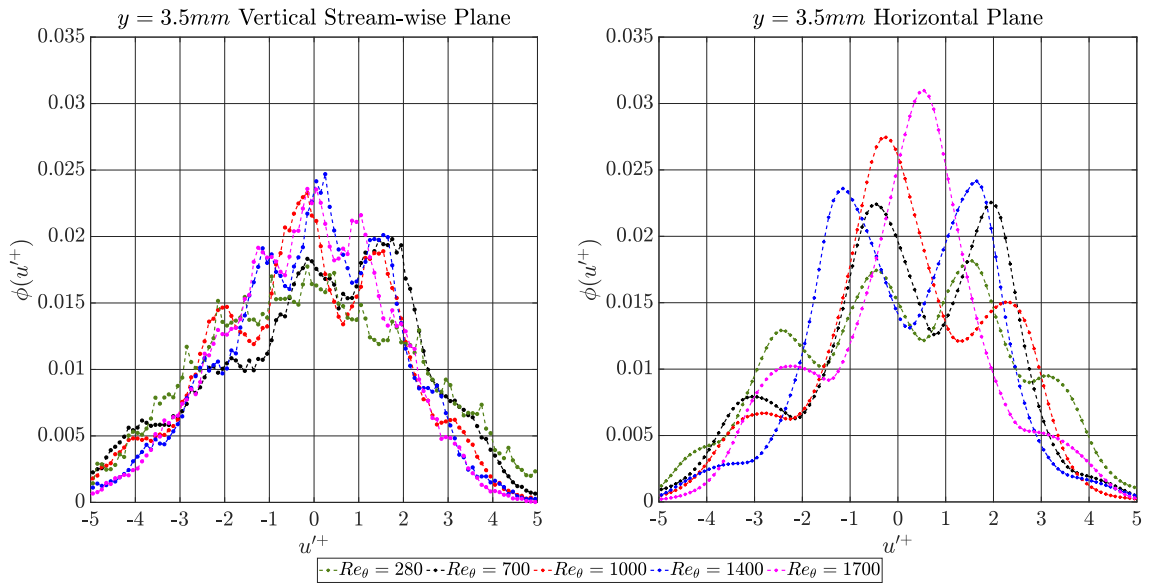
in this study.

At $y = 1.5$ mm, both measurement planes show similar distributions. The lowest Reynolds number, $Re_\theta = 280$, demonstrated the narrowest distribution of $\phi(u')$ with a slightly negative peak. An increase in the Reynolds number led to $\phi(u')$ flattening and forming multiple peaks and valleys which are clearly visible in the horizontal plane graph and most prominent at $Re_\theta = 1700$. The vertical stream-wise plane at this height did not show the same prominent peaks and valleys. An increase in the distance from the wall ($y = 3.5$ mm) led to a highly multi-modal distribution of $\phi(u')$ in the horizontal plane. In this distribution, the multi-modal behavior was strongest at the lower Reynolds numbers while the experiment at $Re_\theta = 1700$ exhibited the weakest multi-modality. The vertical stream-wise plane distribution of $\phi(u')$ at $y = 3.5$ mm also exhibited a strong multi-modal behavior.

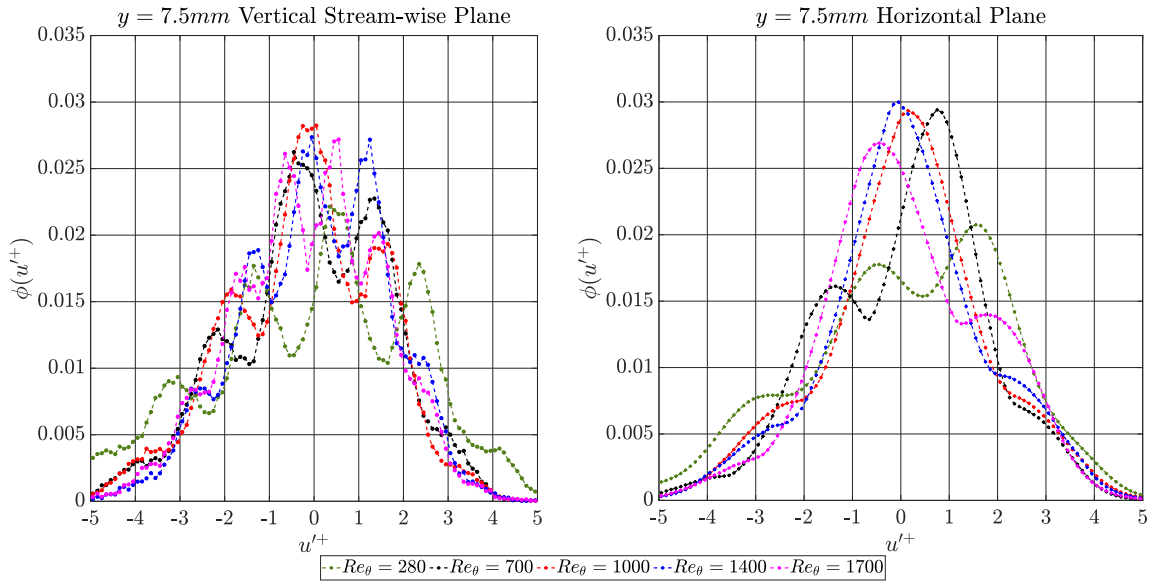
As the distance from the wall further increased to 7.5 mm and 12.5 mm, the $\phi(u')$ dis-



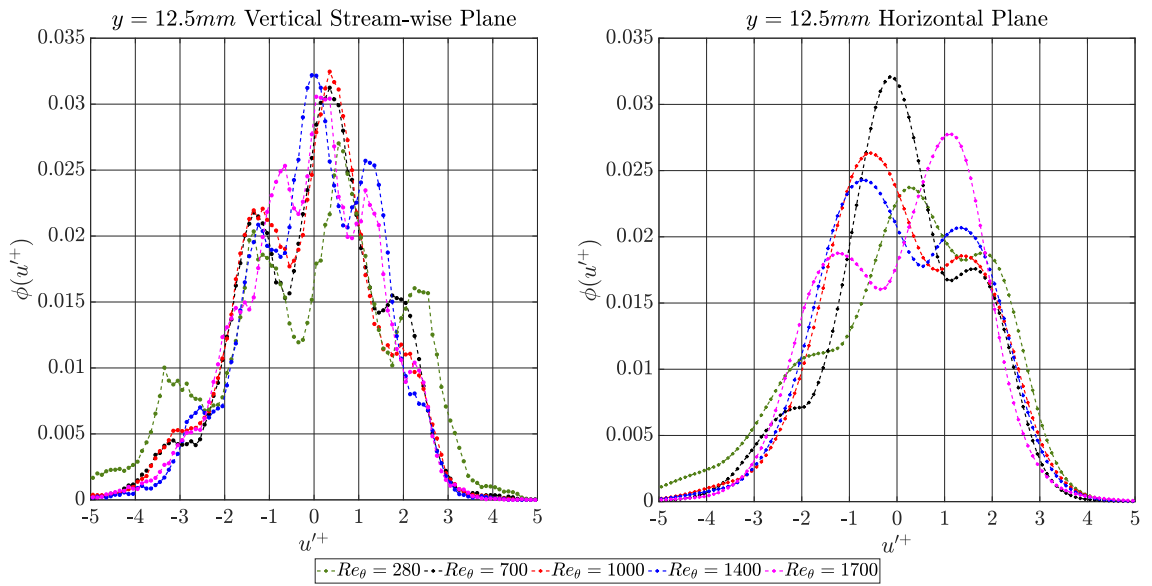
(a)



(b)



(c)



(d)

Figure 3.5: PDFs of u^+ in the horizontal plane (right column) and corresponding intersecting region in the vertical stream-wise plane (left column) at various heights from the bottom wall, (a) 1.5 mm, (b) 3.5 mm, (c) 7.5 mm, (d) 12.5 mm.

tributions in both stream-wise vertical and horizontal planes still exhibited multi-modal behavior. The results in Figure 3.5c and 3.5d however show that in the horizontal plane, these distributions have weaker multi-modal behavior as compared to distributions closer to the wall. The results also showed some Reynolds number dependency of the velocity distribution. Specifically, at $y = 7.5$ mm, there is a single prominent peak in $\phi(u')$ for $Re_\theta > 1000$ compared to relatively equal prominence peaks at $y = 3.5$ mm, while the two lowest Re_θ cases show a relatively strong multi-modality. A similar behavior was observed at $y = 12.5$ mm along with the gradual formation of a new peak at $Re_\theta = 1700$ associated with a positive u' . The vertical stream-wise plane $\phi(u')$ distribution at $y = 7.5$ mm and $y = 12.5$ mm did not demonstrate a similar organized behavior. Comparison with the distribution at $y = 3.5$ mm in the vertical stream-wise plane indicates a weakening multi-modal behavior at greater heights, as the peak near $u' \approx 0$ grew in magnitude while the other peaks diminished and the whole family of curves became slightly narrower.

The behaviors observed in the $\phi(u')$ distributions suggest that multiple phenomena govern stream-wise turbulent velocity (u') behavior. Table 3.2 shows the values of y^+ that correspond to various heights and Reynolds numbers considered in this study. At $y = 1.5$ mm, the $\phi(u')$ distribution at $Re_\theta = 280$ was smooth, which transformed into a multi-modal distribution with an increase in the Reynolds number. A plausible explanation of this behavior could be the stronger influence of viscous shear at the lowest Reynolds number since the height $y = 1.5$ mm corresponds to $y^+ \approx 5$ at $Re_\theta = 280$, implying that the flow at this height is strongly influenced by the adjacent viscous sublayer. With an increase in the Reynolds number, this location shifted into the buffer layer as illustrated Table 3.2. Similarly, the PDFs at $y = 3.5$ mm exhibited the strongest multi-modal behavior. This height was located primarily in the buffer layer and started to shift towards the logarithmic layer with an increase in the Reynolds number. The heights $y \geq 7.5$ mm correspond to locations

Re_θ	$y = 1.5 \text{ mm}$	$y = 3.5 \text{ mm}$	$y = 7.5 \text{ mm}$
280	5	12	25
700	12	30	60
1000	20	45	100
1400	25	65	135
1700	35	80	170

Table 3.2: Normalized wall coordinates (y^+) of horizontal planes.

in the logarithmic layer for $Re_\theta \geq 700$, where the multi-modal behavior weakened in the $\phi(u')$ distribution. This is an expected behavior as $\phi(u')$ begins to approximate a Gaussian distribution in the logarithmic layer, which is consistent with previous findings [20, 21, 23].

While non-Gaussian behavior in the buffer layer was speculated in previous studies, it had not been quantitatively reported in the literature. To the best of authors' knowledge, the present results for the first time, not only report the presence of non-Gaussian behavior in the buffer layer, but also provide evidence of a multi-modal behavior. It is important to note that the good agreement of the mean velocity and various turbulent characteristics between present measurements and previous DNS and canonical results, as shown earlier, confirm that the observed multi-modal trends are associated with the real physics of the flow rather than an experimental artifact.

The present findings suggest that in the buffer layer, there are relatively few strong turbulent structures that cause the departure from Gaussian behavior. It should be noted that the distributions of $\phi(v')$ and $\phi(w')$ were investigated, and no multi-modality was found in $\phi(v')$ and $\phi(w')$. As the multi-modal behavior was only observed in the $\phi(u')$ distribution, this indicates that the turbulent structures in the buffer layer have a specific orientation biased towards the stream-wise direction. The identity and nature of these structures, and the validity of this hypothesis, requires further investigation.

The prominent multi-modality in horizontal planes suggests that some span-wise phe-

nomenon contributes to this behavior. In the current body of literature, the span-wise behavior of the turbulent boundary layer is not well-reported. It is of interest to thoroughly characterize the nature and characteristics of this unique phenomenon. As the multi-modal behavior of $\phi(u')$ is strongest near the wall in the buffer layer, specifically at $y = 1.5$ mm and $y = 3.5$ mm, these two heights are the focus of a more in-depth investigation.

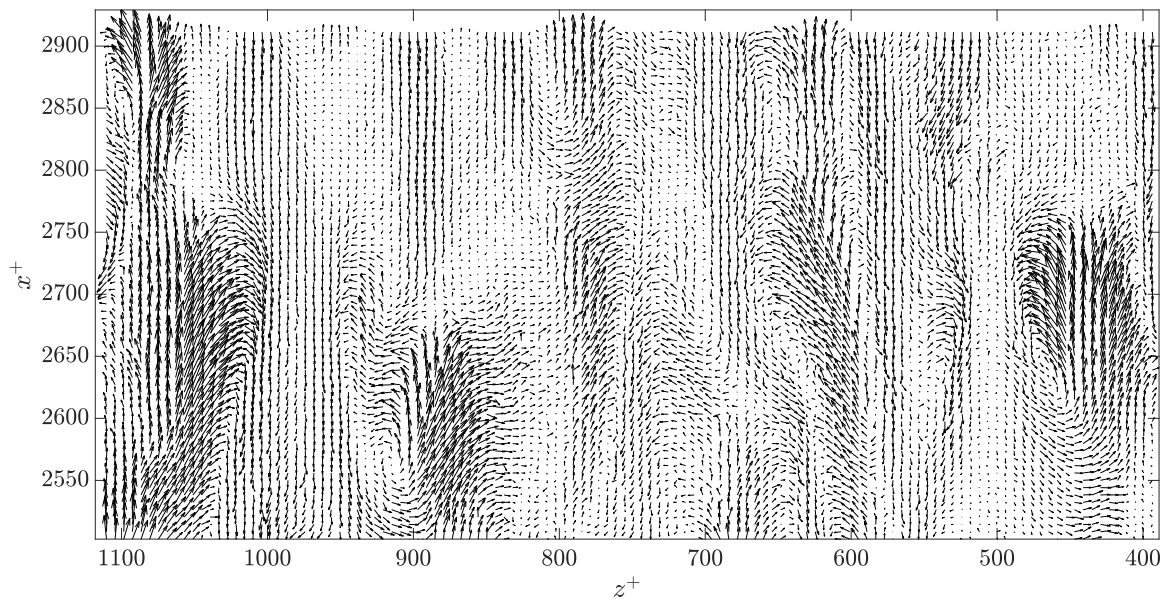
3.3.3 Instantaneous Turbulent Velocity Field Analysis

The observed multi-modal behavior produced the strongest signature in the two measured heights (i.e. $y = 1.5$ mm and $y = 3.5$ mm) located in the buffer layer. As measurements in the horizontal plane provided the most prominent view of the multi-modal behavior relative to the vertical stream-wise plane, the subsequent analyses are primarily focused on characterizing flow behavior observed in the two horizontal planes mentioned above. The turbulent flow structure in the buffer layer is illustrated via sample instantaneous turbulent velocity fields at $y = 1.5$ mm and $y = 3.5$ mm in Figure 3.6 at $Re_\theta = 280$. These plots provide insight into the differences observed in the $\phi(u')$ distributions at these two heights above the wall. Higher Re_θ produced similar turbulent flow patterns as $Re_\theta = 280$, however, due to the increased background turbulence, these patterns were more difficult to observe clearly.

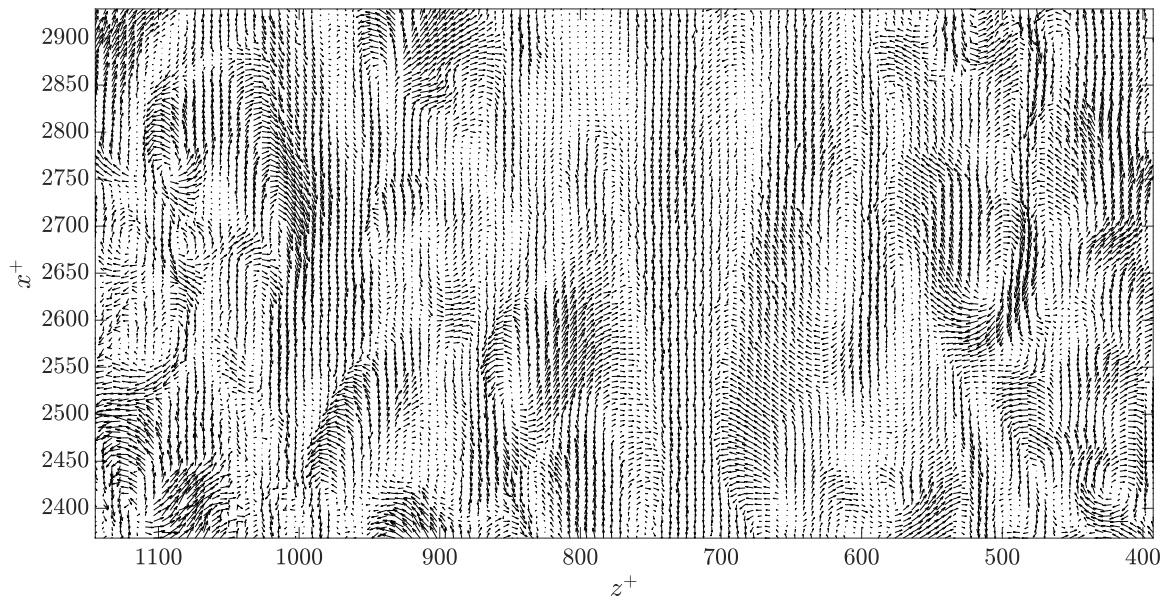
In the turbulent velocity vector fields presented in Figure 3.6, as per the sign convention used, the upward pointing arrows represent positive stream-wise velocity fluctuations ($u' > 0$) while the downward pointing arrows represent negative velocity fluctuations ($u' < 0$). The turbulent velocity field at $y = 1.5$ mm depicts several regions of large magnitude local stream-wise positive fluctuation that appear occasionally throughout the vector field. In contrast, the local negative fluctuations have a smaller magnitude but extended through a large domain of the flow field. This behavior is consistent with the corresponding $\phi(u')$

distribution. The strong infrequent positive fluctuations contribute to the long $u' > 0$ tail in $\phi(u')$, while the weak negative fluctuations are spatially prevalent, hence the peak in $\phi(u')$ is slightly negative. At higher Re_θ , more intense turbulent action appeared to strengthen both positive and negative fluctuations evidenced by the broad distribution and weakly multi-modal behavior as observed in the $\phi(u')$ distributions at those Reynolds numbers. The turbulent velocity vector field at $Re_\theta = 280$ and $y = 3.5$ mm depicts a significantly different behavior than at $y = 1.5$ mm. Multiple positive and negative fluctuating stream-wise velocity regions are present. As with $y = 1.5$ mm, the $u' < 0$ regions span a large stream-wise extent. The $u' > 0$ regions have comparable magnitude to the $u' < 0$ regions and are more frequently observed at this height than at $y = 1.5$ mm. It was also observed that the positive fluctuating regions feature a greater stream-wise length at this height than at the lower height. There appears to be an alternating pattern of positive and negative fluctuating regions in the span-wise direction. These regions are separated by areas with very low u' magnitudes. The spatial distribution and organization of these stream-wise turbulent velocity regions depict a visual resemblance to the near-wall streak structures and turbulent patterns documented in the literature [4, 38].

The investigation of the turbulent velocity field has shown near-wall stream-wise oriented regions with strong u' signatures. The magnitude of the u' signature was found to increase with an increase in distance from the wall i.e. from 1.5 mm to 3.5 mm. The strong multi-modal distribution of $\phi(u')$ is associated with these regions. It was noted earlier that the multi-modal behavior in $\phi(u')$ at $y = 3.5$ mm was weakest at $Re_\theta = 1700$. At this Reynolds number, this height corresponds to $y^+ \approx 80$, which is in the lower logarithmic layer. This behavior is consistent with previous studies that reported approximately Gaussian behavior in the logarithmic layer [20, 21, 23]. It can be concluded that the multi-modal behavior of $\phi(u')$ is linked to turbulent phenomena found primarily in the buffer layer.



(a)



(b)

Figure 3.6: Instantaneous turbulent velocity fields from the horizontal plane experiments at $Re_\theta = 280$ located at (a) 1.5 mm and (b) 3.5 mm above the wall. Mean boundary layer flow is in the positive x -direction.

Near-wall streak structures are generally aligned with the mean flow that are found in the buffer layer of the turbulent boundary layer. Stream-wise vortices and other vortical structures are also found in this layer. To investigate whether the observed multi-modal behavior in the $\phi(u')$ distribution is related to vortices, a vorticity threshold technique is used to detect vortices.

The vorticity threshold was calculated utilizing a Gaussian weighted average filter over each instantaneous turbulent vorticity field. This is a low-pass 2D Gaussian filter of size (F) with standard deviation (σ) where both quantities were computed based on the dimensions of the planar vorticity field ($S = 256 \text{ vectors} \times 192 \text{ vectors}$) as shown in Eqns. 3.3 and 3.4. The output of this filter was multiplied by a constant of 0.7, manually selected and optimized for high quality vortex detection. This operation produces a vorticity threshold field that detects vortices when applied to the corresponding instantaneous turbulent vorticity field.

$$\sigma = 2 \text{ floor} \left(\frac{S}{16} \right) + 1 \quad (3.3)$$

$$F = 2 \text{ ceil}(2\sigma) + 1 \quad (3.4)$$

A sample instantaneous turbulent vorticity field in the horizontal plane with the superimposed corresponding turbulent velocity vectors at $Re_\theta = 280$ and $y = 3.5 \text{ mm}$ is depicted in Figure 3.7a. There are numerous regions of stream-wise oriented positive and negative fluctuating vorticity that resemble stream-wise vortex signatures. Several of these regions are adjacent to each other and have high vorticity magnitudes. The map of the corresponding detected vortices based on the vorticity threshold are illustrated in Figure 3.7b.

As illustrated in the figure, the high vorticity regions are well captured and the detected vortices are aligned primarily with the mean flow direction as expected. Next, u' is ex-

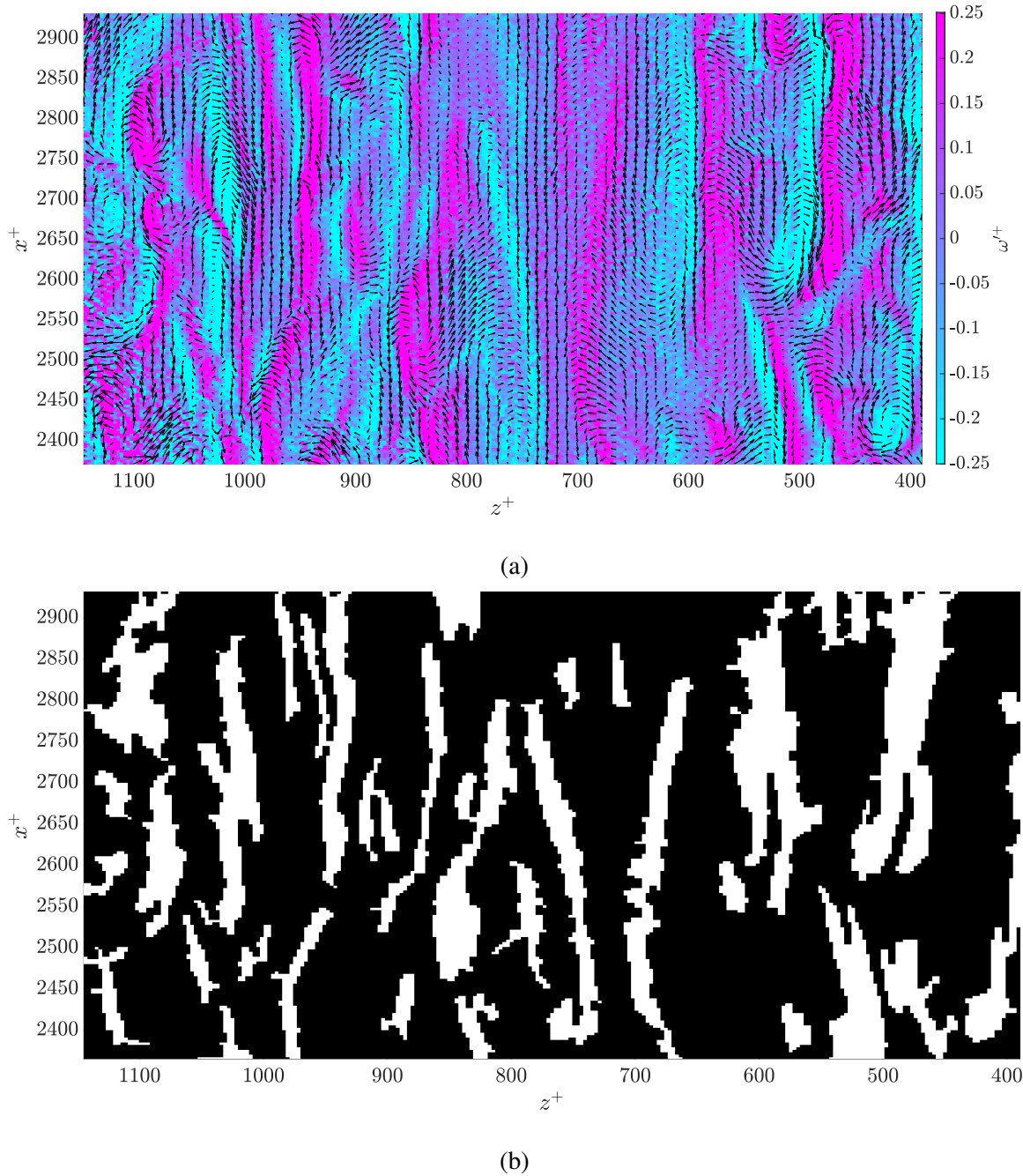


Figure 3.7: (a) Instantaneous turbulent vorticity field with superimposed turbulent velocity vectors. (b) Detected vortices (white) for this vorticity field after vorticity threshold is applied. Horizontal plane experiment at $y = 3.5$ mm and $Re_\theta = 280$. Mean boundary layer flow is in the positive x -direction.

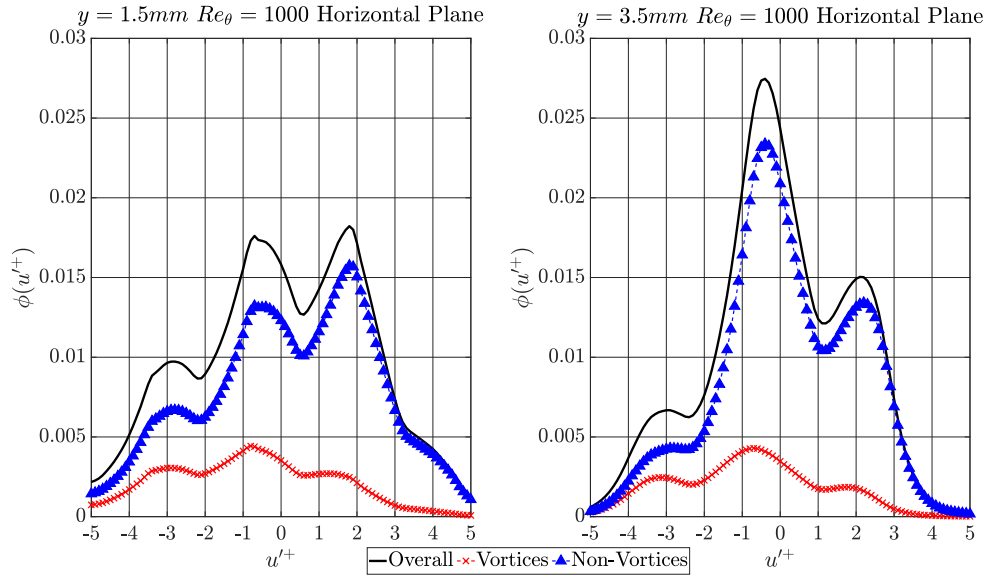


Figure 3.8: PDFs of u'^+ for detected vortices, non-vortices, and the overall distribution based on applied vorticity threshold technique. The vortices and non-vortices PDFs are normalized with the overall PDF.

tracted from the turbulent velocity fields within the detected vortex regions. The PDFs of u' were then calculated for the regions associated with detected vortices and non-vortices as illustrated in Figure 3.8.

At the figure shows, at both $y = 1.5$ mm and $y = 3.5$ mm, the PDFs' shape in both vortex and non-vortex regions does not significantly change and both distributions show multi-modal behavior. Similar trends are observed at all Reynolds numbers. The smaller magnitudes present in the detected vortices distribution reflects only the fewer measurement points present in this distribution relative to the non-vortices distribution and the overall PDF. The presence of multi-modality in both vortical and non-vortical regions indicates that the multi-modality in $\phi(u')$ is not exclusive to vortices. This conclusion however does not imply that there is no relationship between the streaks and stream-wise vortices. In fact, the relationship between the two has been the topic of prior research where the streaks and

stream-wise vortices participate in a cyclical exchange of energy [39, 40].

3.3.4 On the Mechanism of Multi-Modal $\phi(u')$ Formation

Advanced mathematical analysis techniques have been applied to characterize the nature of turbulent flows. One such technique is the Proper Orthogonal Decomposition (POD). The POD technique decomposes a given quantity into several eigenfunctions, known as POD modes (ψ_j), each with an associated coefficient (a_j) a function of the calculated eigenvalues, as shown in Eqn. 3.5 for u' . The eigenfunctions are found from solving the eigenvalue problem in Eqn. 3.6 with eigenvalues λ_j while the coefficients are calculated by projecting the eigenfunctions onto the specified fluid quantity, see Eqn. 3.7 [41]. The objective of POD is to generate a decomposition of the specified quantity with minimal difference between the quantity and its POD. It is important to note that each POD mode does not always represent any real fluid quantity or behavior but rather flow energy patterns. However, there have been numerous insights on real fluid behavior based on POD characteristics making this technique suitable for the analysis of turbulent flow structure [41–44].

$$u' = \sum a_j \psi_j \quad (3.5)$$

$$\int \langle u'(x, t) u'^T(x, t) \rangle \psi_j(x') dx' = \lambda_j \psi_j(x) \quad (3.6)$$

$$a_j(t) = \int u'(x, t) \psi_j(x) dx \quad (3.7)$$

The behavior of multi-modal $\phi(u')$ was further investigated using the Proper Orthogonal Decomposition of the measured turbulent stream-wise velocity fields. In this investigation, the method of snapshots was used on measured PIV data and the decomposition was calculated using the open-source implementation in the OpenPIV toolbox [41, 45]. This tech-

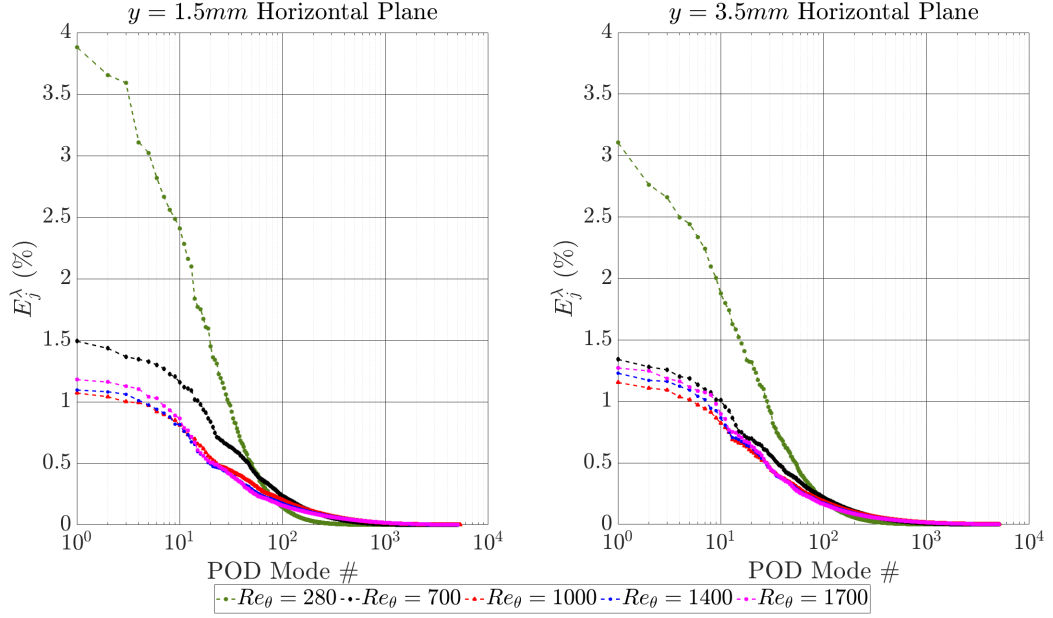


Figure 3.9: Stream-wise POD eigenspectra for all tested Reynolds numbers at 1.5 mm and 3.5 mm above the bottom wall.

nique generates one POD mode per instantaneous vector field measured in experiments, therefore there are approximately 5000 POD modes computed per experimental run in the present study. The energy associated with each POD mode is known as the eigenspectra (E_j^λ), which is a function of the eigenvalues calculated as shown in Eqn. 3.8. This quantity defines the relative contribution of each POD mode to the original turbulent velocity fields. The eigenspectra of u' in the horizontal planes at heights of $y = 1.5$ mm and 3.5 mm are plotted in Figure 3.9.

$$E_j^\lambda = \frac{\lambda_j}{\sum \lambda_j} \cdot 100\% \quad (3.8)$$

At both tested heights the same trend is observed where the most energetic POD modes are the very low-order (< 10) modes, as expected. The most energetic mode, POD mode 1, contains between 1% and 2% of the total energy content in the decomposition at higher

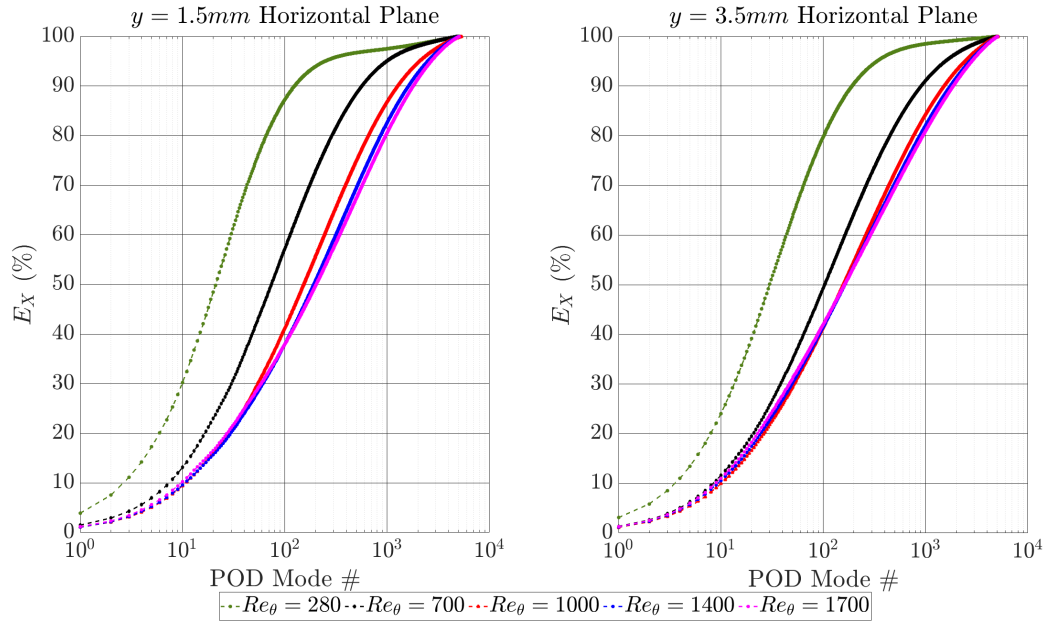


Figure 3.10: Stream-wise cumulative POD eigenspectra for all tested Reynolds numbers at 1.5 mm and 3.5 mm above the horizontal wall.

Reynolds numbers, while at $Re_\theta = 280$ the first POD mode contains between 3% and 4%. Higher-order POD modes have a lower energy content per mode as both figures indicate the respective eigenspectra decreases quickly in a non-linear fashion. At low Reynolds numbers the eigenspectra decreases faster than at high Reynolds numbers producing an intersection of the curves around POD mode 100. As the POD mode number increases further, eventually the largest magnitude of E_j^λ for a given POD mode is found at $Re_\theta = 1700$.

The trends observed in the eigenspectra distribution indicate that a substantial amount of energy is present within higher order POD modes especially at higher Reynolds numbers. The cumulative eigenspectra (E_X) describes the fraction of total energy contained within the POD modes up to X% of the total energy, starting with mode 1. The cumulative energy content corresponding to the data in Figure 3.9 is plotted in Figure 3.10, respectively.

The two families of curves in the figure exhibit very similar behavior. At $Re_\theta \geq 1000$, approximately the first 100 POD modes are required to capture the first 40% of the total energy content. Decreasing the Reynolds number indicates fewer POD modes are required to reach this energy signal due to a larger E_j^λ . These graphs also exhibit the behavior where the number of POD modes required to reach a specific total energy content generally increases with Reynolds number. This is most clearly observed at $y = 1.5$ mm where 60% of the total energy content requires ~ 30 modes at $Re_\theta = 280$ and ~ 350 modes at $Re_\theta = 1700$. These curves indicate that for $Re_\theta \geq 700$, more than 100 POD modes cumulatively contain 50% of the total energy.

The energy distribution in these POD modes is then utilized to investigate what quantity of POD modes are needed to produce the observed multi-modal behavior in $\phi(u')$. This will establish the relative significance of each POD mode to the statistical behavior of u' . For this purpose, u' was reconstructed using the POD modes that constitute the 75th (E_{75}), 85th (E_{85}), 95th (E_{95}), and 100th (E_{100}) percentile of the total energy content, i.e. the cumulative energy up to that percentile. The $\phi(u')$ distribution for these percentiles are illustrated in Figure 3.11.

As observed in the figure, at $y = 1.5$ mm, the $\phi(u')$ distribution corresponding to E_{75} , referred to as $\phi(u'_{75})$, shows a smooth uni-modal distribution. At the 85th percentile, $\phi(u'_{85})$, the distribution remains uni-modal but becomes wider and flatter. Once 95% of the total energy content is included (i.e. 95th percentile), a weak tri-modal distribution is observed in $\phi(u'_{95})$. A full multi-modal distribution is established at the 100th percentile. This indicates that the multi-modal behavior does not manifest in the $\phi(u')$ distribution until a very large fraction of the total u' signal is included. A similar trend is observed at $y = 3.5$ mm, where $\phi(u'_{75})$ begins as relatively narrow and uni-modal, then $\phi(u'_{85})$ is broader, and the weak multi-modal behavior appears at $\phi(u'_{95})$. From these figures, it is clear the peaks

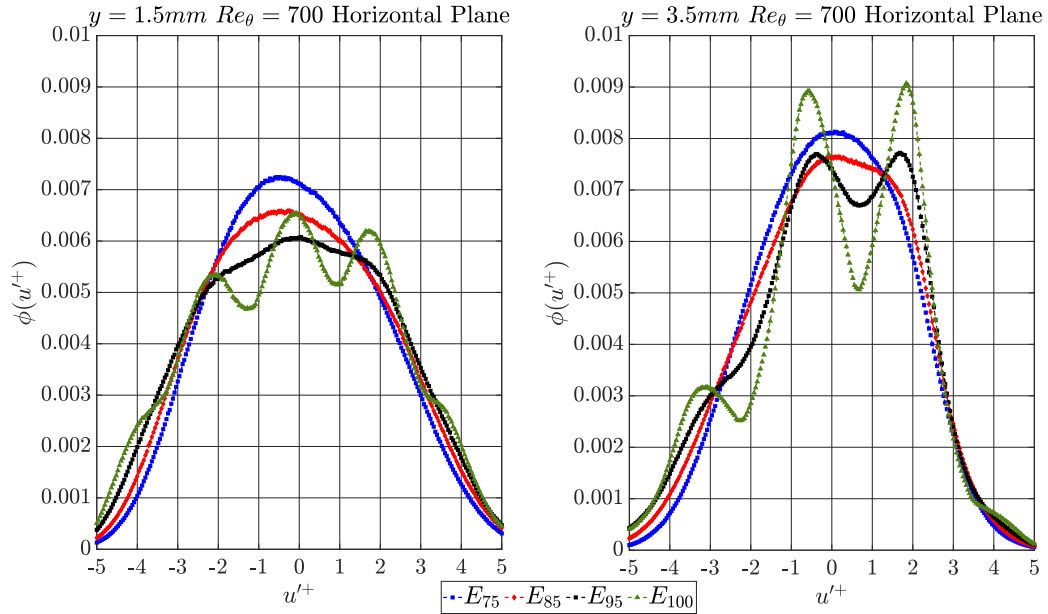


Figure 3.11: PDFs of u' at $Re_\theta = 700$ based on POD reconstructions using different percentiles of the total POD energy; E_{75} (blue), E_{85} (red), E_{95} (black), and E_{100} (green).

and valleys of the multi-modal $\phi(u')$ distributions are formed by the contributions of the higher order POD modes, i.e. POD modes located between E_{85} and E_{100} . The percentiles of u' POD modes at which the multi-modal behaviors are observed at different Reynolds numbers are summarized in Table 3.3.

As the results in the above table shows, at the lowest Reynolds number of 280, no multi-modal behavior is observed at $y = 1.5$ mm but at $y = 3.5$ mm, $Re_\theta = 280$ exhibited a unique tetra-modal behavior when 99% of the total POD energy is considered. All Reynolds numbers higher than 280 exhibited multi-modal behavior at both heights but at high percentiles of POD modes. These results demonstrate that the multi-modal behavior in $\phi(u')$ is a higher-order phenomena that cannot be captured by low to middle order POD modes and that the energy contributions from high order POD modes (top 5-15% modes) play a crucial role in influencing the velocity distribution. As per Figure 3.10, depending on the Reynolds number, between the first 100 to 1000 POD modes cumulatively constitute about 85% of

Re_θ	$y = 1.5$ mm	$y = 3.5$ mm
280	Uni-modal only	Bi-modal: 97% Tri-modal: 98% Tetra-modal: 99%
700	Bi-modal: 97% Tri-modal: 98%	Bi-modal: 88% Tri-modal: 98%
1000	Bi-modal: 94% Tri-modal: 98%	Bi-modal: 96% Tri-modal: 99%
1400	Bi-modal: 97%	Tri-modal: 85%
1700	Bi-modal: 96% Tri-modal: 99%	Bi-modal: 98%

Table 3.3: Approximate percentiles of POD energy content required to manifest multi-modality in $\phi(u')$ distribution.

the total energy, while the remaining (over 4000) POD modes (15% of the total energy) collectively contribute to the multi-modal $\phi(u')$ behavior despite containing a relatively small amount of energy per mode.

To further investigate, u' was reconstructed using the POD modes from two separate energy regions, 0% to 85% and 85% to 100% of the cumulative eigenspectra. From the reconstructed u' fields, $\phi(u')$ was then calculated for both cases and illustrated in Figure 3.12 at $Re_\theta = 1000$.

The $\phi(u'_{85})$ distribution shows a broad behavior indicating that a wide range of turbulent velocity magnitudes are associated with these POD modes. The upper 15% of the cumulative energy content, $\phi(u'_{85-100})$ shows a narrow distribution indicating a limited range of low magnitude turbulent velocities associated with these POD modes. It is interesting to note that neither the $\phi(u'_{85})$ distribution nor the $\phi(u'_{85-100})$ distribution are multi-modal but only when the two distributions are combined, the multi-modality is realized. This behavior is observed in all Reynolds numbers considered in this study, except $Re_\theta = 280$ at $y = 1.5$ mm where no multi-modality was observed in the original $\phi(u')$ distribution. The non-linearity

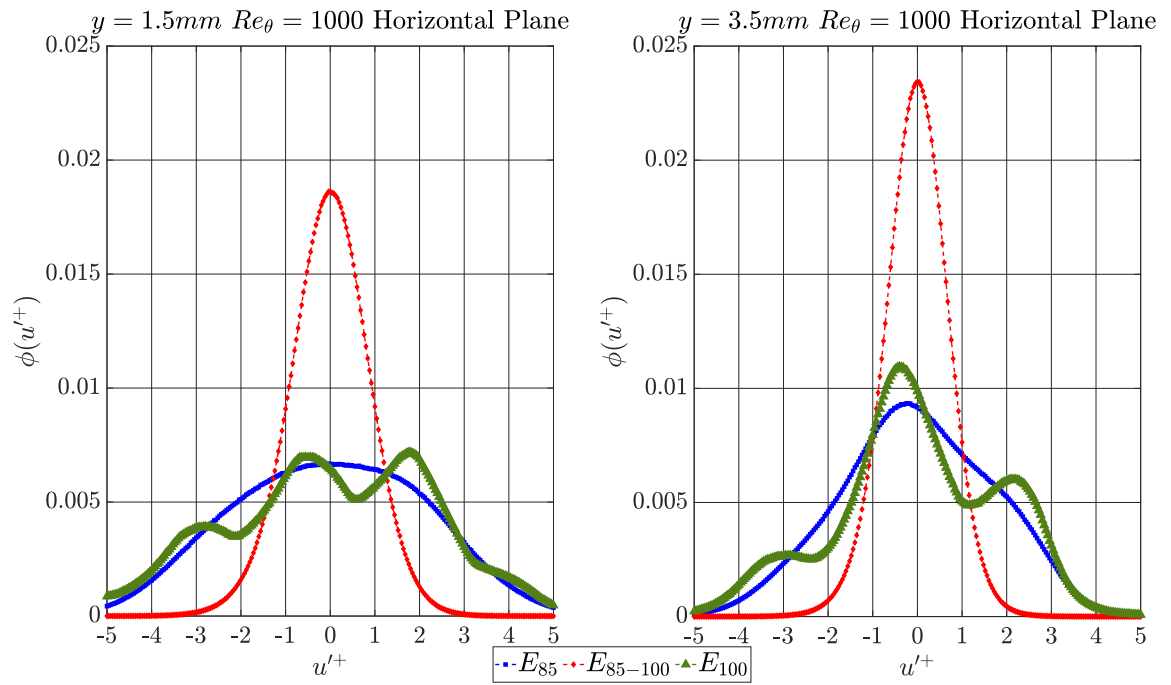


Figure 3.12: PDFs of u'^+ at $Re_\theta = 1000$ based on POD reconstructions of bottom 85% (0% to 85%) and top 15% (85% to 100%) of the cumulative POD energy.

observed in the eigenspectra is present in the POD coefficients, a_j , providing a non-linear weighting to each constituent POD mode of the reconstructed velocity field. The behavior of these PDFs indicates that the upper 15% of POD modes according to the cumulative energy distribution, characterize a process that preferentially selects certain u' values to produce the observed multi-modality.

One possible physical explanation for the formation of multiple modes in $\phi(u')$ is due to complex dissipative behavior. This hypothesis was tested by performing POD on the turbulent kinetic energy dissipation rate calculated from the turbulent velocity field using the method provided by Doron et. al. for planar PIV measurements as shown in Eqn. 3.9 [46]. The dissipation rate was separated based on the 85% POD energy threshold, that is the dissipation rate associated with POD modes containing 0% to 85% of the total POD energy and the dissipation rate associated with POD modes containing 85% to 100% of the total POD energy. The PDFs of the dissipation rate normalized by the friction velocity and kinematic viscosity (ϵ^+) are presented in Figure 3.13 for the two heights $y = 1.5$ mm and 3.5 mm at $Re_\theta = 1000$. The dissipation rate based on all POD modes is also presented for comparison.

$$\epsilon = 3 \left[\left(\frac{\partial u}{\partial x} \right)^2 + \left(\frac{\partial v}{\partial y} \right)^2 + \left(\frac{\partial u}{\partial y} \right)^2 + \left(\frac{\partial v}{\partial x} \right)^2 + 2 \left(\frac{\partial u}{\partial y} \frac{\partial v}{\partial x} \right) + \frac{2}{3} \left(\frac{\partial u}{\partial x} \frac{\partial v}{\partial y} \right) \right] \quad (3.9)$$

The results show that the distribution of $\phi(\epsilon_{85}^+)$ has a significant overlap with the dissipation rate based on all POD modes, indicating that the lower order POD modes well resolve the bulk of the dissipation rate. The $\phi(\epsilon_{85-100}^+)$ distribution indicates that substantially higher dissipation rates are associated with higher POD modes. The clear separation of the high-magnitude dissipation rate PDF at higher POD modes (i.e. $\phi(\epsilon_{85-100}^+)$) and

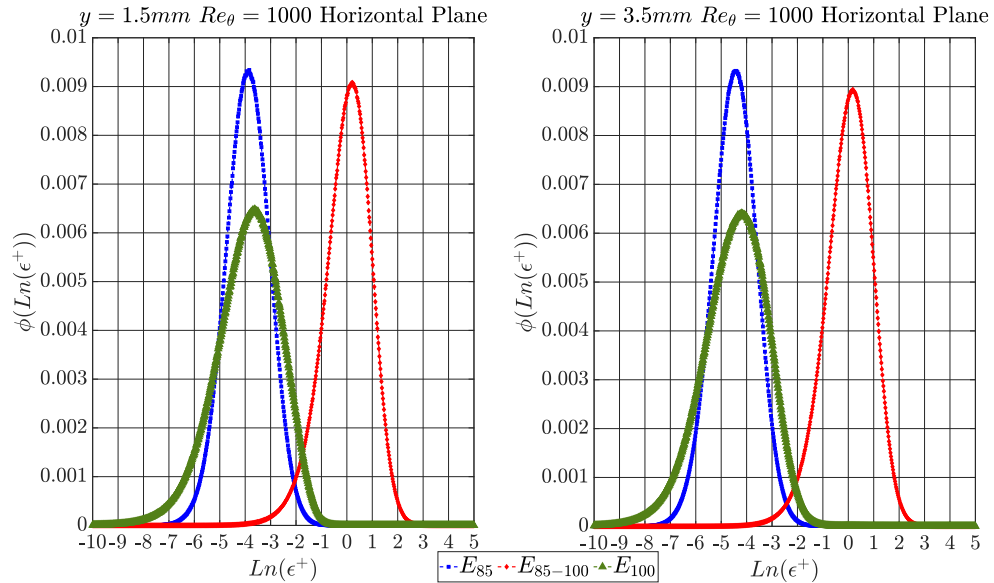


Figure 3.13: PDFs of natural logarithm normalized dissipation based on reconstructions of the POD of the estimated dissipation rate. The distributions are separated based on the cumulative energy thresholds from the u' POD.

the low-magnitude dissipation rate PDF at lower POD modes was observed at all tested Reynolds numbers. This separation of dissipation rates based on the POD energy threshold (i.e. 85%) that is originally associated with uni-modal and multi-modal $\phi(u')$, suggests that multi-modality in $\phi(u')$ is influenced by the presence of strong dissipation at high POD modes, which are associated with smaller scales of turbulent motion.

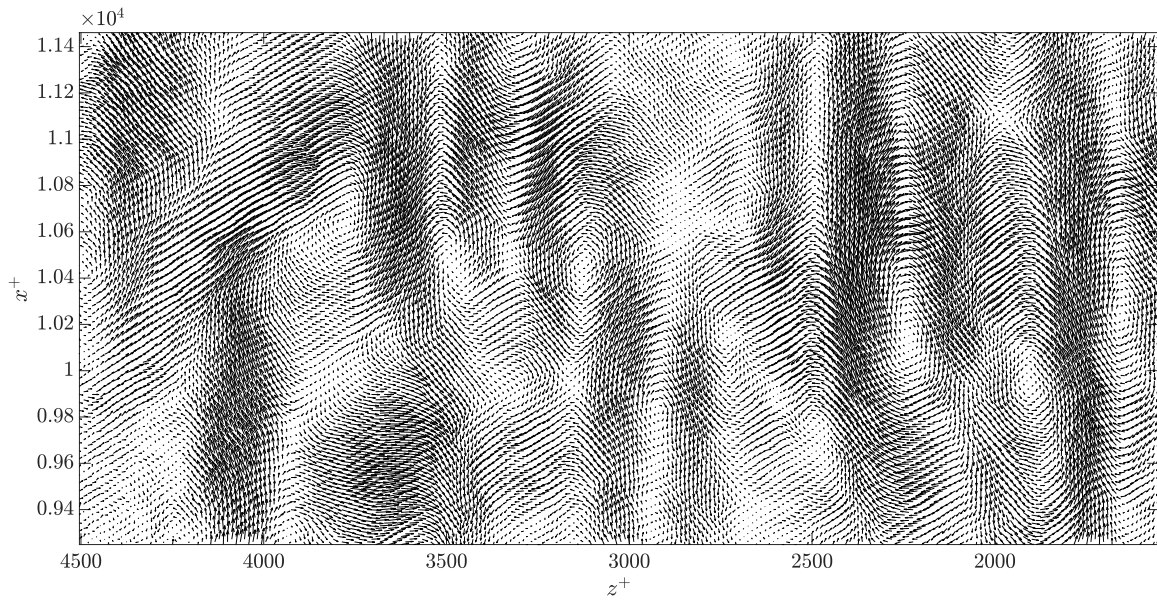
Further investigation into the nature of the reconstructed POD modes provides deeper insight into the underlying flow dynamics. By reconstructing instantaneous turbulent velocity fields from groups of POD modes, it is possible to observe the spatial distribution and interaction of detected phenomena. The POD modes corresponding to the ranges: 0%-20%, 20%-40%, etc., up to 80%-100% of the cumulative energy in the POD of u' were each reconstructed with example turbulent velocity vector fields depicted in Figure 3.14. It is observed that the 0%-20% POD reconstruction contained streak-like shapes separated by

strong shear layers and occasional roll-ups. From 20%-40% up to 40%-60% several eddy-like patterns were observed that were largest and most sparse at 20%-40% while smaller and numerous at 40%-60%. At higher than approximately 80% cumulative energy, no clear eddy patterns were observed, instead small-scale motion patterns with some stochastic signature were present.

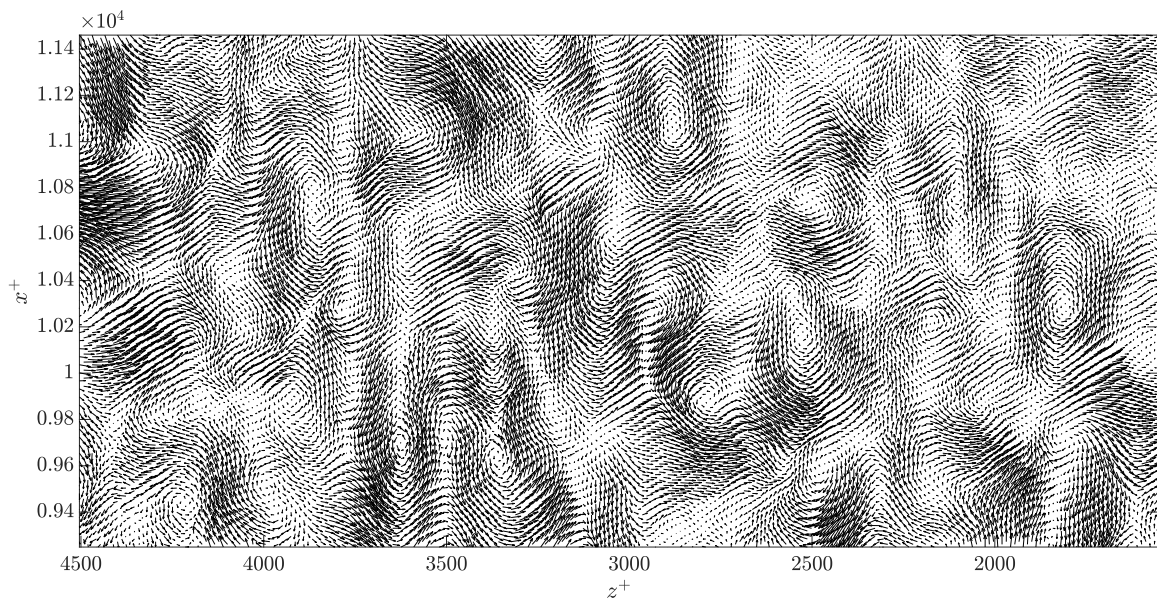
One interesting behavior present in these POD reconstructed vector fields is the formation of large eddy-like patterns at low order POD modes. These eddy-like features are likely to have been generated by instability in the shear layer between adjacent streaks. As the POD modes increase, the size of the observed eddy-like patterns was found to decrease while, the number of those patterns increased. This process is reminiscent of the turbulent energy cascade where vortices of decreasing size transport energy toward the dissipative scale. The highest order POD modes appear to be corresponding to small scales of motion, and as previous results have demonstrated, are associated with the strongest dissipation magnitude, which is consistent with the energy cascade process. Similar patterns of the reconstructed vector fields at different POD modes were also observed at other Reynolds numbers.

Figure 3.14d shows that the reconstructed vector field of the top percentile of POD modes is comprised of numerous, relatively small-scale turbulent patterns throughout the flow domain. As discussed earlier, the top 15 percentile of POD modes contribute to the multi-modal behaviour (see Figure 3.11 and Table 3.3). This indicates that there must exist a mechanism through which these small-scale turbulent features interact with the larger scale eddy-like patterns to invoke the multi-modal behaviour. It can be hypothesized that at certain scales, strong, nonlinear energy exchange occurs between these turbulent features, which is not exclusive to vortices. This hypothesis is consistent with the near-wall cycle process analytically proposed by Waleffe and Kim [39, 40] that describes a cyclical energy

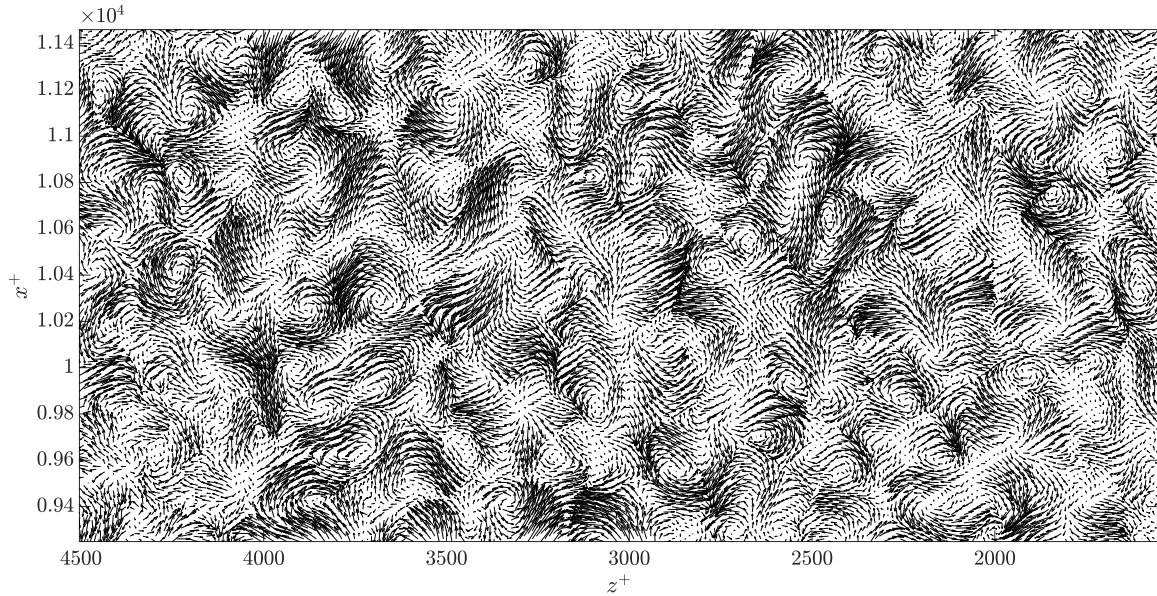
exchange where turbulent kinetic energy is transferred from the mean flow to stream-wise vortices and then to streak structures. Some of this energy then returns to the stream-wise vortices via non-linear streak instability while some energy is dissipated. They argued that certain wavenumber conditions must be satisfied to support the cyclical energy transfer and prevent viscous decay [39, 40]. The smallest scales of turbulence are not resolved in the present study; hence, the computed dissipation rate is taken to approximate energy transfer toward smaller scales. The high order POD modes and their associated small-scale turbulent motions are not strictly dissipative in nature. As POD mode numbers are analogous to wavenumbers, one physical interpretation of the observed multi-modal behaviour could be part of the cyclical energy transfer where some energy from the small-scale turbulent features is returned to the larger scale turbulent motions.



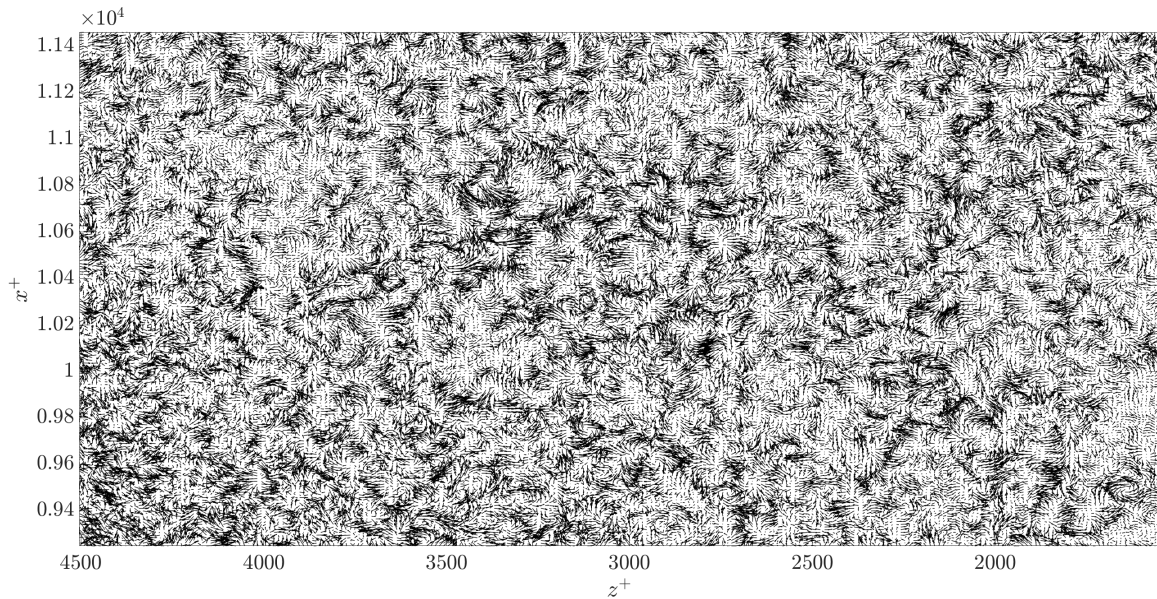
(a)



(b)



(c)



(d)

Figure 3.14: POD reconstruction of turbulent velocity vector fields from horizontal plane experiments at $Re_\theta = 1000$ located 3.5 mm above the wall. Panel (a) contains the reconstruction from E_{0-20} , (b) E_{20-40} , (c) E_{40-60} , (d) E_{80-100} . Mean boundary layer flow is in the positive x -direction.

3.4 Conclusions

In this study, the near-wall dynamics of the turbulent boundary layer were investigated utilizing the multi-plane PIV technique. Planar velocity measurements over multiple orthogonal planes were successfully able to capture 3D turbulent phenomena suitable for a comprehensive investigation. The stream-wise turbulent velocity PDF manifested multi-modal behavior primarily within the buffer layer. These findings indicate that the often used assumption of Gaussian turbulent statistics is not always true in the turbulent boundary layer. The cause of the multi-modal $\phi(u')$ distribution was investigated in the horizontal plane where results indicated the multi-modal behavior was not induced by the strong longitudinal vortices present in the buffer layer. This necessitated a more advanced analysis technique in the form of the Proper Orthogonal Decomposition to characterize the observed multi-modal behaviors of $\phi(u')$.

The POD analysis of u' presented multiple interesting results. First, the energy associated with higher order modes was significant suggesting that these modes cannot be neglected. This observation led to the demonstration that the upper 15% of the cumulative eigenspectra was the contributor to the observed multi-modal behavior of $\phi(u')$. It was found that these high order POD modes correlate to a large magnitude of turbulent energy dissipation rate. Observations of reconstructed turbulent velocity fields from the POD indicate the presence of eddy-like turbulent patterns that progressively get smaller in size as the POD mode number increases until manifestation of small-scale turbulent features at higher POD modes constituting top 15% of the cumulative energy content. These results form the basis of the hypothesis that the multi-modality observed in $\phi(u')$ is driven by a complex energy exchange process between large and small scale turbulent motion.

Bibliography

- [1] S. Pal, M. Lopez, M. Schmidt, M. Ramonet, F. Gilbert, I. Xueref-Remy, and P. Cialis, “Investigation of the atmospheric boundary layer depth variability and its impact on the ^{222}Rn concentration at a rural site in France,” *Journal of Geophysical Research*, vol. 120, pp. 623–643, 2015.
- [2] M.R. Head, and P. Bandyopadhyay, “New aspects of turbulent boundary-layer structure,” *Journal of Fluid Mechanics*, vol. 107, pp. 297–338, 1981.
- [3] X. Wu, and P. Moin, “Direct numerical simulation of turbulence in a nominally zero-pressure-gradient flat-plate boundary layer,” *Journal of Fluid Mechanics*, vol. 630, pp. 5–41, 2009.
- [4] J. Jeong, F. Hussain, W. Schoppa, and J. Kim, “Coherent structures near the wall in a turbulent channel flow,” *Journal of Fluid Mechanics*, vol. 332, pp. 185–214, 1997.
- [5] S.J. Kline, W.C. Reynolds, F.A. Schraub, and P.W. Runstadler, “The structure of turbulent boundary layers,” *Journal of Fluid Mechanics*, vol. 30, no. 4, pp. 741–773, 1967.
- [6] R.J. Adrian, C.D. Meinhart, and C.D. Tomkins, “Vortex organization in the outer region of the turbulent boundary layer,” *Journal of Fluid Mechanics*, vol. 422, pp. 1–54, 2000.

- [7] H.E. Fiedler, "Coherent Structures in Turbulent Flows," *Progress in Aerospace Sciences*, vol. 25, no. 3, pp. 231–269, 1988.
- [8] P.W. Runstadler, S.J. Kline, and W.C. Reynolds, *An experimental investigation of the flow structure of the turbulent boundary layer*. No. MD8. Stanford University California, 1963.
- [9] S.S. Lu, and W.W. Willmarth, "Measurements of the structure of the Reynolds stress in a turbulent boundary layer," *Journal of Fluid Mechanics*, vol. 60, no. 3, pp. 481–511, 1973.
- [10] J.M. Wallace, H. Eckelmann, and R.S. Brodkey, "The wall region in turbulent shear flow," *Journal of Fluid Mechanics*, vol. 54, no. 1, pp. 39–48, 1972.
- [11] R.F. Blackwelder, and R.E. Kaplan, "On the wall structure of the turbulent boundary layer," *Journal of Fluid Mechanics*, vol. 76, no. 1, pp. 89–112, 1976.
- [12] R.F. Blackwelder, and E. Eckelmann, "Streamwise vortices associated with the bursting phenomenon," *Journal of Fluid Mechanics*, vol. 94, no. 3, pp. 577–594, 1979.
- [13] P. Davidson, *Turbulence: An Introduction for Scientists and Engineers*. Oxford, UK: Oxford University Press, 2nd ed., 2015.
- [14] C. Meneveau and Y. Li, "On The Origin of Non-Gaussian Statistics in Hydrodynamic Turbulence," *Physical Review Letters*, vol. 95, 2005.
- [15] J. Jimenez, "Turbulent Velocity Fluctuations Need Not Be Gaussian," *Journal of Fluid Mechanics*, vol. 376, pp. 139–147, 1998.
- [16] F.N. Frenkiel and P.S. Klebanoff, "Probability Distributions and Correlations in a Turbulent Boundary Layer," *Physics of Fluids*, vol. 16, no. 6, pp. 727–737, 1973.

- [17] Z. She and S.A. Orszag, "Physical model of Intermittency in Turbulence: Inertial-Range Non-Gaussian Statistics," *Physical Review Letters*, vol. 66, no. 13, pp. 1701–1704, 1991.
- [18] G.G. Katul, M.B. Parlange and C.R. Chu, "Intermittency, Local Isotropy, and non-Gaussian Statistics in Atmospheric Surface Layer Turbulence," *Physics of Fluids*, vol. 6, no. 7, pp. 2480–2492, 1994.
- [19] A. Noullez, G. Wallance, W. Lempert, R.B. Miles and U. Frisch, "Transverse Velocity Increments in Turbulent Flow Using the RELIEF Technique," *Journal of Fluid Mechanics*, vol. 339, pp. 139–147, 1997.
- [20] H.H. Fernholz and P.J. Finley, "The Incompressible Zero-Pressure-Gradient Turbulent Boundary Layer: An Assessment of the Data," *Progress in Aerospace Sciences*, vol. 32, no. 4, pp. 245–311, 1996.
- [21] A.K. Gupta and R.E. Kaplan, "Statistical Characteristics of Reynolds Stress in a Turbulent Boundary Layer," *Physics of Fluids*, vol. 15, no. 6, pp. 981–985, 1972.
- [22] S.P. Dinavahi, K.S. Breuer, and L. Sirovich, "Universality of Probability Density Functions in Turbulent Channel Flow," *Physics of Fluids*, vol. 7, no. 5, pp. 1122–1129, 1995.
- [23] J. Andreopoulos, F. Durst, Z. Zaric, and J. Jovanovic, "Influence of Reynolds Number on Characteristics of Turbulent Wall Boundary Layers," *Experiments in Fluids*, vol. 2, pp. 7–16, 1984.
- [24] Y. Tsuji, B. Lindgren, and A.V. Johansson, "Self-similar Profile of Probability Density Functions in Zero-Pressure Gradient Turbulent Boundary Layers," *Fluid Dynamics Research*, vol. 37, pp. 293–316, 2005.

- [25] C. Meneveau and I. Marusic, “Generalized Logarithmic Law for High-order Moments in Turbulent Boundary Layers,” *Journal of Fluid Mechanics*, vol. 719, R1, pp. 1–11, 2013.
- [26] J. Jovanovic, F. Durst, T.G. Johansson, “Statistical Analysis of the Dynamic Equations for Higher Order Moments in Turbulent Wall Bounded Flows,” *Physics of Fluids A: Fluid Dynamics*, vol. 5, pp. 2886–2900, 1993.
- [27] A. Elatar, and K. Siddiqui, “The characteristics of coherent structures in low Reynolds number mixed convection flows,” *Fluid Dynamics Research*, vol. 47, p. 33, 2015.
- [28] A. Elatar, and K. Siddiqui, “The influence of bottom wall heating on the mean and turbulent flow behavior in the near wall region during mixed convection,” *International Journal of Thermal Sciences*, vol. 77, pp. 233–243, 2014.
- [29] K. Dennis and K. Siddiqui, *Multi-Plane Characterization of the Turbulent Boundary Layer*. 5th Joint US-European Fluids Engineering Summer Conference. Montreal, Canada, 2018.
- [30] K. Dennis and K. Siddiqui, *Investigation of Turbulent Flow Behavior in a Heated Boundary Layer*. ASME-JSME-KSME Joint Fluids Engineering Conference. San Francisco, USA, 2019.
- [31] K. Dennis and K. Siddiqui, *Three-Dimensional Characterization of Bursting and Sweeping Phenomena in the Turbulent Boundary Layer*. The Joint Canadian Society for Mechanical Engineering and CFD Society of Canada International Congress 2019. London, Canada, 2019.
- [32] E.A. Cowen and S.G. Monismith, “A hybrid digital particle tracking velocimetry technique,” *Experiments in Fluids*, vol. 22, pp. 199–211, 1997.

- [33] A.K. Prasad, R.J. Adrian, C.C. Landreth and P.W. Offutt, “Effect of resolution on the speed and accuracy of particle image velocimetry interrogation,” *Experiments in Fluids*, vol. 13, pp. 105–116, 1992.
- [34] F.H. Clauser, “The Turbulent Boundary Layer,” *Advances in Applied Mechanics*, vol. 4, pp. 1–51, 1956.
- [35] A.A. Aliabadi, M. Moradi, D. Clement, W.D. Lubitz, and B. Gharabaghi, “Flow and Temperature Dynamics in an Urban Canyon Under a Comprehensive Set of Wind Conditions, Wind Speeds, and Thermal Stability Conditions,” *Environmental Fluid Mechanics*, vol. 19, pp. 81–109, 2019.
- [36] X. Wu, P. Moin, J.M. Wallace, J. Skarda, A. Lozano-Duran and J.P. Hickey, *Transitional-Turbulent Spots and Turbulent-Turbulent Spots in Boundary Layers*. Proceedings of National Academy of Sciences, USA, PNAS.1704671114, 2017.
- [37] H. Schlichting and K. Gersten, *Boundary Layer Theory*. Springer, 8th ed., 1999.
- [38] P. Schlatter, Q. Li, R. Orlu, F. Husain, and D. Henningson, D., “On the near-wall vortical structures at moderate Reynolds numbers,” *European Journal of Mechanics B/Fluids*, vol. 48, pp. 74–93, 2014.
- [39] F. Waleffe and J. Kim, *How Streamwise Rolls and Streaks Self-sustain in a Shear Flow*. in *Self-sustaining Mechanisms of Wall-bounded Turbulence*. Southampton, UK and Boston, USA: Computational Mechanics Publications, 1997.
- [40] F. Waleffe and J. Kim, *How Streamwise Rolls and Streaks Self-sustain in a Shear Flow: Part 2*. American Institute of Aeronautics and Astronautics. Albuquerque, USA, 1998.
- [41] P. Holmes, J.L. Lumley, G. Berkooz, and C.W. Rowley, *Turbulence, Coherent Struc-*

- tures, Dynamical Systems and Symmetry*. Cambridge, UK: Cambridge University Press, 2nd ed., 2012.
- [42] N. Aubry, P. Holmes, J.L. Lumley, and E. Stone, “The dynamics of coherent structures in the wall region of a turbulent boundary layer,” *Journal of Fluid Mechanics*, vol. 192, pp. 115–173, 1988.
- [43] D. Greig, K. Siddiqui, P. Karava, and A. Elatar, “Investigation of fundamental flow mechanisms over a corrugated waveform using proper orthogonal decomposition and spectral analyses,” *International Journal of Thermal Sciences*, vol. 96, pp. 160–172, 2015.
- [44] A. Elatar, and K. Siddiqui, “The effect of mixed convection on the structure of channel flow at low Reynolds numbers,” *International Journal of Heat and Fluid Flow*, vol. 46, pp. 29–42, 2014.
- [45] R. Gurka, A. Liberzon and G. Hetsroni, “POD of vorticity fields: A method for spatial characterization of coherent structures,” *International Journal of Heat and Fluid Flow*, vol. 27, no. 3, pp. 416–423, 2006.
- [46] P. Doron, L. Bertuccioli, J. Katz and T.R. Osborn, “Turbulence Characteristics and Dissipation Estimates in the Coastal Ocean Bottom Boundary Layer from PIV Data,” *Journal of Physical Oceanography*, vol. 31, pp. 2108–2134, 2001.

Chapter 4

Visualization and Characterization of Thermals in a Heated Turbulent Boundary Layer

4.1 Introduction

The exchange of mass, momentum, and heat at a solid-fluid interface is one classical area of study in fluid mechanics. The interfacial transport of these quantities is governed by the behaviors of the developed hydrodynamic and thermal boundary layers. In numerous engineering applications and environmental phenomena, the encountered boundary layer is turbulent in nature and characterized by non-linear dynamical processes that create challenges for an in-depth investigation of the underlying flow phenomena. The presence of heat transfer further increases flow complexity due to the non-linear coupling of the key thermofluid variables. A better insight into turbulent boundary layer dynamics is necessary, to improve the understanding of underlying processes that are important in a wide range

of environmental and engineering fields, for example, the influence of atmospheric boundary layer stratification on the dynamic wind loading on structures, transport of species and weather patterns [1–5]. To facilitate the continued improvement of engineering systems and design correlations, and our predictive models for natural phenomena, a more comprehensive understanding of turbulent boundary layer dynamics in the presence of heat transfer is crucial.

In heated turbulent boundary layer flows, inertia, viscous shear, and buoyancy all interact to govern overall flow behavior. The relative influence of the inertial force and buoyant force is quantified by the bulk Richardson number (Ri) as defined in Eq. 4.1. In this equation, U is the mean freestream velocity, ΔT is the temperature difference between bulk fluid and solid, β is the coefficient of thermal expansion, g is gravitational acceleration, and L is the characteristic length scale [6].

$$Ri_L = \frac{Gr_L}{Re_L^2} = \frac{gL\beta\Delta T}{U^2} \quad (4.1)$$

This parameter defines three broad categories of flow dynamics in the presence of heat. When $Ri_L \ll 1$, flow inertia is dominant and the heat transfer mode is termed forced convection. In the regime where $Ri \approx 1$, the buoyant force is of comparable magnitude to flow inertia leading to a mixed convection regime. When $Ri \gg 1$, the buoyant force dominates the flow leading to the natural convection mode [7–9]. In this mode, when the Grashof number is very low and the inertial effects are very weak, the convective motion is negligible and the heat from a horizontal flat plate is transported via conduction. While the inertial effects are still weak, an increase in the Grashof number by increasing the wall temperature leads to the buoyant force overcoming the viscous force and inducing the buoyancy-driven

convective motion. In the presence of a relatively cooler horizontal plate placed at a certain height above the heated plate, fluid cools at the cold plate, increases its density and sinks down toward the hot plate, thus, forming a closed cyclical fluid flow pattern as the well-known Benard convective cells. As the hot wall temperature continues to rise, the buoyant force becomes significantly dominant compared to the viscous force, leading to the breakdown of convective cells and buoyant turbulence [10]. In the absence of a cold upper wall however, the closed cycle convective cells do not form. In this configuration, parcels of heated fluid known as thermals can detach and rise from the heated wall, which have been observed and qualitatively visualized [9, 11].

The presence of buoyancy can have a significant effect on boundary layer dynamics, especially in mixed convection conditions where inertia and the buoyant force are of comparable magnitude. The presence of a significant buoyant force has been reported to induce an early laminar to turbulent transition within the boundary layer [12]. Computational research studies often neglect the contributions of the buoyant force in the governing equations, opting to treat temperature as a passive scalar [13, 14]. While this treatment is valid in the limit of Ri approaching zero (i.e. forced convection), in the mixed convection regime such an assumption undermines the presence and impact of thermals. Previous computational research that included the buoyant force, rarely reported on the presence of thermals and often presented findings at one Richardson number [13–16]. In some cases, this is due to the research objective being focused on describing the inertia-driven turbulent phenomena and not the buoyancy-driven hydrodynamics [15, 16]. Recently, the present authors have reported on a 3D visualization of the heated turbulent boundary layer [17]. Several behaviors were documented where buoyant thermal-like regions exhibited complex and 3D turbulent behaviors including the participation and generation of eddies while rising through the boundary layer. The experimental findings reported there were qualitative in

nature and the presented thermal detection technique was only useful in one reported experimental condition, limiting the technique's broad applicability.

The presence of buoyancy driven secondary flow structures, such as thermals, can have a significant impact on the overall boundary layer flow behaviour. However, the formation and dynamics of thermals rising from the heated wall through a boundary layer flow is a complex process. Most of the current knowledge about this phenomenon originates from flow visualization studies, which provide a qualitative description of this complex process [6, 9, 18]. Thermals are known to be three-dimensional structures however there is a scarcity of experimental work to characterize their 3D nature within the turbulent boundary layer. In addition, there is a fundamental lack of knowledge on how buoyancy-driven thermals within the turbulent boundary layer are influenced by the relative contributions of buoyancy and bulk flow inertia.

The objective of the present study is to experimentally investigate and characterize the three-dimensional behaviors of buoyant thermals in the turbulent boundary layer over a range of Richardson numbers. This research builds upon the present authors' previous study by developing a robust technique to detect thermals that is effective over a wide range of Richardson numbers. From the analysis of detected thermals, new insights are presented on the behavior of thermals and their interactions with the surrounding boundary layer flow including the size, spatial distribution, and motion of buoyant thermals.

4.2 Experimental Setup

Experiments were performed in a closed loop low-disturbance wind tunnel. Airflow was driven by a variable-speed axial flow fan capable of producing 60 m/s velocity in the test section. The background turbulence was previously investigated using Laser Doppler Ve-

locimetry (LDV) was found to vary between 0.5–0.9 % for test section velocities between 3–60 m/s. The low turbulence rating was achieved by using several conditioning screens upstream of the test section. An active cooling system integrated with the wind tunnel, was used to maintain the air temperature at the inlet of the test section to within 1 °C of room temperature. The test section in the wind tunnel has square cross section 46 cm on each side and is 114 cm in length, as depicted in Figure 4.1. The sides of the test section were made of clear acrylic for visualization while the bottom wall was made of black matte vinyl coated aluminum. The boundary layer at the test section inlet was tripped using a 6.3 mm × 6.3 mm × 43 cm steel rod.

The test section bottom wall was embedded with 16 T-type 36 AWG special limits of error thermocouples (Omega Engineering) with an uncertainty of ± 0.5 °C. A 36 cm × 110 cm 240V, 3080W silicone surface heater (Zesta Engineering) was used to heat the entire bottom wall where the wall temperature was controlled to within 0.5 °C of a given set temperature with a PID controller (Zesta Engineering). Fibreglass and expanded polystyrene insulation were placed underneath the heater to minimize convective heat loss from below.

During experiments, air flow was started in the wind tunnel first, then the surface heater and active cooling unit were activated. The system was allowed to reach a steady state condition before data collection began. Experiments were conducted at five bulk Richardson numbers, 0.05, 0.1, 0.3, 1.0 and 2.0, where the characteristic length scale is the distance downstream of the test section inlet. The tested Richardson numbers were achieved from a selection of wall temperatures and momentum thickness-based Reynolds numbers, as shown in Table 4.1.

The generated turbulent boundary layer flow was visualized utilizing the Particle Image Velocimetry (PIV) technique applied over multiple orthogonal planes as shown in Figure 4.1 [19]. The vertical stream-wise plane visualized fluid motion in the x - y plane, the verti-

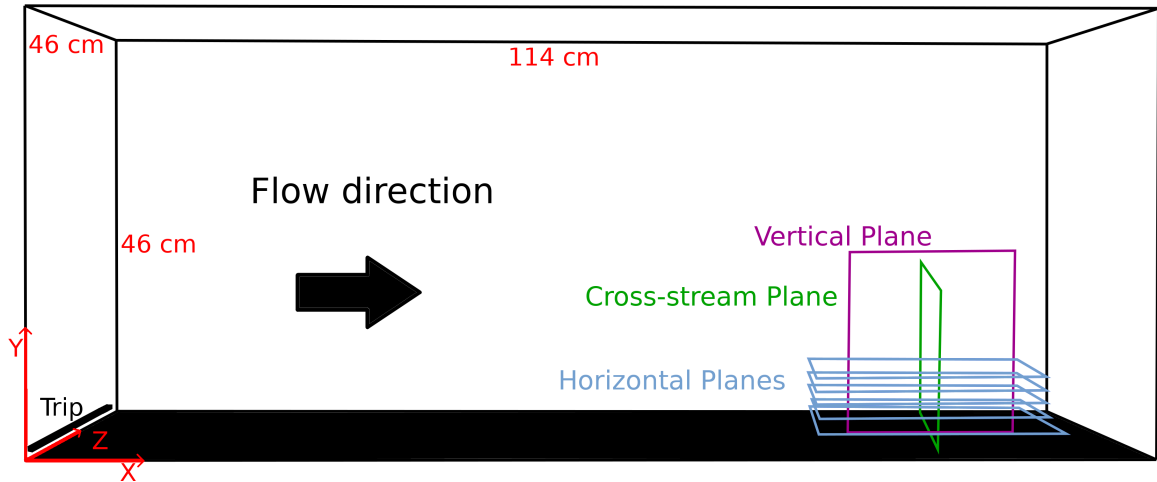


Figure 4.1: Diagram of the experimental setup.

	Ri_L				
	0.05	0.1	0.3	1.0	2.0
Re_θ	1400	1000	700	280	280
T_W ($^{\circ}\text{C}$)	90	90	90	55	90
U (m/s)	6.0	4.0	2.5	1.0	1.0

Table 4.1: Summary of experimental conditions.

cal cross-stream plane visualized the y - z plane, and each of the two considered horizontal planes, located at $y = 3.5$ mm and 7.5 mm above the wall, captured motion in the x - z plane. In all tests, the visualized field of view was ~ 80 cm (128 trip heights) downstream of the test section inlet to ensure the trip bar signature vanished at the measurement location.

A dual-cavity 120mJ Nd:YAG laser (120XT 532nm, SoloPIV) provided optical illumination by generating laser light beams at 15 Hz per cavity. A 12 Megapixel (4096×3072 pixels) CMOS camera (Flare, IO Industries) was used to capture images controlled by an image acquisition system (DVR Express CORE, IO Industries). A 50 mm f/1.4 (Nikon) and 70-300 mm f/4 camera lens (Sigma Corp.) were used in experiments. Laser pulse timing was synchronized to the camera via a four-channel pulse delay generator (555-4C, Berkeley Nucleonics). Theatrical fog seed particles (Directors Choice, Ultratec) were injected upstream of the test section and flow conditioning screens by a fog machine. Before image recording began in each experiment, the injected fog was allowed to circulate and disperse within the wind tunnel for several minutes to ensure uniform distribution of seed particle. Recorded images from each experiment were then exported to a workstation PC for image processing and analysis. Each experiment comprised of at least 10,000 images and each pair of images was captured at a rate of 15 Hz. It is important to note that in this study, PIV images were used primarily for flow visualization and hence, the cross-correlation and associated PIV image analyses for velocity computations were not performed except an analysis to characterize thermal motion in the later part of the paper.

4.3 Visualization of Thermal-like Phenomena

Typical PIV images show uniform distribution of seed particles (once the particles are thoroughly mixed with the flow). In the present study, the images contained regions of uniform particle distribution (brighter regions due to particles' illumination) and dark regions with

a very low seed particle density. As the seed particles were allowed to uniformly mix before measurements, the dark regions in images were not due to improper seed particles' mixing. Furthermore, these dark regions were found to be the strongest near the heated wall and their rising patterns suggest that they are associated with thermals produced from the heated wall. The plausible reasons for them being associated with dark regions is the rapid thermal expansion of air within these emerging structures and the evaporation of liquid droplets due to higher temperature. This sharply decreased the seed particle density causing these structures to appear dark. Figure 4.2 depicts the qualitative behaviors of these presumed thermals in each considered measurement plane. The significant geometric similarity of these "dark" structures with those of the thermals reported in the literature supports this assertion [6, 9, 18].

In the left-most column of Figure 4.2, images from the vertical stream-wise plane depict multiple interesting behaviors at three Richardson numbers. Starting in the top row at $Ri_L = 0.05$, where the relative influence of buoyancy is weakest, a small and narrow dark region at the bottom of the image is observed. This dark region adjacent to the bottom wall is named the "production layer" and was found to be the origin of all thermals observed rising through the boundary layer. In the center of this image, the thermals above the production layer are found to be small and their presence is indicated by a slightly darker region of the high seed density fluid. The observed thermal signature is faint due to the relatively high magnitude of turbulent mixing that brought seed particle into each thermal. Increasing the Richardson number to 0.3, constitutes a substantial increase in buoyancy force magnitude quantified by the Grashof number. This manifested as an increase in the size of both the production layer and the observed thermals (see middle image in the left column). The thermals in the center of the image appear darker due to the lower seed density present. The thermal on the left side of the image features a roll-up signature that

could have been generated by the Kelvin-Helmholtz instability between the thermal and the adjacent high seed density fluid. Increasing Ri_L to 2.0, where the buoyancy force is dominant compared to the inertial force, the image in the bottom left column of Figure 4.2 depicts a large production layer that extends up and to the right forming thin bands connecting to free floating thermals. The two relatively large “mushroom slice” shaped thermals in this image show multiple roll-up signatures on each side of a central stem. The large thermals and production layer observed in this image are evidence of the relatively large buoyant force magnitude.

The center column of the figure contains images from the horizontal plane at a height of 3.5 mm from the heated wall, where due to the large viewable area, numerous large-scale span-wise features are observed. The image in the top of the middle column corresponds to the $Ri_L = 0.05$ case and depicts an abundance of relatively small-scale thermals visible in different shades of gray, depending on the level of seed density, indicating different levels of turbulent mixing. The observed thermals show some alignment with the mean flow direction, while there is no clear organization in the span-wise direction. Increasing the Richardson number to 0.3 (middle image), the thermals appear to be larger than those observed at $Ri_L = 0.05$ and more clearly aligned with the stream-wise direction. The relatively stronger buoyant force appears to resist turbulent mixing evidenced by a smaller variation in the shades of gray present in the image. At $Ri_L = 2.0$ (bottom image in the middle column), thermals are very large and well-aligned in the stream-wise direction. These thermals also appear to be clearly separated from each other with little evidence of the turbulent mixing due to the strong influence of the buoyant force.

The cross-stream plane provides a very unique perspective of processes in a heated turbulent boundary layer. In this viewing plane, mean flow is coming out of the page toward the observer, minimizing the influence of the stream-wise velocity on observed behaviors.

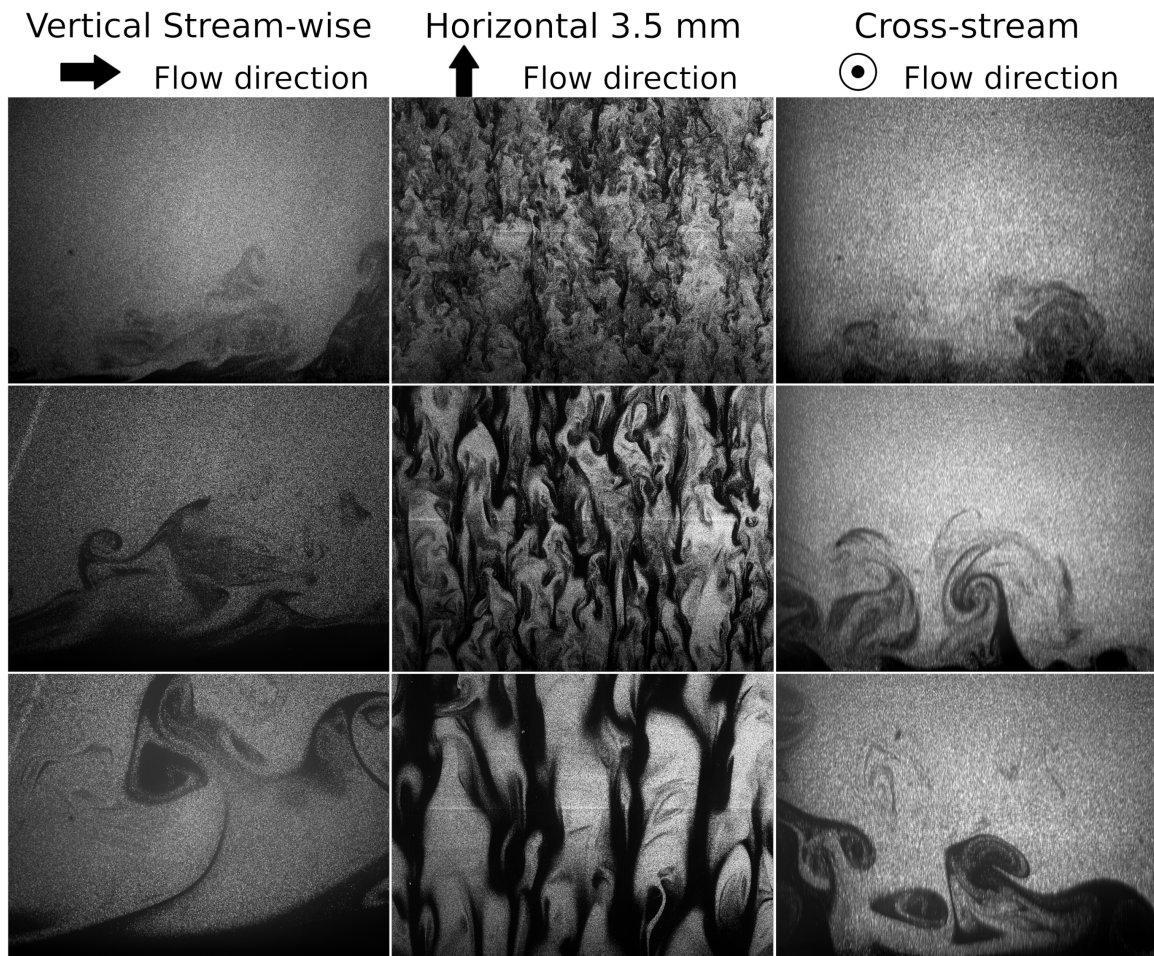


Figure 4.2: A set of images depicting the formation of thermals in all three measured planes at three Richardson numbers: 0.05 (top row); 0.3 (middle row); and 2.0 (bottom row). The field of view in the vertical stream-wise plane is 6 cm by 4.5 cm; horizontal plane: 23 cm by 17 cm; cross-stream plane: 8 cm by 5 cm.

At $Ri_L = 0.05$ (top image in the right column), thermals are depicted as somewhat darker regions near the wall. There is a substantial amount of seed particle present within these thermals due to strong turbulent mixing acting to break apart the low seed density thermals. As the Richardson number increased to 0.3, more visually apparent thermal signatures emerged (see middle image in the right column). The image illustrates a pair of rising thermals and a jet-like region of well-seeded fluid in between them that is rushing towards the wall. This jet-like region is likely associated with a turbulent sweep event. The shear between these thermals and the possible sweep event has deformed the rising thermals and produced a roll-up like signature in the right side thermal. The thermal signatures become stronger at $Ri_L = 2.0$ (bottom image in the right column), which shows relatively large thermals rising with the right-most thermal being deformed due to the span-wise motion of well-seeded fluid to the left. Towards the center of the image, a unique floating-like thermal is visible that is fully detached from the bottom wall. The center of this free-floating thermal shows a band of high seed density fluid indicating that the thermal is enveloping surrounding fluid in the out of plane direction. On the left side of this image, a large thermal is observed that is rising and extending to the top of the viewable area, similar to the vertical stream-wise plane image (bottom image, left column). This thermal features two interesting roll-up patterns where low seed density fluid appears to mix into the high seed density region and vice-versa. These patterns are likely due to high seed density fluid piercing into the thermal in a bursting process.

It was asserted that the dark regions observed in captured images were thermals and hence associated with warm fluid. It is important to note however that this assertion is based upon the visualized behaviors and not temperature measurements of the flow. While there are many devices capable of measuring air temperature within a boundary layer, few are capable of the high temporal resolution (on the order of 100Hz) required to capture the

detailed temperature field of the observed thermal-like structures and their surroundings. In the absence of such information, the thermal-like patterns reported in the present study provide a unique perspective into interesting three-dimensional thermofluid phenomena. Based on the earlier assertion and for clarity, the dark regions in the acquired images are hereinafter referred to as “thermals”.

4.4 Thermal Detection Technique

The images presented in Figure 4.2 show a contrast between the dark low seed density thermals and the well-seeded brighter regions of the background flow. To characterize the behavior of the observed thermals, it is necessary to develop a robust image processing technique to detect thermals within thousands of acquired images. The process and criterion required to perform the task of classifying objects within an image is known as image segmentation. Typically, image segmentation techniques are based on the gray-level distribution within a given image and the technique seeks to determine a gray-level threshold to segment all pixels within the image. One of the most well-known techniques to determine this threshold is Otsu’s method [20]. This method determines the threshold that minimizes the gray-level variance of the group above and below the threshold. Otsu’s method performs the best when there is a clear distinction between the gray-levels within the background and the gray-levels within the objects to be segmented, i.e. a bi-modal histogram. However, the images in the present cases, especially at low Ri , feature a uni-modal histogram and non-uniform background where there is significant gray-level overlap between thermals and high seed density fluid. This makes Otsu’s method unsuitable for thermal detection. An improved segmentation technique was developed by the present authors for thermal detection that utilized a refined form of Otsu’s method [17]. In this technique, 20 thresholds were computed from the original image histogram and each of the resulting

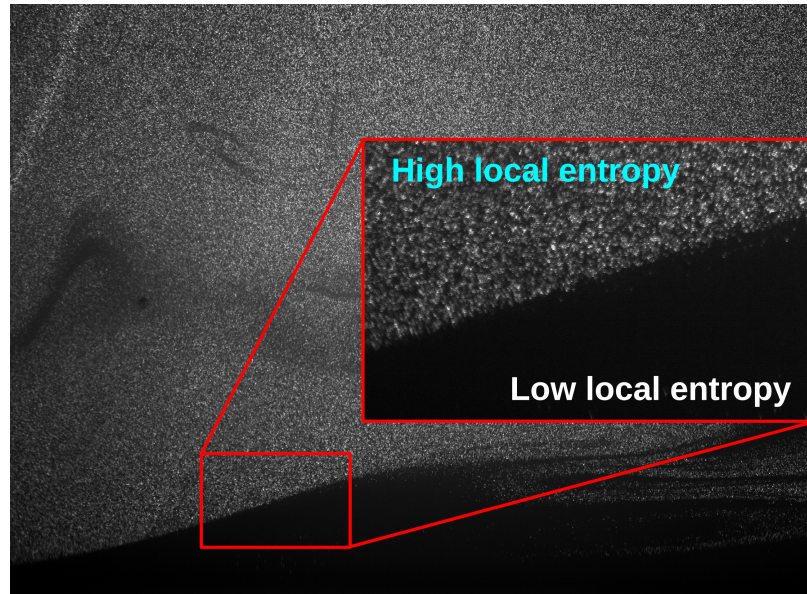


Figure 4.3: An image illustrating the thermal and the surrounding flow. Inset depicts the difference in texture, quantified by local entropy, between high seed density background flow and low seed density thermal regions.

21 segmented groups were filtered and reconstructed to detect thermals. While successful at $Ri_L > 0.3$, it failed to adequately detect thermals at low Ri due to gray-level overlap between thermals and the background.

In order to overcome the shortcomings of the previously described techniques, a more robust thermal detection technique has been developed in this study. In the developed technique, image texture is used as the segmentation criterion. The well-seeded region observed in experimental images has a different texture than the low seed density thermal region, as illustrated in the inset of Figure 4.3, where the thermal region appears “smooth” while the well-seeded region appears “rough”.

The parameter used to quantify this visual difference is the signal entropy, which defines the disorder present in a given signal [21, 22]. In image processing, the entropy (H) of an $M \times N$ image is defined based on the normalized histogram probability for the given image

$(p_{i,j})$ and is expressed in Eqn. 4.2, [22].

$$H = - \sum_{i=1}^M \sum_{j=1}^N p_{i,j} \log_2 p_{i,j} \quad (4.2)$$

This definition can also be applied to a local region within a given image generating the local image entropy. The bright, well-seeded region in the inset of Figure 4.3 contains a high local entropy while the dark thermal region has a low local entropy. The high entropy value in the bright region is due to the “rough” texture quantified by relatively large magnitude local gray level fluctuations. The low local entropy in the thermal region is caused by the more uniform gray level distribution. The difference in local entropy between thermal and non-thermal regions is the primary segmentation criterion in the developed technique.

The steps of newly developed texture-based thermal detection technique are described in the following and sequentially illustrated in Figure 4.4. First, the local entropy in a user-specified region of interest within a given raw image is calculated (Figure 4.4a) generating the local entropy distribution (see Figure 4.4b). A Gaussian low-pass filter is then applied to the entropy image to reduce noise (see Figure 4.4c). Next, a threshold image is computed from the filtered entropy image utilizing a Gaussian weighted average filter (Figure 4.4d). The initial segmentation is then conducted pixel-by-pixel using the threshold image. In this process, a given pixel in the segmented image is set to white if the gray level of the corresponding pixel in the filtered entropy image exceeds the gray level of the corresponding pixel in the threshold image, otherwise, it is set to black. The initial segmented image is shown in Figure 4.4e. The last step is to filter any remnant noise by using a minimum area threshold to produce the final segmented image that separates thermals from the

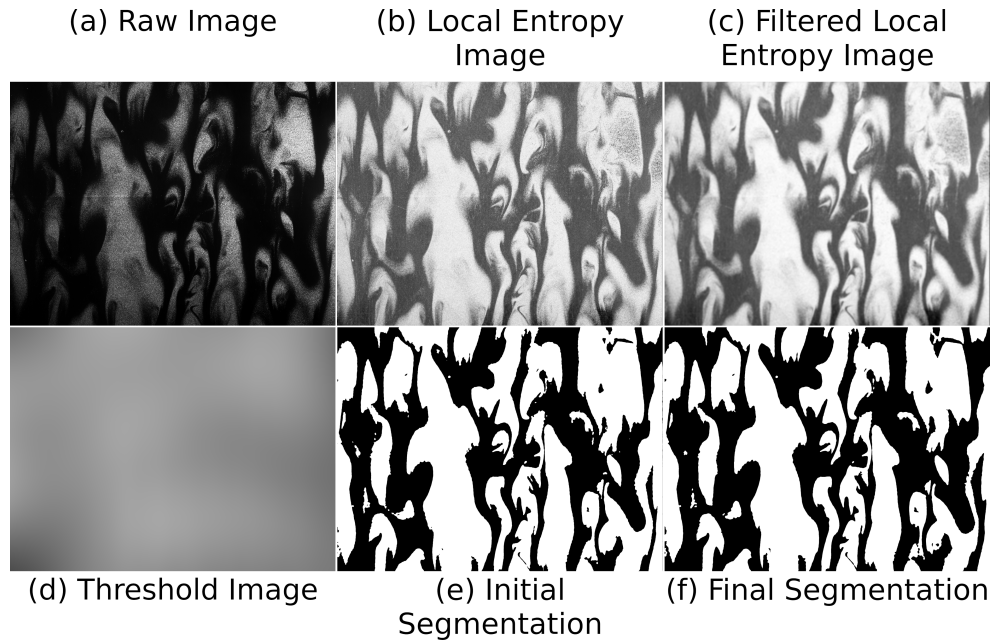


Figure 4.4: Illustration of the texture-based segmentation technique steps. Raw image is from $Ri_L = 2.0$ horizontal plane experiment, 3.5 mm above the wall.

background flow (see Figure 4.4f). In the vertical and cross plane images, detected thermal images were smoothed and nearby objects were connected together with an additional Gaussian low-pass filter and minimum area threshold.

In an implementation of the texture segmentation technique, there are multiple user-defined parameters including: the local entropy computation window (region of interest), minimum area thresholds, and the details of the respective Gaussian filters. In the present implementation, each parameter was optimized at each tested Richardson number and visualization plane to produce high-quality thermal detection. For images recorded in the vertical stream-wise plane and cross-stream plane, the local entropy window was set to 9×9 for all Ri_L . In the horizontal planes this window was also 9×9 except for $Ri_L = 1.0$ where it was 15×15 . The low-pass Gaussian filter corresponding to the step in Figure 4.4c was of size 33×33 with a standard deviation of 8 for all experiments. The Gaussian weighted average filter

used to compute the threshold image, is a low-pass 2D Gaussian filter with a size (F) and standard deviation (σ) that varied with image dimensions (S) as shown in Eqns. 4.3 and 4.4, respectively.

$$\sigma = 2 \text{ floor}\left(\frac{S}{16}\right) + 1 \quad (4.3)$$

$$F = 2 \text{ ceil}(2\sigma) + 1 \quad (4.4)$$

The output of this 2D filter was multiplied by a constant between 1.08 and 1.12 that was optimized for each tested Richardson number and visualization plane to produce high quality segmentation. This constant influences the sensitivity of the initial segmentation (see Figure 4.4e) where larger values lead to detected thermals larger than expected (i.e. over-segmentation) and smaller values produce under-segmentation. The minimum area threshold was set to 200 pixels in all experiments. For the vertical stream-wise plane and cross-stream plane, additional filtering was performed using a 61×61 Gaussian low-pass filter with a standard deviation of 15, then a secondary minimum area threshold of 1500 pixels was applied to produce the final segmentation result.

4.4.1 Verification

The performance of the proposed texture-based segmentation technique was tested against experimental images from all measurement planes covering the range of Richardson numbers. Figure 4.5 presents samples of a qualitative comparison between thermals detected by the new technique versus those visually observed in the original images. The comparison includes images from all orientations of the measurement planes at different Richardson numbers.

The cross-stream plane images (right column) show good detection of the large thermals

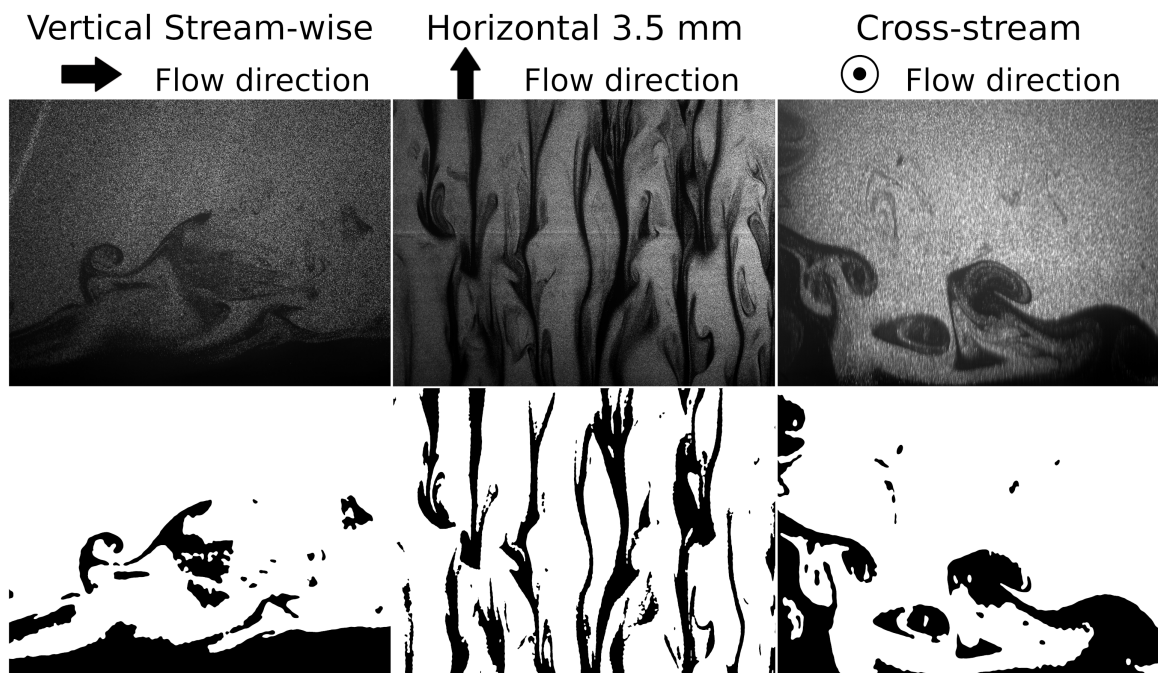


Figure 4.5: Sample images showing original images (top row) and segmented images from the thermal detection technique (bottom row). Detected thermals are shown in black in the segmented images. Vertical stream-wise plane images are from experiment performed at $Ri_L = 0.3$, horizontal plane images from $Ri_L = 1.0$, and cross-stream images from $Ri_L = 2.0$.

at $Ri_L = 2.0$. The thermal on the right was well-resolved by the new technique however, the thin band on the left side of this thermal was not detected. The free-floating thermal in the center was also captured well and shows a white band corresponding to the well-seeded region within this thermal. The left-most thermal was correctly segmented and the bursting motion of high seed density fluid was separated from the adjacent thermal. The vertical stream-wise plane case at a lower Richardson number showed that the production layer and adjacent thermal were nicely resolved. The thermal above the production layer showed some mixing with high-seed density fluid on the right side which led to a part of this region being classified as non-thermal. This demonstrates the sensitivity of the detection scheme to the local seed particle density. The horizontal plane image was from the experiment at $Ri_L = 1.0$ where there are several stream-wise oriented bands of thermals, which are captured quite well. The decrease in buoyant force relative to inertia does not appear to negatively impact segmentation quality.

The observed sensitivity to local seed particle density is due to the nature of the image entropy, which is the basis for segmentation in the developed technique. As the local entropy increases in proportion to the local gray-level variations in a given region, any change in the local seed particle density (i.e. number of bright spots in a given region) causes a detectable change in local entropy. One advantage of using image entropy, or any image texture descriptor, is a decrease in sensitivity to background non-uniformity. This is clearly visible in Figure 4.4a and Figure 4.4b where the raw image shows a clear non-uniformity in brightness within the high seed density fluid from left to right however, the local entropy image is more uniform in these regions as only the local texture was described.

The results in Figure 4.5 qualitatively demonstrate that the new texture-based thermal detection technique properly detects thermals and captures their shapes reasonably well.

However, a quantitative assessment of technique's accuracy is necessary in order to use segmented data to characterize detected thermals. For this purpose, a sample of images were randomly selected from each experiment. In each sample, thermals were detected using the following three segmentation techniques: Otsu's method, the multi-threshold technique, and the newly developed texture-based technique. The thermals in each of the sample images were also manually identified and demarcated, which served as reference to evaluate the detection accuracy of the three segmentation techniques mentioned above.

A quantitative assessment was conducted by comparing the fraction of the common area (A_C), false positive area (A_{FP}), and false negative area (A_{FN}) of each detected thermal. A given segmented reference thermal such as the one depicted in the left panel of Figure 4.6 is compared to the segmentation produced by a given algorithm, outlined in the middle pane of the figure. The common area is defined as the area of the reference thermal that is correctly detected by the given segmentation technique illustrated in the right panel of the figure. The area of a given reference thermal detected by the segmentation technique but not detected in the reference thermal was taken as the false positive area (A_{FP}). The false negative area is the area of the reference thermal not detected by the given segmentation technique (A_{FN}). Each of the computed areas (i.e. common area, false positive area, and false negative area) are normalized by the corresponding reference thermal area.

The common area, false positive area, and false negative area were computed and averaged over all reference thermals identified in flow visualization images. The thermal detection performance of each segmentation technique in the vertical stream-wise plane reported in Table 4.2.

A high performing thermal detection algorithm will maximize the mean common detection area ($\overline{A_C}$) while simultaneously minimizing the mean false positive area ($\overline{A_{FP}}$) and mean false negative area ($\overline{A_{FN}}$). From the results in the vertical stream-wise plane, Otsu's

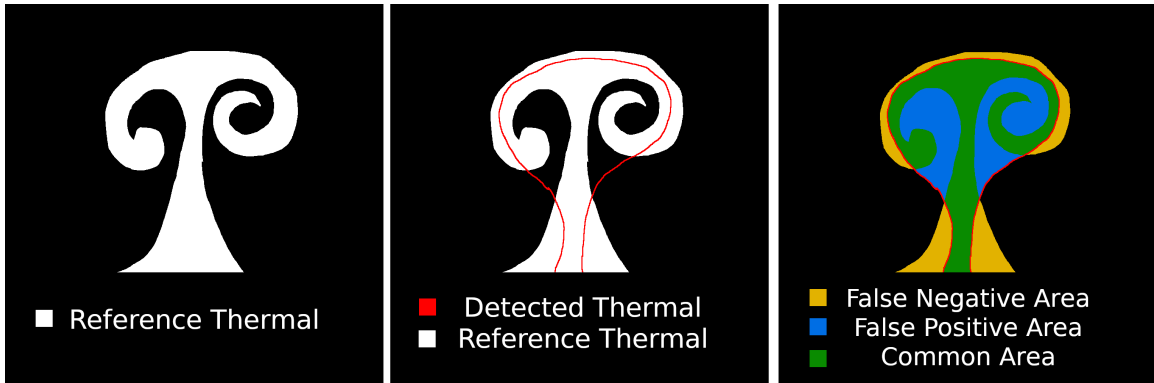


Figure 4.6: Sequence of images showing the quantities used for thermal detection verification.

Vertical Stream-Wise Plane						
	$\overline{A_C}$	$\overline{A_{FP}}$	$\overline{A_{FN}}$	$\overline{A_C}$	$\overline{A_{FP}}$	$\overline{A_{FN}}$
Ri_L	2.0	2.0	2.0	0.3	0.3	0.3
Otsu's Method	98%	577%	2%	99%	1130%	0.1%
Multi-threshold	80%	17%	20%	91%	36%	9%
Texture	79%	22%	22%	80%	27%	21%

Table 4.2: Performance of segmentation algorithms considered in the vertical stream-wise plane.

method appears to detect thermals extremely well. However, the mean false positive area provides the reason behind this high common area detection. In all tests the mean false positive area for Otsu's method exceeds 100% indicating that this technique is detecting a region much larger than any reference thermal. This is an extreme case of undesirable over-segmentation, illustrated in Figure 4.7c by the large black (thermal) regions that do not correlate well to the reference thermal image (Figure 4.7b) . The mean false negative area, an indicator of under-segmentation, agrees with this over-segmentation behavior where for Otsu's method A_{FN} is always less than 2%. Due to the poor performance of Otsu's method in all visualization planes and Richardson numbers, focus is now directed

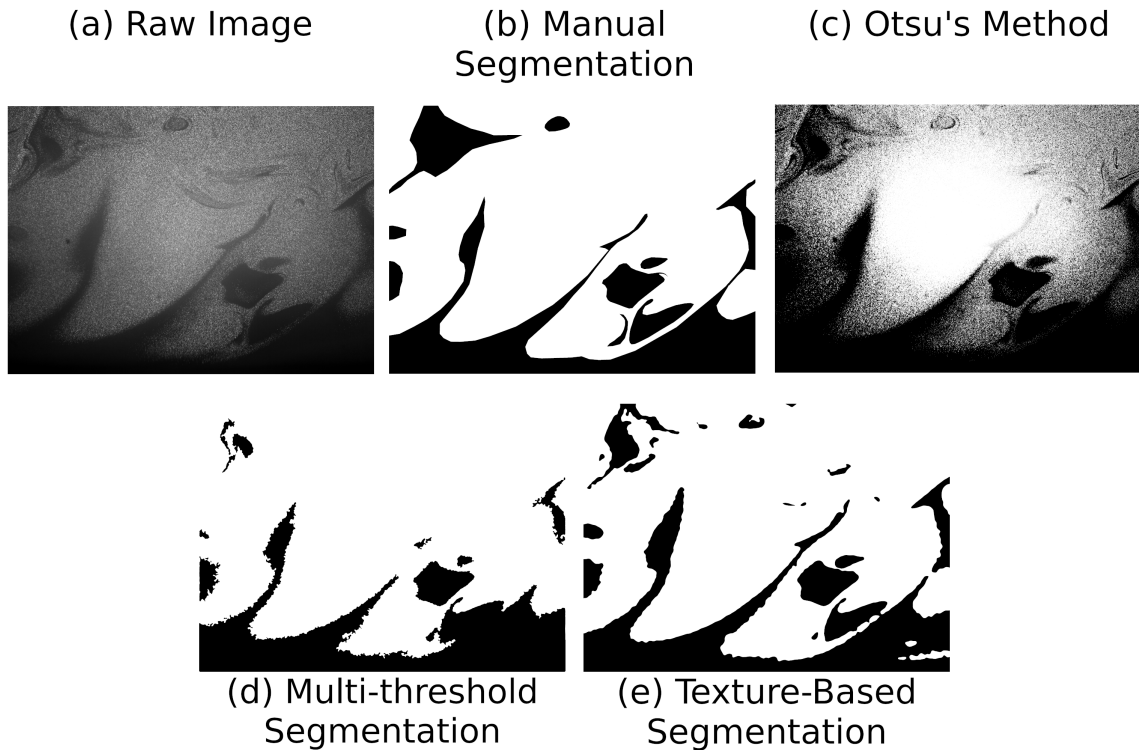


Figure 4.7: Comparison of the original image and manual segmentation to the tested thermal detection techniques. These images are from the vertical plane experiment at $Ri_L = 2.0$.

toward the multi-threshold technique and texture-based technique.

The multi-threshold and texture segmentation techniques show comparable performance in the vertical plane. The two techniques offer very similar performance at $Ri_L = 2.0$ evidenced by nearly the same $\overline{A_C}$, $\overline{A_{FP}}$, and $\overline{A_{FN}}$ results. Figure 4.7d and e provide a more qualitative comparison between the algorithms. Compared to the manual segmentation result, the multi-threshold technique captures fewer details than the texture based technique at $Ri_L = 2.0$. At $Ri_L = 0.3$, however the multi-threshold technique shows an over-segmentation behavior as $\overline{A_C}$ increases to 91% and $\overline{A_{FP}}$ increases to 36% while $\overline{A_{FN}}$ decreases to 9%. In contrast the texture-based technique shows little change in performance at $Ri_L = 0.3$.

In the horizontal plane, the texture-based segmentation technique captures thermals with $\overline{A_C}$ of 92% and 82% at $Ri_L = 2.0$ and 0.3 respectively, see Table 4.3. This is very comparable with the multi-threshold technique common detection area. The mean false positive and mean false negative results show a clear advantage for the texture-based technique where both quantities were lower or comparable to the multi-threshold technique's results. This represents an overall increase in segmentation quality when using the texture-based segmentation technique over the multi-threshold segmentation technique. The improvement in performance is visible in the left side of the images in Figure 4.8 where the original image is relatively dark due to background non-uniformity. The multi-threshold technique is sensitive to non-uniform backgrounds, evidenced by the over-segmentation (large black thermal regions) on the left side of Figure 4.8c. The texture-based technique is less sensitive to the background leading to thermal detection on the left side that more closely matches the manual segmentation.

Horizontal Plane 3.5 mm						
	$\overline{A_C}$	$\overline{A_{FP}}$	$\overline{A_{FN}}$	$\overline{A_C}$	$\overline{A_{FP}}$	$\overline{A_{FN}}$
Ri_L	2.0	2.0	2.0	0.3	0.3	0.3
Otsu's Method	99%	86%	0.2%	98%	160%	2%
Multi-threshold	96%	29%	4%	79%	21%	21%
Texture	92%	19%	8%	82%	16%	18%

Table 4.3: Performance of segmentation algorithms considered in the horizontal plane 3.5 mm above the wall.

Out of all visualization planes tested, the cross-stream plane was the most challenging for the tested detection algorithms. In the cross-stream plane, the multi-threshold technique produced $\overline{A_C}$ of 64% at $Ri_L = 2.0$ and 63% at $Ri_L = 0.3$, see Table 4.4. The multi-threshold technique detected thermals with a significant under-segmentation behavior evidenced by a large magnitude of $\overline{A_{FN}}$, about 37% at both tested Ri_L . This behavior is visible in Figure

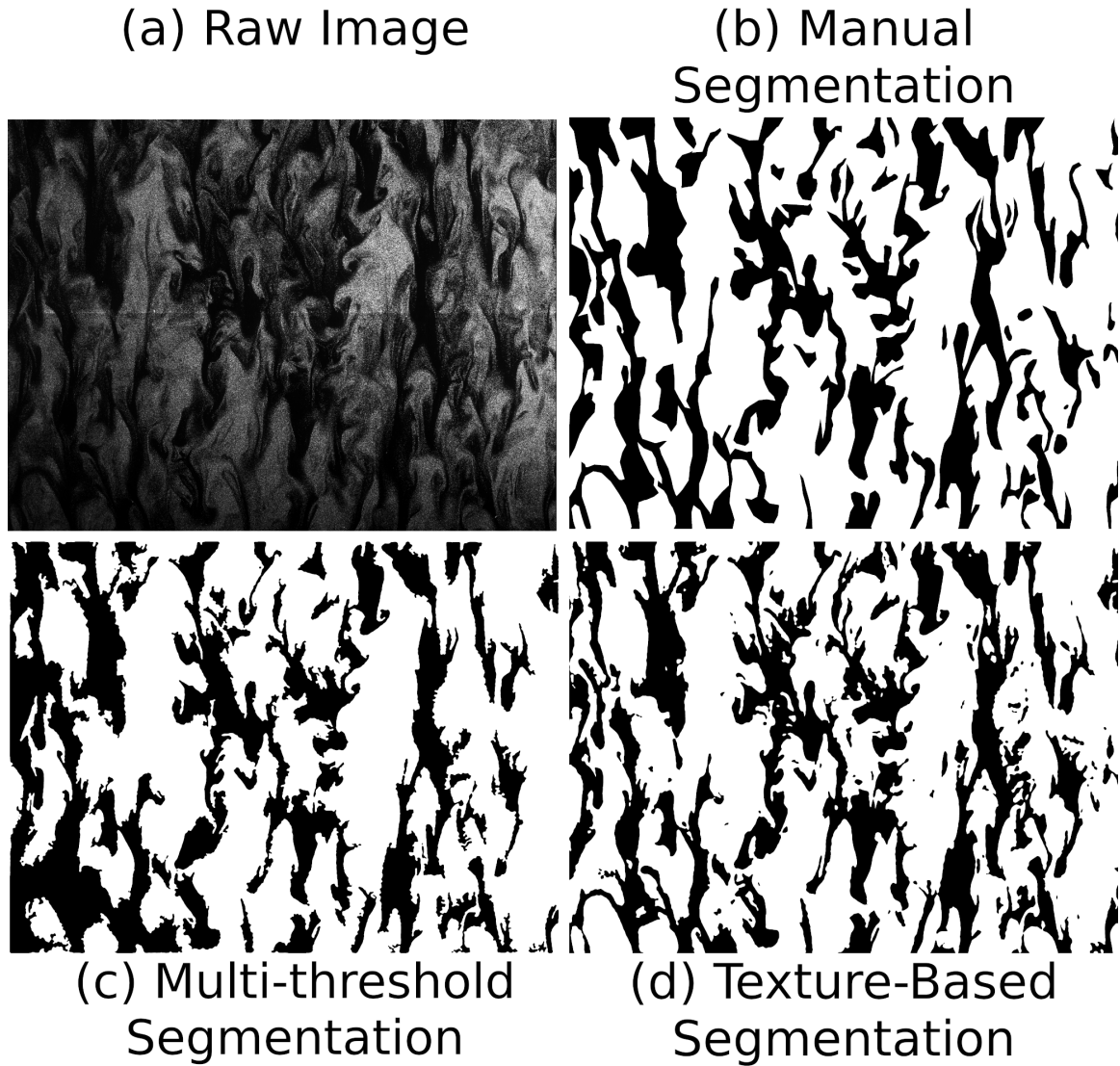


Figure 4.8: Comparison of the original image and manual segmentation to the multi-threshold and texture-based thermal detection techniques. These images are from the horizontal plane experiment at $Ri_L = 0.3$.

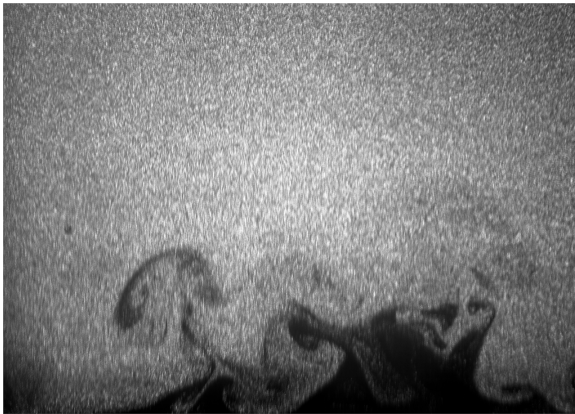
4.9c where a piece of a thermal rising through the boundary layer in the center of the image was not detected. This missed detection is likely due to relatively weak visual signature of this thermal piece. The texture-based segmentation technique performed significantly better in the cross plane where $\overline{A_C}$ was 73% and 75% at $Ri_L = 2.0$ and $Ri_L = 0.3$ respectively. The mean false positive area in both multi-threshold and texture-based techniques were comparable. The under-segmentation behavior observed in the multi-threshold technique was significantly reduced when using the texture-based technique, demonstrated by decreases in $\overline{A_{FN}}$.

Cross Plane						
	$\overline{A_C}$	$\overline{A_{FP}}$	$\overline{A_{FN}}$	$\overline{A_C}$	$\overline{A_{FP}}$	$\overline{A_{FN}}$
Ri_L	2.0	2.0	2.0	0.3	0.3	0.3
Otsu's Method	94%	249%	6%	98%	573%	1%
Multi-threshold	64%	6%	36%	63%	12%	38%
Texture	73%	11%	27%	75%	12%	25%

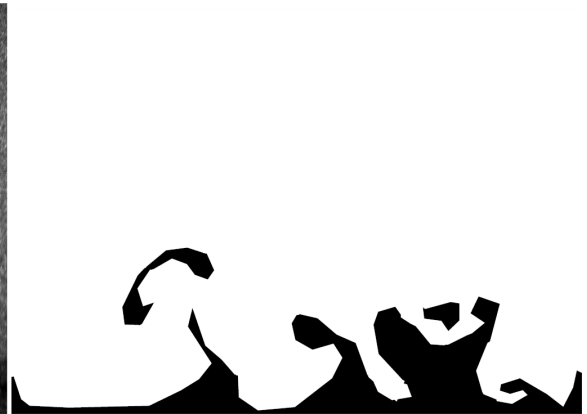
Table 4.4: Performance of segmentation algorithms considered in the cross stream plane.

The texture-based segmentation algorithm utilizes image texture, quantified by the local entropy distribution to detect thermals from PIV-style images. This technique provided the best thermal detection performance, consistently detecting thermals in all visualization planes and all tested Ri . Otsu's method was found to produce strong undesirable over-segmentation. The multi-threshold technique, an advanced form of Otsu's method, showed strong performance however it is ineffective in images with non-uniform backgrounds and weak thermal signatures. The texture-based technique offers the best performance that most closely matches a manual segmentation, making it suitable for automatic thermal detection.

(a) Raw Image



(b) Manual Segmentation



(c) Multi-threshold Segmentation



(d) Texture-Based Segmentation



Figure 4.9: Comparison of the original image and manual segmentation to the multi-threshold and texture-based thermal detection techniques. These images are from the cross plane experiment at $Ri_L = 0.3$.

4.5 Characterization of Thermal Behaviors

In the experimental images presented in Figure 4.2, thermals appeared to change their size and spatial distribution as the Richardson number varied. To provide quantitative insight into these observed trends, the texture-based thermal detection algorithm was used to detect thermals in the image dataset acquired at each case. From the image of detected thermals, the size and spatial distribution of thermals were computed. Detected thermal images were sampled such that any given thermal did not appear twice in consecutive images, ensuring statistical independence of detected thermals and minimizing bias error.

The size distribution of thermals is quantified using the thermal area coverage (C_T) defined as the ratio of the total area of all detected thermals in a given frame (A_T) to the field of view area (A_F), see Eq. 4.5. The thermal area coverage was averaged over all recorded images generating the mean thermal area coverage ($\overline{C_T}$) at a given Richardson number. Figure 4.10 contains the variation of ($\overline{C_T}$) with Ri_L in all measurement planes considered.

$$C_T = \frac{A_T}{A_F} \quad (4.5)$$

The thermal area coverage was found to generally increase with Richardson number. Relative to the vertical stream-wise and cross-stream planes, in the two horizontal planes, the magnitude of $\overline{C_T}$ was larger by a factor of at least 2 for all Ri_L considered. In the cross-stream and vertical stream-wise planes, $\overline{C_T}$ was about 0.05 at $Ri_L = 0.03$ then increased to just under 0.1 for $Ri_L = 0.3$. At a Richardson number of unity, a decrease in $\overline{C_T}$ was found before the thermal area coverage increased again at $Ri_L = 2.0$. The two considered horizontal planes demonstrated the same behavior with thermal area coverage starting at approximately 0.25 at low Ri_L before increasing up to 0.35 at $Ri_L = 0.3$ then increasing

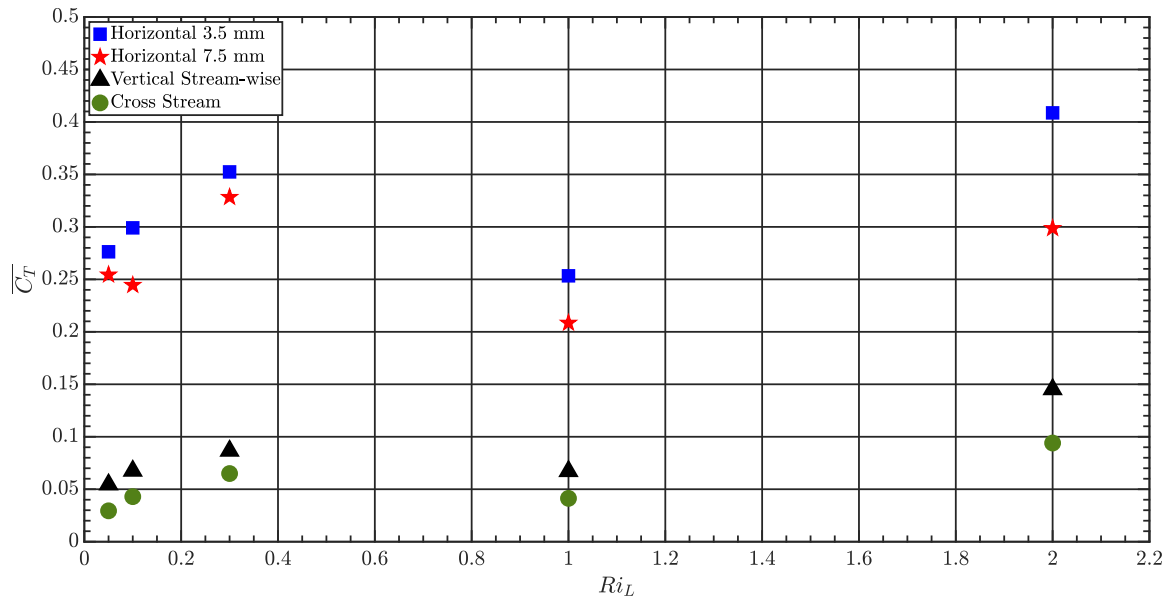


Figure 4.10: Mean thermal area coverage ($\overline{C_T}$) versus Richardson number for all measurement planes.

further to over 0.4 at $y = 3.5$ mm and decreasing slightly to 0.3 at $y = 7.5$ mm. A clear decrease in $\overline{C_T}$ in both horizontal planes was found at $Ri_L = 1.0$ as with the other two measurement planes. This decrease in thermal area coverage is most likely due to the decrease in buoyant force magnitude due the lower wall temperature used to achieve this Richardson number compared to the other tested Richardson numbers. That is, at all other cases the wall temperature was kept at 90°C (i.e. a similar Grashof number), while the Reynolds number was varied by changing the wind speed to achieve the desired Richardson numbers (see Table 1). However, between the cases of $Ri_L = 1$ and 2 , the Reynolds number was kept constant and the lower Richardson number of unity was achieved by lowering the Grashof number (see Table 1). The trend at $Ri_L = 1$ in Figure 4.10 indicates that the absolute magnitude of buoyancy force plays an important role in the formation of thermals, in addition to its magnitude relative to the inertial force.

The results in Figure 4.10 provide the estimates of fractional area coverage of thermals

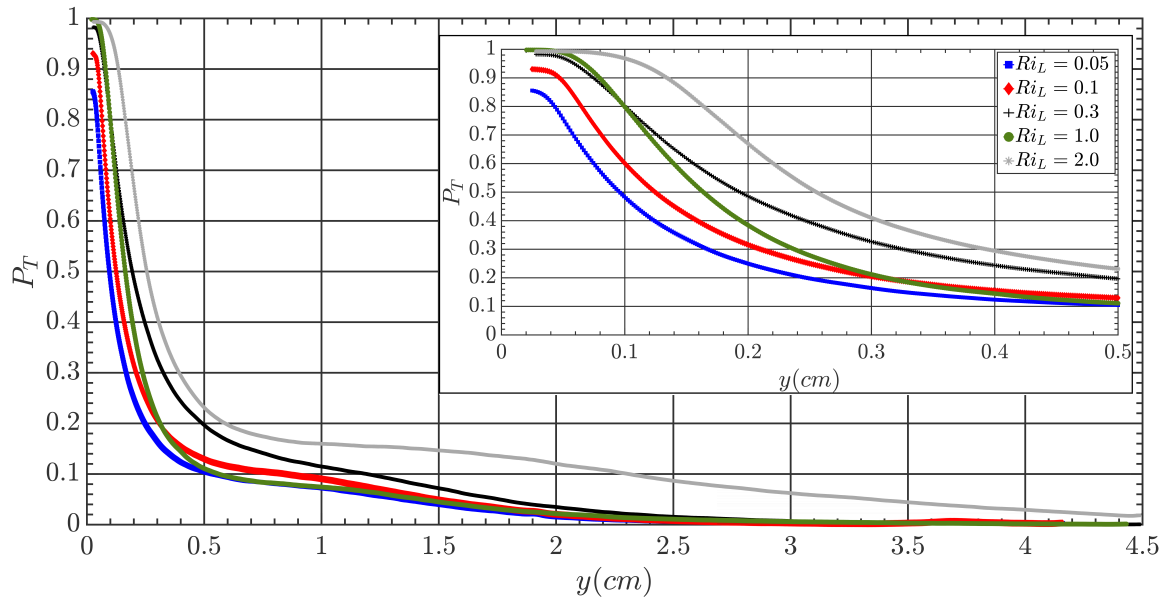


Figure 4.11: Plots of P_T versus y for all Ri_L from experiments performed in the vertical stream-wise plane. Inset contains the same profiles in a magnified view of the near-wall region.

in the overall measurement field of view. The three-dimensional spatial distribution of thermals was determined by considering each spatial location (i.e. each pixel in a given image) that corresponds to the detected thermals in a given experiment. This quantity was then spatially averaged in one direction to the given measurement plane to determine the thermals presence in the corresponding orthogonal direction. The presence of thermals is quantified as the probability of thermals' occurrence at a given spatial position (P_T). In the vertical stream-wise plane, this was calculated from the detected thermal images and spatially averaged in the x-direction providing $P_T(y)$, which characterized the average probability of thermals' occurrence at a given y -location. The results are presented in Figure 4.11 for all cases.

From the figure, each P_T curve starts at its respective maximum value close to the wall then rapidly decreases as y increases. In all profiles, P_T starts at near unity indicating a

very high chance of thermal detection in this region. However, P_T decreases relatively sharply with increases in y at all Ri_L and after $y \approx 0.5$ cm, P_T does not vary as strongly with y . The qualitative observations at $Ri_L = 2.0$, found that thermals were large and observed far away from the wall. This observation agrees with the P_T distribution at $Ri_L = 2.0$ as the curve shows the highest probability of thermals' presence throughout the measurement domain. Decreasing Ri_L shows a general decrease in P_T as there are fewer thermals and the chances of their occurrence decrease with an increase in the distance above the wall. The inset of Figure 4.11 provides more detail on the near-wall region. Here the maxima in each P_T curve generally decreases with decreasing Ri_L . The $Ri_L = 1.0$ P_T distribution features a unique behavior where the curve intersects the $Ri_L = 0.3$ P_T profile while decreasing with increasing y to follow the $Ri_L = 0.05$ and 0.1 profiles. The curve corresponding to $Ri_L = 1.0$ has nearly the same maxima as the P_T curve for $Ri_L = 0.3$ and 2.0 near the wall, but it quickly decreases and closely follows the $Ri_L \leq 0.1$ curves for $y > 0.5$ cm. The cause for this behavior is likely the lower buoyant force magnitude as discussed earlier. The trend at $Ri_L = 1.0$ indicates that although the generation of thermals in the vicinity of the heated wall is considerable but due to lower buoyant force magnitude, these thermals did not sustain themselves further away from the wall.

One unique behavior observed in the qualitative results is the presence of a thermal production layer that was observed in a majority of visualized images at high Ri_L . The transition from frequently observed production layer detections to intermittent thermal detections is the cause for the strong variations of P_T with y in the near-wall region ($y < 0.5$ cm). From the P_T profiles, the mean production layer thickness (t_p) was estimated based on the near-wall inflection point in the P_T distribution, results presented in Table 4.5.

As expected, the production layer thickness increases with Ri_L for all tested Ri_L . The 1.1 mm thick production layer at $Ri_L = 1.0$ is only slightly larger than t_p at $Ri_L = 0.3$. As

Ri_L	t_p (mm)
0.05	0.5
0.1	0.7
0.3	1.0
1.0	1.1
2.0	1.7

Table 4.5: Estimated production layer thickness from vertical stream-wise plane thermal detection probability profiles.

mentioned earlier, the lower buoyant force magnitude relative to the other tested Richardson numbers is likely the cause for this behavior.

Figure 4.12 shows the wall-normal probability distribution of detected thermals in the cross-stream plane. Please note that unavoidable illumination artifacts in some regions of the images introduced bias in the detections of thermals and hence, data from those regions are excluded from the plot. The results show that close to the wall, the probability of thermals' occurrence is high, above 0.8 for $Ri_L = 2.0$ and about 0.6 for the lower Richardson numbers. In comparison with the results in vertical stream-wise plane where $P_T > 0.8$ for all Ri_L , this suggests that the production layer does not extend uniformly in the span-wise (z) direction.

Increasing distance from the wall shows a sharp decrease in P_T , similar to the P_T distribution in the vertical stream-wise plane. The $Ri_L = 1.0$ distribution decreases more sharply with increasing y and tends to follow the P_T curves for $Ri_L \leq 0.1$, a behavior also observed in the vertical stream-wise plane. At $Ri_L = 2.0$, P_T decreases relatively weakly with y as thermals are largest and most frequently observed at this flow condition, in agreement with the qualitative assessment discussed earlier. At lower Ri_L thermals are less likely to be detected more than 2 cm away from the hot wall.

In the horizontal planes, $P_T(z)$ describes the probability of thermals' presence in the span-

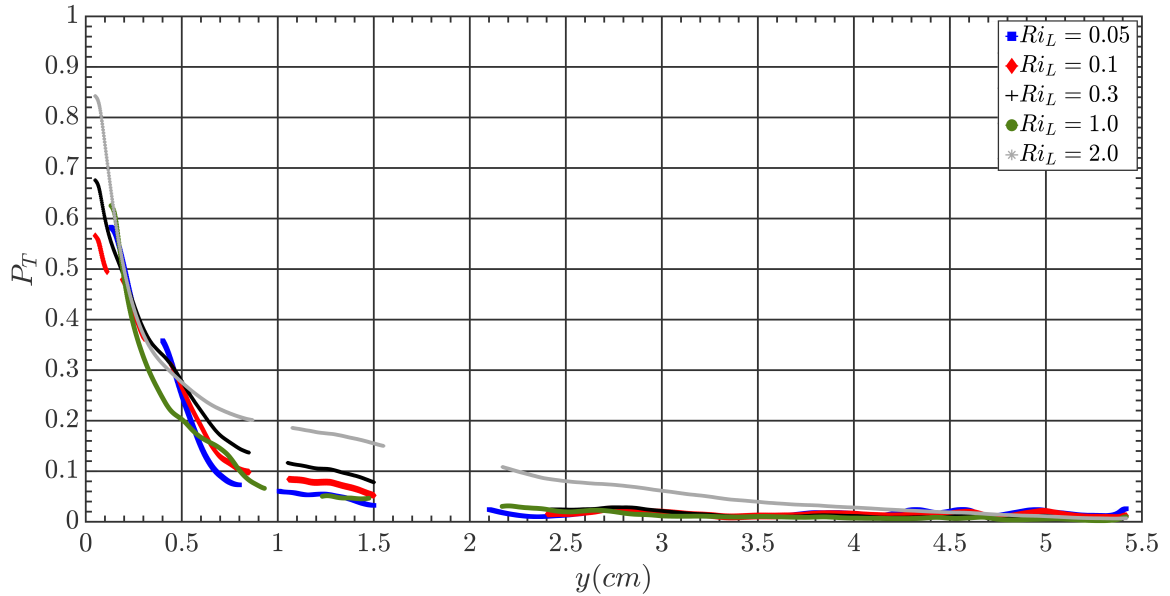
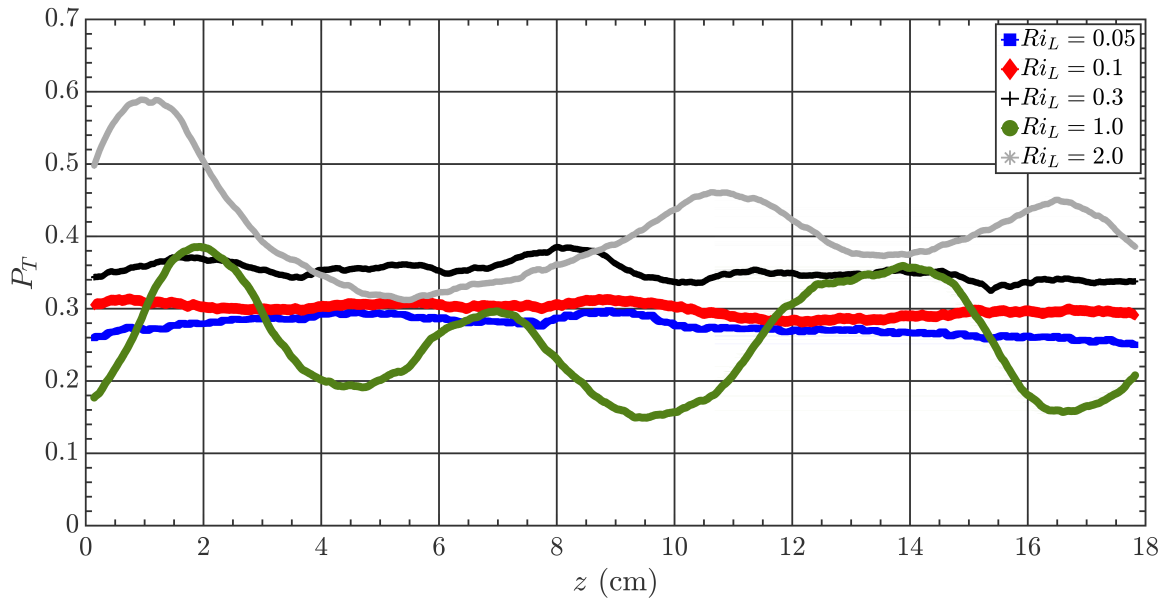


Figure 4.12: Wall-normal distribution of P_T in the cross stream plane for all Ri_L considered.

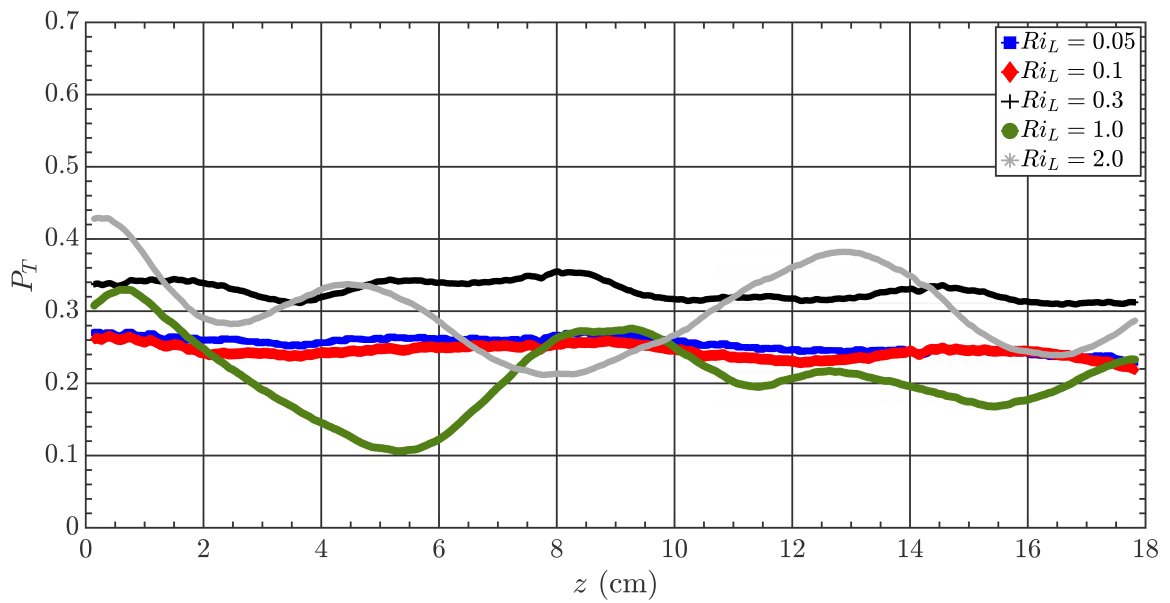
wise direction and the results are illustrated in Figure 4.13. The field of view width in this figure is smaller than the measurement field of view width to exclude the detection bias due to illumination artifacts present near the right end of the measurement field of view. The P_T distribution in the horizontal plane at $y = 3.5$ mm (Figure 4.13a) shows a periodic behavior with relatively large amplitude at higher Richardson numbers ($Ri_L \geq 1.0$). This shows that detected thermals have a propensity towards orientation in the stream-wise mean flow direction, as $P_T(z)$ is averaged in the stream-wise direction and preferentially formed rows distributed across the span of the boundary layer. The visualized images qualitatively show this trend (see Figure 4.2 and Figure 4.5). The results however, does not show any phase consistency in the span-wise peaks and valleys between the P_T curves at $Ri_L = 1.0$ and 2.0 . At Ri_L values less than unity, the P_T distributions are relatively flat and contain no clear periodic behavior. This suggests that detected thermals are distributed more uniformly in the span-wise direction (see Figure 4.2). The cause of this behavior is likely the strong turbulent mixing acting to deform and redistribute thermals.

At higher Richardson numbers, the buoyant force magnitude seems to be large enough to resist turbulent mixing leading to the observed span-wise thermal self-organization. Note that the height of $y = 3.5$ mm in the unheated boundary layer, corresponds to $y_{noheat}^+ \approx 15$ which is located slightly above the mean thermal production layer at $Ri_L \geq 1.0$, $y = 1 - 2$ mm (see Table 4.5). One possible explanation of this span-wise behavior is that buoyant fluid is released from the local production layer producing the peaks in the span-wise P_T distribution while, due to mass conservation, relatively cooler fluid travels downward in replenishing motions corresponding to the valleys in P_T . This leads to alternating regions of rising and falling fluid resembling convective cells organized in the span-wise direction across the boundary layer. Due to the very weak near wall turbulence in the lower buffer layer and viscous sublayer of the hydrodynamic boundary layer, this buoyancy driven motion is locally dominant. At low Richardson numbers, ($Ri_L \leq 0.3$), however, stronger turbulent boundary layer mixing breaks apart self-organizing buoyancy driven motion as $y = 3.5$ mm is located in the upper buffer layer and lower logarithmic layer ($y_{noheat}^+ \approx 30$ to 70) depending on the Richardson number.

In the horizontal plane at 7.5 mm above the wall, the $P_T(z)$ distribution (Figure 4.13b) shows similar behavior as to that observed at $y = 3.5$ mm although the overall probability of thermals' occurrence slightly decreased, which is expected. At high Richardson numbers ($Ri_L \geq 1.0$), large amplitude oscillations are still present indicating a similar physical process is occurring. The standard deviation of P_T at $Ri_L \geq 1.0$ and $y = 7.5$ mm is approximately 20% smaller than the standard deviation of P_T at $y = 3.5$ mm, indicating that the span-wise variations of P_T are smaller at a greater distance from the wall. This is an expected behavior as stronger turbulent mixing is present in the upper buffer layer ($y_{noheat}^+ \approx 40$). The profiles of P_T at lower Richardson numbers ($Ri_L \leq 0.3$) are relatively flat and show a behavior similar to that at $y = 3.5$ mm.



(a)



(b)

Figure 4.13: Plots of P_T versus z for all Ri_L from experiments performed in the (a) $y = 3.5$ mm and (b) $y = 7.5$ mm horizontal plane.

4.5.1 Thermal Motion

In the present study, PIV was used to visualize the heated boundary layer flow structure. The PIV technique acquires images in the form of image pairs where the time difference between the two images is short enough to capture the spatial shift in the seed particles' motion. In the current case, due to the presence of thermal signatures in PIV dataset, the image pairs also captured the spatial movement of thermals. Hence, this aspect was exploited to compute the advection velocity of thermals. It should be noted that this is a non-trivial task since thermals have been observed in a wide variety of complex and irregular geometries over the range of Richardson numbers considered. Two such complex flow patterns are the roll-up signatures likely associated with Kelvin-Helmholtz instability most frequently observed in the vertical stream-wise plane and the mushroom slice shaped rising thermal pattern often observed in the cross-stream plane (see Figure 4.2). The shape of thermals varies significantly in time as the thermals are influenced by dynamical phenomena in their surroundings. However, for the very short time between each image in a given PIV image pair, on the order of $100 \mu\text{s}$, thermals have a limited shape change allowing for local instantaneous velocity computation. From the visualized thermal images captured in the present study, a preliminary approximation of the velocity magnitude associated with thermal roll-up signatures and rising thermal signatures was computed from a sample of PIV image pairs at $Ri_L = 2.0$. To the best of authors' knowledge, this is the first reported approximation of thermal's advection velocity in a mixed convection turbulent boundary flow in the scientific literature. Due to the inherent complexity of the problem only a basic velocity magnitude estimate is assessed, and the readers are expected to treat it as a first-order approximation.

For roll-up signatures that are expected to feature both rotational and translational motion, only the translational velocity was estimated. Rising thermal patterns often feature one

or more roll-ups on both sides of a central stem. Only translational velocity at the top of these rising thermals was approximated in this investigation. The velocities of both roll-up signatures and rising thermal signatures were estimated by first manually identifying and isolating each thermal signature from a pair of corresponding images as shown in the top row of Figure 4.14. The texture-based thermal detection technique was then applied to each image in the image pair. This generated two black and white binary images of the detected thermal signature, each corresponding to an original image in the pair. The centroid of each detected thermal was computed next. The translational motion of the detected thermal was then calculated as the displacement of each detected thermal's centroid. The bottom row of Figure 4.14 illustrates the observed translational motion of the detected thermal signatures. The black line corresponds to the outline of the detected thermal in the first frame of the pair and the red line corresponds to the detected thermal outline in the second frame.

From the above figure, the detected thermals do show some shape change, which influences the location of thermal's centroid and hence, introduces uncertainty in the velocity estimation. To quantify this influence, the detected centroid of the thermal in the first binary image was shifted towards the detected thermal centroid in the second binary image of the pair based on the computed displacement from the two images. The two thermal centroids, one based on the actual thermal shape in the second binary image and the other based on the translational shift of the centroid from the first binary image were then compared. Any discrepancy between these two centroids can be attributed to non-translational motion, including shape changes, in the detected thermals. The testing was conducted for at least 10 samples and it was found that this discrepancy produced a mean velocity magnitude uncertainty of ± 12.5 cm/s in the vertical stream-wise plane and ± 2.5 cm/s in the cross-stream plane.

The approximate thermal velocity magnitude was then computed from the detected ther-

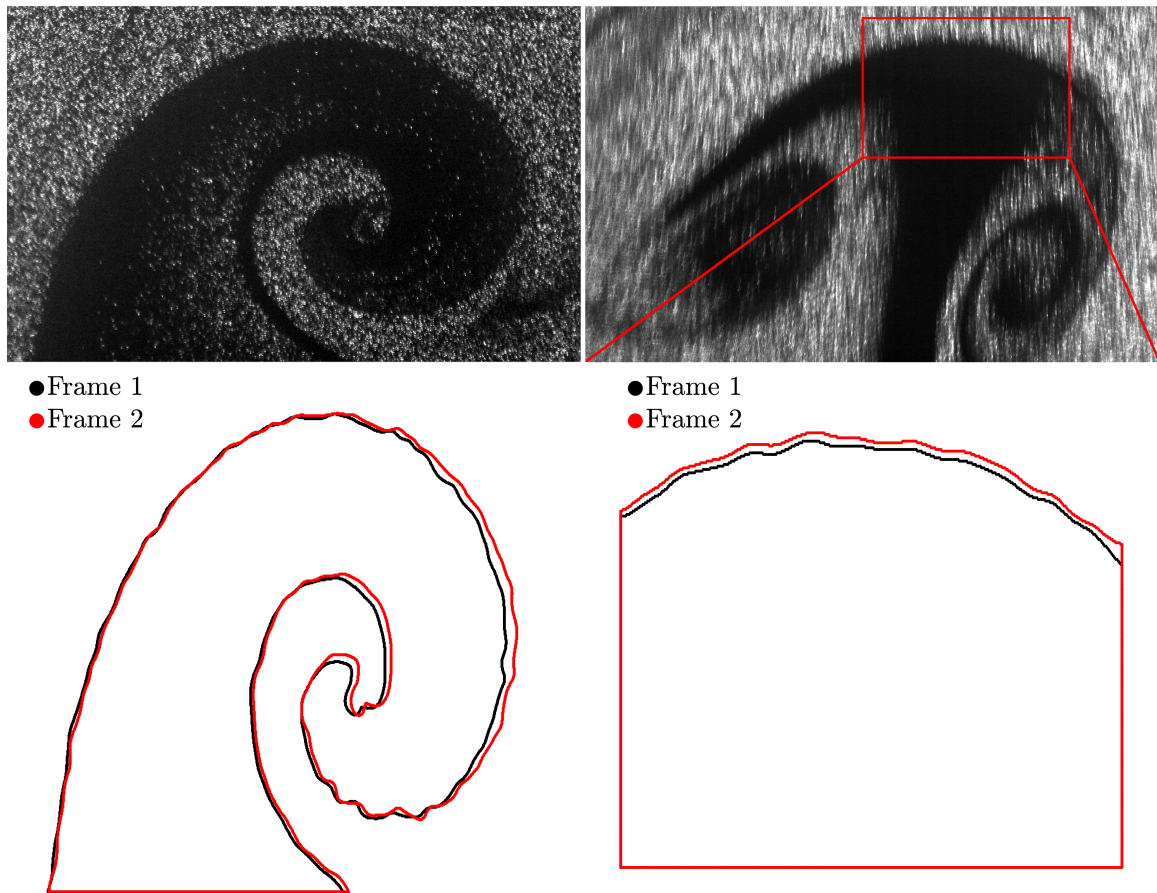
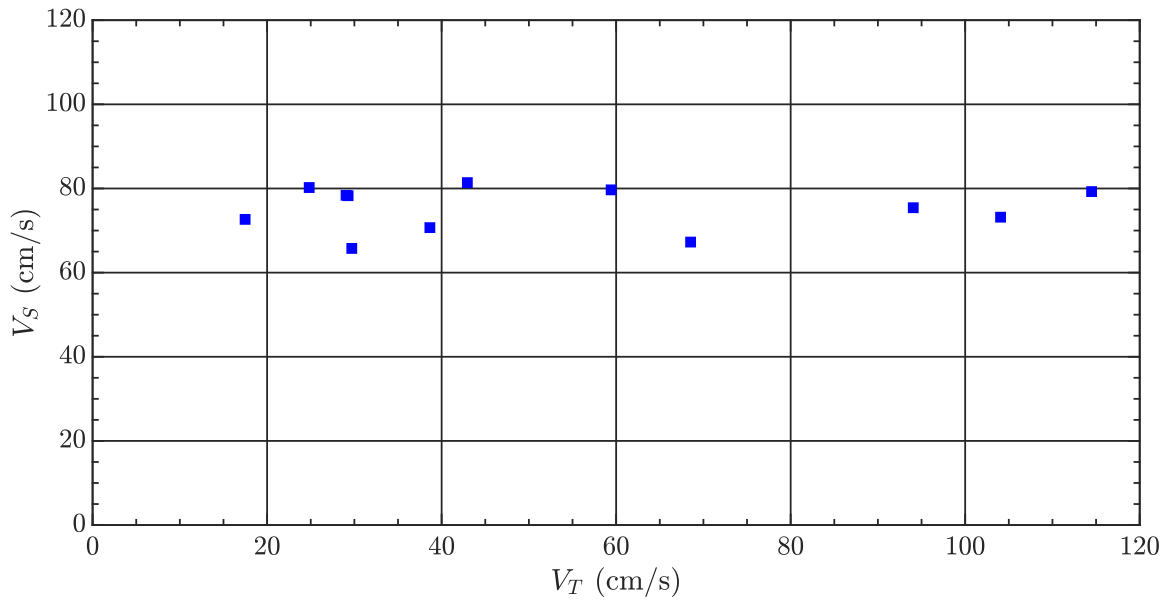


Figure 4.14: Top row: Region of interest for velocity estimation in the original images of (left) roll-up signature in the vertical stream-wise plane and (right) rising thermal signature in the cross-stream plane. Bottom row: Detected thermal boundaries for each frame in the corresponding image pairs.

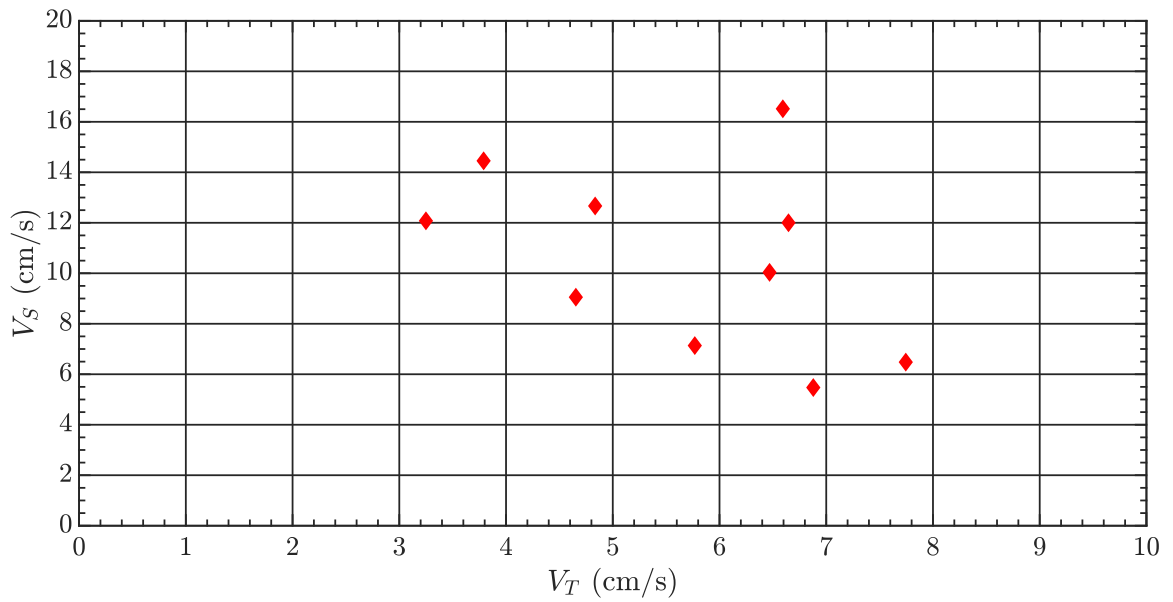
mal centroid displacement using the time between frames in the captured image pair. The instantaneous velocity field in the high-seed density non-thermal region of a given image pair was also computed using an in-house PIV code that utilized a 48×48 pixel square interrogation window for the cross-correlation corresponding to a 96×96 pixel search window. The instantaneous velocity field in the region surrounding of each detected thermal was extracted from the computed PIV data and spatially-averaged. The relationship between the estimated thermal advection resultant velocity magnitude (V_T) and the surrounding spatially-averaged instantaneous resultant velocity magnitude (V_S) is presented in Figure 4.15.

The distribution of V_S versus V_T for roll-up signatures in the vertical stream-wise plane at $Ri_L = 2.0$ (Figure 4.15a) shows a wide range of approximate detected thermal velocities between about 20 cm/s to 120 cm/s, while the corresponding surrounding instantaneous velocity magnitude was in a relatively narrow range between 60 cm/s and 80 cm/s. This indicates that the roll-up signatures in the thermals can travel at velocities substantially different from their immediate surroundings. This implies that the detected roll-ups are not simply advected by the local boundary layer flow but rather these phenomena can exhibit their own unique motion.

The shape change in detected thermal signatures provides evidence that the detected thermals evolve on a time-scale comparable to the surrounding boundary layer flow. Thermal motion is observable over the 100 microsecond-scale time between consecutive PIV images in a pair. The fluid inside a detected thermal away from the edges is likely to influence bulk motion in addition to shape changes and exhibit their own unique velocity. While fluid inside a thermal cannot be directly analyzed with the techniques discussed in this study, these rough velocity estimates suggest that detected roll-up signatures are fast-moving and active participants in heated turbulent boundary layer dynamics.



(a)



(b)

Figure 4.15: Estimated thermal velocity magnitude (V_T) versus the spatially-averaged surrounding velocity magnitude (V_S) at $Ri_L = 2.0$ for (a) roll-up signatures in the vertical stream-wise plane and (b) rising thermals in the cross-stream plane.

The rising thermal signatures detected in the cross-stream plane at $Ri_L = 2.0$ were found to have an estimated velocity magnitude between 3 cm/s and 8 cm/s (see Figure 4.15b) while, the surrounding flow has a velocity magnitude from 5 cm/s to 17 cm/s. Similar to the roll-up thermal signatures, the velocity of rising thermals is in some instances is found to be substantially different from the local instantaneous velocity magnitude. Due to the unique perspective offered by the cross-plane, this estimated velocity difference between detected thermals and local instantaneous velocity is associated with wall-normal and span-wise velocities (i.e. v and w) only. From the graph, it appears that the detected rising thermals generally have a smaller estimated velocity magnitude than their respective surroundings. This is consistent with the perspective that the thermals detected in the cross-plane are not passive followers of turbulent boundary layer phenomena.

4.6 Conclusion

This research study performed PIV-styled visualization of heated turbulent boundary layer flow. Images captured in multiple planes with respect to the mean flow direction depicted dark, low-seed density regions close to the hot wall that are most likely thermals. These dark regions facilitated visualization and qualitative assessment of the thermal distribution where numerous key phenomena were observed such as bursting and sweeping style events, turbulent eddy patterns, and the presence of a production layer. A texture-based thermal detection technique was developed in order to automatically detect dark thermals over thousands of experimental images. From detected thermal images the thermal area coverage was estimated, which was found to increase with increasing Richardson number, as expected. The computed spatial distribution indicated that within 2 mm of the wall a production layer was observed; thermals were most frequently detected close to the wall. At high Richardson numbers, in the horizontal planes relatively closer to the wall, the

detected thermals showed clear mean flow alignment and span-wise organization. These results were used to hypothesize the presence of near-wall convective cell-like structures of alternating rising and falling fluid that drive thermals which are deformed and mixed by turbulence further away from the wall.

The detected thermal images were also utilized to generate a first-order approximation, for the first time, of the advection velocity of observed roll-ups and mushroom-slice shaped rising thermal patterns in the vertical stream-wise plane and cross-stream plane, respectively, at $Ri_L = 2.0$. While the presented results provide sufficient information to open discussion on the motion of detected thermals, it does not address the fundamental complexity of the problem in regard to fully-generalized motion tracking where rigid translation, rigid rotation, and deformation are occurring simultaneously. Results indicate that detected thermals can exhibit motion at a substantially different velocity from the surrounding fluid. It is likely that the internal thermal structure driving the observed motion is a highly active region of dynamic fluid phenomena.

Bibliography

- [1] V.B. Omubo-Pepple, C. Israel-Cookey, and G.I. Alaminokuma, “Effects of Temperature, Solar Flux and Relative Humidity on the Efficient Conversion of Solar Energy to Electricity,” *European Journal of Scientific Research*, vol. 35, no. 2, pp. 173–180, 2009.
- [2] S. Pal, M. Lopez, M. Schmidt, M. Ramonet, F. Gilbert, I. Xueref-Remy, and P. Cialis, “Investigation of the atmospheric boundary layer depth variability and its impact on the ^{222}Rn concentration at a rural site in France,” *Journal of Geophysical Research*, vol. 120, pp. 623–643, 2015.
- [3] S. Brand, “The Effects on a Tropical Cyclone of Cooler Surface Waters due to Upwelling and Mixing Produced by a Prior Tropical Cyclone,” *Journal of Applied Meteorology*, vol. 10, pp. 865–874, 1971.
- [4] W.M. Gray, “The Formation of Tropical Cyclones,” *Meteorology and Atmospheric Physics*, vol. 67, pp. 37–69, 1998.
- [5] G. Solari, “The New Culture of the Wind and Its Effects,” *Wind Science and Engineering*, pp. 169–271, 2019.
- [6] J. Turner, *Buoyancy Effects in Fluids*. Cambridge, UK: Cambridge University Press, 1973.

- [7] C.I.H. Nicholl, "Some dynamical effects on a turbulent boundary layer," *Journal of Fluid Mechanics*, vol. 40, no. 2, pp. 361–384, 1970.
- [8] A. Elatar, and K. Siddiqui, "The influence of bottom wall heating on the mean and turbulent flow behavior in the near wall region during mixed convection," *International Journal of Thermal Sciences*, vol. 77, pp. 233–243, 2014.
- [9] J.R. Maughan, and F.P. Incropera, "Secondary flow in horizontal channels heated from below," *Experiments in Fluids*, vol. 5, pp. 334–343, 1987.
- [10] P. Davidson, *Turbulence: An Introduction for Scientists and Engineers*. Oxford, UK: Oxford University Press, 2nd ed., 2015.
- [11] R.R. Gilpin, H. Imura, and K.C. Cheng, "Experiments on the Onset of Longitudinal Vortices in Horizontal Blasius Flow Heated from Below," *Journal of Heat Transfer*, vol. 100, pp. 71–77, 1978.
- [12] H. Imura., R.R. Gilpin, and K.C. Cheng, "An Experimental Investigation of Heat Transfer and Buoyancy Induced Transition from Laminar Forced Convection to Turbulent Free Convection over a Horizontal Isothermally Heated Plate," *Journal of Heat Transfer*, vol. 100, pp. 429–434, 1978.
- [13] G. Araya and L. Castillo, "DNS of turbulent thermal boundary layers up to $Re = 2300$," *International Journal of Heat and Mass Transfer*, vol. 55, pp. 4003–4019, 2012.
- [14] X. Wu, and P. Moin, "Transitional and turbulent boundary layer with heat transfer," *Physics of Fluids*, vol. 22, p. 8, 2010.
- [15] H. Hattori, T. Houra, and Y. Nagano, "Direct numerical simulation of stable and unstable turbulent thermal boundary layers," *International Journal of Heat and Fluid*

- Flow*, vol. 28, pp. 1262–1271, 2007.
- [16] D. Li, K. Luo, and J. Fan, “Buoyancy effects in an unstably stratified turbulent boundary layer flow,” *Physics of Fluids*, vol. 29, p. 17, 2017.
- [17] K. Dennis and K. Siddiqui, *Characterization of Thermals in a Heated Turbulent Boundary Layer*. ASME-JSME-KSME Joint Fluids Engineering Conference. San Francisco, USA, 2019.
- [18] E.M. Sparrow, R.B. Husar, and R.J. Goldstein, “Observations and other characteristics of thermals,” *Journal of Fluid Mechanics*, vol. 41, no. 4, pp. 793–800, 1970.
- [19] K. Dennis and K. Siddiqui, *Multi-Plane Characterization of the Turbulent Boundary Layer*. 5th Joint US-European Fluids Engineering Summer Conference. Montreal, Canada, 2018.
- [20] N. Otsu, “A Threshold Selection Method from Gray-Level Histograms,” *IEEE Transactions on Systems, Man, and Cybernetics*, vol. 9, no. 1, 1979.
- [21] C.E. Shannon, “A Mathematical Theory of Communication,” *The Bell System Technical Journal*, vol. 27, pp. 379–423, 623–656, 1948.
- [22] R.M. Haralick, K. Shanmugam, and I. Dinstein, “Textural Features for Image Classification,” *IEEE Transactions on Systems, Man, and Cybernetics*, vol. 3, no. 6, pp. 610–621, 1973.

Chapter 5

The Influence of Unstable Thermal Stratification on Near-Wall Turbulent Boundary Layer Characteristics

5.1 Introduction

The behavior of numerous engineering systems and environmental phenomena are influenced by the transport of heat, momentum, and constituent species through the hydrodynamic and thermal boundary layers. The exchange of these quantities between bulk fluid and solid wall is known to strongly influence several engineering parameters including the induced friction drag, and heat and mass transfer rates. Often, it is desirable to optimize these parameters in engineering systems and predictive models. In environmental engineering, momentum and mass transport in the atmospheric boundary layer is known to govern the distribution of greenhouse gases, pollution dispersion as well as the wind loading on structures [1, 2]. The performance of power generation systems, such as emerging pho-

photovoltaic (PV) panels whose electrical conversion efficiency decreases above a given temperature, is strongly influenced by the heat transport through the boundary layer between bulk fluid and the PV panel surface [3]. To facilitate the proper operation of existing and emerging engineering systems, and the advancement of current scientific knowledge on environmental phenomena, it is of interest to improve the present understanding of boundary layer dynamics.

The boundary layer encountered in a majority of engineering and environmental applications is turbulent in nature and characterized by highly three-dimensional motion and complex dissipative phenomena. The hydrodynamic turbulent boundary layer consists of multiple layers. The inner region contains the viscous sub-layer, buffer layer, and logarithmic layer and the dynamics of the inner region are known to heavily influence bulk transport [4–6]. In this region, the unstable interactions between flow inertia and the viscous shear force generate numerous unique turbulent phenomena and structures [7–9]. The characteristics, dynamics, and governing mechanisms of these phenomena has been a highly active area of research [10–12]. Many practical applications of boundary layer flow involve heat transfer from the solid wall. In this configuration, the buoyant force contributes to overall flow dynamics, and heat transfer greatly increases the difficulty of flow characterization due to non-linear coupling of the thermofluid variables. The relative magnitude of the buoyant force to flow inertia is quantified using the bulk Richardson number (Ri_L) as defined in Eq.5.1 where g is gravitational acceleration, L is a characteristic length scale, β is the volumetric coefficient of thermal expansion, ΔT is the temperature difference between bulk fluid and solid wall, and U is the free-stream velocity [13].

$$Ri_L = \frac{Gr_L}{Re_L^2} = \frac{gL\beta\Delta T}{U^2} \quad (5.1)$$

The Richardson number defines three key cases of thermofluid interaction. When the mean inertia-driven flow is weak, i.e. $Ri_L \gg 1$, the buoyant force dominates leading to natural convection. The strong buoyant force leads to the formation of so-called thermals, which are parcels of warm fluid that originate in the vicinity of the heated wall and rise in the fluid domain. In contrast, forced convection occurs when inertia is much stronger than the buoyant force, i.e. $Ri_L \ll 1$. Mixed convection flow is a unique state where the buoyant force and flow inertia are of comparable magnitudes making $Ri_L \sim 1$. The structure and dynamics of mixed convection boundary layer flow are governed by the interaction between flow inertia and the buoyant force. Often in the literature, the Richardson number is defined in the context of “stable” and “unstable” stratification. This refers to an alternative formulation of Ri where $Ri > 0$ describes stable thermal stratification, where the positive density gradient vector (i.e. direction of increasing density) is aligned with the gravitational force. This places lower density fluid above higher density fluid, often encountered when fluid passes over a relatively cool surface. In contrast, $Ri < 0$ describes unstable thermal stratification. In this context, the positive density gradient vector is in the opposite direction of the gravitational force (i.e. high density fluid above low density fluid) in an unstable state.

The mixed convection boundary layer flow structure has been studied experimentally in a channel configuration where thermals were observed while being advected by the mean flow [14, 15]. One study reported an earlier than anticipated laminar to turbulent transition in the presence of wall heating [16]. Computational research on the characteristics of the heated turbulent boundary layer often excludes the effect of buoyancy by treating temperature as a passive scalar [17, 18]. While this approach is valid for some forced convection flows, it is not suitable for mixed convection due to the coupling between thermofluid variables. The heat transfer rate, skin friction coefficient, and turbulent intensity have all been experimentally investigated in stably stratified boundary layers utilizing hot-

wire probes [19]. The magnitudes of turbulent parameters were reported to decrease as stable thermal stratification increases [19]. This is attributed to the utilization of turbulent energy in working against buoyancy forces [13]. Recently, two DNS-based research studies investigated the heated turbulent boundary layer in unstable thermal stratification over a flat plate at $Ri_\theta = 0.01$, where θ is the momentum thickness, and included the influence of the buoyant force [20, 21]. One study documented an increase in turbulent stresses while both studies reported the modification of turbulent coherent structures where logarithmic layer structures were lifted away from the wall. A larger number of near-wall streak structures were also reported to be present above a heated wall [20, 21]. It was proposed that buoyancy increases the wall-normal turbulent velocity component leading to an increase in the Reynolds shear stress and wall-normal turbulent heat flux [20]. The present author experimentally characterized heated turbulent boundary layer structure over a range of Richardson numbers between $Ri_L = 0.05$ and $Ri_L = 2.0$ in chapter 4. Thermals were observed to rise through the boundary layer and participate in complex turbulent interactions with the inertia-driven boundary layer flow. A method of detecting thermals was developed and applied to experimental images to detect and characterize thermals, however the turbulent statistics in the boundary layer flow was not the focus of that study.

In the current state of knowledge, the behavior of turbulent boundary layer flow over a smooth horizontal flat plate in the absence of wall heating is well-known as is the behavior of natural convection over a heated horizontal wall. In unstable stratified mixed convection turbulent boundary layer flow however, the present understanding is quite limited. The current knowledge on this flow is primarily based on a limited number of studies. From the computational aspect, these studies neglect the buoyant force entirely or are limited to one Richardson number. From the experimental aspect, present knowledge is often based on flow visualization, bulk flow characterization, or work focused on stable stratification

within the turbulent boundary layer. There is a need for comprehensive experimental research that characterizes the modification of the three-dimensional turbulent boundary layer dynamics by wall heating during unstable thermal stratification. The present study is focused on a detailed investigation of the three-dimensional mechanisms that govern mixed convection turbulent boundary layer dynamics and characterize the modification of key turbulent parameters by wall heating.

5.2 Experimental Setup

Mixed convection turbulent boundary layer experiments were performed in a closed loop low-disturbance wind tunnel that featured a 46 cm \times 46 cm square test section that is 1.14 m long, as illustrated in Figure 5.1. A variable frequency controller allowed variation of the test section flow velocity which could reach up to 60 m/s with a background turbulence between 0.5–0.9% in the range of wind speeds 3–60 m/s previously investigated using Laser Doppler Velocimetry (LDV). This background turbulence rating was achieved via several flow conditioning screens upstream of the test section. An active cooling system was used to maintain air temperature to within ± 1 °C of room temperature.

The test section side walls were made of clear acrylic to facilitate visualization and the bottom wall was made of aluminium coated with smooth black matte vinyl to reduce light reflection. The aluminum wall was embedded with 16 T-type 36 AWG special limits of error (SLE) thermocouples (± 0.5 °C uncertainty) to measure the wall temperature. A 36 cm \times 110 cm 3080W, 240V silicone surface heater was fitted to the bottom wall to supply wall heating. The heater was controlled by a PID controller (Zesta Engineering) which held the wall temperature to within ± 0.5 °C of a given set temperature. Fibreglass and expanded polystyrene were used to insulate the bottom wall assembly, minimizing heat loss.

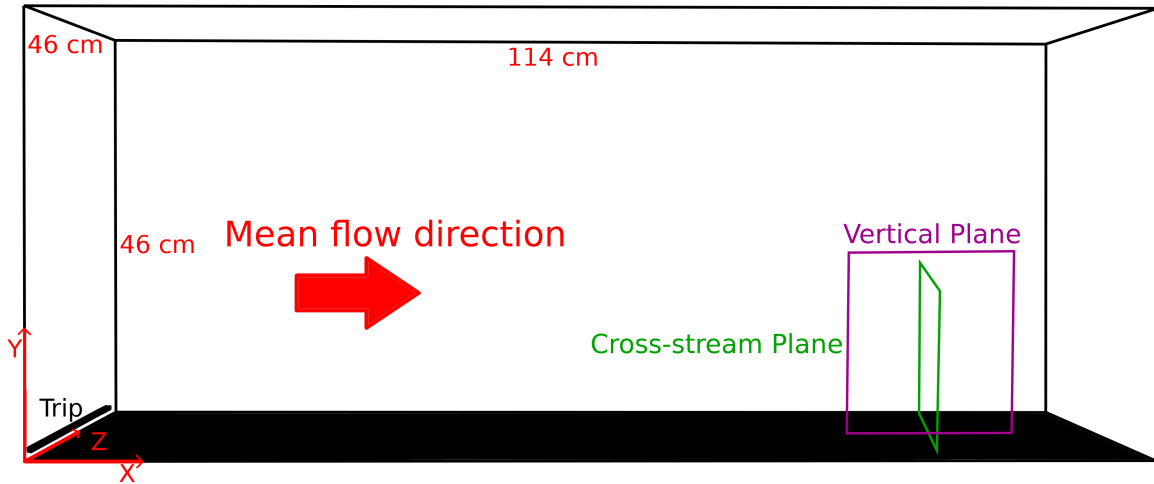


Figure 5.1: Diagram of the experimental setup.

	Ri_L				
	0.01	0.03	0.05	0.1	0.3
Re_θ	1700	1700	1400	1000	700
T_w ($^\circ\text{C}$)	45	90	90	90	90
U (m/s)	7.5	7.5	6.0	4.5	2.5

Table 5.1: Summary of experimental conditions.

The boundary layer was tripped using a $6.3 \text{ mm} \times 6.3 \text{ mm} \times 43 \text{ cm}$ steel rod placed on the bottom wall at the inlet to the test section. The turbulent boundary layer formed, then passed over the heated wall. A combination of wall temperatures (T_w) and free-stream velocities (U) listed in Table 5.1 were used to achieve a range of Richardson numbers between 0.01 and 0.3 corresponding to strongly inertia driven ($Ri_L = 0.01$) to weakly inertia driven flow ($Ri_L = 0.3$).

Particle image velocimetry (PIV) was used over multiple planes with respect to the mean flow direction to capture high-resolution 2D velocity fields. This technique has been utilized by the present authors to successfully characterize turbulent boundary layer flows as discussed in chapter 3 and 4. Figure 5.1 shows the measurement planes considered in the present study where all measurement planes were located 80 cm downstream of the trip bar,

ensuring no signature of the trip bar was present in the measurement region. The vertical stream-wise plane captured two-dimensional velocity fields in the x - y plane and the cross-stream plane resolved two-dimensional velocity fields in the y - z plane. The combination of measurement in these planes, facilitated a detailed analysis of three-dimensional flow phenomena.

Laser illumination was provided by a dual-cavity 120mJ Nd:YAG laser (SoloPIV 120XT 532nm) operating at 15Hz per cavity. A set of optics converted the laser beam into a 1 mm thick light sheet. A 12 MegaPixel CMOS camera (Flare, IO Industries) was used to record PIV images at a resolution of 4096×3072 pixels. A 50 mm f/1.4 (Nikon) and 70-300 mm f/4 (Sigma Corp.) camera lens were used in experiments. PIV images were recorded via a high-speed image recording system (DVR Express CORE, IO Industries). The laser and camera were synchronized using a four-channel pulse delay generator (555-4C, Berkeley Nucleonics). The seed particle used in experiments was theatrical fog (Directors Choice, Ultratec) that was injected upstream of the test section by a fog machine. Seed particle was allowed to disperse for several minutes inside the recirculating wind tunnel before data acquisition began. At least 10,000 experimental images were captured at a rate of 30 Hz in each test, corresponding to at least 5,000 velocity vector fields computed at 15 Hz.

From captured PIV images, velocity computation was performed using an in-house MATLAB program. The software utilizes Fast Fourier Transform (FFT) based cross-correlation with 50% overlap of square interrogation windows. The interrogation window sizes ranged from 32×32 pixels to 64×64 pixels, corresponding to search windows between 64×64 pixels to 128×128 pixels, respectively. This produced instantaneous velocity vectors with a spatial resolution between 0.4 mm/vector (vertical stream-wise plane) and 0.5 mm/vector (cross-stream plane). Spurious vectors, which numbered less than 1% in all experiments, were detected and corrected using a local median filter and Adaptive Gaussian Window

(AGW) interpolation. The techniques of PIV uncertainty estimation developed by Prasad et. al. 2000 [22] and Cowen and Monismith 1997 [23] were used to estimate uncertainty based on the seed particle size, AGW interpolation, peak locking, out-of-plane motion, and velocity gradients. Based on the experiments at $Ri_L = 0.03$ where the velocity gradients and wall temperature were at their respective maxima, the maximum velocity measurement uncertainty was estimated to be ± 6.3 cm/s corresponding to 0.8% of the free-stream velocity.

5.3 Results

The captured experimental images often show regions of low seed particle density near to the heated wall. This was caused by thermal expansion of air adjacent to wall as it was heated, as well as, the evaporation of the fog solvent. The lack of seed particles prevented velocity computation within these regions. These low-seed particles regions were clearly visible in the PIV images and the comparison of their shape and dynamics with previous experimental studies, confirmed that these regions are most likely rising thermals as discussed in chapter 4 [15, 24]. As the velocity field within these thermals could not be computed due to the lack of seed particles, these thermal regions were detected using a thermal detection technique developed in chapter 4, and subsequently removed from the consideration of velocity fields. Thermals generated significant signatures in PIV images for cases where $Ri_L \geq 0.05$. Hence, the thermal detection technique was used to remove vectors in computed vectors fields in experiments conducted at $Ri_L \geq 0.05$ while at lower tested Ri_L , no thermal detection was necessary.

Figure 2 depicts sample PIV images and the corresponding instantaneous turbulent velocity vector field superimposed on the instantaneous planar turbulent kinetic energy (TKE) to illustrate the presence of thermals and the treatment. The results are shown for the vertical

stream-wise plane and cross stream plane at $Ri_L = 0.3$ and at $Ri_L = 0.03$. At $Ri_L = 0.3$, the thermals in the vertical stream-wise plane PIV image show a complex structure with multiple thermal ligaments, i.e. dark bands of fluid, near the bottom wall. This structure was most likely produced by the interaction of stream-wise inertia-driven boundary layer turbulence deforming and breaking apart buoyant thermals. Note that only the regions with very strong thermal-dominant flow have a near-complete lack of seed particles. As a thermal starts to interact with the surrounding seeded fluid and undergoes mixing, diffusion and dispersion, it contains enough seed to allow velocity computation. In the corresponding turbulent velocity field, the detected strong thermals have been removed. However, the adjacent regions where the thermals have strong interactions with the surrounding inertia-driven flow, the velocity fields were well-resolved and were found to be associated with large magnitudes of turbulent kinetic energy (TKE), as expected in the buoyancy-driven motion of thermals.

The cross-stream plane provides a unique perspective on boundary layer flow as the stream-wise velocity is not present. The PIV image at $Ri_L = 0.3$ shows multiple thermal signatures each rising from the hot wall with a mushroom cloud like shape, a typical feature of rising thermals. In the turbulent vector field, each of the detected thermal signatures is adjacent to upward directing velocity vectors and a relatively high TKE magnitude. On the left side of the vector field, there is a large region of high TKE magnitude fluid bursting away from the wall that extends up to $y = 4$ cm. This region features a large clock-wise rotating recirculation on the right side of the bursting event which appears to assist with channeling fluid away from the wall. This region corresponds to the relatively faint thermal signature in the PIV image. The weak thermal signature produced by the relatively high seed particle density within the thermal facilitated velocity computation and the detection of this turbulent phenomena.

At lower Ri_L , thermal signatures in PIV images are weak and fewer vectors are removed. It was found that at $Ri_L \leq 0.03$ no thermal detection was needed as the seed particle density was sufficiently high within thermals for velocity computation. In the vertical stream-wise plane PIV image in the lower panel of Figure 5.2, thermals are difficult to clearly identify due to the amount of seed particle within them but are still present. The associated turbulent velocity field shows several regions throughout the field of view associated with high TKE magnitude. These high TKE regions are likely associated with thermals due to their behavior of generally moving away from the wall and traveling slower than the mean flow in the stream-wise direction, consistent with observation at $Ri_L = 0.3$. While mixing and diffusion has increased seed density within each thermal, the underlying thermal motion has not significantly changed. In the cross-stream plane at $Ri_L = 0.03$, the PIV image shows a visually weaker thermal signature compared to the PIV image taken at $Ri_L = 0.3$. The turbulent velocity field however, contains a strong bursting phenomenon on the left side that extends up to $y = 3$ cm. This phenomenon is associated with a higher TKE magnitude than events observed in the cross-stream plane at $Ri_L = 0.3$. Simultaneously, on the right side of the image, relatively small recirculation events are observed.

From the presented PIV images, thermals with a strong visual signature appear most often adjacent to the heated wall. As large low-seed density thermal regions were removed from the corresponding instantaneous vector fields, this reduced the number of velocity vectors available to describe the velocity distribution in a meaningful way. The fraction of available (i.e. non-removed) velocity vectors to the total number of possible velocity vectors (V_A) at each height above the wall (y) is presented in Figure 5.3. In experiments where no thermal detection was required, i.e. $Ri_L \leq 0.03$, $V_A = 1$ for all values of y as all velocity vectors available for computation were utilized. At higher Ri_L , some vectors were removed from consideration via thermal detection causing V_A to decrease.

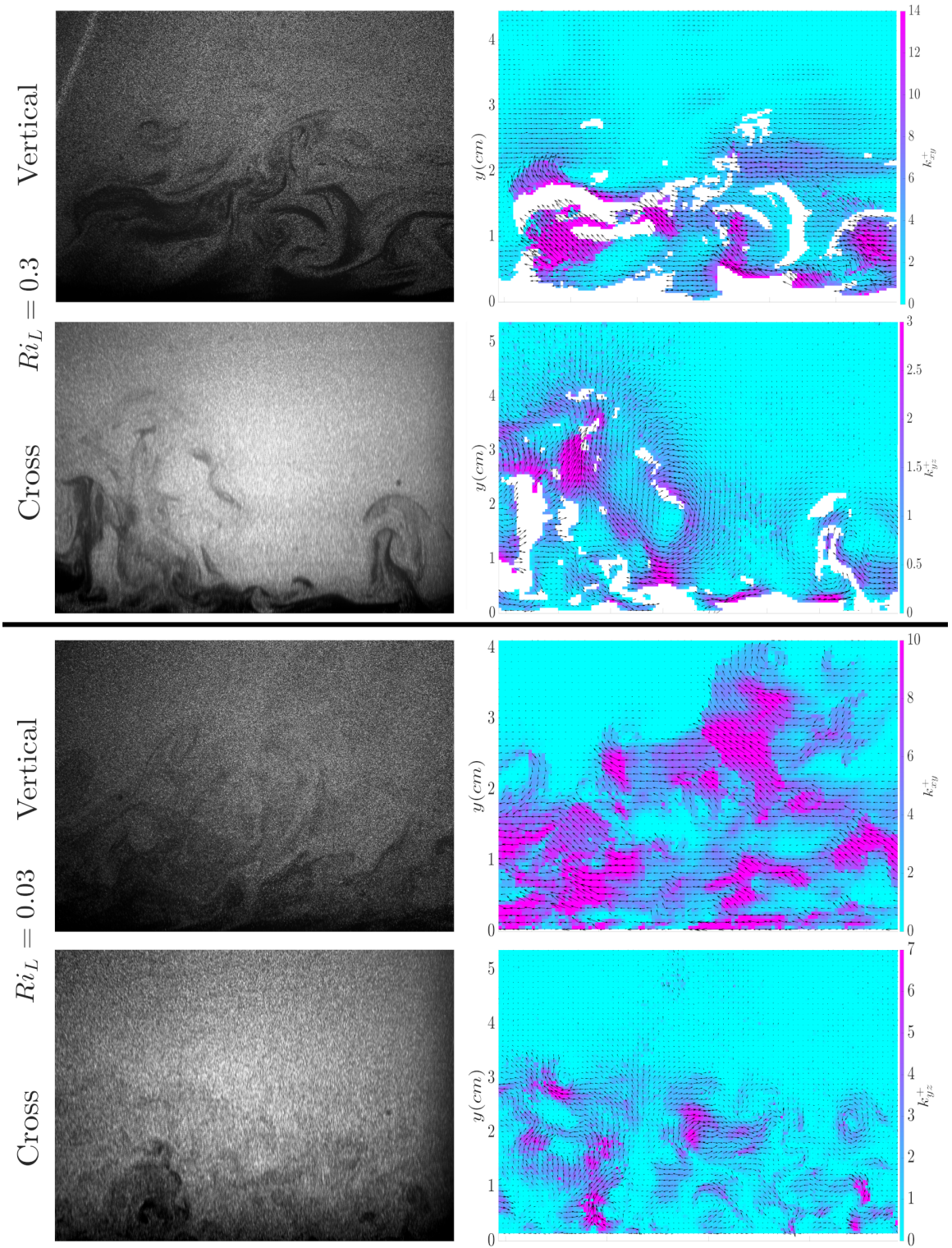
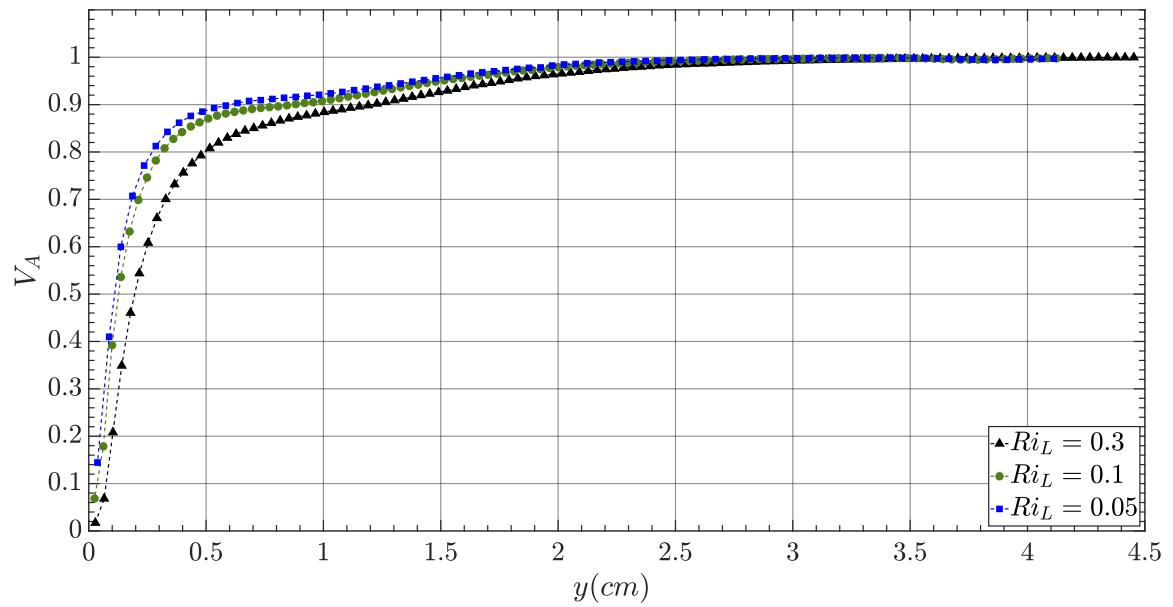


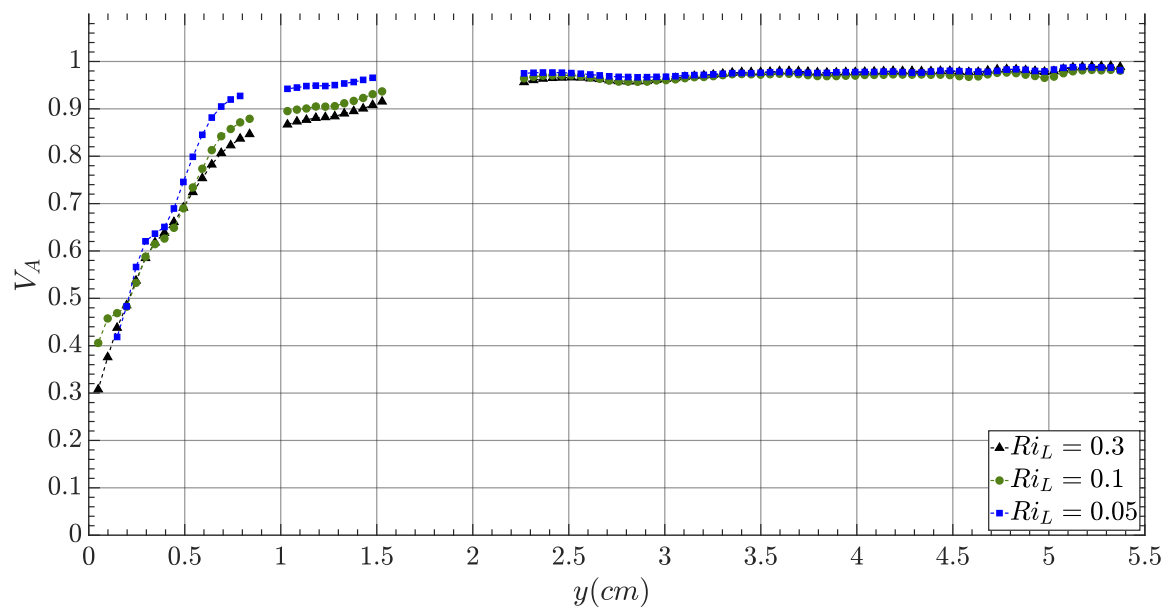
Figure 5.2: A set of PIV images (left column) and corresponding instantaneous turbulent velocity vector field superimposed on a colormap of instantaneous planar turbulent kinetic energy (right column). The top panel corresponds to $Ri_L = 0.3$ and the bottom panel corresponds to $Ri_L = 0.03$. The top row in each panel is taken from the vertical stream-wise plane where mean flow is from left to right. The bottom row in each panel is from the cross-stream plane where mean flow is out of the page. All PIV images have been cropped and brightness/contrast enhanced.

The plotted data for the cross-stream plane in Figure 5.3b has discontinuities, which are due to artifacts present in experimental images that biased thermal detection, and hence excluded. The results show that in both considered measurement planes, the presence of low seed density thermals significantly reduces the number of available velocity vectors in the region close to the heated wall ($y < 1$ cm). At the wall, V_A in the vertical stream-wise plane is between 0 and 0.1 for all Ri . Similarly, in the cross-stream plane $V_A \approx 0.35$ at $y = 0$. Increasing y leads to a rapid increase in V_A in both measurement planes until $V_A \approx 0.8$ to 0.9 which occurs at $y \approx 0.5$ cm in the vertical stream-wise plane and $y \approx 1$ cm in the cross-stream plane. At these respective locations V_A begins to increase slowly with increasing y . Further away from the wall ($y \geq 1.5$ cm) V_A tends towards unity indicating a large majority vectors at these y -coordinates are available for computations.

At $V_A \approx 0.8$, V_A stops increasing rapidly with increasing y due to a weakening presence of low seed density thermals. It is expected then that for y -coordinates where $V_A \leq 0.85$, a significant bias in the velocity signal will be present as a large quantity of vectors are not considered. To minimize bias, all velocity data and turbulent statistics are only considered for the region where $V_A \geq 0.85$. In the vertical stream-wise plane this corresponds to the domain $y \geq \approx 0.4$ cm and in the cross-stream plane $y \geq \approx 0.7$ cm.



(a)



(b)

Figure 5.3: Fraction of velocity vectors available for computation at different distances above the wall for (a) vertical stream-wise plane and (b) cross-stream plane.

5.3.1 Mean Turbulent Statistics

Vertical Stream-wise Plane

The mean stream-wise velocity profiles obtained in the vertical stream-wise plane are presented in Figure 5.4. The profiles are presented in dimensional form and grouped according to Re_θ , the Reynolds number based on the free-stream velocity and the momentum thickness (see Table 5.1), to compare heated versus unheated flow behavior. The experimental setup for the unheated wall tests was the same as the setup documented in this paper. The details of the unheated wall experiments have been previously discussed in chapter 3. The results show that the mean velocity profiles in the presence and absence of heating are very similar in shape and magnitude in the log-linear region. Due to higher fraction of thermals close to the heated wall, the lower portion of the log-linear region was not captured at low Re_θ .

Figure 5.5 shows the mean velocity profiles normalized by inner wall layer scaling, for the heated wall cases. The friction velocity was computed from the slope of the dimensional velocity profile in log-linear region and fluid properties were evaluated at the film temperature. The measured velocity profiles show good agreement with the canonical log-law of the wall for a smooth wall. Note that the log-law profile extends until it intersects the viscous sublayer profile. These results indicate that wall heating over the range $0.01 \leq Ri_L \leq 0.3$ does not cause a significant change in the mean stream-wise velocity in the logarithmic layer. As the dimensional heated and unheated velocity profiles were nearly the same, it follows that the computed friction velocities would be approximately equal. It is important to note that while the friction velocity did not change significantly, as the buffer layer and viscous sublayers are not captured in the present study, there is no evidence to conclude that the wall shear stress is unchanged.

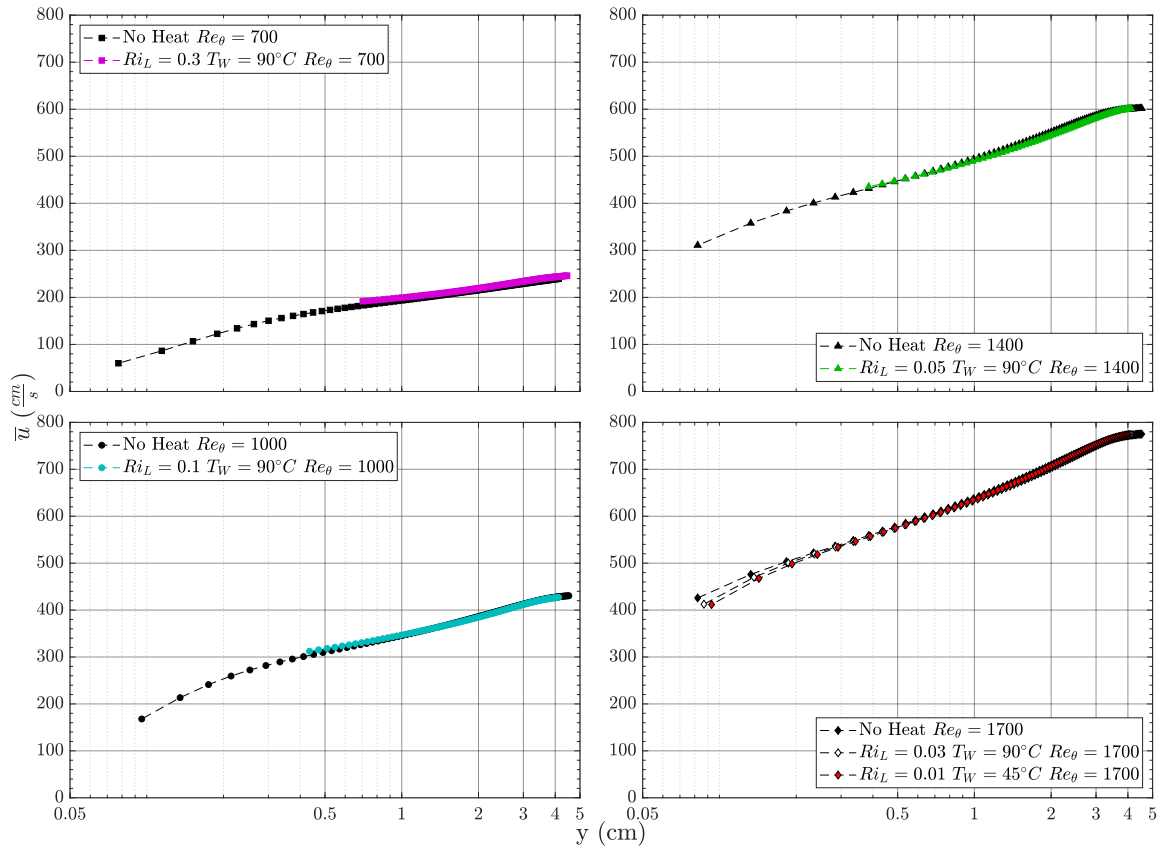


Figure 5.4: Arrangement of the mean stream-wise velocity profiles in a 2×2 grid based on Re_θ .

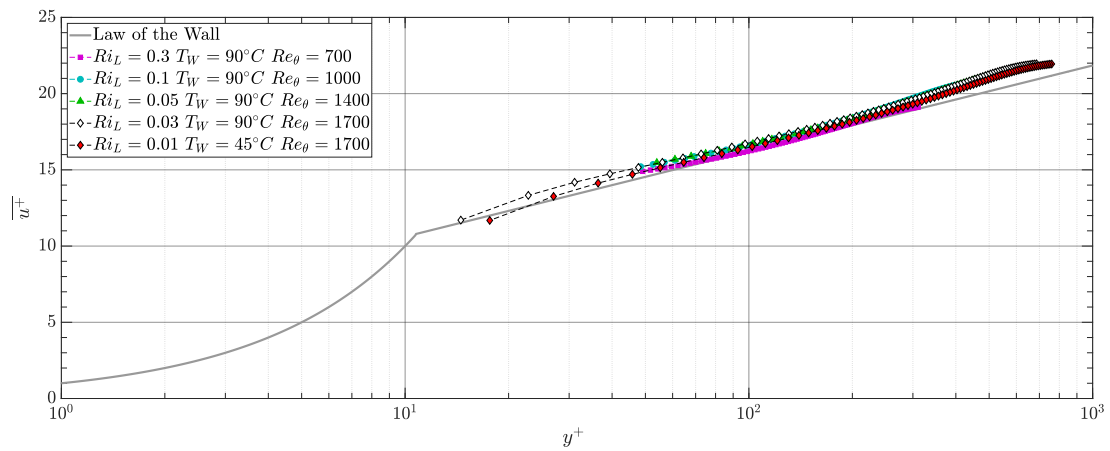


Figure 5.5: Mean stream-wise velocity profiles only for the heated wall cases expressed in inner layer coordinates.

The mean Reynolds stress profiles computed are presented in Figure 5.6 for the stream-wise Reynolds stress ($\overline{u'u'}$) and wall-normal Reynolds stress ($\overline{v'v'}$) and Figure 5.7 for the Reynolds shear stress ($\overline{u'v'}$). At $Re_\theta = 700$, the unheated wall case is compared to the heated wall experiment conducted at $Ri_L = 0.3$. The full stress profile could not be computed due to the presence of thermals in the near-wall region. In the log layer however, a consistent decrease in $\overline{u'u'}^+$ is present. At $Re_\theta = 1000$ and 1400 for $Ri_L = 0.1$ and $Ri_L = 0.05$, similar trends are observed where the mean stream-wise stress is larger in the absence of wall heating. In these cases, the near-wall increase in $\overline{u'u'}^+$ magnitude is not detected due to thermals. At $Re_\theta = 1700$ for $Ri_L \leq 0.03$, where no strong thermal signatures are found, the near-wall $\overline{u'u'}^+$ curves show little change compared to the unheated case. Further away from the wall in the log layer, a decrease in $\overline{u'u'}^+$ is present consistent with the other flow conditions tested.

The right column of Figure 5.6 depicts the mean wall-normal Reynolds stress profile. At $Re_\theta = 700$, there is a significant decrease in the stress magnitude in the presence of wall heating at $Ri_L = 0.3$. The same behavior is observed at $Ri_L = 0.1$ where the peak $\overline{v'v'}^+$ is about 0.8 compared to the unheated case that had a peak near 1.1. At $Ri_L = 0.05$ however, the heated and unheated profiles are very similar for $y^+ < 200$. As y^+ increased further, $\overline{v'v'}^+$ decreased compared to the unheated wall profile. At $Ri_L \leq 0.03$, the peak $\overline{v'v'}^+$ was found to be larger in the presence of wall heating than the unheated wall case. Moving away from the wall leads to a decrease in wall-normal Reynolds stress until the stress in the heated wall cases becomes smaller in magnitude than $\overline{v'v'}^+$ for the unheated case.

The mean Reynolds shear stress profiles presented in Figure 5.7 depict trends similar to the stream-wise and wall-normal mean stresses. At $Ri_L \geq 0.1$ the $\overline{u'v'}^+$ magnitudes are significantly lower in the presence of wall heating than the no heating cases. For $Ri_L \leq 0.03$ however, the mean Reynolds shear stress profile show similar magnitudes to the unheated

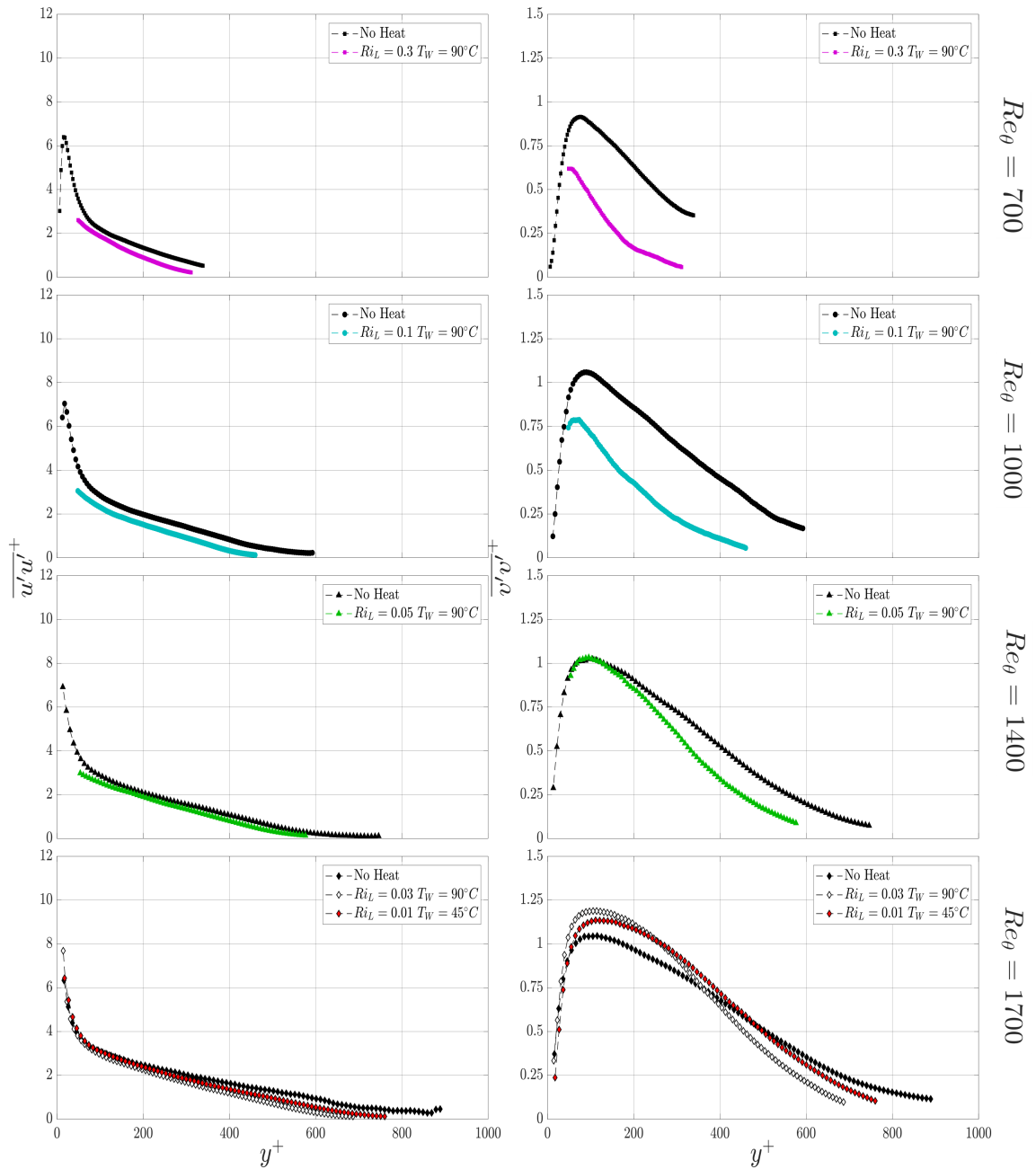


Figure 5.6: Vertical profiles of $\overline{u'u'}$ (left column) and $\overline{v'v'}$ (right column) in wall coordinates for heated and unheated cases obtained in the vertical stream-wise plane. The plots are grouped according to Re_θ .

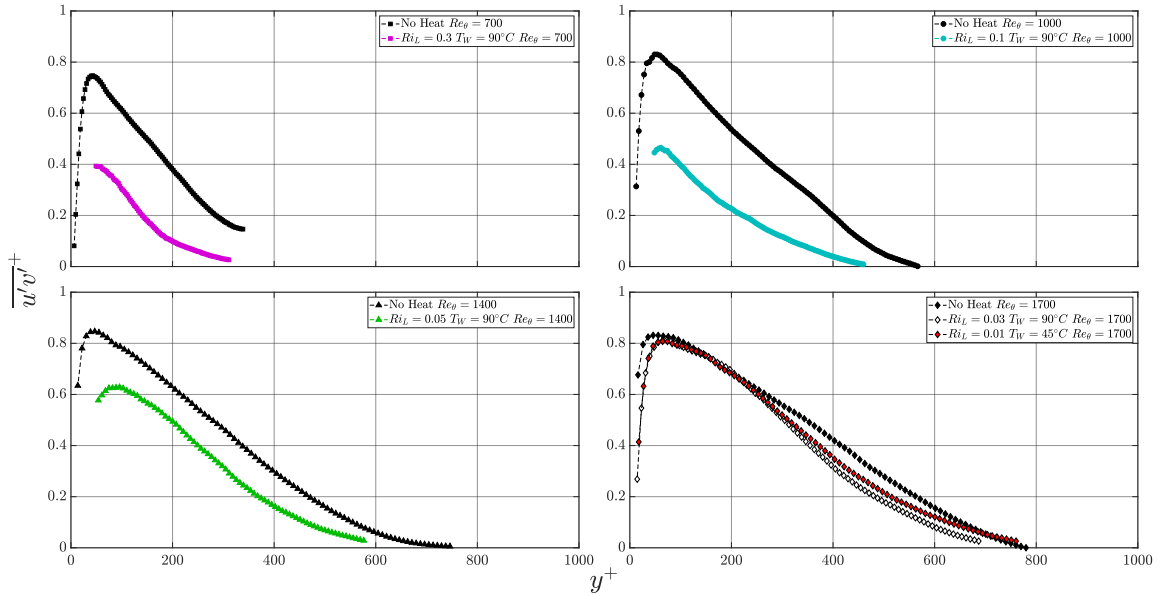


Figure 5.7: Vertical profiles of $\overline{u'v'}^+$ for heated and unheated cases, in the vertical stream-wise plane, expressed in wall coordinates. Plots are grouped according to Re_θ .

tests. Although, at $y^+ > 200$, $\overline{u'v'}^+$ magnitudes for the heated wall cases were slightly smaller than that for the unheated case.

Cross Stream Plane

In the cross-stream plane, the mean stress profiles were computed for the wall-normal Reynolds stress ($\overline{v'v'}$) and the span-wise Reynolds stress ($\overline{w'w'}$) and the results are presented in Figure 5.8. Note that the magnitude of $\overline{v'w'}$ was found to be two orders of magnitude smaller than $\overline{v'v'}$ and $\overline{w'w'}$, hence the contributions of $\overline{v'w'}$ to overall flow behavior are insignificant hence, this quantity is omitted from the presented results. The mean span-wise Reynolds stress profile at $Re_\theta = 700$ in the unheated wall case shows a sharp increase in magnitude near the wall, reaching a peak magnitude and then a gradual decrease in magnitude with increasing distance from the wall. At $Ri_L = 0.3$, a decrease in $\overline{w'w'}^+$ was observed in the near-wall region, however the difference in stress magnitudes decreases as

distance from the wall increased. At $Ri_L = 0.1$, the peak $\overline{w'w'^+}$ was larger than the unheated case. This was also observed at $Ri_L = 0.05$ where the difference between heated wall and unheated wall peak $\overline{w'w'^+}$ was larger than the difference at $Ri_L = 0.1$. In both of these cases however, the near-wall behavior is not fully captured due to thermals' data exclusion. At $Ri_L \leq 0.03$, the $\overline{w'w'^+}$ magnitudes were significantly larger in the presence of wall heating. However, $\overline{w'w'^+}$ magnitudes decrease rapidly with increasing y^+ leading to a lower stress magnitude further away from the wall.

From the computed mean Reynolds stress profiles, each of the presented stresses have demonstrated some change compared to the unheated case. The stream-wise turbulent stress was found to decrease slightly in the log-layer at all tested Ri_L cases. The span-wise Reynolds stress showed a consistent increase in peak stress in the presence of wall heating. The wall-normal Reynolds stress demonstrated a similar increase in peak stress magnitude in the cross-stream plane however this was only observed for $Ri_L \leq 0.03$ in the vertical stream-wise plane. It is expected however that in the presence of wall heating, v' increases which influences the other turbulent variables.

5.3.2 Modification to Wall-Normal Turbulent Velocity Component

In the vertical stream-wise plane, $\overline{v'v'^+}$ showed the most significant change in the presence of wall heating by decreasing as Ri_L increased. This behavior is inconsistent with previously reported findings [20, 21]. To determine the cause of this behavior, the vertical stream-wise plane results become the focus of study.

To investigate the nature of the modification to v' by wall heating, the probability density function (PDF) of v' ($\phi(v'^+)$) is calculated and presented in Figure 5.9 for all considered Ri_L and the corresponding unheated cases. The results clearly show that in the presence of wall heating $\phi(v')$ becomes tri-modal. The plots also show an increase in the peak PDF value at

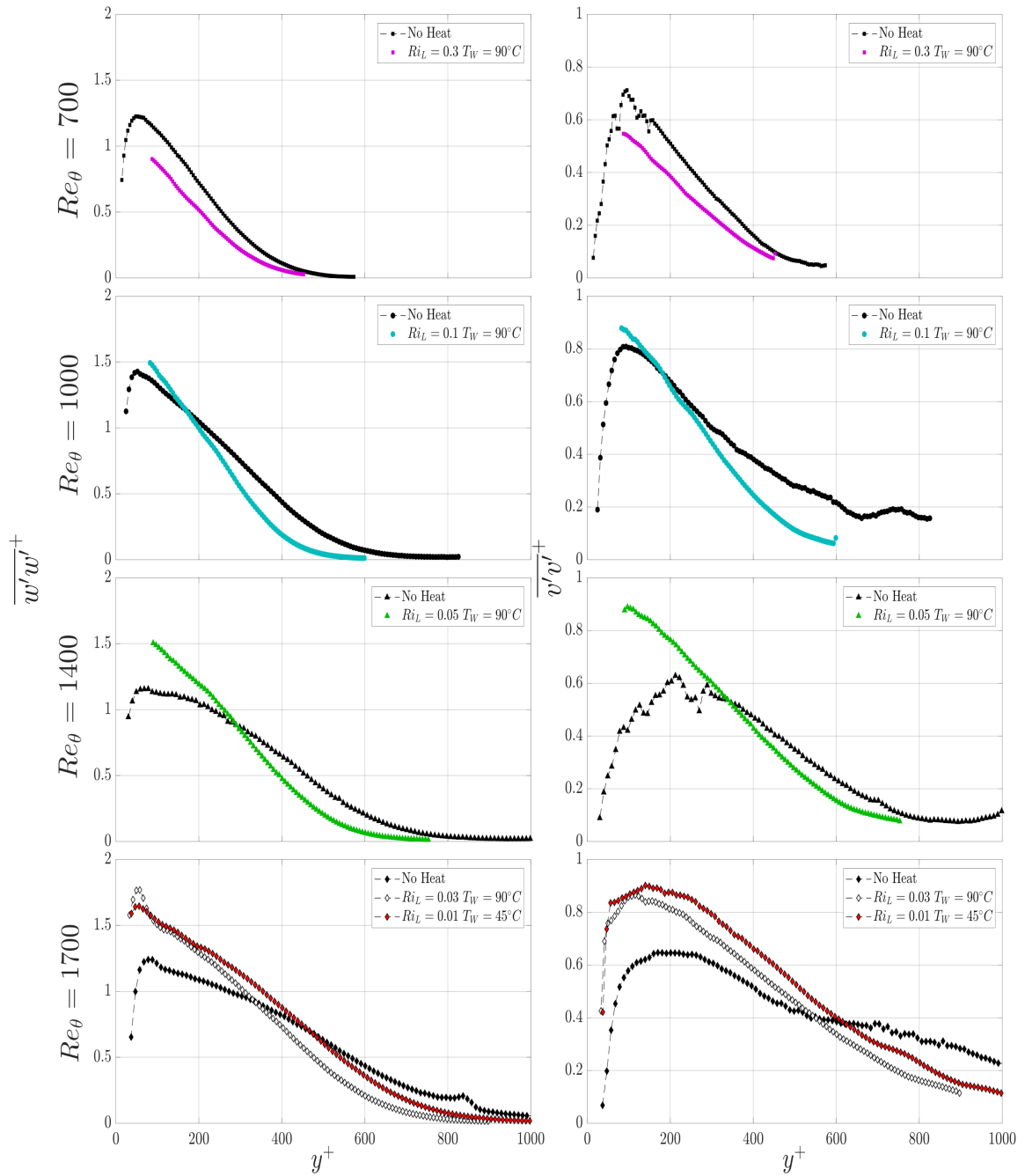


Figure 5.8: Vertical profiles of $\overline{w'w'}$ (left column) and $\overline{v'v'}$ (right column) in wall coordinates for heated and unheated cases obtained in the cross stream plane. The plots are grouped according to Re_θ .

$v' \approx 0$ relative to the unheated cases, indicating that relatively small magnitudes of wall-normal turbulent velocity are observed relatively more often in the presence of wall heating. The approximately symmetric secondary mode in $\phi(v')$ is likely due to the combined effects of buoyant thermals rising from the wall and replenishing fluid sinking towards the wall. The region in $\phi(v')$ between the primary mode at $v' \approx 0$ and the buoyancy-driven secondary mode is a relatively inactive region at $v'^+ \approx \pm 1$. Compared to the unheated case, there are significantly fewer velocity vectors associated with this range of v'^+ magnitudes. In the region of relative inactivity ($v'^+ \approx \pm 1$), there are small peaks in $\phi(v')$ which are most prominent for $Ri_L \leq 0.1$. These peaks may be attributed to a secondary phenomenon associated with the buoyancy driven rising and falling motion.

The buoyancy-driven secondary mode in $\phi(v')$ appears to increase in v' magnitude as Ri_L increases. At $Ri_L = 0.01$ the peak in the buoyant mode of $\phi(v')$ was $v' \approx \pm 2.0$ while at $Ri_L = 0.3$, the peak was approximately ± 3.5 . This behavior is consistent with previous reports of wall heating increasing the magnitude of v' . The observed tri-modal behavior in v' clearly defines one basic modification to the turbulent velocity field that influences the other fluid variables. This change in $\phi(v')$ also propagates through its gradients, defining one pathway for wall heating to influence several key turbulent quantities that depends on v and the gradients of v . However, this description does not explain the decrease in $\overline{v'v'^+}$ (see Figure 5.6). This behavior can be explained through the time-history of v' at $Ri_L = 0.3$ and $Ri_L = 0.01$ at a point far away from the wall ($y = 4$ cm) where no thermals were detected as shown in Figure 5.10. In the velocity data obtained from each experiment, many observations of the time history of v' at various spatial positions were performed and similar trends were observed. The velocity time histories presented are each a sample from a given experiment illustrating the observed trends.

The time history signal at $Ri_L = 0.3$ shows that the magnitude of v'^+ rarely exceeded ± 1 ,

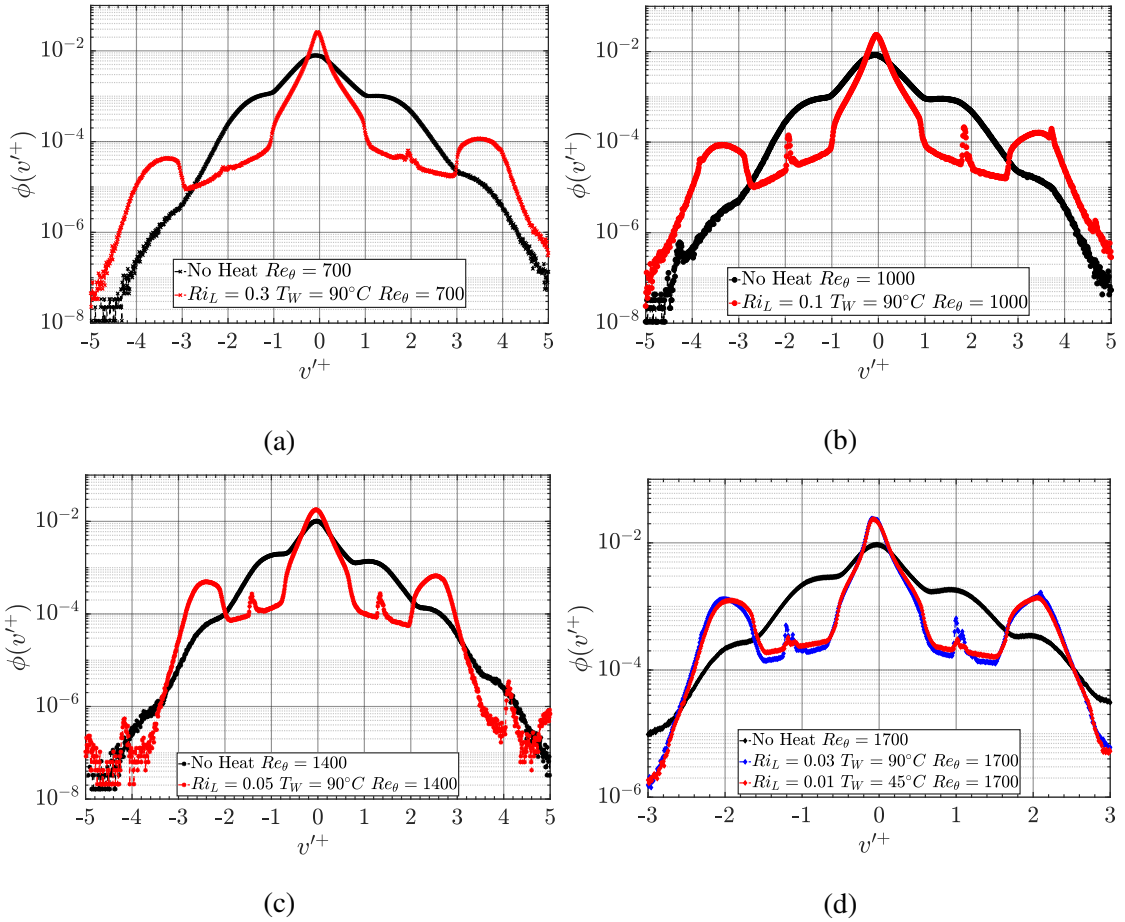
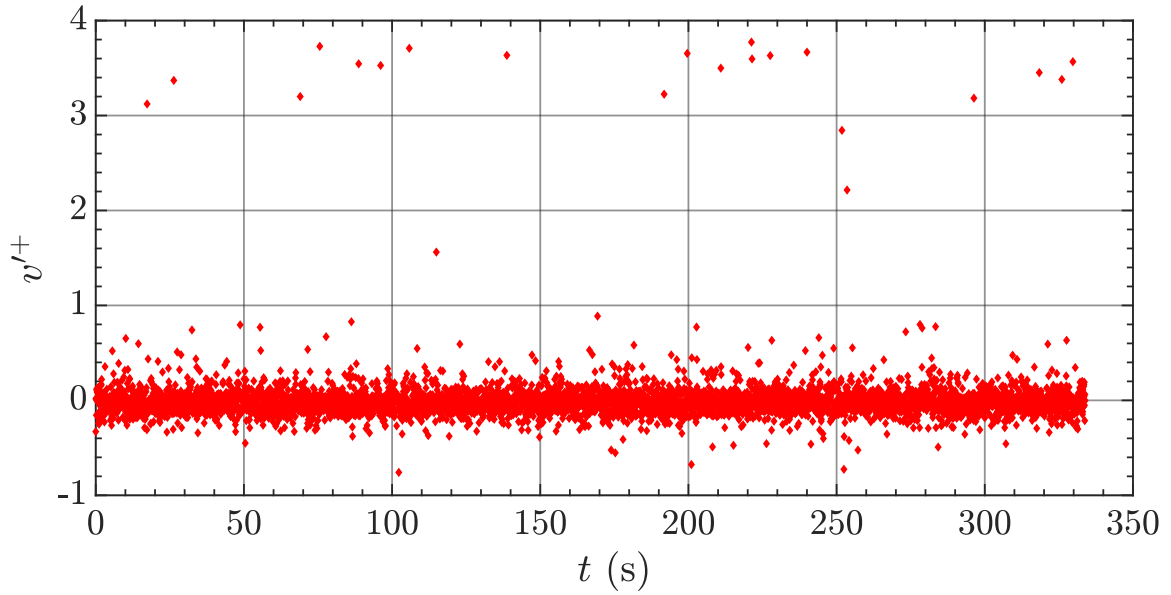
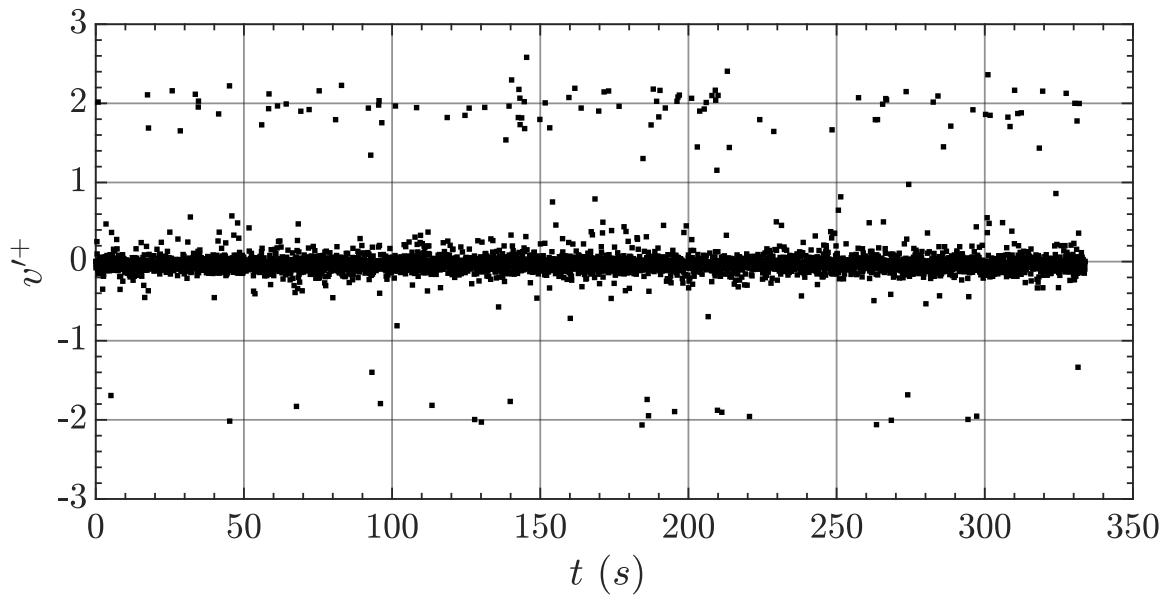


Figure 5.9: PDFs of v' for heated and unheated cases obtained in the vertical stream-wise plane. The plots are grouped according to Re_θ .



(a)

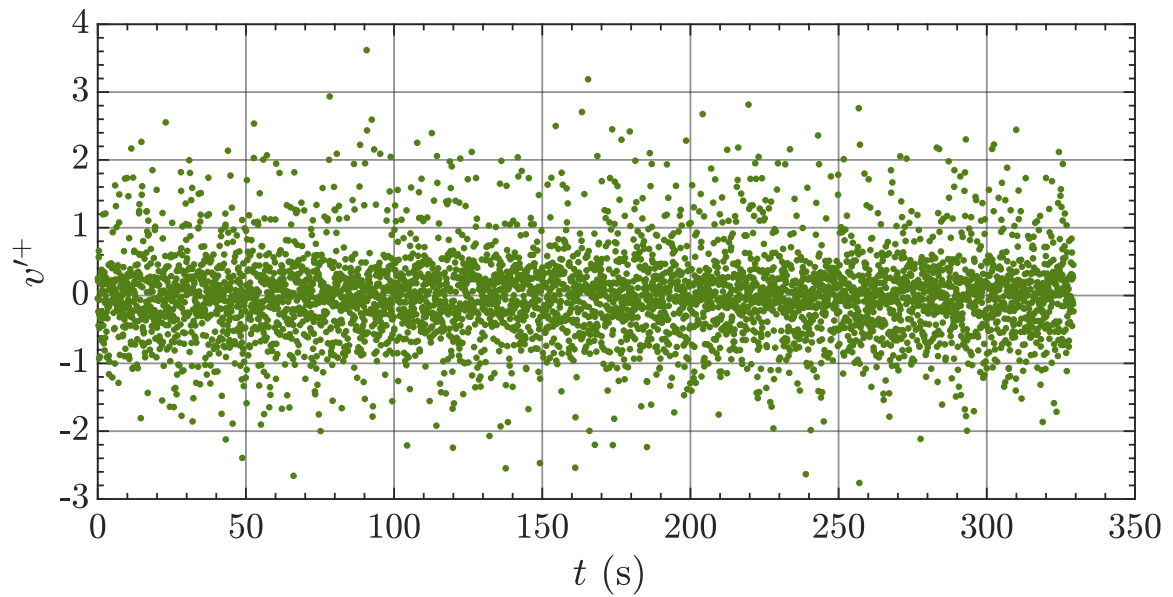


(b)

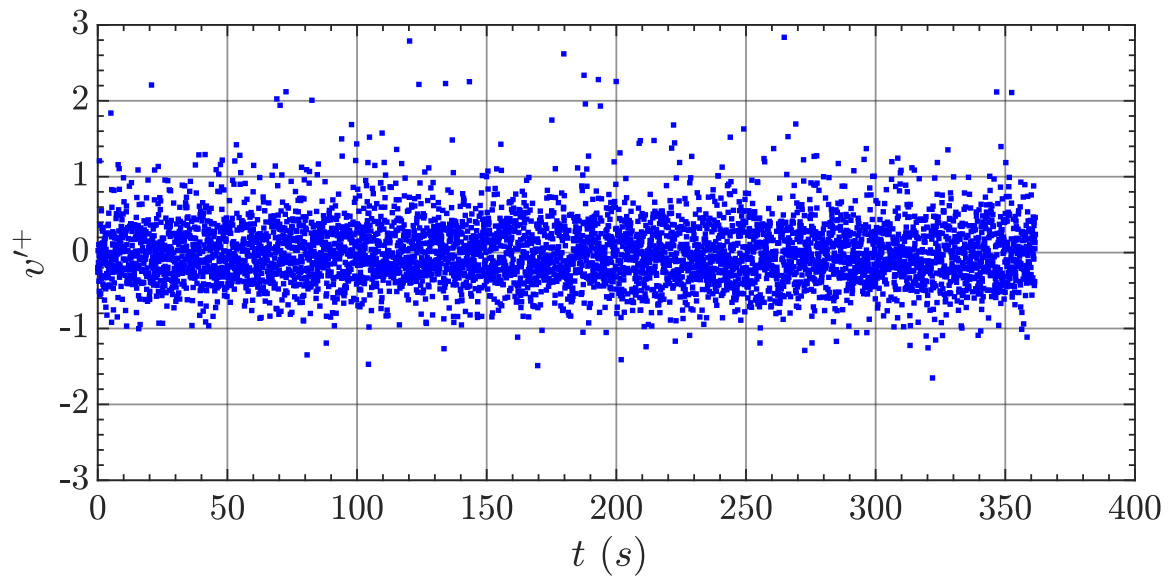
Figure 5.10: Time history of v'^+ signal at a point 4 cm above the wall. (a) is from the $Ri_L = 0.3$ case ($Re_\theta = 700$, $T_W = 90$ °C) and (b.) is from the $Ri_L = 0.01$ case ($Re_\theta = 1700$, $T_W = 45$ °C) in the vertical stream-wise plane.

however when a large fluctuation occurred it tended to produce $v'^+ \approx 3.5$. This agrees with the $\phi(v')$ distribution. The close clustering of v'^+ about zero suggests that the standard deviation of v'^+ is small while the large departures that are biased toward positive v'^+ suggest non-zero skewness and a large kurtosis in the underlying $\phi(v')$ distribution. At $Ri_L = 0.01$, the v'^+ time history shows more frequent fluctuations with a magnitude greater than one and a comparatively more symmetric distribution (see Figure 5.10b). Comparison with the unheated wall experiments in Figure 5.11 show that at $Re_\theta = 1700$ v'^+ there are fewer excursions of $|v'^+| \geq 2$ relative to the observations at $Ri_L = 0.01$. This is evidence of a decreased kurtosis in the absence of wall heating. The magnitudes of wall normal turbulent velocity in the range $-0.5 \leq v'^+ \leq 0.5$ is more populated at $Ri_L = 0.01$ than $Re_\theta = 1700$ suggesting a decrease in the standard deviation of v' . At $Re_\theta = 700$, the v'^+ time history shows a wider distribution of velocity fluctuations between $-2 \leq v'^+ \leq 2$ compared to $Ri_L = 0.3$. This is evidence of a larger magnitude of the standard deviation of v' in the absence of wall heating. The large departures from the mean that were present at $Ri_L = 0.3$ are absent at $Re_\theta = 700$ indicative of a smaller kurtosis.

From these time history plots it appears that at $Ri_L = 0.3$, v'^+ is often small in magnitude indicating fluid is traveling with the mean flow. Intermittently, a thermal bursts and rises from the heated wall and its passage produces the large magnitude fluctuations of v'^+ . This behavior is quantified with the mean inner layer normalized standard deviation (σ^+) and mean kurtosis (K) of v' as shown in Table 5.2. The kurtosis is based on the fourth-order statistical moment and standard deviation (σ_x) defined in Eqn. 5.2 for an arbitrary quantity (x) observed N times.



(a)



(b)

Figure 5.11: Time history of v'^+ signal at a point 4 cm above the wall. (a) is from the unheated $Re_\theta = 700$ case and (b.) is from the unheated $Re_\theta = 1700$ case in the vertical stream-wise plane.

	Ri_L		No heat	
	0.01	0.3	$Re_\theta = 1700$	$Re_\theta = 700$
σ^+	78%	51%	71%	76%
K	10	58	5.5	4.5

Table 5.2: Mean standard deviation and kurtosis of v' for a selection of cases.

$$K = \frac{\frac{1}{N} \sum_{i=1}^N (x_i - \bar{x})^4}{\sigma_x^4} \quad (5.2)$$

From the table, wall heating in the $Ri_L = 0.01$ case causes a slight increase in the typical wall-normal velocity fluctuation (σ^+). Thermals and associated replenishing motions occur but are relatively weak compared to higher Ri_L cases, leading to an increase in K at $Ri_L = 0.01$. At $Ri_L = 0.3$ however, wall heating produced a significant change in the higher order v' statistics. First, σ^+ decreased from 76% to 51% indicating fluid is typically moving less compared to the unheated case in the wall-normal direction with respect to the mean flow. However, K increased by over an order of magnitude indicating that the wall-normal flow behavior is relatively calm before suddenly bursting into action for a short time, likely associated with the passage of a thermal, before returning to a relatively calm state.

These findings now provide a complete description for the observed behaviors in the wall-normal Reynolds stress. At all Ri_L , the buoyant force drives wall-normal fluid motion leading to the formation of the tri-modal $\phi(v')$ distribution. At these low Ri_L , thermals are rapidly mixed and diffused into the inertia driven flow. The resulting heat and momentum transfer from buoyant thermal to inertia driven flow enhances the local v' distribution. This causes increases in the wall-normal Reynolds stress in the near-wall region. At higher Ri_L , the buoyant force is sufficiently large in magnitude relative to inertia to resist inertia-

driven mixing and diffusion. This leads to large thermals that intermittently burst from the production layer and rise through the turbulent boundary layer as discussed in chapter 4. This behavior has been visualized by Sparrow [24] depicted in Figure 1.11. As a thermal passes through the boundary layer, it entrains the surrounding fluid while also producing a wake [13]. The entrainment process and intermittent thermal bursting process likely take relatively high magnitude v' fluid away from the boundary layer flow leaving fluid moving at the local mean velocity and producing a decrease in $\overline{v'v'^+}$.

The observed behaviors of v' confirm that the modification to $\overline{u'v'^+}$ is caused by changes in v' . This conclusion is further supported by the very small change in $\overline{u'u'^+}$ with increasing Ri_L . As $\phi(v')$ is tri-modal, it is of interest to characterize the PDF of $v'v'^+$.

The PDF of $v'v'^+$ at all considered Ri_L is bi-modal, containing the primary mode corresponding to $v'^+ \approx 0$ and a secondary mode that agrees well with peaks observed in Figure 5.9. The symmetry of $\phi(v')$ is clear in $\phi(v'v'^+)$ as the multi-modality is preserved. The secondary mode in $\phi(v'v'^+)$ is most likely associated with buoyancy driven motion. The peak in the secondary mode appears to increase with Ri_L . An interesting trend in these PDFs is that the peak of the likely buoyancy driven secondary mode was found to occur at an increasing value of $\phi(v'v'^+)$ with Ri_L as shown in Table 5.3. This is an expected behavior as the buoyant force becomes more dominant relative to flow inertia as the Richardson number increases. The secondary peak Reynolds wall-normal stress magnitude ($v'v'_{SP}^+$) was plotted against Ri_L in Figure 5.13.

These results indicate that $v'v'_{SP}^+$ increases monotonically with Ri_L in a relationship that appears log-linear in nature. It is important to note that except $Ri_L = 0.01$, the wall temperature and hence the Rayleigh and Grashof numbers, were constant in all experiments (only Reynolds number changed). Similarly, at $Ri_L = 0.01$ and 0.03, the Reynolds number was constant. This indicates that Re , Ra , and Gr cannot capture the observed v' behavior alone

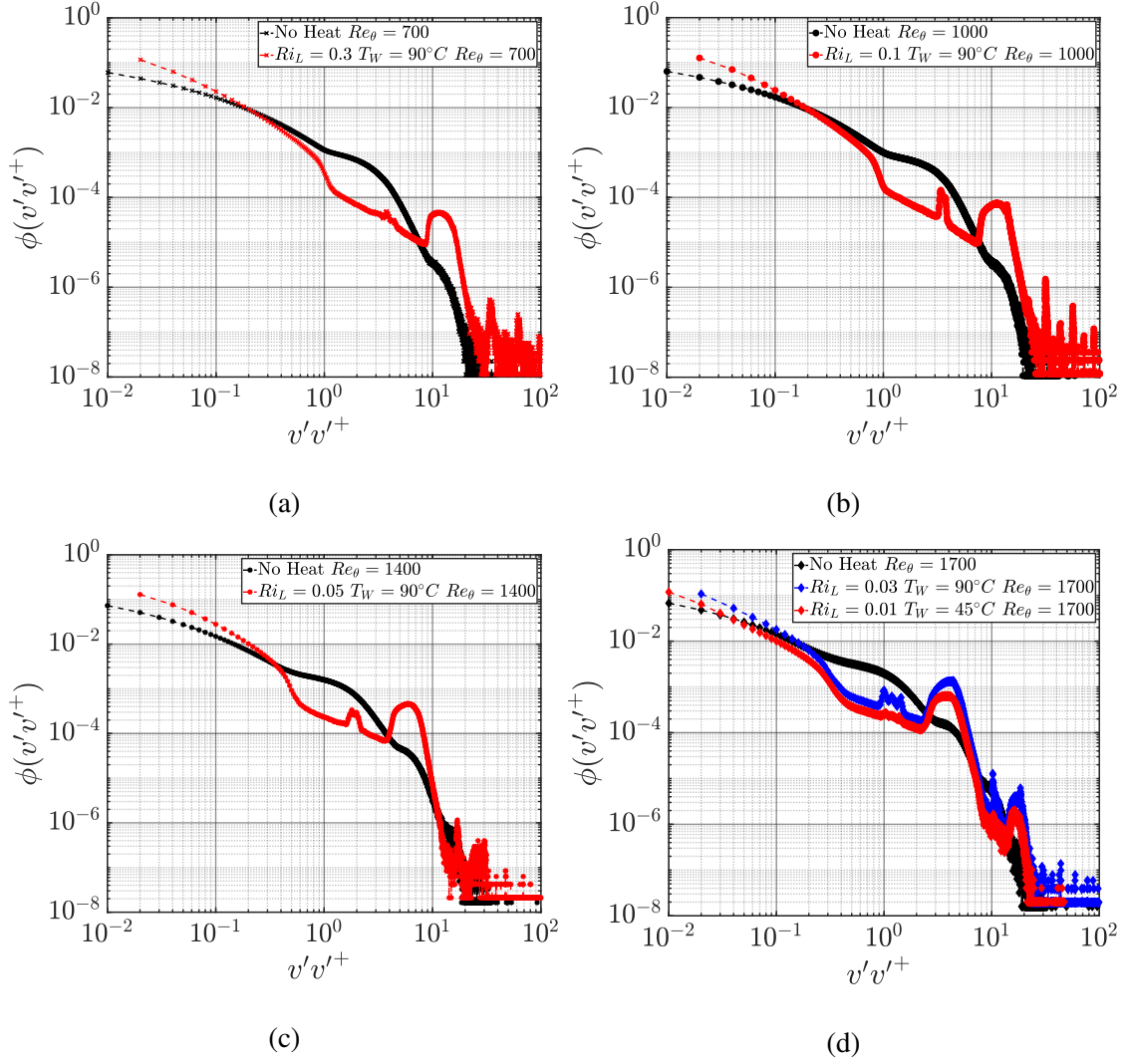


Figure 5.12: PDFs of $v'v'^+$ for heated and unheated cases obtained in the vertical stream-wise plane. The plots are grouped according to Re_θ .

Ri_L	$v'v'_{SP}^+$
0.01	3.7
0.03	4.4
0.05	5.9
0.1	11.5
0.3	11.7

Table 5.3: Secondary peak magnitude of $v'v'^+$ at each Richardson number case.

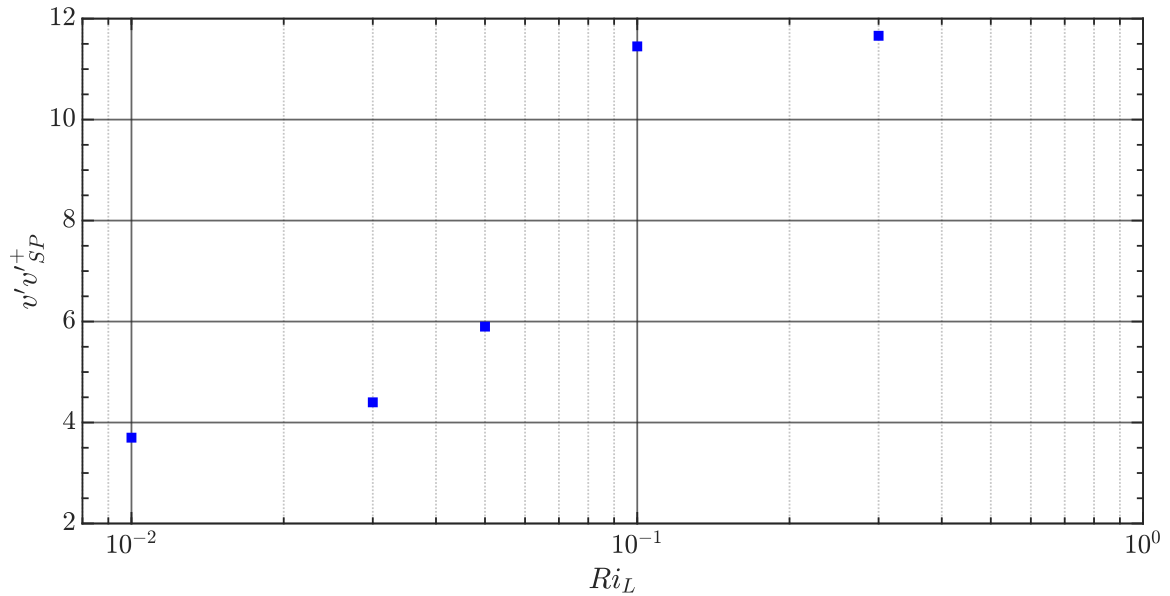


Figure 5.13: Plot of the secondary peak in $\phi(v'v'^+)$ versus Ri_L .

and the contributions of both buoyancy and inertia must be present to characterize this flow behavior. It is also important to note that the increase in $v'v'_{SP}^+$ with increasing Ri_L is much smaller from $Ri_L = 0.1$ to 0.3 compared to the other Richardson numbers. This is likely due to the buoyant force magnitude becoming sufficiently large to alter flow structure as thermals gradually become spatially dominant.

5.4 Conclusion

The objective of this study was to investigate and characterize the processes contributing to the modification of turbulent fluid variables in the presence of wall heating in the thermally unstable boundary layer. PIV experiments were performed on the turbulent boundary layer passing over a heated wall over a range of Richardson numbers to characterize both inertia dominant flow and weakly buoyancy influenced flow. Instantaneous velocity fields captured over multiple planes illustrated energetic bursting and ejection phenomena. Mod-

ifications to the turbulent stresses were reported including a dependence of $\overline{v'v'}^+$ on Ri_L likely associated with the intermittency of thermals bursting and rising through the boundary layer. The PDF of v' was found to be multi-modal in the presence of wall heating. The associated wall-normal turbulent stress PDF was also multi-modal and featured a buoyancy associated mode whose stress magnitude increased with Richardson number. The observed multi-modality in $\phi(v')$ influences the other flow variables through v and its gradients. The energetic and intermittent thermal bursting phenomena driven by the buoyant force are most likely responsible for modifications to the turbulent variables.

Bibliography

- [1] S. Pal, M. Lopez, M. Schmidt, M. Ramonet, F. Gilbert, I. Xueref-Remy, and P. Cialis, “Investigation of the atmospheric boundary layer depth variability and its impact on the ^{222}Rn concentration at a rural site in France,” *Journal of Geophysical Research*, vol. 120, pp. 623–643, 2015.
- [2] G. Solari, “The New Culture of the Wind and Its Effects,” *Wind Science and Engineering*, pp. 169–271, 2019.
- [3] V.B. Omubo-Pepple, C. Israel-Cookey, and G.I. Alaminokuma, “Effects of Temperature, Solar Flux and Relative Humidity on the Efficient Conversion of Solar Energy to Electricity,” *European Journal of Scientific Research*, vol. 35, no. 2, pp. 173–180, 2009.
- [4] H. Schlichting and K. Gersten, *Boundary Layer Theory*. Springer, 8th ed., 1999.
- [5] P. Davidson, *Turbulence: An Introduction for Scientists and Engineers*. Oxford, UK: Oxford University Press, 2nd ed., 2015.
- [6] S.B. Pope, *Turbulent Flows*. Cambridge, UK: Cambridge University Press, 2000.
- [7] M.R. Head, and P. Bandyopadhyay, “New aspects of turbulent boundary-layer structure,” *Journal of Fluid Mechanics*, vol. 107, pp. 297–338, 1981.

- [8] R.J. Adrian, C.D. Meinhart, and C.D. Tomkins, "Vortex organization in the outer region of the turbulent boundary layer," *Journal of Fluid Mechanics*, vol. 422, pp. 1–54, 2000.
- [9] S.J. Kline, W.C. Reynolds, F.A. Schraub, and P.W. Runstadler, "The structure of turbulent boundary layers," *Journal of Fluid Mechanics*, vol. 30, no. 4, pp. 741–773, 1967.
- [10] X. Wu, and P. Moin, "Direct numerical simulation of turbulence in a nominally zero-pressure-gradient flat-plate boundary layer," *Journal of Fluid Mechanics*, vol. 630, pp. 5–41, 2009.
- [11] J. Jeong, F. Hussain, W. Schoppa, and J. Kim, "Coherent structures near the wall in a turbulent channel flow," *Journal of Fluid Mechanics*, vol. 332, pp. 185–214, 1997.
- [12] N. Hutchins, and I. Marusic, "Large-scale Influences in Near-wall Turbulence," *Philosophical Transactions of the Royal Society A*, vol. 365, pp. 647–664, 2007.
- [13] J. Turner, *Buoyancy Effects in Fluids*. Cambridge, UK: Cambridge University Press, 1973.
- [14] R.R. Gilpin, H. Imura, and K.C. Cheng, "Experiments on the Onset of Longitudinal Vortices in Horizontal Blasius Flow Heated from Below," *Journal of Heat Transfer*, vol. 100, pp. 71–77, 1978.
- [15] J.R. Maughan, and F.P. Incropera, "Secondary flow in horizontal channels heated from below," *Experiments in Fluids*, vol. 5, pp. 334–343, 1987.
- [16] H. Imura., R.R. Gilpin, and K.C. Cheng, "An Experimental Investigation of Heat Transfer and Buoyancy Induced Transition from Laminar Forced Convection to Tur-

- bulent Free Convection over a Horizontal Isothermally Heated Plate,” *Journal of Heat Transfer*, vol. 100, pp. 429–434, 1978.
- [17] G. Araya and L. Castillo, “DNS of turbulent thermal boundary layers up to $Re = 2300$,” *International Journal of Heat and Mass Transfer*, vol. 55, pp. 4003–4019, 2012.
- [18] X. Wu, and P. Moin, “Transitional and turbulent boundary layer with heat transfer,” *Physics of Fluids*, vol. 22, p. 8, 2010.
- [19] S.P.S. Arya, “Buoyancy effects in a horizontal flat-plate boundary layer,” *Journal of Fluid Mechanics*, vol. 68, no. 2, 1975.
- [20] H. Hattori, T. Houra, and Y. Nagano, “Direct numerical simulation of stable and unstable turbulent thermal boundary layers,” *International Journal of Heat and Fluid Flow*, vol. 28, pp. 1262–1271, 2007.
- [21] D. Li, K. Luo, and J. Fan, “Buoyancy effects in an unstably stratified turbulent boundary layer flow,” *Physics of Fluids*, vol. 29, p. 17, 2017.
- [22] A.K. Prasad, “Particle image velocimetry,” *Current Science*, vol. 79, no. 1, pp. 51–60, 2000.
- [23] E.A. Cowen and S.G. Monismith, “A hybrid digital particle tracking velocimetry technique,” *Experiments in Fluids*, vol. 22, pp. 199–211, 1997.
- [24] E.M. Sparrow, R.B. Husar, and R.J. Goldstein, “Observations and other characteristics of thermals,” *Journal of Fluid Mechanics*, vol. 41, no. 4, pp. 793–800, 1970.

Chapter 6

Conclusions

The hydrodynamic boundary layer is one of the classical problems in fluid mechanics. The dynamics and processes present in the boundary layer govern the interaction between solid and fluid which is critical to the continued operation and improvement of numerous engineering systems and to advancing our understanding of many environmental phenomena. A majority of the encountered boundary layer flows are turbulent and often involve heat exchange between the fluid and the solid boundary. In heated boundary layer flows, inertia interacts with the buoyant force and their interactions play a dominant role in regulating energy and mass exchange between the fluid and the heated boundary. The mixed convection turbulent boundary layer is a challenging fluid problem due to its natural complexity, however, it has great significance in a wide range of engineering and environmental fields. New contributions to the knowledge advancement on mixed convection turbulent boundary layer behavior are highly valuable to the fluid mechanics and broader engineering and scientific community.

Due to the combined complexity of mixed convection turbulent boundary layer flow and the governing equations, there is no analytical solution to this flow problem. While numerical

solutions can be found utilizing DNS, this approach is very computationally expensive. Furthermore, these numerical solutions often consider simplified assumptions that affect the extent to which these solutions can capture the underlying physics. This makes the experimental approach the most suitable for investigating this complex boundary layer flow phenomena. In experimental investigations, measurements of the key fluid variables, often velocity, temperature, and pressure, are recorded and analyzed to describe fluid phenomena.

One of the most important aspects of any fluid dynamics experiment is the technique used to characterize flow behavior. The nature and structure of turbulent flows make it challenging for a measurement technique to characterize and describe the turbulent behavior over all its length and time scales. The methods to analyze turbulent flow (e.g. Reynolds decomposition, low and high order statistical analysis, and etc.) require simultaneous three-dimensional flow velocity measurements for a comprehensive understanding of flow behavior. While point measurement techniques such as hot-wire anemometry and LDV can successfully measure all velocity components, there is limited information available on the spatial velocity distribution. Existing planar measurement techniques are highly effective for measurement with high spatial resolution, however these techniques only provide two velocity components. Three-dimensional flow measurement is a highly active area of research and development. The recently proposed Rainbow Volumetric Velocimetry technique and other recent color-based techniques show promise for high quality three-dimensional flow measurement, however these methods are often limited to small volume depths.F

To address knowledge gaps in the current scientific literature, the overall objectives of the present thesis work are as follows:

- Develop a volumetric illumination technique and associated data analysis algorithm for three-dimensional flow characterization.
- Determine the behavior of thermals in the mixed convection turbulent boundary layer

over a range of Richardson numbers.

- Identify and characterize the mechanism(s) responsible for the modification of turbulent boundary layer structure over a range of Richardson numbers.
- Investigate and characterize the mechanism(s) that govern the modification to turbulent statistics by wall heating within the mixed convection turbulent boundary layer.

The chapter 2 was focused on the development of a volumetric illumination technique and associated data analysis algorithm for three-dimensional flow characterization. The new illumination technique known as the color permutation method leverages mathematical combinatorics to greatly increase the out-of-plane spatial resolution for a limited number of colors by permuting the colors in the out-of-plane direction. This facilitates an extension of the volume dimensions such that larger volume depths can be measured. Similarly, an increase in out-of-plane spatial resolution is realized in the color permutation method over an illumination technique where no color permutation is utilized. A detailed algorithm was presented that extensively employed image processing and analysis techniques to construct three-dimensional trajectory fields from color streak images. The basic performance of the algorithm was tested on several synthetic images and results indicated the developed algorithm is feasible and suitable for further development. The newly developed technique shows promise for high quality flow visualization and measurement of three-dimensional flows such as the mixed convection turbulent boundary layer.

To characterize the mixed convection turbulent boundary layer, first it is necessary to investigate the behavior of unheated turbulent boundary layer flow. Experiments performed with the unheated wall act primarily as a reference case for mixed convection turbulent boundary layer experiments. However, despite over 100 years of turbulent boundary layer research, there are still numerous phenomena related to the unheated boundary layer flow where limited knowledge is available. One such area is on the turbulent statistics which are

an under-reported quantity in the turbulent boundary layer. The objective of chapter 3 was to characterize the spatial distribution of the turbulent velocity probability density function in the unheated turbulent boundary layer. Planar PIV measurements gathered flow velocity over multiple orthogonal planes with respect to the mean boundary layer flow direction. From the computed velocity fields, a multi-modal behavior was found in the PDF of the stream-wise turbulent velocity. The multi-modal signal was strongest in the buffer layer and found to not be associated with stream-wise vortices. A POD analysis revealed the multi-modality in the PDF was attributed to high order POD modes which are associated with a high turbulent kinetic energy dissipation rate magnitude. Reconstructed turbulent velocity fields from POD led to the hypothesis that the observed multi-modality is influenced by an energy transfer mechanism between large and small scale turbulent motions. The observations and conclusions of this study show similarity with the near-wall cycle phenomena reported in the literature.

In mixed convection turbulent boundary layer flow investigations, the presence of buoyant thermals was observed. Rarely in the current body of literature have thermals been documented in mixed convection turbulent boundary layer flow. There is very little available knowledge on how the behavior of thermals changes in the mixed convection flow regime as the relative contributions of inertia and buoyancy (i.e. Ri) are varied. The objective of chapter 4 was to investigate the behavior of thermals in the mixed convection turbulent boundary layer over a range of Richardson numbers. This research objective was achieved through a PIV-based visualization of thermals in the mixed convection turbulent boundary layer at Richardson numbers between 0.01 (inertia dominant flow) and 2.0 (buoyancy dominant flow). Captured images showed buoyant thermals rising through the boundary layer and multiple unique interactions between thermals and bulk boundary layer flow were observed. A texture-based image processing algorithm was developed to detect thermals in

experimental images. From images of detected thermals, the size and spatial distribution of thermals in 3D was determined. These results were used to define a three-dimensional mixed convection turbulent flow structure that featured near-wall convective cell-like behaviors. This thermal detection algorithm permitted, for the first time, the estimation of thermals' velocity and the velocity of "roll-ups" containing buoyant fluid.

The observed changes to the turbulent boundary layer structure reported in chapter 4 were significant. The objectives of chapter 5 are to (1) identify and characterize the mechanism(s) responsible for the modification of turbulent boundary layer structure over a range of Richardson numbers and (2) investigate and characterize the mechanism(s) that govern the modification to turbulent statistics by wall heating within the mixed convection turbulent boundary layer. The first objective of this chapter explains which mechanism is responsible for the change in turbulent boundary layer structure in mixed convection. The second objective is to explain how and why the identified mechanism operates in the observed manner. These objectives were achieved through multi-plane PIV experiments over the range $Ri_L = 0.01$ to 0.3 . Due to the low seed particle density of thermals, the velocity field could not be computed inside thermals. The thermal detection algorithm was used to remove thermals where no velocity could be calculated. From the computed velocity fields, Reynolds decomposition was performed and the turbulent statistics calculated. Results indicate that the wall-normal velocity, v , is strongly modified by the presence of wall heating. The modification this velocity component is due to the buoyant force which drives the observed convective cell-like behavior in the near-wall region and drives the intermittent bursting action of thermals from the production layer. The PDF of v became multi-modal at all Richardson numbers considered. This multi-modality propagated through v' and the spatial gradients of v which modifies multiple turbulent quantities including the Reynolds stresses, turbulent production, and dissipation rate. The magnitude of the secondary mode

in the PDF of v'^2 was found to increase monotonically with Ri , however neither Re or Gr showed the same trend. This indicates that inertia and buoyancy alone cannot describe the modification to flow structure, and the relative contributions of these forces is a key governing factor of mixed convection turbulent boundary layer flow behavior.

This study has thoroughly investigated mixed convection turbulent flow behavior. Multiple knowledge gaps in the literature were addressed through research on flow measurement techniques, unheated turbulent boundary layer investigations, and mixed convection turbulent boundary layer investigations.

New Knowledge Generated

- A new technique for volumetric color illumination based on color permutations.
- Formation of multi-modality in the probability density function of u' in the near-wall region of the unheated turbulent boundary layer.
- Identification of a potential mechanism responsible for the multi-modal behavior in the PDF of u' .
- Identification of key interactions between buoyant thermals and surrounding boundary layer flow.
- Image processing algorithm to detect thermals in experimental images.
- Size and spatial distribution of thermals was reported in 3D which was used to define the underlying mixed convection turbulent boundary layer flow structure.
- The velocity of buoyant thermals and vortex-like regions containing buoyant fluid was estimated for the first time in the literature.
- Clear evidence on the mechanism of turbulence modification by wall heating in the

turbulent boundary layer in the form of multi-modality in the PDF of v .

Each of the constituent research investigations performed in this study identified challenges and limitations in addition to the new contributions to the body of knowledge, outlining the direction of future research. Based on the findings of this study, the follow recommendations are made for future research.

Future Recommendations

- The newly developed color permutation method requires experimental implementation to identify practical limitations and integrate a technique for time-stamping to facilitate high-quality three-dimensional velocity field computation.
- The image analysis algorithm for the color permutation method only produces streak trajectories and must be modified to generate velocity fields using images of time-stamped streak trajectories.
- A deeper investigation into the POD analysis of the multi-modal u' PDF should be performed to validate the energy transfer mechanism hypothesis.
- The detailed temperature field inside the mixed convection turbulent boundary layer and associated thermals was not measured due to limitations in present temperature measurement systems. Future work should be focused on advancing temperature measurement techniques to capture these temperature fields, which are vital for further advancement of knowledge.
- Perform high-speed visualization of thermals at high Ri to further investigate the spatio-temporal dynamics of thermals and gain further insights into the interactions between thermal and adjacent boundary layer flow.
- Perform high quality velocity measurements utilizing a technique that can determine

flow velocity within thermals. This is crucial in order to characterize the turbulence associated with thermals which is important to understanding their role and contributions to the overall behavior in the turbulent boundary layer.

Appendix A

PIV Uncertainty

The uncertainty associated with PIV velocity computation was estimated based on the errors associated with particle size, AGW interpolation, velocity gradients, peak locking, image dynamic range, and out-of-plane motion [1]. The seed particle used in this study was theatrical fog with a particle diameter much smaller than the size of a pixel on the camera. Therefore, each particle is taken to occupy one pixel in the PIV image.

Uncertainty estimation in the computed PIV velocity fields was based on the approaches developed by Cowen and Monismith, and Prasad et. al. [1, 2]. Experiments conducted at $Re_\theta = 1700$ (unheated wall) and $Ri_L = 0.03$ (heated wall) were used to estimate uncertainty in this study as these experimental conditions produced the largest magnitude of velocity gradients. The procedure to compute the estimated PIV uncertainty is given below.

1. The mean values of the velocity gradients were computed in the stream-wise and wall-normal directions from raw PIV data. The maximum mean velocity gradient was in the stream-wise direction ($\partial u/\partial y$) at 4%.
2. Velocity gradient errors were estimated from Figure 5e in Cowen and Monismith [1].

Taking the sum of mean and RMS errors produced the total error due to the velocity gradient.

$$\epsilon_{VG} = 0.04 \text{ pixels} \quad (\text{A.1})$$

3. Given the fog seed particle is much smaller than pixel size thus we use a particle diameter of 1 pixel and estimate the error due to particle diameter using Figure 5a in Cowen and Monismith [1].

$$\epsilon_{SP} = 0.0668 \text{ pixels} \quad (\text{A.2})$$

4. Due to the small particle size additional error is introduced as discussed by Prasad et al. [2]. It was estimated that the error due to seed particle diameters approaching zero is 40% larger than for a seed particle with 1 pixel diameter. The findings of Prasad et al. [2] are based on a center of mass interpolation scheme which is substantially more likely to manifest peak-locking than the Gaussian scheme utilized in the present study [1]. To better describe the interpolation scheme used in this study, the particle size error was increased by 20%.

$$\epsilon_{SP} = 0.08 \text{ pixels} \quad (\text{A.3})$$

5. Error based on out-of-plane motion was estimated based on the magnitude of the wall-normal velocity. The mean plus one standard deviation of the wall-normal velocity was computed to correspond to a displacement of 12 μm . As this is much smaller than the 1 mm thick light sheet used in this study, error due to out-of-plane motion can be neglected.

6. The adaptive Gaussian window interpolation scheme utilized in this study has a known error found in Figure 5f of Cowen and Monismith [1]

$$\epsilon_{AGW} = 0.08 \text{ pixels} \quad (\text{A.4})$$

The total error in the stream-wise velocity is therefore

$$\epsilon_{AGW} + \epsilon_{SP} = 0.16 \text{ pixels} \quad (\text{A.5})$$

When converted to velocity this corresponds to ≈ 6.3 cm/s. Taking the errors in the wall-normal velocity to be the same as the errors in the stream-wise velocity leads to an overall error magnitude of ≈ 8.9 cm/s.

Bibliography

- [1] E.A. Cowen and S.G. Monismith, “A hybrid digital particle tracking velocimetry technique,” *Experiments in Fluids*, vol. 22, pp. 199–211, 1997.
- [2] A.K. Prasad, R.J. Adrian, C.C. Landreth and P.W. Offutt, “Effect of resolution on the speed and accuracy of particle image velocimetry interrogation,” *Experiments in Fluids*, vol. 13, pp. 105–116, 1992.

Appendix B

Introduction to Digital Image Processing

Traditionally photography and imaging utilize light sensitive material to capture light from a given scene that would be carefully processed in a dark room into a photograph. In this technique, the distribution of incident light on the light sensitive medium, i.e. camera film, is a continuous function of the medium's spatial coordinates. This is known as a continuous tone image. In recent years the field of digital photography has developed where digital photographs are captured.

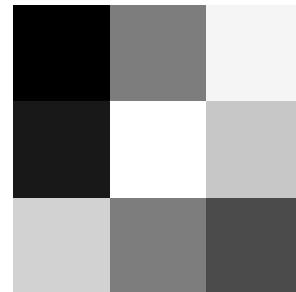
A digital image is a matrix of size $M \times N$ whose elements represent visual information [1]. Each matrix element is named a pixel, a portmanteau of “picture” and “element”. The quantity stored in each pixel is known as a gray level which represents the pixel's brightness. The number of gray levels in a digital image is often power of 2. An image with 256 gray levels is said to be an 8-bit image as $2^8 = 256$. Here 8 refers to the number of bits in the binary representation of the image. In an 8-bit image, the gray level of each pixel has the domain $[0, 255]$ and in general for an N -bit image this domain is $[0, 2^N - 1]$ [1]. Each possible gray level in an image corresponds to a brightness defined in a colormap. The colormap specifies how to map each gray level to a brightness on a display. The

conventional colormap defines the gray level zero to pure black and $2^N - 1$, e.g. 255 for an 8-bit image, to pure white with a linear scaling between the domain limits corresponding to various shades of gray. This discussion is limited to only gray-scale images for simplicity as the topics discussed here are applicable to color images.

Part of the goal of digital photography is to generate digital images that are indistinguishable from traditional photography. To this end, digital images must have sufficient spatial resolution and brightness resolution to accurately describe the underlying continuous light distribution. To achieve this goal, digital images often contain pixels that represent very small spatial regions relative to the image size and a large range of available gray levels, known as the dynamic range. Presently it is common to encounter digital images containing millions of pixels and at least 256 gray levels.

In this chapter primarily 8-bit gray-scale images and 1-bit binary images that can only represent black and white are covered. A sample 8-bit image is presented in B.1 where i refers to the row and j refers to the column. The image presented, \mathbf{A} , has dimensions $M = 3$ and $N = 3$. When displayed using a colormap, pixel $\mathbf{A}(0, 0) = 0$ corresponds to pure black and pixel $\mathbf{A}(1, 1) = 255$ is pure white. The whole image when viewed appears as illustrated below.

$$\mathbf{A}(i, j) = \begin{bmatrix} 0 & 125 & 245 \\ 24 & 255 & 199 \\ 210 & 125 & 75 \end{bmatrix} \quad (\text{B.1})$$



Visual representation of \mathbf{A} .

As digital images contain many pixels each with a gray level in an expected range, often

statistical approaches are employed to describe digital images. One of the most well-known statistical tools is the histogram which for digital images describes the number of pixels associated with each gray level [1]. For the image corresponding to \mathbf{A} there is one pixel associated with each of the gray levels present in the image except gray level 125 which has two pixels, $\mathbf{A}(0, 1)$ and $\mathbf{A}(2, 1)$. For a larger image such as the *Coins* image, the histogram is depicted in Figure B.1b.

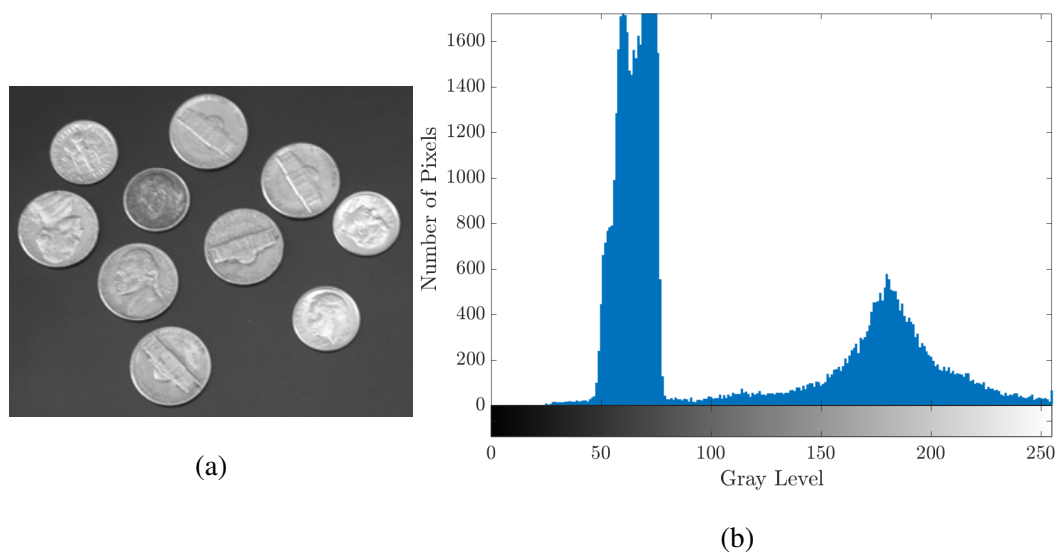


Figure B.1: The *Coins* image (a) and its corresponding histogram (b).

From the image histogram, several image behaviors can be readily identified and quantified. A mostly dark image will feature a histogram distribution strongly biased towards low gray levels [1]. Similarly a mostly bright image will produce a histogram skewed toward high gray levels. The term contrast refers to the amount of available dynamic range utilized by a given image. In an image with low contrast, the histogram will appear very narrow. On the other hand, a high contrast image is represented by a wide histogram that fills most to all of the available dynamic range. For the *Coins* image histogram, good contrast is observed as most of the dynamic range is utilized. The dark background occupies a large space in the image and correspondingly the histogram depicts many pixels whose gray level is around

75. The brighter coins produce the histogram signature near gray level 175.

When a digital image is captured there is often noise present in the generated image signal. Prior to extracting detailed information from images it is necessary to suppress noise. Moreover, enhancing visual quality and specific image features such as edges is often desirable. To achieve these goals the use of image filters are required.

There are two primary classes of image filters, spatial domain filters and frequency domain filters [1]. Spatial filters operate directly on the pixels by considering a local neighborhood around each pixel and modifying the central pixel according to a given equation or condition. One of the most well known spatial filters is the 2D convolution operation. In this process a given convolution kernel, a matrix of size $K \times L$ which is often square and usually both K and L are odd numbers, is rotated by 180 degrees to produce a computational molecule (\mathbf{g}). This then “slides” over the source image by visiting each pixel in \mathbf{A} according to the equation in B.2 to generate the filtered image \mathbf{C} .

$$\mathbf{C} = \mathbf{A} * \mathbf{g} = \sum_p \sum_q \mathbf{g}(i - p, j - q) \mathbf{A}(p, q) \quad (\text{B.2})$$

For this equation it is clear that the convolution is only defined for values of p and q that produce a valid coordinate in \mathbf{C} . However this means pixels near the image boundaries of \mathbf{A} will be ignored. To avoid this issue the size of \mathbf{A} is increased often by adding zeros [1]. The result of this process is a filtered image where the gray level of each pixel was modified based on the adjacent pixels according to the convolution kernel. The choice of convolution kernel enables a wide range of outcomes for the convolution operation. This includes arithmetic averaging also known as a low-pass filter, weighted averaging, and derivative calculation. The averaging filters are often used for noise reduction and blurring while

derivative filters are found in edge detection and image enhancement applications [1].

Order-statistic filters operate in a similar manner to the convolution filter. A user-defined window, often a square region, is generated and this traverses the source image selecting a local neighborhood around a central pixel. The pixels in each local neighborhood are sorted according to gray level and a user-specified command is applied to the sorted pixels. This command often selects the smallest, largest, or median gray level and stores this in the corresponding central pixel in the output image. This process is repeated for all pixels in the source image. When the median command is utilized this operation is named the local median filter, one of the most powerful noise suppression filters available.

The second class of filters operate in the frequency domain. Before any filtering is performed however, an image in the spatial domain must be transformed to the frequency domain. This is achieved using the Fourier Transform, which in the 2D discrete image context is the 2D Discrete Fourier Transform (DFT). Mathematically, the DFT takes the form shown in B.3 for a source image, \mathbf{A} , and DFT output, $\hat{\mathbf{D}}$ where both images are of size $M \times N$ [1].

$$\hat{\mathbf{D}}(m, n) = \frac{1}{\sqrt{MN}} \sum_{p=0}^{M-1} \sum_{q=0}^{N-1} \mathbf{A}(p, q) e^{-2\pi i \left(m \frac{p}{M} + n \frac{q}{N} \right)} \quad (\text{B.3})$$

In this definition the indices p and q refer to spatial positions in \mathbf{A} while indices m and n correspond to frequency coordinates in $\hat{\mathbf{D}}$. The exponential contains the imaginary unit $i = \sqrt{-1}$. The DFT provides information on the frequency content of an image. In a noisy image or an image with sudden changes in gray level, it is expected to find a significant high frequency signature in the DFT. Similarly for images with low noise or very slow variations in gray level the DFT will show a stronger low frequency signal.

In the context of filtering, it is desirable to enhance or reduce certain frequencies found in an image. A low-pass filter in the frequency domain acts to reduce the high-frequency magnitude present in the DFT of a source image. Often this is for the purpose of suppressing noise. Similarly, a high-pass filter can be used to reduce the low-frequency contribution in an image. This is suitable for edge enhancement. Regardless of filter type used, the filtering operation is achieved through functions such as the Gaussian or Butterworth filter [1]. After this function is applied to the DFT of the source image, the inverse DFT is calculated producing the final output image.

Often in image processing, there are one or more objects of interest within a given image that must be detected. These objects include but are not limited to letters, numbers, and geometric shapes. It is necessary to develop a technique to separate the desirable regions of an image from the undesirable noise and background signal. The process and methodology of categorizing an image into one or more distinct groups is known as image segmentation [1]. In most applications the goal is to separate desirable foreground objects from the background, consequently there are only two distinct groups.

The most basic form of segmentation, known as manual segmentation, requires an external observer to manually select which pixels of an image belong to each group. This technique is highly sensitive to observer bias produced by the presence or absence of experience and is an unsuitable approach for large quantities of images due to observer fatigue. Gray level thresholding eliminates these problems and can easily be applied to large collections of images. In this technique, each pixel is classified based on whether its gray level is above or below a user-defined threshold. This introduces the problem of selecting a suitable threshold for a given image.

Consider the *Coins* image in Figure B.1a. It is desirable to determine the total amount of money in the picture. To achieve this, it is necessary to segment the coins from the back-

ground. From Figure B.1b, it is clear that the dark background and bright coins produce a weakly bimodal histogram. In this case one obvious choice of threshold is a point between the two histogram peaks. An arbitrarily selected gray level of 100 can be used to segment the image to produce Figure B.2a.

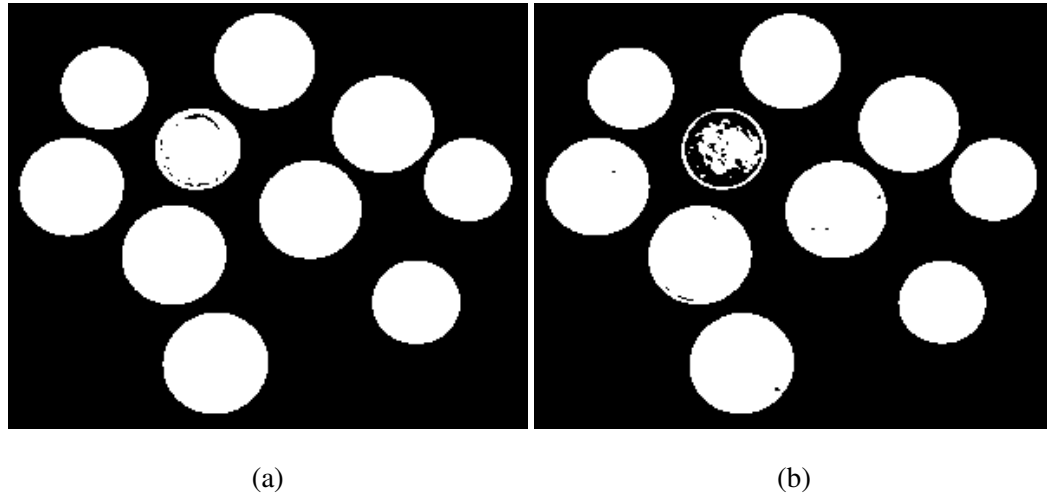


Figure B.2: The *Coins* image segmented via (a) gray level threshold at 100 and (b) segmented using Otsu's method where the calculated threshold was 126.

In this segmentation result white corresponds to regions above the threshold, in this case detected coins, and black is the background. Comparing to the original *Coins* image shows very good agreement with the actual coins. The choice of 100 as a gray level threshold was arbitrary in this example. From the histogram it is possible to reasonably select any gray level between ≈ 80 and ≈ 140 . In general the histogram of an image is not clearly bimodal, making threshold selection difficult. A more robust technique is therefore required to determine a suitable gray-level threshold.

Otsu's method [2] first developed in 1979 determines a threshold for segmenting an image into two groups based on the histogram distribution for a given image. The technique seeks to calculate the threshold for which the gray level variance of each segmented group

is minimized. When Otsu's method is applied to the *Coins* image, a threshold of 126 is calculated leading to the segmentation result depicted in Figure B.2b.

Comparing the segmentation result by Otsu's method to the manually selected threshold find that overall the results are very similar. The coins were generally well detected in both approaches. One coin towards the middle of the image was not well captured using the threshold generated by Otsu's method. Comparing with the source image reveals that this particular coin has a darker surface finish making a large part of it incorrectly placed in the background. In a practical application this issue can be resolved with subsequent processing as the coin's perimeter was well captured, sufficient to identify its value.

Gray level thresholding is the most basic technique of image segmentation. In the decades since Otsu's method there have been numerous newly developed segmentation techniques based on a wide range of image criterion including histograms, higher order statistics, geometry, and other advanced concepts [1].

Bibliography

- [1] W. Pratt, *Introduction to Digital Image Processing*. Boca Raton, FL: CRC Press, 2014.
- [2] N. Otsu, "A Threshold Selection Method from Gray-Level Histograms," *IEEE Transactions on Systems, Man, and Cybernetics*, vol. 9, no. 1, 1979.

Curriculum Vitae

Name:	Kadeem Dennis
Post-Secondary Education	<p>University of Western Ontario London, ON 2016 - 2020 Ph.D.</p> <p>University of Ottawa Ottawa, ON 2013 - 2016 M.A.Sc.</p> <p>University of Ottawa Ottawa, ON 2009 - 2013 B.A.Sc. <i>Cum Laude</i></p>
Honours and Awards:	<p><i>ASME Graduate Returning Scholar</i> 2019</p> <p><i>Ontario Graduate Scholarships</i> 2018-2019</p> <p><i>ASME Graduate Student of the Year</i> 2018</p> <p><i>Milton Van Dyke Award</i> American Physical Society, Division of Fluid Dynamics L. Leblanc, M. Manoubi, K. Dennis, Z. Liang, and M. I. Radulescu (2012). <i>Dynamics of unconfined spherical flames: influence of buoyancy.</i> American Physical Society, Division of Fluid Dynamics, Gallery of Fluid Motion, arXiv:1210.8438v2 [physics.flu-dyn] http://arxiv.org/abs/1210.8438v2 2012</p>

- Related Work Experience:** Teaching Assistant
The University of Western Ontario
2016 - 2019
- Part-Time Professor
University of Ottawa
January 2015 to April 2015
- Research Assistant
University of Ottawa
September 2012 to January 2013
- Theses:** *Experimental Investigation on the Impact of Wall Heating on Mixed Convection Turbulent Boundary Layer Flow Structure*
Doctoral Thesis
University of Western Ontario
- Mechanical Modification of Cells by Pressure Waves and its Application to Traumatic Brain Injury*
Masters Thesis
University of Ottawa
- The Implementation of a High Power LED in Schlieren Photography and Construction of a Large-Scale Shadowgraphy System*
Undergraduate Thesis
University of Ottawa

Journal Publications:

K. Dennis, L. Maley, Z. Liang, and M. I. Radulescu (2013). *Implementation of Large-Scale Shadowgraphy in Hydrogen Safety Phenomena*. Fifth International Conference on Hydrogen Safety.

L. Leblanc, M. Manoubi, K. Dennis, Z. Liang, and M. I. Radulescu (2013). *Dynamics of unconfined spherical flames: Influence of buoyancy*. Physics of Fluids. Volume 25, Issue 9. DOI: 10.1063/1.4820018

Conference Publications:

K. Dennis and K. Siddiqui (2019). Characterization of Thermals in a Heated Turbulent Boundary Layer. Proceedings of The ASME-JSME-KSME Joint Fluids Engineering Conference 2019 (AJKFluids 2019).

K. Dennis and K. Siddiqui (2019). Investigation of Turbulent Flow Behavior in a Heated Boundary Layer. Proceedings of The ASME-JSME-KSME Joint Fluids Engineering Conference 2019 (AJKFluids 2019).

K. Dennis and K. Siddiqui (2019). Three-Dimensional Characterization of Bursting and Sweeping Phenomena in the Turbulent Boundary Layer. Proceedings of The Joint Canadian Society for Mechanical Engineering and CFD Society of Canada International Congress 2019 (CSME-CFDSC Congress 2019).

K. Dennis and K. Siddiqui (2018). Multi-plane Characterization of the Turbulent Boundary Layer. Proceedings of the 5th Joint US-European Fluids Engineering Summer Conference (FEDSM 2018).

K. Dennis and K. Siddiqui (2018). A Multi-color Technique for Volumetric Flow Measurements. Proceedings of the Canadian Society for Mechanical Engineering International Congress 2018 (CSME Congress 2018).

K. Dennis and K. Siddiqui (2017). A Multi-color Grid Technique for Volumetric Velocity Measurements. Proceedings of the 2017 ASME Fluids Engineering Division Summer Conference (FEDSM 2017).

K. Dennis, G. Maines, D. Modulevsky, K. Hudier, M. Obeid, A. Pelling, J.J. Lee, M.I. Radulescu (2017). *On the Mechanism of Cellular Damage by Shock Waves*. 24th International Symposium on Military Aspects of Blast and Shock (MABS24).

K. Dennis, L. Maley, Z. Liang, and M. I. Radulescu (2014). *Implementation of Large-Scale Shadowgraphy in Hydrogen Explosion Phenomena*. International Journal of Hydrogen Energy. Volume 39, Issue 21. pp 11346-11353. July 15 2014.

DOI: 10.1016/j.ijhydene.2014.05.002

M. Manoubi, K. Dennis, Z. Liang, and M. I. Radulescu (2013). *Large Scale Visualization of Unconfined H₂-Air Deflagrations in Non-Homogeneous Mixtures*. 24th International Colloquium on the Dynamics of Explosions and Reactive Systems (ICDERS).

L. Leblanc, M. Manoubi, K. Dennis, Z. Liang, and M. I. Radulescu (2013). *Influence of Buoyancy in Unconfined Deflagrations: Experiments in Soap Bubbles*. Seventh International Seminar on Fire and Explosion Hazards.

L. Leblanc, M. Manoubi, K. Dennis, Z. Liang, and M. I. Radulescu (2012). *Dynamics of unconfined spherical flames: influence of buoyancy*, American Physical Society, Division of Fluid Dynamics, Gallery of Fluid Motion, arXiv:1210.8438v2

Public Speaking and Presentations:

Engineering Open House Presenter. Conducting live laboratory demonstrations and presenting information about the engineering program to prospective students and their families. Every March and November from 2016 to present.

K. Dennis and K. Siddiqui (2019). *Characterization of Thermals in a Heated Turbulent Boundary Layer*. ASME-JSME-KSME Joint Fluids Engineering Conference 2019 (AJK-Fluids 2019).

K. Dennis and K. Siddiqui (2019). *Investigation of Turbulent Flow Behavior in a Heated Boundary Layer*. ASME-JSME-KSME Joint Fluids Engineering Conference 2019 (AJK-Fluids 2019).

K. Dennis and K. Siddiqui (2019). *Three-Dimensional Characterization of Bursting and Sweeping Phenomena in the Turbulent Boundary Layer*. Joint Canadian Society for Mechanical Engineering and CFD Society of Canada International Congress (CSME-CFDSC Congress 2019). June 2-5 2019. London, Canada.

K. Dennis and K. Siddiqui (2018). *Multi-plane Characterization of the Turbulent Boundary Layer*. 5th Joint US-European Fluids Engineering Summer Conference (FEDSM 2018). July 2018. Montreal, Canada.

K. Dennis and K. Siddiqui (2018). *A Multi-color Technique for Volumetric Flow Measurements*. Canadian Society for Mechanical Engineering International Congress 2018. May 2018. Toronto, Canada.

K. Dennis, L. Maley, Z. Liang, and M. I. Radulescu (2013) *Implementation of Large-Scale Shadowgraphy in Hydrogen Safety Phenomena*. Fifth International Conference on Hydrogen Safety. September 2013. Brussels, Belgium.

L. Leblanc, M. Manoubi, K. Dennis, Z. Liang, and M. I. Radulescu (2013). *Influence of Buoyancy in Unconfined Deflagrations: Experiments in Soap Bubbles*. Seventh International Seminar on Fire and Explosion Hazards. May 2013. Providence, Rhode Island, USA.

Technical Skills

Manufacturing: Circuits for sensing and data acquisition, metal and woodworking, mill and lathe experience.

Computer Languages: C/C++, Java, LabVIEW, L^AT_EX, MATLAB, Python.

Computer Applications: OpenFOAM, OpenMP, SolidWorks.

Computer Operating Systems: GNU/Linux, Windows.